Modelling and control of an buoyancy driven airship

Xiaotao Wu

Ecole Centrale de Nantes

ÉCOLE DOCTORALE

Sciences et Technologies de l'Information et Mathématiques

Année 2011 N° B.U. :

THESE DE DOCTORAT EN COTUTELLE

Diplôme délivré d'une part, par l'Ecole Centrale de Nantes
et par l'Université de Technology de Chine du Sud (Chine) d'autre part

Spécialité : AUTOMATIQUE ET INFORMATIQUE APPLIQUEE

Présentée et soutenue publiquement par :

Xiaotao WU

le : 30 Mai 2011

à l'Université de Technology de Chine du Sud, Guangzhou, Chine

TITRE

Modélisation et Commande d'un Dirigeable Propulsé par la Force de Flottabilité

JURY

Président :	Weizhou SU	Professeur, Université de Technology de Chine du Sud, Chine
Rapporteurs :	Rogelio LOZANO	Directeur de Recherche, CNRS
	Chun-Yi SU	Professeur, Université Concordia, Canada
Examinateurs :	Claude MOOG	Directeur de Recherche, CNRS
	Yueming HU	Professeur, Université de Technology de Chine du Sud, Chine
Invité :	Hailong PEI	Professeur, Université de Technology de Chine du Sud, Chine

Directeur de thèse : Claude MOOG
Laboratoire : IRCCyN
Co- Directeur de thèse : Yueming HU
Laboratoire : Faculté d'Automatique, Université de Technology de Chine du Sud, Chine

N° ED : 503-127

Abstract

A new concept of airship without thrust, elevator or rudder is considered in this thesis. It is actuated by a moving mass and a mass-adjustable internal air bladder. This results into the motion of the center of gravity and the change of the net lift. The development of this concept of airship is motivated by energy saving. An eight degrees-of-freedom complete nonlinear mathematical model of this airship is derived through the Newton-Euler approach. The interconnection between the airship's rigid body and the moveable mass is clearly presented. The dynamics in the longitudinal plane is analyzed and controlled through a LQR method, an input-output feedback linearization, and the maximal feedback linearization with internal stability. Thanks to maximal feedback linearization, an efficient nonlinear control is derived. In this process, modelling, analysis, and control are solved for special cases of the airship, which become gradually closer to the most general model. The most constrained special case reduces to a two degree-of-freedom system. It is shown that the basic properties of this two DOF mechanical system remain instrumental for the analysis and synthesis of advanced airship models. These properties are far from being obvious from the most complex model. Through a singular perturbation approach, the superposition of the two control actions in the longitudinal plane and in the lateral plane is shown to achieve the control of the dynamics in three dimension.

RÉSUMÉ

Un nouveau concept de dirigeable sans propulseur, ni gouvernail de direction, ni gouvernail de profondeur est considéré dans cette thèse. Il est actionné par une masse mobile et une vessie d'air en interne dont la masse est réglable. Cela résulte en un déplacement du centre de gravité et un changement de la force de flottabilité nette. Le développement de ce concept de dirigeable est motivé par les économies d'énergie. Un modèle complet à huit degrés de liberté de ce dirigeable est obtenu par l'approche de Newton-Euler. L'interconnection entre le corps rigide du dirigeable et de la masse mobile est clairement présentée. La dynamique dans le plan longitudinal est analysée et commandée par la méthode LQR, une linéarisation entrée-sortie, et la linéarisation maximale par bouclage, avec stabilité interne. Grâce à la linéarisation maximale par bouclage, une commande non linéaire efficace est déduite. Dans ce processus, la modélisation, l'analyse et la commande sont résolues pour les cas particuliers du dirigeable qui deviennent peu à peu moins contraints et se rapprochent du cas le plus général. Le cas le plus contraint se réduit à un système qui a deux degrés de liberté. Il est montré que les propriétés de base de certains systèmes mécaniques simples restent déterminantes pour l'analyse et la synthèse des dirigeables avancés. Ces propriétés sont loin d'être évidentes sur le modèle complet. Grâce à une approche de perturbations singulières, la superposition des deux actions de contrôle dans le plan longitudinal et dans le plan latéral conduit à une commande pertinente pour la dynamique en trois dimensions.

REMERCIEMENTS

First of all, I would like to thank my two supervisors: Dr. Claude H. Moog and Prof. Yueming Hu.

Dr. Moog, I appreciate for your enduring guidance, encouragement and support throughout my three-year PhD program in France. I am very fortunate and honored to be able to work with you, Dr. Moog. During the last three years, you always show your knowledgeability, responsibility, and patience to me. I look forward to learning more from you for much longer.

Prof. Yueming Hu, I really appreciate for your involvement six year ago when I applied a master position. During these six years, you gave me lots of opportunities to cultivate my capacity. I especially would like to thank your encourage in this period. Without your encourage, I can not have this achievement. This six-year period, I have been working with your, is the most important segment in my lift.

I would like to thank the *China Scholarship Council* for its generous fund support for my study in France. With this fund support, I can focus on the research in the last three years. I also would like to thank the *Education Department of the Chinese Embassy in France* and the *Guangzhou Service Center for Scholarly Exchange* for lots of advantage they offered.

I sincerely thank all my instructors at *Institut de Recherche en Communications et Cybernétique de Nantes (IRCCyN)* for sharing their insights and enthusiasm, and being generous with their time. I Would like to particularly thank Dr. Aoustin Yannick, Dr. Chevallereau Christine, Dr. Chriette Abdelhamid, and Dr. Khalil Wisama, who have repeatedly helped me in complex situations. The director of IRCCyN Dr. Malabre Michel and the secretary of the control team Ms. Thureau Emily also helped me in numerous ways. Lots of my colleagues in IRCCyN, like Ezzat Marwa, Menard Tomas, and Henaff Sebastien, also offer lost of helps to me.

Thanks to my teachers and colleagues in the *Automation College* and the *Engineering Research Center of Precision Electronic Manufacturing Equipments MOE* of *South China University of Technology*. Particularly, I thank Dr. Liu Yu who gave me lots of supports during my PhD study.

My sincere thanks to my family for their love, understanding, and persistent encouragement. My parents, Wu Jishu and Zhan Yuxiang, elder brother Wu Juntao, sister-in-law Li Ying, and my nephew Wu Zhuoyan, have always been a great source of inspiration.

Dedication

dedicated to my family

Nomenclature

α the angle of attack

θ the pitch angle

λ_2,λ_1,λ_0 parameters of the feedback controller

ξ the flight path angle

ρ_a the density of the air

∇ the volume of the airship

$\mathbf{\Omega}$ the angular velocity of the airship in the body frame, $\mathbf{\Omega} \equiv (\Omega_1, \Omega_2, \Omega_3)^T$

Ω_i the ith element of $\mathbf{\Omega}$

$\boldsymbol{b}$ the position of the airship in the inertial frame

$\boldsymbol{B}$ the momentum of the added mass

$\boldsymbol{P_p}$ the momentum of the moveable mass, $\boldsymbol{P_p} \equiv (P_{p1}, P_{p2}, P_{p3})^T$

$\boldsymbol{P}$ the total momentum of the airship's rigid body

C_i^j aerodynamic coefficients

$\boldsymbol{e_1}, \boldsymbol{e_2}, \boldsymbol{e_3}$ the body frame unit vectors

$\boldsymbol{F_a}$ the aerodynamic force, $\boldsymbol{F_a} \equiv diag\{X_a, Y_a, Z_a\}$

$\boldsymbol{F_{at}}$ the aerodynamic force with respect to the body frame

$\boldsymbol{F_I}$ the added inertial force

$\boldsymbol{F_s}$ the total external force acting on the airship's rigid body

$\boldsymbol{F_{int}}$ the internal force acting on the moveable mass by the body

$\mathcal{I}$ the identity matrix of appropriate dimensions

$\boldsymbol{F_{GB}}$ the resultant force of the gravity and the buoyancy in the inertial frame

$\boldsymbol{F_{GBt}}$ the resultant force of the gravity and the buoyancy in the body frame

J the second diagonal element of $\boldsymbol{J_s}$

J_i the ith diagonal element of $\boldsymbol{J}$

$\boldsymbol{J_f}$ the added inertial matrix, $\boldsymbol{J_f} \equiv diag\{m_{44}, m_{55}, m_{66}\}$

$\boldsymbol{J_s}$ the moment of inertia of m_s, $\boldsymbol{J_s} \equiv diag\{J_x, J_y, J_z\}$

$\boldsymbol{J}$ the moment of inertia of m_s and the added mass, $\boldsymbol{J} = diag\{J_1, J_2, J_3\} = \boldsymbol{J_f} + \boldsymbol{J_s}$

k the parameter of the feedback controller

$\boldsymbol{i, j, k}$ the inertial frame unit vectors

$\boldsymbol{K}$ the angular momentum of the added mass

$\boldsymbol{K_s}$ the total angular momentum of the airship's rigid body

m_b the mass of the internal air bladder

m_h the uniformly distributed mass of the hull

m_s the stationary mass of the airship

m_v the total mass of airship, $m_v = m_s + \bar{m}$

m_w the center offset mass

$\bar{m}$ the mass of the moveable mass

m_i the ith element of $\boldsymbol{M}$

m_0 the net buoyancy of the airship

m the mass of the airship displaced air

M_a the aerodynamic pitch moment

$\boldsymbol{M_a}$ the aerodynamic moment, $\boldsymbol{M_a} \equiv diag\{L_a, M_a, N_a\}$

$\boldsymbol{M_{at}}$ the aerodynamic moment with respect to the body frame

$\boldsymbol{M_{add}}$ the inertia matrix

$\boldsymbol{M_f}$ the added mass matrix, $\boldsymbol{M_f} \equiv diag\{m_{11}, m_{22}, m_{33}\}$

$\boldsymbol{M_{GB}}$ the resultant moments of gravity and buoyancy in the inertial frame

$\boldsymbol{M_{GBt}}$ the resultant moments of gravity and buoyancy in the body frame

$\boldsymbol{M_I}$ the added inertial moment

$\boldsymbol{M_s}$ the total external moment acting on the airship's rigid body

$\boldsymbol{M_{int}}$ the internal moment acting on the moveable mass by the body

$\boldsymbol{M}$ $\boldsymbol{M} \equiv diag\{m_1, m_2, m_3\} = \boldsymbol{M_f} + m_s\mathcal{I}$

$\boldsymbol{r_b}$ the position vector of m_b in the body frame

$\boldsymbol{r_p}$ the position vector of the moveable mass in the body frame, $\boldsymbol{r_p} \equiv (r_{p1}, r_{p2}, r_{p3})^T$

$\boldsymbol{r_w}$ the position vector of m_w in the body frame

$\boldsymbol{R_1}$ the rotation matrix from the body frame to the inertial frame

$\boldsymbol{R_2}$ the rotation matrix from the velocity frame to the body frame

T_{add} the kinetic energy of fluid disturbances

u the internal force applied on the moveable mass along the e_1 axis, $u \equiv u_1$

$\boldsymbol{u}$ the internal force acting on the moveable mass by the airship, $\boldsymbol{u} \equiv (u_1, u_2, u_3)^T$

u_4 the control of the mass of the internal air bladder

$\boldsymbol{v}$ the velocity vector of airship in the body frame, $\boldsymbol{v} \equiv (v_1, v_2, v_3)^T$

$\boldsymbol{v_p}$ the velocity of the moveable mass in the body frame

v_p the velocity of the moveable mass in the vertical plane

X_a the drag element in the aerodynamic force

Z_a the lift element in the aerodynamic force

Contents

List of Figures

List of Tables

Chapter 1

Introduction

Contents

1.1 A Brief History of the Airship

1.1.1 Early period: before 1960s

The airship, also called blimp, has a much longer history than fixed-wing aircrafts, and it is the first aircraft to enable controlled and powered flight. The airship was conceived by a French aeronautical theorist Meusnier by the first time in 1784, soon after that, a French inventor Blanchard piloted a ancient airship and crossed the English Channel (Wikipedia, 2010).

The first engine-powered airship emerged in 1852 with a steam engine equipped on the it. In 1884, the first fully controllable airship, *La France* - a French army airship, was launched by Renard and Krebs. This airship was the first one who did the full round trip flight with a landing on the starting point.

In 1900, with the launch of the *Zeppelin LZ*1 as shown in Fig. 1.1, ”The Golden Age” of airships began, and this is also the beginning of the most successful and well-known airship family: *the Zeppelins*. ”The Golden Age” of airships lasted to the 1940s. During this period, airships had been developed dramatically, both in application and technology.

In application, there mainly existed the following aspects:

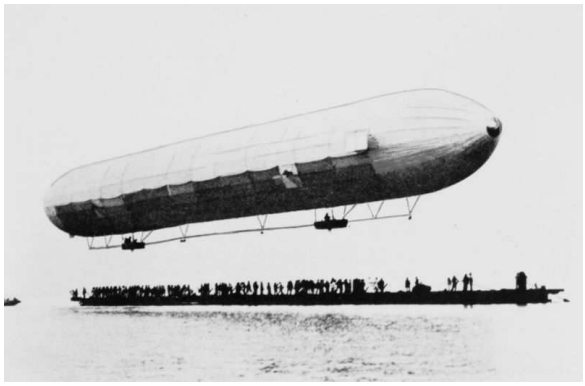

Figure 1.1: First Zeppelin LZ1 flight shown above a boat at Lake Constance. Zeppelin LZ1 was the first truly successful experimental rigid airship with 128 m length, 11.70 m diameter, 11,300 m^3 volume, 28 km/h maximum speed. It used a 130 kg weight to control the attitude by sliding it forward or aft.

Figure 1.2: LZ 127 Graf Zeppelin airship. The first airship finished the round-the-world flight and the polar (the arctic) flight. It also executed 64 regular transatlantic trips, traveling mainly from Germany to Brazil. It had been operated safely for 9 years.

- As bombers in combats. This military purpose only executed in the World War I before 1917 due to the vulnerability of the airship.

- As observing platforms. This is an important role for the airship in combats and this service lasted for a long time. In the early war, small blimps were used to scout air attacks from counterparts. Later, US navel used lots of blimps to escort ships in the World War II, and this achieved a great success. Blimps equipped with radars were sent to search submarines and protected ships from attacks. The duties of airship also included aerophoto reconnaissance, naval mine-laying and mine sweeping.

- As long distant transport vehicles. Many international flights were operated by airships. Some of them kept high level safety records, for instance, ZL 127 $Graf\ Zeppelin$ as shown in Fig. 1.2 flew over 1,600,000 km (including the first circumnavigation of the globe) without any single passenger injury.

From a technical aspect, lots of fundamental researches had been done in this periods, especially in the 1920s and 1930s. These fundamental researches located in materials, structures, aerodynamic forces, control, et al, which is the base of the airship engineering. Some outstanding scientific pioneers and their classical works are listed in the following: the researches on the aerodynamics of airships by M. Munk (Munk, 1922, 1923, 1924), W. S. Diehl (Diehl, 1922) et al., the researches on the structure by E. H. Lewitt (Lewitt, 1922), S. Friedrich (Friedrich, 1923) et al., the researches on the stability and

control of the airship by A. F. Zahm (Zahm, 1926), F. Rizzo (Rizzo, 1924) et al. and the researches on the materials by R. Haas, A. Dietzius (Haas and Dietzius, 1918) et al. These details can be found in (Khoury and Gillett, 1999).

As well-known cases, during the 1920s and the 1930s, many spectacular disasters happened and caused large casualties, such as the crash of the ZRS 4-Akron in 1933 and the explosion accident of the Hindenburg in 1937. However besides the problems of the reliability of airships, there still existed lots of human factors which caused the accidents. For instance, the crash of ZR-1 was due to the wrong command which ordered the airship to fly into appalling weather conditions (Purandare, 2007). The history of airship development before 1960 is displayed in Fig 1.3.

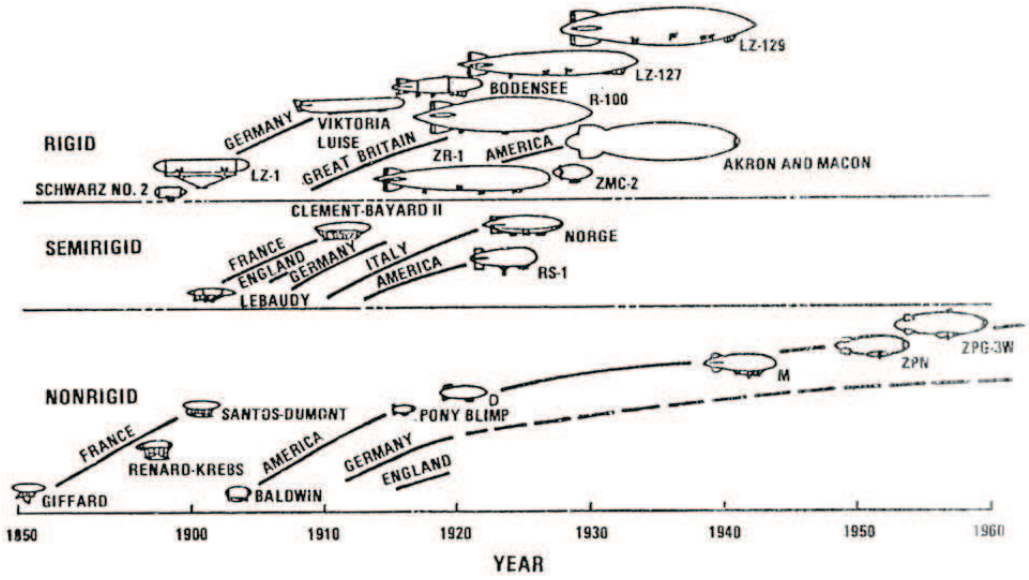

Figure 1.3: History of airship development. *Source* (Goodyear Aerospace Corp., 1975)

1.1.2 Modern period: from 1960s to 1990s

After World War II, the US Navy continued to successfully operate their blimps in early warning role (US Navy, 2008; Marcy, 1978). However, the oil crisis happened in 1973, the interest in the airship arose because people wanted to find a aircraft with low fuel consumption. Because of this motivation, some important international conference took place to discuss the new applications and technical peculiarities of the airship (Vittek, 1975). During the 1970s and 1980s, some airships were designed and constructed, for instance, the AD500/Skyship-500 and Skyship-600 by a British company *Airship Industries*.

A very important airship program in this period was the SkyShip/Sentinel 5000. In 1987, *Westinghouse/Airship Industries* were awarded a 170 million dollar contract to design an Airborne Early Warning (AEW) airship which was required to undertake a 3-day endurance at high altitude with

various surveillance equipments (Gomes, 1990). The airship to fulfill this mission is also called the YEZ-2A and it is the first large military non-rigid airship to be built after World War II. According to the plan, this airship was 129 m length and 7000 cubic meters. Its commercial variant was designed to have a 140-seater twin deck gondola. But after a full scale prototype mock-up was constructed in 1988, the program was stopped because of funding problems.

These modern airships started some new applications, such as advertising, passenger sight-seeing, TV photography, surveillance purposes et al (see Fig. 1.4 and 1.5) (Liao and Pasternak, 2009). However, from the technical point of view, there is not much innovation from the airships in the early of the twentieth century.

Figure 1.4: A Goodyear airship. Goodyear began producing airship envelopes in 1911. It's airships are used for advertising purposes and for use as a television camera platform for aerial views of sporting events. Most of them are semi-rigid airships and manned airships

Figure 1.5: A Zeppelin NT airship. The german company recovered the construction of the Zeppelin series airship in 1990s. Different from the original rigid zeppelin airships, the modern zeppelin airships are semi-rigid. These airship can take 2 crews and 12 passengers with maximum speed 125 km/h, who is smaller than the old zeppelin.

1.2 Autonomous Unmanned Airship

1.2.1 Recent development of the airship

Even though the US SkyShip/Sentinel 5000 was not finished and did not have a chance to prove its viability in both military and commercial aspects. But it brought a new concept to the world-High Altitude Platform (HAPs) as shown in Fig. 1.6 which has attracted many people's interest in the

recent twenty years.

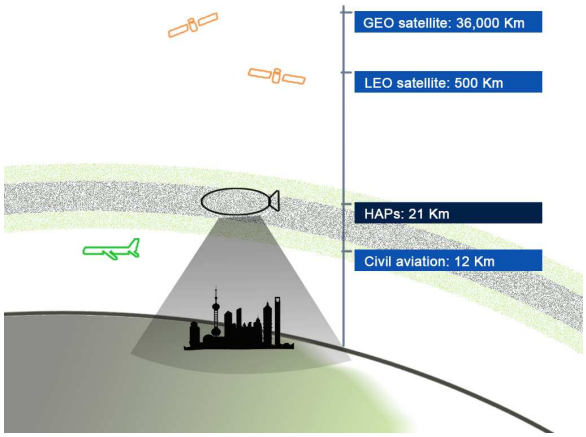

Figure 1.6: A High Altitude Platform (HAP) is a quasi-stationary platform which provide communication or surveillance service to a large area. This platform locates in the stratosphere. It is expected to stay in the sky for years without maintenance.

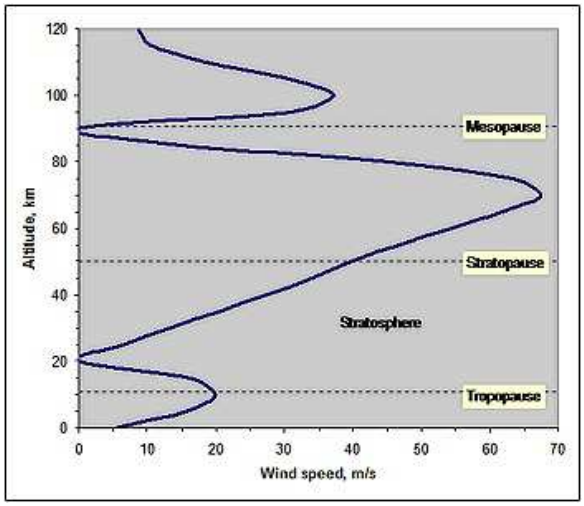

Figure 1.7: Average wind speed in the stratosphere is minimal at altitudes of about 19-22 km (Values vary with season and location). This is the reason why the HAPs is proposed at an altitude around 21 km.

High altitude platforms, also called stratospheric platforms, are located 17- 22 km above the ground, and keep quasi-geostationary positions. The stratosphere is characterized by a highly stable weather condition with stable winds (as shown in Fig. 1.7) and no cloud. Such a platform has the potential capability to serve as a wireless communication relay station and as a high resolution observing station (Widiawan and Tafazolli, 2006; Elfes et al., 1998; Tozer and Grace, 2001; Aragón-Zavala et al., 2008), which can cover a very large area. Thus, high-quality communication and surveillance can be achieved with a considerably smaller cost. Communications services including broadband, WiMAX, 3G, and emergency communications, as well as broadcast services, are under consideration in this mission. Recently, a HAP experiment has taken place on 31st August 2005 at Kiruna, Sweden, which has successfully tested the usage of a HAP at 25 km altitude, operating in the mm-wave band to send data via Wi-Fi to a coverage area of 60 km in diameter (Grace et al., 2005).

Planes (such as M55 Geophysica) (Myasishchev Design Bureau, 2002), unmanned hydrogen powered planes (such as US global observer) and unmanned solar powered planes (such as NASA pathfinder plus) also can be used as the HAPs. However, in contrast to these vehicles, a high altitude unmanned airship has the following features: driven by solar power makes its long aerial endurance, and generally this platform can take 1000 kg to 3000 kg payload which is low-cost to carry out similar tasks which are usually done by satellites (Haifeng et al., 2007). Lockheed Martin's experiment in

2008 had achieved to keep the airship in the sky for 2 weeks (Lockheed Martin Corporation, 2008).

From the beginning of the 21st century, major countries in the world have independently started research on high altitude platforms (US Navy, 2008). In 2003, Lockheed Martin was awarded a US$ 149 million contract from the US Missile Defense Agency to develop an airship that can maintain a quasi-geostationary position at 20 km. Right now, the second period of the research is carried out, and because of budgetary constraints, a full-scale prototype was expected in the summar of 2010 (Defense Industry Daily, 2006; Lockheed Martin Corporation, 2008; Hopkins, 2010). Europe has the ESA-HALE program (Lindstrand, 2000; Grace et al., 2004) which leads the stratospheric communication research based on HAP. Japan has a so-called SPF program (Yokomaku, 2001). There is also similar research in UK, South Korea and Brazil. In January 2010, a solar-powered airship has been successfully tested and it is expected to cross the English Channel soon (ProjetSol'R, 2010). In June 2010, Northrop Grumman has won a contract with the US Army to provide a Long-Endurance, Multi-intelligence Vehicle (LEMV). The platform selected by Northrop Grumman is based on a hybrid airship, and is designed to lift a payload of 1200 kg to 6000 m for periods more than 3 weeks (Northrop Grumman, 2010). A summary of airship projects in recent years are listed in Tab. 1.1.

Designer	Model	Unique features	Max. altitude (m)	Max. speed (mph)	Country
ATG/WorldSkyCat	Skycat-20	VTOL and cargo aircraft	3,000	97	UK
Skyhook-Boeing	SkyHook JHL-40	Heavy lift four rotor and 40-ton lifting capacity	N/A	80	Canada/US
Lockheed Martin	HAA	Solar-powered, high altitude,unmanned, and un-tethered	18,000	28	US
Techsphere Systems International	SA-60	Spherical shape and low altitude	3,000	35	US
Southwest Research Institute	HiSentinel Airship	Stratospheric and solar-powered	> 22,000	N/A	US
21st Century Airship Inc.	N/A	Spherical shape	Low altitude	35	Canada
Millennium Airship Inc.	SkyFreighter	Hybrid, heavylift,and VTOL	6,000	80	Canada/US
Ohio Airships Inc.	DynaLifter PSC-3	Winged hybrid,VTOL, and heavy lift	3,000	115	US
Zeppelin Luftschifftechnik Gmbh	Zeppelin LZ NT-07	Semi-rigid, internal rigid framework consisting of carbon fiber triangular frames and aluminum members	2,500	81	Germany
LTA Corporation	Alize 50	Lenticular shape, semi-rigid,and VTOL	2,000	81	France
AEROS	Aeroscraft ML866 model	Control of static heaviness,heavy lift,and VTOL	3,000	115	US
Northrop Grumman/Airship Industries	N/A	Long endurance and multi-intelligence	6,000	N/A	US/UK

Table 1.1: Summary of airship projects in recent years.

The remarkable difference from ancient airship researches is that modern researches concentrate

on the unmanned flying. That means the airship no more needs any pilot on board to control the airship. But based on partial remote human control, feedback control and autonomous waypoint navigation, an airship is expected to finish a certain task automatically. This kind of airship is called autonomous unmanned airship as shown in Fig. 1.8.

Many works have been devoted to solve problems encountered in this process, such as new surface materials, energy suppling method (Knaupp and Mundschau, 2004) and control problems. This thesis focuses on the modelling and control problems.

1.2.2 Basic knowledge of the unmanned airship

From the airship's appearance, there is no much difference between a manned airship and an unmanned one. Both have the following similar structures (see Fig. 1.8). Control surfaces (elevators and rudders), a gondola and engines are fixed on the hull. Control surfaces are used to control the heading of movement, and engines offer the thrust. Some airships use vectored thrust which replaces control surfaces to control the heading. In the inside of the airship, there exist two elastic inner bladders, one for storing helium, the other is an adjustable air bladder is used to control the airship's motion in the vertical direction (see Fig. 1.9).

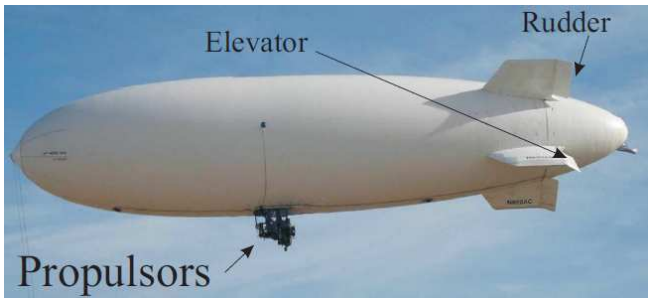

Figure 1.8: Conventional unmanned airships are operated for a wide range of missions from scientific research to surveillance duties. Unmanned airships can be designed to meet specific mission parameters set by clients and include unique features such as hybrid power systems, multiple redundancy, autopilot and an advanced handling system.

Different from a wing-fixed airplane, generally, an airship has a slow translational velocity and a large volume, which leads the inertial forces to be considered (for a fixed-wing airplane, this is not the case). Another problem is that the center of buoyancy (CB), the center of volume (O) and the center of gravity (CG) locate at different places as shown in Fig. 1.10.

Current unmanned airship research is based on a classical 6 degrees-of-freedom equations of motion which are developed using the Newton-Euler method for each degree of freedom. These equations are presented in the form as the following by the conventional notations:

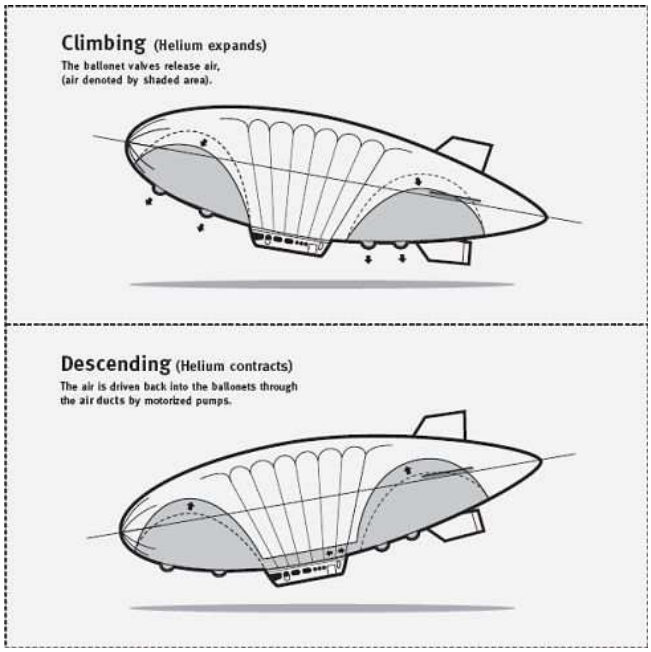

Figure 1.9: Climbing and descending control through adjusting the inner air bladders. Opening the valves to release the air increases the net lift and leads to climb. Contrarily, blowing the air into the bladders decreases the net lift and leads to descend.

$$M\begin{bmatrix} \dot{u} \\ \dot{v} \\ \dot{w} \\ \dot{p} \\ \dot{q} \\ \dot{r} \end{bmatrix} = F_d(u,v,w,p,q,r) + A(u,v,w,p,q,r) + G(\lambda_{31},\lambda_{32},\lambda_{33}) + P(\text{propulsion forces and moments}) \tag{1.1}$$

where, M=6x6 Mass matrix

F_d=6x1 matrix Dynamic Forces vector

A=6x1 matrix Aerodynamics vector

G=6x1 matrix gravitational and Buoyancy vector

P=6x1 matrix Propulsion vector

Generally, there exist two important assumptions for this model. One is that the airship is assumed to be a geometrical symmetrical ideal airship. Another one is that the center of the gravity and the center of volume of the airship are assumed to be exactly overlapped.

The controls of this airship are the deflections of the control surfaces (or the vector thrust) and the thrust. The mission of the unmanned airship is to track a given trajectory and keep a desired attitude.

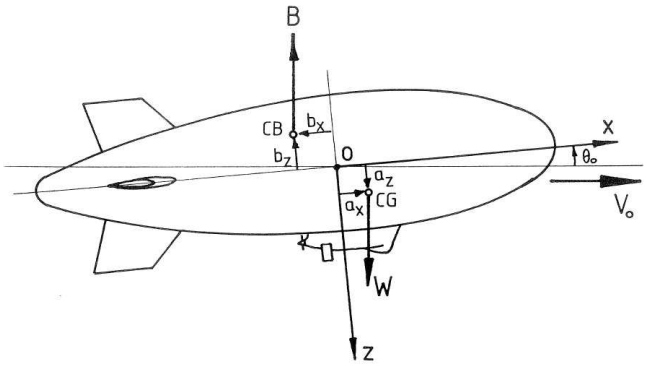

Figure 1.10: The center of gravity and the center of buoyancy do not overlap. This is an obvious different point from the fixed-wings airplanes. This misalignment causes complexity and unstability *Source* (Cook, M. V., 1990).

1.2.3 A survey on the control strategy

A general control strategy on the autonomous unmanned airship whose model presented by (1.1) is a linear control scheme based on linearized and decoupled models. More precisely, the original nonlinear model is linearized through some approaches, such as a small perturbation method, and then, the system states are decoupled according to the dynamic planes they belong to, such as the states on the longitudinal plane and the ones on the lateral plane (Khoury and Gillett, 1999). Controls are designed for the linearized and decoupled subsystems instead of the original nonlinear system (1.1). Methods which are used to design the control include PID (Purandare, 2007), LQR (Liu, 2009), robust control (Ouyang, 2003), damping feedback (Cai et al., 2007; Ortega et al., 2002; Astolfi et al., 2002), backstepping methods (Repoulias and Papadopoulos, 2008; Beji et al., 2002; Coron, 1999) and others (Healey and Lienard, 1993; Kim et al., 2003; Khoury and Gillett, 1999). In these references, conventional actuators, such as control surfaces and thrusts, are used to stabilizer the attitude and the position (Morin and Samson, 1995; Pettersen and Egeland, 1999).

One major achievement of modern nonlinear control is feedback linearization (Isidori, 1989; Conte et al., 2007; Isidori and Moog, 1988). This theory has been widely applied for flight controls (Lane and Stengel, 1988; Sun and Clarke, 1994). Unfortunately the airship system is not fully linearizable, the main drawback is that a nonlinear internal dynamics will remain in the closed-loop system which may be unstable. To prove the stability of this nonlinear internal dynamics is a challenge which is solved in this thesis.

1.3 Glide and Buoyancy Engine

To achieve a longer aerial endurance with lower energy consuming, some mechanisms inspire new solutions. The first one is glide. Glide is a motion for heavier-than-air objects which are supported in flight, airborne or underwater, by the dynamic reaction of the medium against their lifting surface, and this flight does not depend on any engine. A force analysis of an airplane in this case is shown in Fig. 1.11.

Another motion is the buoying or sinking which is caused by the net lift. If the net lift of a vehicle is adjustable by varying the weight or volume of the vehicle, it can buoy and sink in the medium. Semi-rigid, rigid airships and submarines adjust the weight to vary the net lift to execute the buoying and sinking. Some autonomous underwater vehicles employ a deformable bladder equipped on the hull to adjust the volume of the vehicle to vary the net lift (Davis et al., 2002). Such a device to adjust the net lift is called the buoyancy engine, and a type of that is shown in Fig. 1.12.

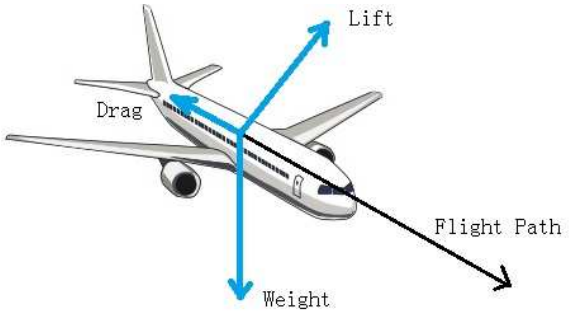

Figure 1.11: The forces acting on the whole aircraft during stable glide. Under this situation, the components of the gravity equals to the drag and lift.

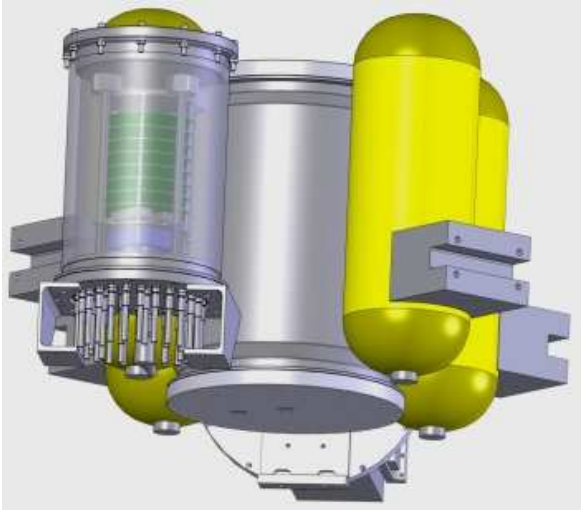

Figure 1.12: An buoyancy pump (engine). This buoyancy pump is equipped on a kind of underwater glider - Slocum. It adjusts the mass of the vehicle through pumping the water.

1.3.1 Gliding vehicles

There are lots of gliding vehicles, such as glider aircrafts, paragliders, et al.. These vehicles can fly freely under the control of the pilot. What's more efficient is that when these vehicles are equipped with propellers, pilots have more "degrees-of-freedom" to control the vehicles. There are also some researches discussing the possibility of steering these gliding vehicles in an autonomous way. From the results available to now, the mathematical models of these crafts are very complicated with a

large number of degrees-of-freedom and complex nonlinear couplings (Zaitsev and Formalskii, 2008; Toglia and Vendittelli, 2010).

1.3.2 Underwater gliders

Due to the same object of the airship research, oceanographers look for an oceanic observation platform which can cruise a long distant and for a long time underwater or offshore with limit energy. In 1989, Henry Stommel published a far-thinking article (Stommel, 1989) envisioning a global ocean observing system based on "a fleet of 1000 small neutrally-buoyant floats" which "migrate vertically through the ocean by changing ballast, and they can be steered horizontally by gliding on wings at about a 35 degrees angle". A class of autonomous underwater vehicles realized Stommel's vision. As opposed to conventional underwater vehicles, they do not use propellers which usual are electrical engines. Autonomous underwater gliders change their volume and buoyancy to cycle vertically in the ocean and use the net lift on wings to convert this vertical velocity into forward motion. This driving mechanism is called as a kind of buoyancy engine. Wing-lift drives forward motion both during the ascend and descend of the vehicles, so they follow sawtooth paths. The shallowest points on the sawtooth are at the surface where satellite navigation and communication are carried out (Jenkins et al., 2003), which made possible a class of small, inexpensive instrument platforms that are changing the way the ocean is observed.

There exist four mature underwater gliders which are Spray, Seaglider, Slocum Batttery and Slcoum Thermal (Davis et al., 2002; Jenkins et al., 2003). These gliders can cover a range 3,000 km to 5,000 km in one to several months with limited on board electrical power. The typical horizontal speed of these gliders is quite low, about 0.25 m/s as opposed to propeller-driven vehicles which travel several meters per second. This does not mean the gliders can not move quickly, but actually, there is a tradeoff between operating range and speed, which is illustrated by the Fig. 1.13 and 1.14 (Furlong et al., 2007). This also can be explained as: normally, the value of the thrust of a motion is proportional to the cube of speed, so higher speed leads smaller range.

1.4 Hybrid Airship and the Buoyancy-driven Airship

Through the analysis in the section 1.2, conventional unmanned airship with propellers is a good choice for a long aerial-endurance platform. According to the relationship of "best transport method" versus speed and lift for vertical/short take-off (V/STOL) aircraft illustrated in (Purandare, 2007), airships are therefore best suited for low-speed applications (Liao and Pasternak, 2009).

To extend the operating range for normal lift and slow speed application, a hybrid airship is an

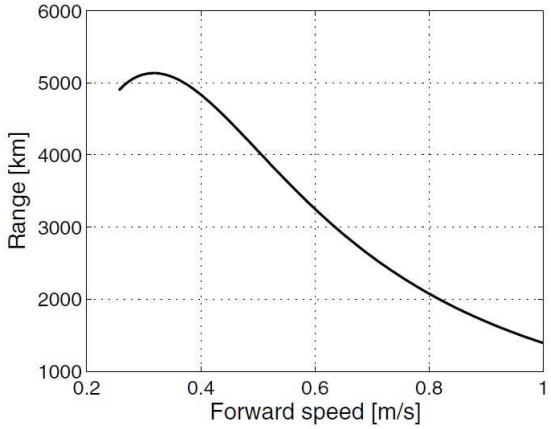

Figure 1.13: Modelled range vs speed for the concept long range AUV. The cruising speed is slower, the operating range is larger and the vehicle is more efficient *Source* (Furlong et al., 2007).

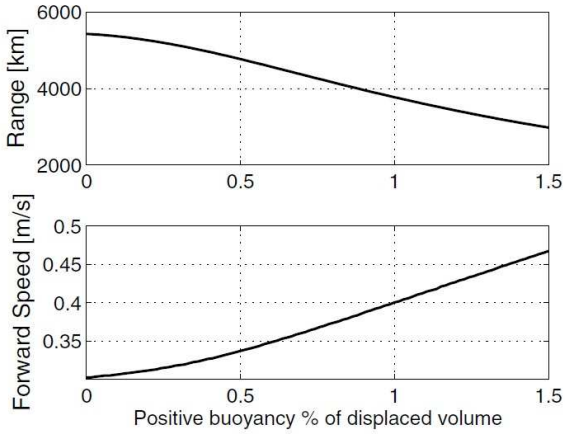

Figure 1.14: Maximum range and associated forward speed for the long range concept AUV vs % buoyancy. An increase in the vehicle's net buoyancy will greatly reduce the total range of the underwater vehicles *Source* (Furlong et al., 2007).

optimal choice. A Hybrid airship is a general term for an aircraft that combines characteristics of heavier-than-air (airplane or helicopter) and lighter-than-air technology. British skycat program, P-791 hybrid airship program developed by Lockheed Martin and Aeroscraft ML866 are good examples, which are designed to be the best of the two worlds by retaining the high speed of conventional aircraft and lifting capacity of aerostatic aircraft.

For long airborne endurance airships, Lockheed Martin Ltd. reported a patent design in 2007, which describes an airship/fix-wing airplane hybrid with conventional propellers as shown in Fig. 1.15. Another Lockheed Martin's hybrid airship with aerodynamic lift capability is shown in Fig. 1.16.

Another hybrid buoyancy-driven airship was proposed by Purandare in (Purandare, 2007), whose appearance is shown in Fig. 1.17. This hybrid airship employs a gliding mechanism and a buoyancy engine which are depicted previously to drive itself, and it drops the conventional propeller and control surfaces. This hybrid airship is called the buoyancy-driven airship in the thesis, and it is the research topic of thesis. The details of this airship is depicted in the next chapter.

1.5 Research Motive and Contributions

The buoyancy-driven airship uses a buoyancy engine to control the ascent and descent, in addition with the gliding mechanism to move forward. Through the prior research in (Purandare, 2007), the buoyancy-driven airship is efficient when the angle of attack in flight is small, and the buoyancy-

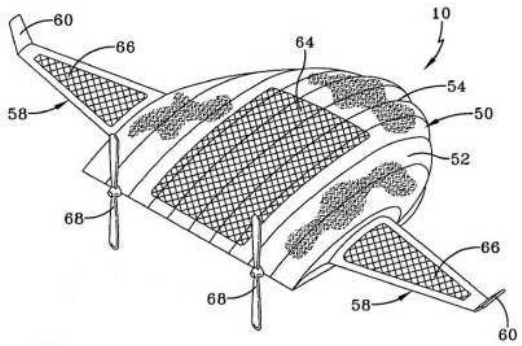

Figure 1.15: Lockheed Martin's inflatable, high-altitude, endurance airship. This hybrid airship uses conventional propeller, without buoyancy engine *Source* (Lavan, 2007).

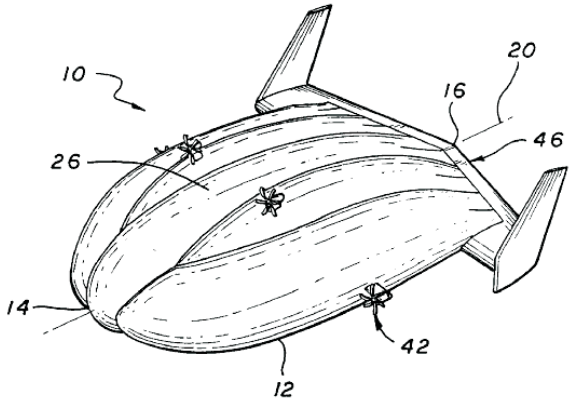

Figure 1.16: Lockheed Martin's semi-buoyant vehicle with aerodynamic lift capability *Source* (Eichstedt et al., 2001).

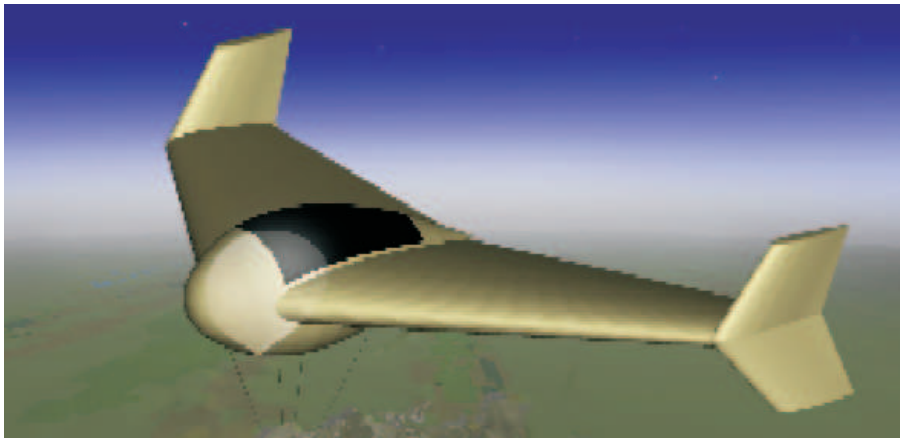

Figure 1.17: The proposed buoyancy-driven airship *Source* (Purandare, 2007).

driven airship is a good substitute of the conventional airship in many situations. It also offers a novel mechanism for unmanned vehicles. Moreover, it employs an internal moveable mass to control the vehicle's attitude, which is a very important mechanism for lots of systems with internal dynamics. Thus, the research of this thesis makes sense for the research of HAPs, UAVs, and lots of complex mechanical systems.

The buoyancy-driven airship is a novel object. To present, the only available reference on this domain is the thesis (Purandare, 2007), and this is a challenge for this research. In this thesis only some theoretical issues are argued, and the main contributions consist of the following four aspects:

- A complete 8-DOF mathematical model for the buoyancy-driven airship in 3D is derived for the first time. In this area, two approaches with the internal dynamics modeled are offered. The modelling is significantly simplified by viewing the airship's rigid body and the moveable mass

independently.

- The fundamental structures of the complex model are investigated by analysis, design and simulations. Many properties of the airship's structure are established, and these properties make sense for the control design.

- Various controls of the planar dynamics are constructed. Approaches based on LQR, input-output feedback linearization, and maximal feedback linearization are presented and compared. It has been shown that the airship is not fully feedback linearizable. Maximal feedback has been solved. Although the latter techniques are usually not trackable for complex aeronautical models, it has been possible to derive analytic control solutions. A major challenge is internal stability and a suitable choice of linearizing coordinates could circumvent this issue and the internal stability has been proven.

  The control laws are state feedbacks and thus require the knowledge of all state available. This will eventually require the design of nonlinear observers. However this latter issue is out of the scope of this thesis.

- A Control scheme based on singular perturbations for the motion in 3D is derived. In this frame, the analytical condition for a stable spiral motion is derived.

Chapter 2

Concept Design and Efficiency Problem

Contents

As introduced in the Introduction chapter, The main difference between the conventional airship and the buoyancy-driven airship is that it employs a movable point mass and a mass-adjustable internal air bladder to control the motion of the airship. They replace the conventional propellers and control surfaces. This new mechanism has been adopted to achieve a high efficiency for aerial vehicles. The structure and the operating mechanism of the buoyancy-driven airship is explicitly explained in this chapter; useful physical properties are presented as well. Comparing with the conventional airship and airplane, the energy efficiency of the buoyancy-driven airship is analyzed through an approximate analytical approach, and some results are presented.

The contribution of this chapter consist in the analysis of the structure and the efficiency problem of the buoyancy-driven airship. From this analysis, the structure of the airship is split into two parts as: the moveable mass which impacts the airship's attitude, and the aerodynamic forces which impacts the flight path. For the efficiency problem, the ideal propulsive powers of both the conventional airship and the buoyancy-driven airship are compared. Partial content of this chapter has been published in (Wu et al., 2011a).

This chapter is organized as follows: section 2.1 explicitly depicts the concept of the buoyancy-driven airship; section 2.2 analyzes the dynamic system through an analytical approach; section 2.3 compares the ideal propulsive powers of the conventional airship and of the buoyancy-driven airship.

2.1 The Considered Hybrid Airship

The main structure of the buoyancy-driven airship proposed in (Purandare, 2007) is shown in Fig. 2.1, which has dropped the conventional actuators, such as diesel or electrical engine, elevator, rudder, etc.

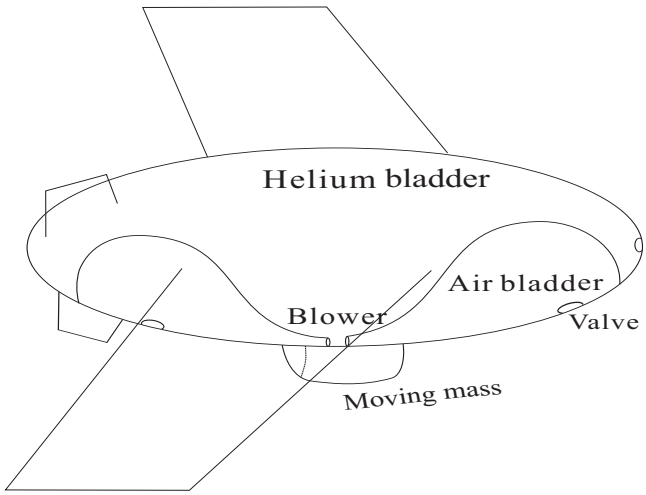

Figure 2.1: Structure of Buoyancy-Driven Airship.

2.1.1 General description

For the structure of the buoyancy-driven airship, it mainly consists of an envelope, wings, an internal air bladder, and a movable mass. These parts are briefly depicted in the following.

The envelope and the wings

Obviously, the function of the envelope and the wings of an airship is to offer enough net lift for the payload for scientific and other instruments. The envelope is assumed to be a rigid one in this thesis. For the modelling of non-rigid airships, (Bennaceur, 2009; Azouz et al., 2002) gives some details.

The lift, namely buoyancy, of the airship comes from two parts: one is the static lift offered by the airship body. This is due to the density of the helium which is smaller than the density of air. Another part is the aerodynamic lift caused by the turbulent mixing of air of varying pressure on the upper and lower surfaces of the body and the wings. The functions to compute the values of these two lift terms will be presented in the modelling section.

For aerial vehicles in flight, beside the lift, there also exists the drag (Kanikdale, 2004). Generally, this drag consists of two primary parts, one is the lift-induced drag, namely induced drag, which

occurs as the result of the creation of lift on a three-dimensional lifting body, such as the wing or fuselage of an airplane. The relation of the lift and the induced drag is shown in Fig. 2.2. Another primary part of the drag consists in the parasitic drag. Parasitic drag, is the drag caused by moving a solid object through a fluid. Parasitic drag is made up of multiple components including viscous pressure drag, namely form drag, and drag due to surface roughness, namely skin friction drag. For different shapes of the objects, the percentage of form drag and skin friction drag is different, as shown in Tab. 2.1.

For an airplane in flight, its drag consists of induced drag and parasite drag (Lutz and Wagner, 1998; Kanikdale, 2004). The variations of these two drags are shown in Fig. 2.3. This curve can be explained as: induced drag tends to be greater at lower speeds because a high angle of attack is required to maintain lift, creating more drag. However, as speed increases the induced drag becomes smaller, but parasitic drag increases because the fluid is flowing faster around protruding objects.

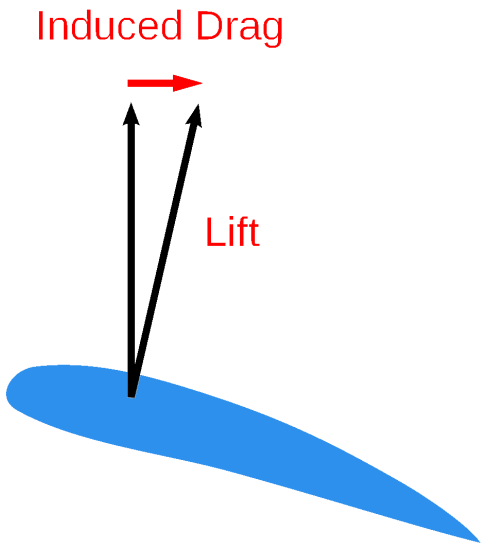

Figure 2.2: The induced drag and the lift. In aviation, the induced drag occurs as the result of the creation of lift on a three-dimensional lifting body *Source* (Wikipedia, 2011).

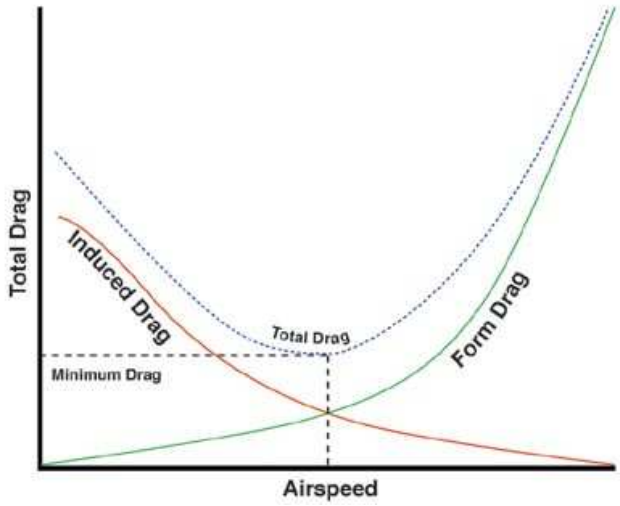

Figure 2.3: The power curve: parasitic and induced drag vs. airspeed. It's important for pilots to maintain certain airspeed where the total drag is the lowest *Source* (Wikipedia, 2011).

For the design of the airship, decreasing total drag is important, no matter for conventional airship or buoyancy-driven airship. But in opposition to fixed-wing aircrafts, airships are subject to significant parasite drag, both form drag and skin friction drag. This is caused as airship's lift is mainly provided by the lighter-than-air ballonets. For a given volume, the percentage of form drag and skin friction drag has relation with a diameter-to length ratio (d/l) (Lutz and Wagner, 1998). The percentage of form drag will increase when the ratio d/l increases as shown in Tab. 2.1. Besides drag, for a given

Table 2.1: From drag and skin friction drag vs. different shapes *Source* (Wikipedia, 2011)

Shape and flow	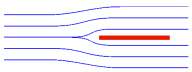	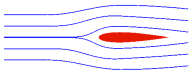	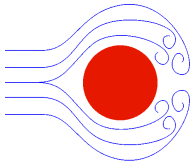	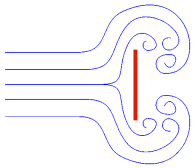
Form drag	0	~10%	~90%	~100%
Skin friction	~100%	~90%	~10%	0

volume, it is also important to decrease the total surface-area since the envelope is a payload for the system.

The center body of the airship is designed to have a low total drag and a high volume/surface-area ratio. To achieve a tradeoff, the shape is a revolved NACA0050 airfoil profile whose coordinates are shown in Fig. 2.4, and it is decided by (2.1).

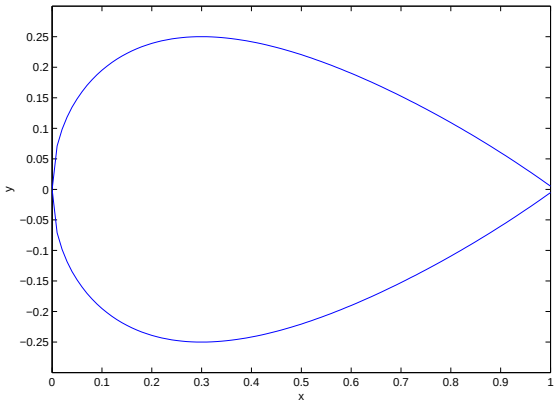

Figure 2.4: The airship's body is an elongated body which is a revolution of such NACA0050 airfoil.

$$y = \frac{t}{0.2}c\left[0.2969\left(\frac{x}{c}\right)^{\frac{1}{2}} - 0.126\left(\frac{x}{c}\right) - 0.3515\left(\frac{x}{c}\right)^{2} + 0.2843\left(\frac{x}{c}\right)^{3} - 0.1015\left(\frac{x}{c}\right)^{4}\right] \tag{2.1}$$

where c is the chord length, and t is the maximum thickness as a fraction of the chord.

Note that the aerodynamics is not an important area in our research. So, sometimes the result is given without lots of analysis. In the rest of this thesis, a simple ellipsoid is used to replace the above revolved NACA0050 airfoil for simplicity.

The internal air bladder

Fig. 2.5 illustrates the internal air bladder fill/discharge system. The volume of the air bladder is variable. The compressor/blower is used to fill the bladder with ambient air, and the valve is used to

release the air from the bladder. By this way, the mass of the bladder is changed, which causes the variations of the total weight of the airship. Thus, its net buoyancy (buoyancy force minus weight) is controllable.

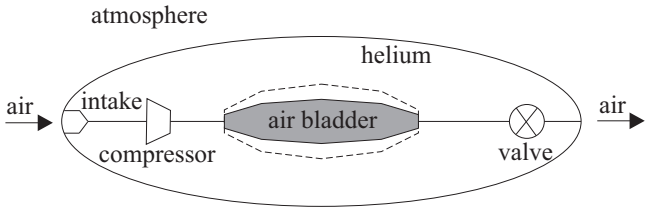

Figure 2.5: The internal air bladder and the mass adjusting mechanism. The altitude of the airship is controlled by this mechanism.

When the ambient air is drawn into the air bladder, the net buoyancy becomes negative, thus, the airship falls down. Conversely, when the air is released from the internal air bladder, the net buoyancy becomes positive, thus, the airship rises. The altitude of the buoyancy-driven airship is mainly controlled by this way.

Here, the description of this mechanism is simplified since the actual realization is more complex; it has to consider the variation of the internal/external pressure, which is beyond the scope of this thesis.

The moveable/moving mass

The moveable mass is located at the bottom of the airship and it can move on the $e_1 - e_2$ plane of the body frame as shown in Fig. 2.6. It can not move in the vertical direction. The motion in the vertical direction is useless for the control and the stability the airship. Actually, the center of gravity of the whole system should be under the horizontal symmetrical plane $e_1 - O - e_2$ (Leonard, 1997a,b).

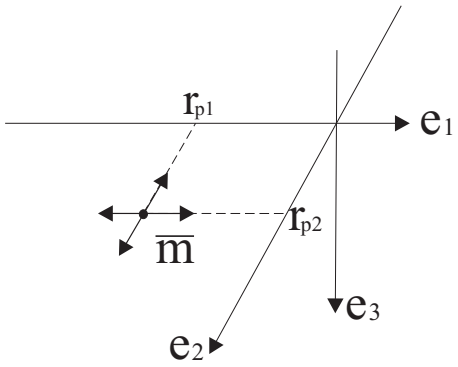

Figure 2.6: The moveable masses moves on the $e_1 - e_2$ plane.

With the motion of the moveable mass, the center of gravity of the airship *CG* moves, which leads to the variation of the attitude of the airship, which is explicitly analyzed in next section and simulated

in the chapter 4.

The use of a moveable mass to control the attitude is an important and interesting mechanism. Some other mechanical system, such as underwater gliders and re-entry vehicles, involve a similar device. However, different forms of moveable masses exist, for instance an additional round mass ring is used as a moveable mass for a underwater glider (Eriksen et al., 2001).

2.1.2 The operating mechanism

The mechanism to operate this kind of airship is described as follows. When the air releases from internal air bladder, the mass of the airship reduces, thus, the net lift becomes positive and the airship rises. Meanwhile, the moveable mass moves to the rear of the airship; the airship gets a positive pitch angle θ, which yields a forward aerodynamic component force acting on the airship. This component force makes it move forward (see Fig. 7.3 and the trajectory is the BC segment of Fig. 7.5). Conversely, when pumping air into the internal air bladder, the mass of the airship increases, thus, the net lift becomes negative and the airship falls. With the moveable mass driven by the body to the front, the pitch angle θ becomes negative, which still yields a forward aerodynamic component force. Therefore the airship moves forward and downwards (see Fig. 7.4 and the trajectory is the AB segment of Fig. 7.5). If the moveable mass is moving to the sides, then the airship will roll. Due to the coupling of roll and rotation moments, the airship flies to the right or left directions (Purandare, 2007). Fig. 7.5 illustrates a typical trajectory of the airship in the vertical plane.

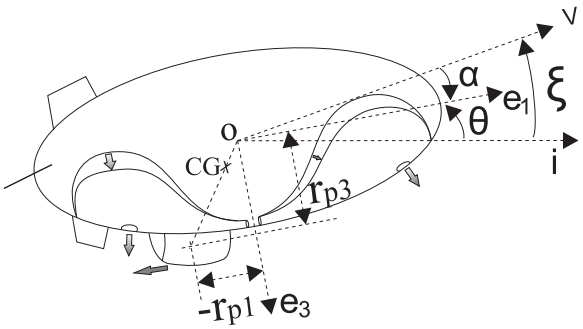

Figure 2.7: The Airship moves upwards and forward.

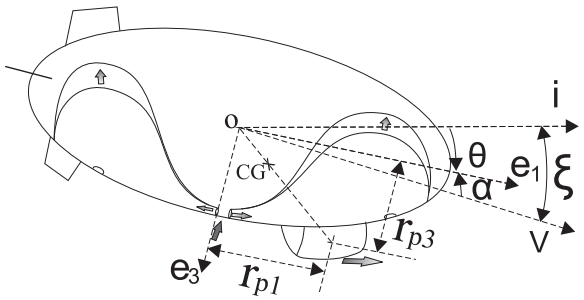

Figure 2.8: The Airship moves downwards and forward.

2.1.3 The mathematical description

The entire mass of the airship is split into several items. Let m_h denote the uniformly distributed mass of the hull, m_b denote the variable mass of the internal air bladder, $\bar{m}$ denote the mass of the moving mass, and m_w denote other internal fixed masses whose center of gravity offsets from O.

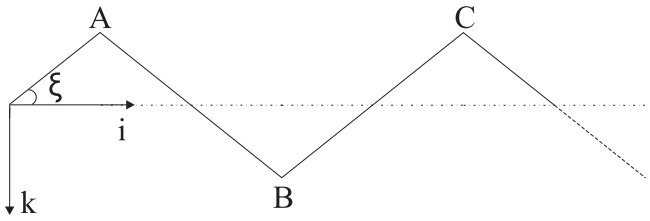

Figure 2.9: Ideal Trajectory of a Buoyancy-Driven Airship.

$\boldsymbol{r_p} \equiv (r_{p1}, r_{p2}, r_{p3})^T$ denotes the position of the moving mass in the body frame. $\boldsymbol{r_b}$ and $\boldsymbol{r_w}$ are the vectors from O to m_b and m_w, shown in Fig. 2.10. In the rest of this thesis, it is assumed that m_b and m_w locate at point O, thus, $\boldsymbol{r_b} = \boldsymbol{r_w} = 0$.

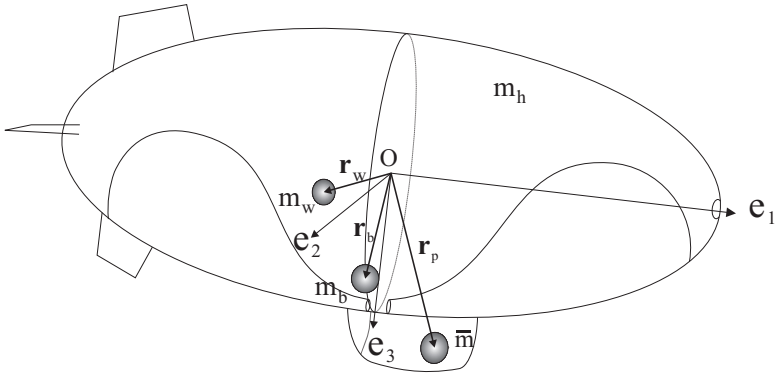

Figure 2.10: Mass Distribution.

The mass m_s is the total stationary mass, thus, $m_s = m_h + m_b + m_w$. The total mass of the vehicle is m_v, so:

$$m_v = m_s + \bar{m} = m_h + m_b + m_w + \bar{m}.$$

Let $m = \rho_a \nabla$ be the buoyancy of the airship with the volume ∇, where ρ_a is the density of the air. Therefore, the net lift of the airship is $m_0 g = m_v g - mg$.

For the airship investigated in this thesis, the basic physical properties are given by $m_h = 269\ kg$, $m_w = 0$, and $\nabla = 301\ m^3$.

2.2 Basic Analysis of the Dynamic System

In this section, a force analysis is done, and some important principles are revealed through this analysis.

2.2.1 Moveable mass and attitude

Here, the interaction between the moveable mass and the airship's body is investigated through an approximate analysis; some principles are presented. It is assumed that the airship is statically suspended in the air; there is no translation and the net lift is equal to zero. In this case, it is assumed that the airship rotates around its center of volume O. Since the center of gravity of the airship's body locates at the center of volume O, thus, the center of gravity of the entire airship CG locates at the straight line connecting O and the center of mass of $\bar{m}$. At the equilibrium, O, CG, and the center of mass of $\bar{m}$ should all locate on a plumb-line. So, if the moveable mass moves to the front, as shown in Fig. 2.11, the airship's body will rotate clockwise, and it stabilizes at a negative pitch angle θ. If the moveable mass moves to the rear, the body will rotate counter-clockwise, and it stabilizes at a positive pitch angle, as shown in Fig. 2.12. For the same reason, if the moveable mass moves to the right or left side, it will yield a positive or negative roll angle ϕ.

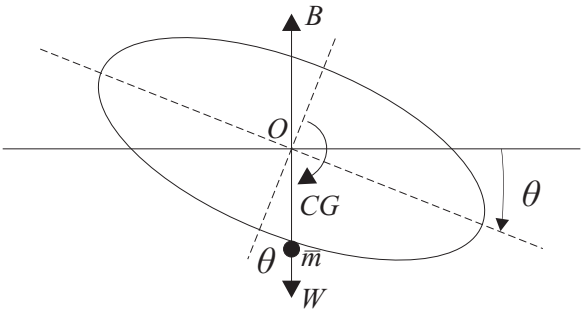

Figure 2.11: The body rotates clockwise.

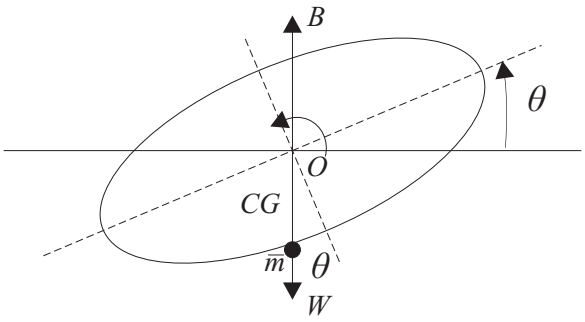

Figure 2.12: The body rotates counter-clockwise.

Note that the above analysis is only an approximate one, the purpose is to illustrate that the attitude of this airship is mainly controlled by the position of the moveable mass, no matter in flight or in a static status. This is simulated in chapter 4. Note that the moveable mass is actuated by the force from the airship's body, and this force is viewed as one of the control inputs of the hold system. Thus, Fig. 2.13 illustrates and concludes these relations. In this figure, $\boldsymbol{u}$ denotes the force to actuate the moveable mass; $\boldsymbol{r_p}$ denotes the position of the moveable mass; Euler angles ϕ, θ, and ψ represent the attitude.

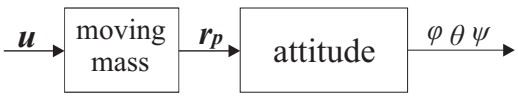

Figure 2.13: The attitude control structure.

Remark: The attitude of the airship is mainly impacted by the motion of the moveable mass.

2.2.2 Aerodynamics and flight path

In the above subsection, the moveable mass and the airship's body are viewed as two independent parts. Here, these two subsystems are viewed as a whole, and the steady-state force-balance of the airship during the descent and the ascent is investigated. These two conditions are illustrated in Fig. 2.14 and 2.15.

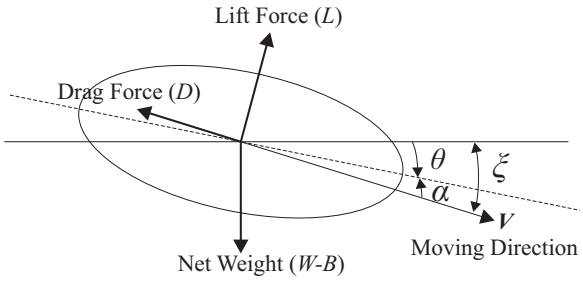

Figure 2.14: Descent forces.

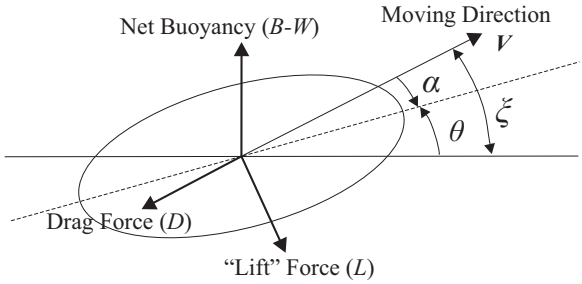

Figure 2.15: Ascent forces.

In these two figures, θ is the pitch angle; α is the angle of attack; ξ is the flight path angle. V is the velocity vector in the inertial frame. L and D are the aerodynamic lift force and drag force. W is airship's total weight (including the moveable mass); B is the buoyancy.

For the descent case, W is greater than B so that the net force is directed downwards as shown in Fig. 2.14. For the ascent case, B is greater than W so that the net force is upwards as shown in Fig. 2.15. Note that for force-balance during descent, the lift force has an upward vertical component (with respect to the wind frame). However, for force-balance during ascent, the lift force must have a downward vertical component to balance the net buoyancy.

The force balance in the horizontal and vertical directions of the wind frame for the descent case is presented in the following:

$$\sum F_{e1} = 0: \quad (W-B)\sin\xi - D = 0 \tag{2.2}$$

$$\sum F_{e3} = 0: \quad (W-B)\cos\xi - L = 0 \tag{2.3}$$

From (2.2) and (2.3), the following result is derived:

$$W - B = \sqrt{D^2 + L^2} \tag{2.4}$$

The force-balance equations for ascent (Fig. 2.15) are as follows:

$$\sum F_{e1} = 0: \quad (B-W)\sin\xi - D = 0 \tag{2.5}$$

$$\sum F_{e3} = 0: \quad (B-W)\cos\xi - L = 0 \tag{2.6}$$

Thus, from (2.5) and (2.6), the following result is derived:

$$W - B = -\sqrt{D^2 + L^2} \tag{2.7}$$

With (2.4) and (2.7), the following remark is derived:

Remark: For the descent and the ascent, if the flight path angle ξ symmetrical and the velocities have the values, the net buoyancy (buoyancy minus weight) is symmetrical for these two motions.

For aerodynamic forces, drag and lift, they have the following general form:

$$D = \frac{1}{2}\rho_a \nabla^{2/3} V^2 C_D \tag{2.8}$$

$$L = \frac{1}{2}\rho_a \nabla^{2/3} V^2 C_L \tag{2.9}$$

where ρ_a is the density of the air; ∇ is the volume of the airship; V is the velocity; C_D and C_L are aerodynamic coefficients.

Substituting the expression of D and L into (2.4), the following result is derived:

$$V^2 = \frac{B - W}{\frac{1}{2}\rho_a \nabla^{2/3} \sqrt{C_D^2 + C_L^2}} \tag{2.10}$$

Remark: The magnitude of the airship's velocity is determined by the net buoyancy which is controlled by the input u_4.

From (2.2) and (2.3), one gets:

$$D\cos\xi - L\sin\xi = 0$$

Thus, the flight path angle ξ and the aerodynamic forces are related as:

$$\tan\xi = \frac{D}{L} \tag{2.11}$$

Summarizing the result (2.11), the following remark is derived:

Remark: The equilibrium of the flight path angle is fixed by the aerodynamics.

To conclude the previous two remarks, the flight path and the velocity of the airship are mainly controlled by the airship's net buoyancy, and the aerodynamic forces, as shown in Fig. 2.16. Here, the control problem of the flight path and of the velocity is called the guidance problem.

From the expression of the aerodynamic forces (2.8) and (2.9), these forces depend on the velocity V and the aerodynamic coefficients, C_D and C_L, which are the functions of the angle of attack α. Obviously, $\alpha = \theta - \xi$. Thus, the aerodynamics forces are decided by the velocity, the Euler angles, and the flight path angle. These relations are illustrated by the Fig. 2.17

Summarizing this section, the structure of the airship's model is presented by Fig. 2.18.

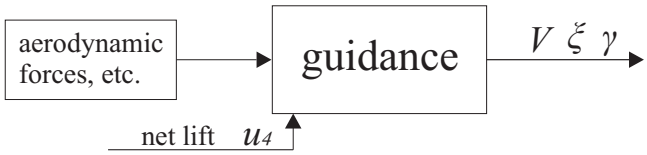

Figure 2.16: The guidance control structure.

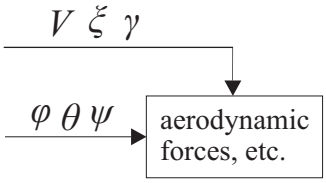

Figure 2.17: The aerodynamics forces are decided by the velocity, Euler angles, and flight path angles.

From Fig. 2.18, it is found that the aerodynamics forces bridge the attitude subsystem and the guidance subsystem. This point is very important for the analysis of the airship's dynamics in chapter 4 where the airship's dynamics is significantly simplified by ignoring the aerodynamic forces temporarily.

2.3 Efficiency Comparison

In this section, the ideal propulsive power of the conventional airship and the buoyancy-driven airship are introduced and compared. Here, the analysis is done in a constant density environment, namely incompressible media, for other situation, such as in compressible media. Details may be found in (Purandare, 2007).

2.3.1 The ideal propulsive power of the conventional airship

Conventional airships employ a propeller to drive the vehicle. It is assumed that a conventional airship moves along a horizontal direction with velocity u. In force-balance condition, the thrust force T is equal to the drag D; the buoyancy is equal to the weight as follows:

$$T = D = \frac{1}{2}\rho_a \nabla^{2/3} u^2 C_{DC}$$

Thus, the ideal propulsive power is:

$$P_C = Tu = \frac{1}{2}\rho_a C_{D0} \nabla^{2/3} u^3 \tag{2.12}$$

The ideal propulsive power per unit gross weight or ideal "specific power" is derived as follows:

$$P_{CS} = \frac{P_C}{W} = \frac{\frac{1}{2}\rho_a C_{D0} \nabla^{2/3} u^3}{W} \tag{2.13}$$

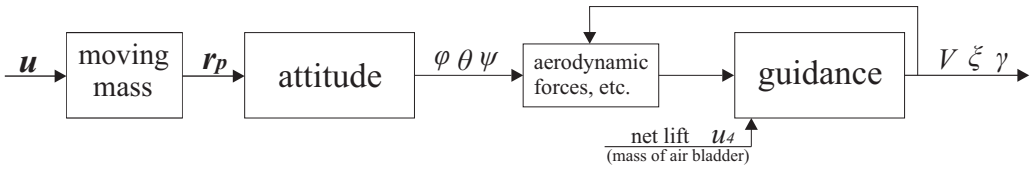

Figure 2.18: The structure of the airship's model.

From (2.13), the ideal specific power is proportional to the cubic of the flight speed for conventional airships. For airplanes it reduces to a linear relation. This implies that airships are suitable for low speed applications.

2.3.2 The propulsive power of the buoyancy-driven airship

Shown in Fig. 2.9, the buoyancy-driven airship mainly behaves following a sawtooth trajectory. Here one cycle which includes an ascent and a descent is considered as in Fig. 2.19.

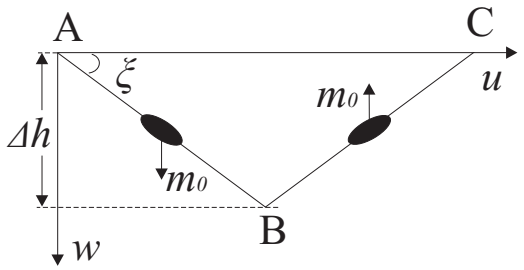

Figure 2.19: A cycle of the flight trajectory

Explicitly explained in (Purandare, 2007), the work needed to track the for AB and BC segments is as follows:

$$\begin{aligned} \omega &= 2m_0 g\Delta h = 2(W-B)\Delta h = 2\sqrt{D^2+L^2}\Delta h \\ &= \rho_a \nabla^{2/3} u^2 (1+\frac{C_D^2}{C_L^2})\sqrt{C_D^2+C_L^2}\Delta h \end{aligned}$$

where the expressions of D and L and (2.11) have been substituted.

The average propulsive power is equal to the work divided by the period as follows:

$$\begin{aligned} P_B &= \frac{\omega}{\tau} = \frac{\omega}{2\Delta h/w} = \frac{\omega}{2\Delta h/u(C_D/C_L)} \\ &= \frac{\rho_a \nabla^{2/3} u^2 (1+\frac{C_D^2}{C_L^2})\sqrt{C_D^2+C_L^2}\Delta h}{2\Delta h/u(C_D/C_L)} = \frac{1}{2}\rho_a \nabla^{2/3} u^3 \frac{C_D}{C_L}(1+\frac{C_D^2}{C_L^2})\sqrt{C_D^2+C_L^2} \end{aligned}$$

where τ is a period, u and w are horizontal and vertical velocities, respectively. For the descent segment AB in Fig. 2.19, the airship's weight is $W + \sqrt{C_D^2+C_L^2}$; for the ascent segment BC in Fig.

2.19, the airship's weight is $W - \sqrt{C_D^2 + C_L^2}$. To compute the power per unit gross weight or "specific power" of one cycle, the weight of the airship is approximately chosen as W. Thus, the specific power P_{BS} of the buoyancy-driven airship is:

$$P_{BS} = \frac{P_B}{W} = \frac{1}{2W}\rho_a \nabla^{2/3} u^3 \frac{C_D}{C_L}(1 + \frac{C_D^2}{C_L^2})\sqrt{C_D^2 + C_L^2} \tag{2.14}$$

2.3.3 Comparison of the efficiency

The power per unit gross weight of the conventional airship and the buoyancy-driven airship are approximately computed. With (2.13) and (2.14), the ratio of ideal buoyancy-to-conventional propulsion specific power r_{sp} is computed as:

$$\begin{aligned} r_{sp} &= \frac{P_{BS}}{P_{CS}} = \frac{\frac{1}{2W}\rho_a \nabla^{2/3} u^3 \frac{C_D}{C_L}(1 + \frac{C_D^2}{C_L^2})\sqrt{C_D^2 + C_L^2}}{\frac{1}{2W}\rho_a C_{D0} \nabla^{2/3} u^3} \\ &= \frac{C_D}{C_{D0} C_L}(1 + \frac{C_D^2}{C_L^2})\sqrt{C_D^2 + C_L^2} \end{aligned} \tag{2.15}$$

where

$$\begin{aligned} C_{D0} &= 0.0589 \\ C_D &= 0.0589 + 0.016\alpha^2 \\ C_L &= 1.269\alpha \end{aligned}$$

These aerodynamic coefficients are taken from (Ouyang, 2003). Thus, r_{sp} is a function of the angle of attack α, and Fig. 2.20 shows r_{sp} versus α from (2.15). A low r_{sp} is preferable as it indicates low propulsive power per unit vehicle weight compared to a conventional propulsion. The figure shows that a minimum exists for r_{sp}.

From Fig. 2.20, it appears that r_{sp} is never lower than 1, which means that the propulsive power per unit gross weight of the buoyancy-driven airship is larger than that of the conventional airship. This result is beyond people's expectation since the buoyancy-driven airship is expected to be more energy-saving than conventional one. However, similar mechanical system, such as underwater glider, has shown great potential in energy-saving. The last experiment on the underwater glider has demonstrated that it can cross the Atlantic, from United States to Spain, without recharging its battery (Shapiro, 2010).

The following is an approach to explain this. The conventional airship uses the standard propeller, such as diesel engine or gasoline engine, normally, the usable horsepower of such engines is around 30%. The buoyancy-driven airship uses the electric energy to actuate the motion of the moveable

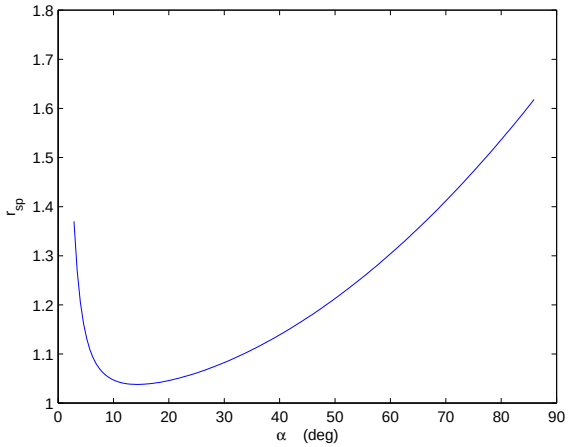

Figure 2.20: Ideal specific power comparison between the conventional airship and the buoyancy driven airship.

mass and the variation of the air bladder. It is believed that the usable horsepower of the buoyancy-driven airship's engine is higher that that of the conventional airship. Thus, the final efficiency of the buoyancy-driven airship may be higher than the conventional one. The buoyancy-driven airship is a substitute to conventional airships in some cases.

2.4 Conclusion

In this chapter, the structure and the operating mechanism of the buoyancy-driven airship are explicitly explained. For the dynamic properties, some basic, but important, principles are analyzed and presented. From these principles, the airship's dynamic model is split into several subsystems. These results are important for the control design in the next chapters. Finally, through an approximate computation, the ideal propulsive power per unit gross weight of the conventional airship and the buoyancy-driven airship are derived. From this result, it is found that the buoyancy driven airship is a candidate to replace the conventional airship in some missions.

Chapter 3

Modelling of the Buoyancy-Driven Airship

Contents

This chapter develops a 8-DOF mathematical model for the buoyancy-driven airship which has a body with fixed wings, internal mass-adjustable air bladders, and a moveable mass. The dynamic model is developed based on physical principles and Newton-Euler Law. Different from the conventional airship, the model developed here is intended to include the main features of buoyancy-driven airships without unnecessary complexity. These characteristics have been depicted in the previous chapter and consist in the control of internal air bladders and of the moveable mass.

There exist lots of references on the modelling of the aerial vehicles and ocean vehicles (Fossen, 1994; Pourzanjani and Roberts, 1991; Bhattacharyya, 1978; Abkowitz, 1975). The mathematical model of the conventional autonomous unmanned airship is mentioned in many references (Ouyang, 2003; Mueller et al., 2004; Beji et al., 2004), but it is first investigated and derived in (Gomes and Ramos Jr, 1998). The dynamics of the buoyancy-driven airship is more complex than that of the conventional one due to the existence of the internal dynamics. In the pioneer research on the buoyancy-driven airship (Purandare, 2007), only the dynamic model on the longitudinal plane was given. This chapter derives the full model of the buoyancy-driven airship in 3D for the first time. Moreover, it offers two approaches to set up the model, considering the airship's rigid body and the moveable mass independently or not. These two approaches have respective advantages. The model derived in the

chapter is the basis of the analysis for the rest of the thesis.

The contribution of this chapter consists in the presentation of the full model of the buoyancy-driven airship for the first time. According to the relation between the airship's body and the moveable mass, the modelling of such a complex mechanical system is significantly simplified and is clearly presented. Partial content of this chapter has been published in (Wu et al., 2009a, 2010, 2011a).

This chapter is arranged as follows: the basic coordinates and definitions of the states are presented in Section 3.1. The inertial frame, body frame, and the wind frame are introduced and the transformations among them are also presented. Section 3.2 gives the airship's equations of kinematics. Since the model is derived through Newton-Euler law, it is necessary to analyze the total forces and moments acting on the airship's body and the moveable mass. This content is presented in Section 3.3. In Section 3.4, for the dynamics of the airship with moveable mass, two modelling approaches are presented and compared. For one approach, the dynamics of the rigid body and moveable mass are viewed independently. The force of interaction between these parts is viewed as a control. For another approach, the system dynamics are described in terms of the total system momentum and the moveable mass momentum. Section 3.5 presents the system's dynamic equations through the first approach. Section 3.6 concludes the full mathematical model of the buoyancy-driven airship in 3D. Section 3.7 concludes this chapter.

3.1 Reference Frame and System States

For aerial vehicle research, four frames may be involved, which are the inertial frame, the body-fixed frame (no-inertial frame), the wind frame, and the Frenet frame (Fossen, 1994). In these frames, the Frenet frame is used for trajectory planing and tracking. The first three frames are briefly introduced in the following.

3.1.1 Inertial frame

The inertial frame is an initially fixed, non-rotating reference frame $G\{i,\ j,\ k\}$, shown in Fig 3.1. The origin G is fixed on an arbitrary point on the earth. The i inertial axis lies in the horizontal plane and normally points to the airship's global moving direction; the j axis is perpendicular to gravity and is subject to right-hand rule; k lies in the direction of the gravity vector and is positive downwards. As well, in the rest of this thesis, bold symbols, $\boldsymbol{i}$, $\boldsymbol{j}$, and $\boldsymbol{k}$, also denote the unit vectors in these directions. As shown in Fig 3.1, the position vector of the airship's center of volume with respect to the inertial frame is $\boldsymbol{b}$ and it is also represented by $(i,\ j,\ k)^T$.

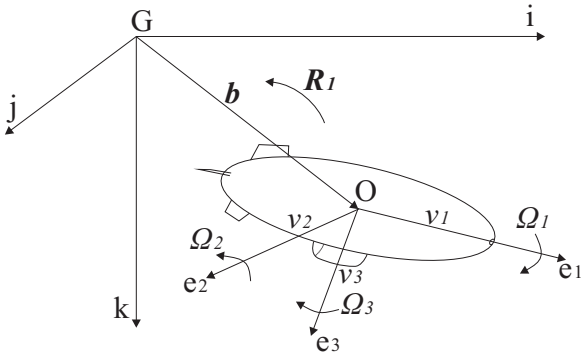

Figure 3.1: The frames and states configuration

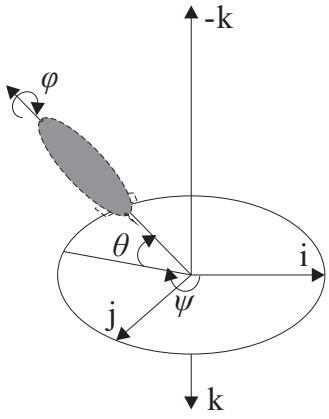

Figure 3.2: The inertial frame and the airship's attitude.

3.1.2 Body-fixed frame and the transformation

The body-fixed frame $O\{e_1,\ e_2,\ e_3\}$, also called body frame or no-inertial frame, is fixed to the airship's body with the origin at the center of volume O and its axes are aligned with the principal axes of the glider. The e_1 axis lies along the long axis of the vehicle and points towards the airship's nose; the e_2 axis lies in the plane of the wings and the axis e_3 points to the bottom and is perpendicular to e_2 as shown in Fig. 3.1.

In this thesis, the velocity of the center of volume O in the inertial frame is $\boldsymbol{V}$. It is decomposed with respect to the body frame as v_1, v_2 and v_3. The angular velocity $\boldsymbol{\Omega}$ is expressed in the body frame as $(\Omega_1,\ \Omega_2,\ \Omega_3)$. The directions of these states are shown in Fig. 3.1.

The orientation of the body frame with respect to the inertial frame is defined by the three angles: roll ϕ, pitch θ, and yaw ψ. In Euler's rotation theorem, they are also called: ϕ angle of self rotation, θ angle of nutation, and ψ angle of precession. Roll ϕ is positive right-wing down, pitch θ is positive nose-up, and yaw ψ is defined as positive right (clockwise) when viewed from above as shown in Fig. 3.2. These three angles are also called Euler angles which represent the attitude of the airship.

Thus, the rotation matrix $\boldsymbol{R_1}$, which maps vectors expressed with respect to the body frame into inertial frame coordinates, consists of these three Euler angles. $\boldsymbol{R_1}$ is constructed by the following three rotations (from the inertial frame $G\{i,\ j,\ k\}$ to the body frame $O\{e_1,\ e_2,\ e_3\}$) (Shi, 1995):

1. rotate around $G-k$ of yaw angle ψ: $G-i \rightarrow G-x_1,\ \ G-j \rightarrow G-y_1$; shown in Fig. 3.3.a.

2. rotate around $G-y_1$ of pitch angle θ: $G-x_1 \rightarrow O-e_1,\ \ G-k \rightarrow G-z_1$; shown in Fig. 3.3.b.

3. rotate around $O-e_1$ of roll angle ϕ: $G-y_1 \rightarrow O-e_2,\ \ G-z_1 \rightarrow O-e_3$; shown in Fig. 3.3.c.

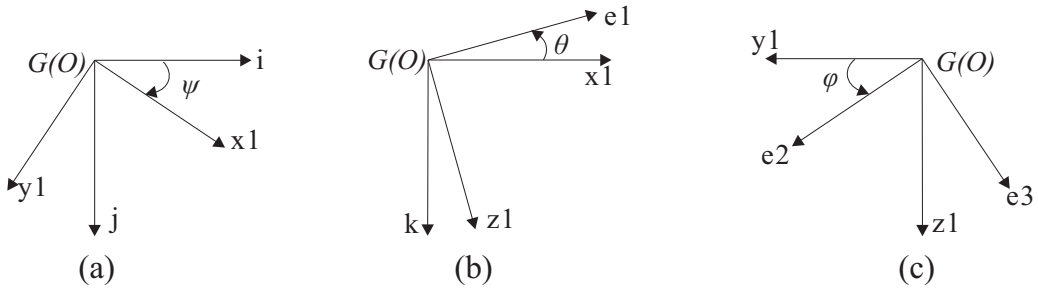

Figure 3.3: The aerodynamic angles

Shown in Fig. 3.3, from the first rotation around $G-i$ of yaw angle ψ, thus,

$$\begin{pmatrix} i \\ j \\ k \end{pmatrix} = \begin{pmatrix} \cos\psi & -\sin\psi & 0 \\ \sin\psi & \cos\phi & 0 \\ 0 & 0 & 1 \end{pmatrix} \begin{pmatrix} x_1 \\ y_1 \\ k \end{pmatrix}$$

From the second rotation around $G-y_1$ of pitch angle θ, thus,

$$\begin{pmatrix} x_1 \\ y_1 \\ k \end{pmatrix} = \begin{pmatrix} \cos\theta & 0 & \sin\theta \\ 0 & 1 & 0 \\ -\sin\theta & 0 & \cos\theta \end{pmatrix} \begin{pmatrix} e_1 \\ y_1 \\ z_1 \end{pmatrix}$$

From the third rotation around $G-e_1$ of roll angle ϕ, thus,

$$\begin{pmatrix} e_1 \\ y_1 \\ z_1 \end{pmatrix} = \begin{pmatrix} 1 & 0 & 0 \\ 0 & \cos\phi & -\sin\phi \\ 0 & \sin\phi & \cos\phi \end{pmatrix} \begin{pmatrix} e_1 \\ e_2 \\ e_3 \end{pmatrix}$$

Synthesize the above three coordinate transformations, the following relation is obtained:

$$\begin{pmatrix} i \\ j \\ k \end{pmatrix} = \begin{pmatrix} \cos\psi & -\sin\psi & 0 \\ \sin\psi & \cos\phi & 0 \\ 0 & 0 & 1 \end{pmatrix} \begin{pmatrix} \cos\theta & 0 & \sin\theta \\ 0 & 1 & 0 \\ -\sin\theta & 0 & \cos\theta \end{pmatrix} \begin{pmatrix} 1 & 0 & 0 \\ 0 & \cos\phi & -\sin\phi \\ 0 & \sin\phi & \cos\phi \end{pmatrix} \begin{pmatrix} e_1 \\ e_2 \\ e_3 \end{pmatrix}$$

namely,

$$\begin{pmatrix} i \\ j \\ k \end{pmatrix} = \boldsymbol{R_1} \begin{pmatrix} e_1 \\ e_2 \\ e_3 \end{pmatrix}$$

where the rotation matrix $\boldsymbol{R_1}$ from the body frame to the inertial frame is:

$$\boldsymbol{R_1} = \begin{pmatrix} \cos\psi\cos\theta & \cos\psi\sin\theta\sin\phi - \sin\psi\cos\phi & \cos\psi\sin\theta\cos\phi + \sin\psi\sin\phi \\ \sin\psi\cos\theta & \sin\psi\sin\theta\sin\phi + \cos\psi\cos\phi & \sin\psi\sin\theta\cos\phi - \cos\psi\sin\phi \\ -\sin\theta & \cos\theta\sin\phi & \cos\theta\cos\phi \end{pmatrix}$$

where $\boldsymbol{R_1^{-1}} = \boldsymbol{R_1^T}$.

3.1.3 Wind frame and the transformation

The aerodynamic forces on an aerial vehicles depend on the velocity and orientation of the vehicles with respect to the airflow. To measure the orientation of the vehicles with respect to the airflow, a wind frame $O\{w_1,\ w_2,\ w_3\}$ is assigned to track the airship's motion as shown in Fig. 3.4. The wind axis w_1 points in the direction of $\boldsymbol{V}$, thus, the aerodynamic force, drag, is in the opposite direction of w_1. The wind axis w_3 lies in the body $e_1 - e_3$ plane and is orthogonal to the vector $(v_1,\ 0,\ v_3)^T$, and the lift force lies in this direction. The orientation of the wind frame with respect to the body frame will be described by the two aerodynamic angles, the angle of attack α and the sideslip angle β. One of its axis is aligned with the velocity of the vehicle as shown in Fig. 3.4

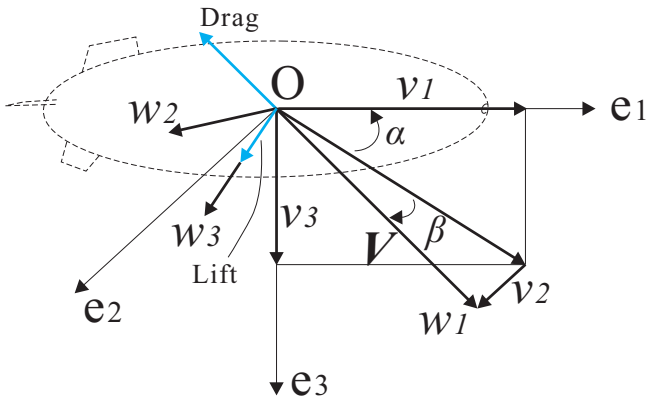

Figure 3.4: The aerodynamic angles

Obviously, from the Fig. 3.4, the following relations are obtained:

$$\begin{aligned} \alpha &= \arctan\frac{v_3}{v_1} \\ \beta &= \arcsin\frac{v_2}{\|\boldsymbol{V}\|} \end{aligned}$$

The rotation matrix from the wind frame to the body frame is given by $\boldsymbol{R_2}$ as follows (Bhatta, 2006):

$$\begin{aligned} \boldsymbol{R_2} &= (\boldsymbol{R}_\alpha)^T(\boldsymbol{R}_\beta)^T = \begin{pmatrix} \cos\alpha & 0 & \sin\alpha \\ 0 & 1 & 0 \\ -\sin\alpha & 0 & \cos\alpha \end{pmatrix}^T \begin{pmatrix} \cos\beta & -\sin\beta & 0 \\ \sin\beta & \cos\beta & 0 \\ 0 & 0 & 1 \end{pmatrix}^T \\ &= \begin{pmatrix} \cos\alpha\cos\beta & \cos\alpha\sin\beta & -\sin\alpha \\ -\sin\beta & \cos\beta & 0 \\ \sin\alpha\cos\beta & \sin\alpha\sin\beta & \cos\alpha \end{pmatrix} \end{aligned}$$

Thus,

$$\begin{pmatrix} e_1 \\ e_2 \\ e_3 \end{pmatrix} = \boldsymbol{R_2} \begin{pmatrix} w_1 \\ w_2 \\ w_3 \end{pmatrix}$$

The orientation of the wind frame with respect to the inertial frame defines the flight path angles of the aerial vehicles, shown in Fig. 3.5. The vertical planar component of the flight path angle is denoted by ξ, and its horizontal planar component is denoted by γ. The positive directions of these angles are shown in Fig. 3.5.

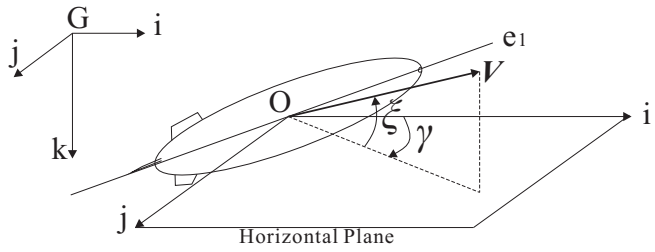

Figure 3.5: The flight path angles

3.2 The Kinematics of the Airship

Here, the airship, including the moveable mass, is viewed as an entire system to compute its kinematics, and it is computed with respect to the inertial frame. From the above analysis, the translation velocity of the airship with respect to the inertial frame is denoted by $\dot{\boldsymbol{b}} = (\dot{i},\ \dot{j},\ \dot{k})^T$; the angular velocity is denoted by $(\dot{\phi},\ \dot{\theta},\ \dot{\psi})^T$. The following two steps set up the relation between states in the inertial frame with the states in the body frame.

- **The transformation of the linear velocity**

The linear velocity with respect to the body frame is given by $\boldsymbol{V} = (v_1,\ v_2,\ v_3)^T$. For a vector, it can be transformed between frames $O\{e_1,\ e_2,\ e_3\}$ and $G\{i,\ j,\ k\}$ through $\boldsymbol{R_1}$. Thus, for $\boldsymbol{V}$ and $\dot{\boldsymbol{b}}$, they have the following relation:

$$\dot{\boldsymbol{b}} = \boldsymbol{R_1 V} \tag{3.1}$$

The expression of $\boldsymbol{R_1}$ is already displayed in the above, in turns of the three Euler angles.

- **The transformation of the angular velocity**

Using Euler angles $(\phi,\ \theta,\ \psi)^T$, the Euler angular velocities with respect to the body frame are defined as follows: angular velocity of roll $\overrightarrow{\Omega_1} = \dot{\phi}\boldsymbol{i}$, angular velocity of pitch $\overrightarrow{\Omega_2} = \dot{\theta}\boldsymbol{j}$, and angular velocity of yaw $\overrightarrow{\Omega_3} = \dot{\psi}\boldsymbol{k}$. Here, $\rightarrow$ denotes a vector. The above definition is valid under the assumption: there is only one axis that rotates at each time. If a rigid body rotates as in Fig. 3.3. The angular velocity is:

$$\vec{\boldsymbol{\Omega}} = \dot{\psi}\boldsymbol{k} + \dot{\theta}\boldsymbol{y_1} + \dot{\phi}\boldsymbol{e_1}$$

The transformation vectors $\boldsymbol{y_1}$ and $\boldsymbol{k}$ to the body frame by the above rotation matrices are as follows (Beji et al. (2004)):

$$\vec{\boldsymbol{\Omega}} = \dot{\psi}\begin{pmatrix} \cos\theta & 0 & \sin\theta \\ 0 & 1 & 0 \\ -\sin\theta & 0 & \cos\theta \end{pmatrix}\begin{pmatrix} 1 & 0 & 0 \\ 0 & \cos\phi & -\sin\phi \\ 0 & \sin\phi & \cos\phi \end{pmatrix}\boldsymbol{e_3} + \dot{\theta}\begin{pmatrix} 1 & 0 & 0 \\ 0 & \cos\phi & -\sin\phi \\ 0 & \sin\phi & \cos\phi \end{pmatrix}\boldsymbol{e_2} + \dot{\phi}\boldsymbol{e_1}$$

In the scalar form as:

$$\begin{pmatrix} \Omega_1 \\ \Omega_2 \\ \Omega_3 \end{pmatrix} = \begin{pmatrix} 1 & 0 & -\sin\theta \\ 0 & \cos\phi & \sin\phi\cos\theta \\ 0 & \sin\phi & \cos\phi\cos\theta \end{pmatrix}\begin{pmatrix} \dot{\phi} \\ \dot{\theta} \\ \dot{\psi} \end{pmatrix}$$

which is simplified as:

$$\boldsymbol{\Omega} = \boldsymbol{R_3^{-1}} \cdot (\dot{\phi},\ \dot{\theta},\ \dot{\psi})^T$$

Thus,

$$\begin{pmatrix} \dot{\phi} \\ \dot{\theta} \\ \dot{\psi} \end{pmatrix} = \boldsymbol{R_3}\boldsymbol{\Omega}$$

which is rewritten as:

$$\dot{\boldsymbol{\eta}} = \boldsymbol{R_3}\boldsymbol{\Omega} \tag{3.2}$$

where

$$\boldsymbol{\eta} = (\phi\ \theta\ \psi)^T$$

and

$$\boldsymbol{R_3} = \begin{pmatrix} 1 & \sin\phi\tan\theta & \cos\phi\tan\theta \\ 0 & \cos\phi & -\sin\phi \\ 0 & \sin\phi/\cos\theta & \cos\phi/\cos\theta \end{pmatrix} \qquad \theta \neq \frac{\pi}{2} + \mathcal{K}\pi$$

Note that $\boldsymbol{R_3}$ involves two Euler angles and its form is not unique, which depends on the order of the rotation in the Fig. 3.3. Moreover, $\boldsymbol{R_3}$ is not an orthonormal matrix, which means that $\boldsymbol{R_3^T} \neq \boldsymbol{R_3^{-1}}$.

Thus, the kinematics of the airship in the inertial frame is given by (3.1) and (3.2).

The above can be described by the Lie algebra approach as follows:

$\boldsymbol{R_1} \in SO(3)$, where $SO(3)$ is 3×3 special orthogonal matrix, defined as follows:

$$SO(3) = \left\{\boldsymbol{R_1} \in \Re^{3\times3} | \boldsymbol{R_1}\boldsymbol{R_1}^T = I, det\boldsymbol{R_1} = 1\right\}$$

where I denotes a 3×3 identity matrix. The attitude and the position of the airship is decided by $(\boldsymbol{R_1}, \boldsymbol{b})$. The configuration space of the system is defined as:

$$SE(3) = \left\{(\boldsymbol{b}, \boldsymbol{R_1}) | \boldsymbol{b} \in \Re^3, \boldsymbol{R_1} \in SO(3)\right\} = \Re^3 \times SO(3)$$

$SE(3)$ can be represented by homogeneous coordinates, as follows:

$$\begin{pmatrix} \boldsymbol{R_1} & \boldsymbol{b} \\ 0 & 1 \end{pmatrix} \in SE(3)$$

$SE(3)$ is a rotation matrix group. For example, if $G \in SE(3)$, then G is a transformation matrix of the rigid body from body frame to the inertial frame.

3.3 The Forces Analysis

To set up the model of the system through the Newton-Euler approach, the forces applied on the system should be found and computed firstly, which is depicted in this section.

Two limiting assumptions are made at the outset of that analysis for practical reasons:

1. the airship forms a rigid body such that aeroelastic effects can be neglected;

2. the rigid body is symmetric about the $e_1 - e_2$ plane; the resulting center of mass of all rigid body components, except the moveable mass, lies in the center of the volume O.

This section consists of two parts, one is devoted to the force analysis of the moveable mass, another is devoted to that of the airship's body.

3.3.1 The forces acting on the moveable masses

As depicted in Fig. 2.10, and 3.6, there exists a moveable mass to control the attitude. Since its mass is $\bar{m}$, and its position is $[r_{p1}\ r_{p2}\ r_{p3}]^T$. $\boldsymbol{u}$ in Fig. 3.6 represents the force applied on the two moveable mass by the rigid body, which is the only coupling between the moveable mass and the rigid body.

Here, $\boldsymbol{u} = [u_1\ u_2\ u_3]^T$. u_1 is the force acting on the mass along e_1 by the actuator, u_2 is the force acting on the mass along e_2 by the actuator, and u_3 is the force acting on the mass along e_3 by the rigid body.

3.3.2 Inertial forces and added mass

In fluid mechanics, the added mass or virtual mass is the inertia added to a system because an accelerating or decelerating body has to move some volume of the surrounding fluid as it moves

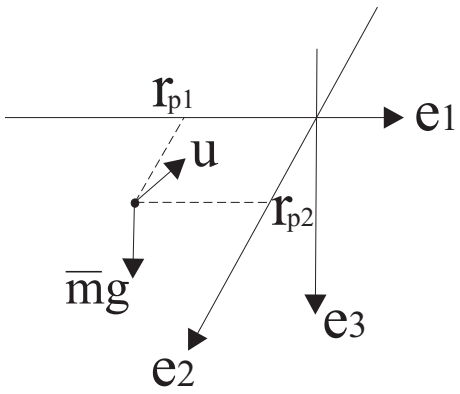

Figure 3.6: The force analysis of the moveable mass.

through it, since the object and fluid cannot occupy the same physical space simultaneously. For simplicity, this can be modeled as some volume of fluid moving with the object since more force is required to accelerate the body in the fluid than in a vacuum (Brennen, 1982). Since the force is equal to the mass times the acceleration, the additional force is included in terms of a virtual *added mass* of the object in the fluid.

A simple example is presented to illustrated the *added mass*. Consider a cylinder of radius r and length L, accelerating at rate $\frac{dv}{dt} = \dot{v}$, shown in Fig. 3.7. The hydro/aerodynamic force in the x direction is obtained by integrating the pressure over the area projected in the x direction:

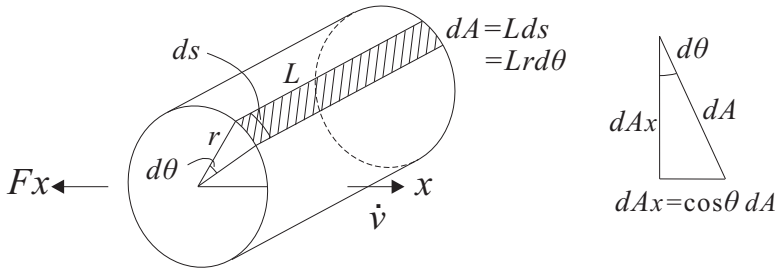

Figure 3.7: The added mass around a cylinder

$$\vec{F}_x = \int P d\vec{A}_x$$

where

- $d\vec{A}_x = \cos\theta dA; \quad dA = Lds; \quad ds = Rd\theta$
- Pressure $P = -\rho\left(\dot{v}r\cos\theta + \frac{1}{2}v^2\right)$

So

$$\begin{aligned} F_x &= \int_0^{2\pi} \left(-\rho\left(\dot{v}r\cos\theta + \frac{1}{2}v^2\right)\right)\cos\theta RLd\theta \\ &= -\rho\cdot rL\cdot\dot{v}r\underbrace{\int_0^{2\pi}\cos^2\theta d\theta}_{=\pi} - \rho\cdot rL\cdot\frac{1}{2}\dot{v}^2\underbrace{\int_0^{2\pi}\cos\theta d\theta}_{=0} \\ &= -\rho\pi r^2 L\dot{v} \end{aligned}$$

where $\dot{v}$ is the acceleration of the body, and the negative sign indicates that the force is in the negative x direction, opposing the acceleration. Thus, this extra force is applied on the body, and the apparent added mass is:

$$m_a = \rho\pi r^2 L$$

Generally, in the potential flows theorem, m_{ij} is computed as follows:

$$m_{ij} = -\rho\int_s \phi_i\frac{\partial\phi_j}{\partial_n}ds \qquad (i,j=1,2,\ldots,6)$$

where n is the outward normal to the surface s which represents the body surface. ϕ_i is the velocity potential of the steady flow due to unit motion of the body in the i^{th} direction.

Munk has shown that the added mass of an elongated body of revolution, such as the body of the buoyancy-driven airship shown in Fig. 2.4, can be reasonable approximated as that of an ellipsoid with the same volume and the same *length*/*width* ratio (Brennen, 1982). For an ellipsoid as shown in Fig. 3.8, the added mass for the axial motion and the vertical motion are given by (3.3) and Tab. 3.1.

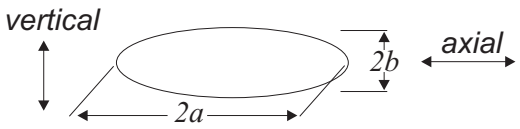

Figure 3.8: An ellipsoid used to compute the added mass in two direction

$$m_{add} = k\cdot\frac{4}{3}\pi\rho ab^2 \tag{3.3}$$

Table 3.1: The value of the factor k for different a/b ratio *Source* (Brennen, 1982).

a/b	1.00	1.50	2.00	2.51	2.99	3.99	4.99	6.01	6.97	8.01	9.02	9.97
k for axial motion	.500	.305	.209	.156	.122	.082	.059	.045	.036	.029	.024	.021
k for vertical motion	.500	.621	.702	.763	.803	.860	.895	.918	.933	.945	.954	.960

For any accelerating or decelerating object, there exist 36 added masses which are denoted by m_{ij}, shown in the following equation (Thomasson, 2000). The added mass m_{ij} is interpreted as a mass

associated with a force on the body in the direction i due to a unit acceleration in the direction j. Subscripts, 1, 2, and 3 denote the translations along e_1, e_2, and e_3, respectively. 4, 5, and 6 denote the rotations around e_1, e_2, and e_3, respectively.

$$\boldsymbol{F} = \begin{pmatrix} m_{11} & m_{12} & m_{13} & m_{14} & m_{15} & m_{16} \\ m_{21} & m_{22} & m_{23} & m_{24} & m_{25} & m_{26} \\ m_{31} & m_{32} & m_{33} & m_{34} & m_5 & m_{36} \\ m_{41} & m_{42} & m_{43} & m_{44} & m_{45} & m_{46} \\ m_{51} & m_{52} & m_{53} & m_{54} & m_{55} & m_{56} \\ m_{61} & m_{62} & m_{63} & m_{64} & m_{65} & m_{66} \end{pmatrix} \begin{pmatrix} \dot{v}_1 \\ \dot{v}_2 \\ \dot{v}_3 \\ \dot{\Omega}_1 \\ \dot{\Omega}_2 \\ \dot{\Omega}_3 \end{pmatrix} \tag{3.4}$$

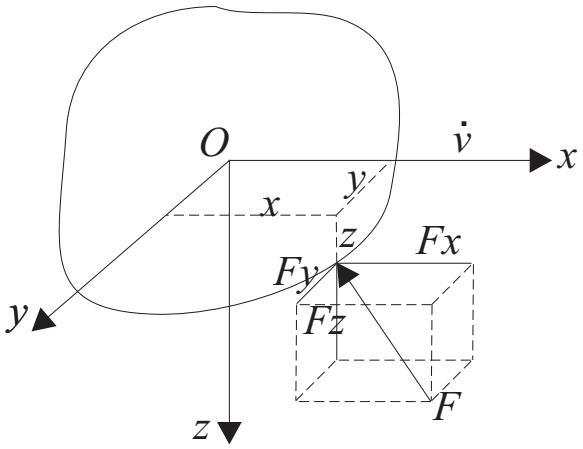

Figure 3.9: The inertial force for an irregular object

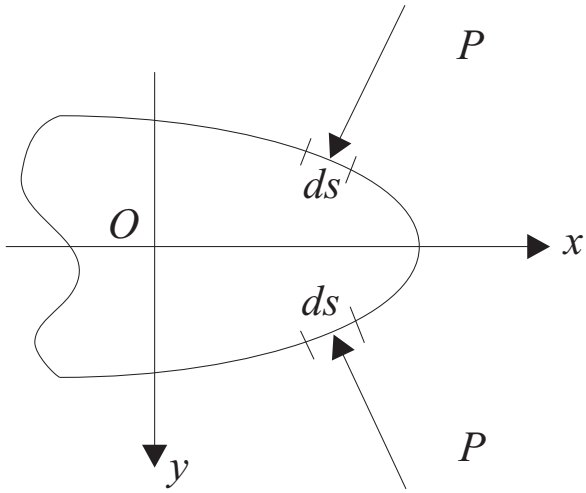

Figure 3.10: The inertial force for a symmetric object.

According to (3.4), assume that an irregular object moves along the x direction with acceleration $\dot{v}$ as shown in Fig. 3.9. For an irregular object, the force F does not follow the x direction, its components in the three axis are:

$$\begin{cases} F_x = -m_{11}\dot{v} \\ F_y = -m_{21}\dot{v} \\ F_z = -m_{31}\dot{v} \end{cases}$$

and the three moments around the three axis are:

$$\begin{cases} M_x = -m_{41}\dot{v} \\ M_y = -m_{51}\dot{v} \\ M_z = -m_{61}\dot{v} \end{cases}$$

But if there exists a symmetric plane for an object, as the $x-z$ plane of the object shown in Fig. 3.10, the above force F_y and moment M_y are equal to zero since the pressure on symmetrical surfaces are identical. Thus, $m_{21} = m_{51} = 0$ for this case.

For the airship, it is assumed that there exist three symmetric planes $e_1 - e_2$, $e_1 - e_3$ and $e_2 - e_3$, thus, all non-diagonal components in the above added mass matrix are equal to zero, and only the components on the diagonal are kept.

The following will derive the inertial force caused by the added mass with respect to the body frame.

In an ideal fluid, the kinetic energy T_{add} of fluid disturbances is (Shi, 1995):

$$T_{add} = \frac{1}{2}\sum_{i=1}^{6}\sum_{j=1}^{6} m_{ij}\epsilon_i\epsilon_j = \frac{1}{2}\left(m_{11}v_1^2 + m_{22}v_2^2 + m_{33}v_3^2 + m_{44}\Omega_1^2 + m_{55}\Omega_2^2 + m_{66}\Omega_3^2\right)$$

where $\epsilon_1 = v_1, \epsilon_2 = v_2, \epsilon_3 = v_3, \epsilon_4 = \Omega_1, \epsilon_5 = \Omega_2, \epsilon_6 = \Omega_3$. The momentum $\boldsymbol{B} \equiv (B_1, B_2, B_3)^T$ and the angular momentum $\boldsymbol{K} \equiv (B_4, B_5, B_6)^T$ of fluid disturbances are related to the kinetic energy T_{add}:

$$B_i = \frac{\partial T_{add}}{\partial \epsilon_i} \quad (i = 1, 2, \cdots, 6).$$

So,

$$\boldsymbol{B} = \boldsymbol{M_f}\boldsymbol{v}$$
$$\boldsymbol{K} = \boldsymbol{J_f}\boldsymbol{\Omega}.$$

where $\boldsymbol{M_f} \equiv diag\{m_{11}\ m_{22}\ m_{33}\}$ and $\boldsymbol{J_f} \equiv diag\{m_{44}\ m_{55}\ m_{66}\}$.

The inertial force $\boldsymbol{F_I}$ and moment $\boldsymbol{M_I}$ acting on the airship are as follows,

$$\begin{cases} \boldsymbol{F_I} = -\frac{d\tilde{\boldsymbol{B}}}{dt} = -\left(\frac{d\boldsymbol{B}}{dt} + \boldsymbol{\Omega}\times\boldsymbol{B}\right) = -\boldsymbol{M_f}\dot{\boldsymbol{v}} + \left(\boldsymbol{M_f}\boldsymbol{v}\right)\times\boldsymbol{\Omega} \\ \boldsymbol{M_I} = -\frac{d\tilde{\boldsymbol{K}}}{dt} = -\left(\frac{d\boldsymbol{K}}{dt} + \boldsymbol{\Omega}\times\boldsymbol{K} + \boldsymbol{v}\times\boldsymbol{B}\right) = -\boldsymbol{J_f}\dot{\boldsymbol{\Omega}} + \left(\boldsymbol{J_f}\boldsymbol{\Omega}\right)\times\boldsymbol{\Omega} + \left(\boldsymbol{M_f}\boldsymbol{v}\right)\times\boldsymbol{v} \end{cases}$$

where $\frac{d\boldsymbol{B}}{dt}$, $\frac{d\boldsymbol{K}}{dt}$ denote the time-derivative of momentum $\boldsymbol{B}$ and angular momentum $\boldsymbol{K}$ with respect to the inertial frame, $\frac{d\tilde{\boldsymbol{B}}}{dt}$ and $\frac{d\tilde{\boldsymbol{K}}}{dt}$ denote the time-derivative in the body frame. Here, the components $\left(\boldsymbol{M_f}\boldsymbol{v}\right)\times\boldsymbol{\Omega}$ and $\left(\boldsymbol{J_f}\boldsymbol{\Omega}\right)\times\boldsymbol{\Omega} + \left(\boldsymbol{M_f}\boldsymbol{v}\right)\times\boldsymbol{v}$ are Coriolis effects which can not be observed in the inertial frame.

3.3.3 Aerodynamic forces and moments

The aerodynamic model of the airship is an age-old research topic, and it has been rarely reconsidered since the airship peak during twenty to thirties of last century. In this domain, a wealth of

research was performed by Maxwell Munk in the 1920's to 1930's, which provided the basis for subsequent modelling and other design (Munk, 1924, 1923). The aerodynamic model presented here was developed using the procedure outlined by Jones and De Laurier. This model includes expressions for axial force, and moment on an axis symmetric airship. The effect of these aerodynamic forces $\boldsymbol{F_a}$ and moments $\boldsymbol{M_a}$ are present as follows,

$$\begin{aligned} \boldsymbol{F_a} &\equiv (X_a, Y_a, Z_a)^T \\ \boldsymbol{M_a} &\equiv (L_a, M_a, N_a)^T. \end{aligned}$$

X_a, Y_a, and Z_a are drag, sideforce, and lift, respectively. In some previous sections, X_a and Z_a are denoted by D and L. L_a, M_a, and N_a are roll moment, pitch moment, and yaw moment, respectively.

The aerodynamic forces act on the center of buoyancy CB. By convention, the decomposed aerodynamic forces $\boldsymbol{F_a}$ lie in the velocity frame (namely the wind frame), and the moments $\boldsymbol{M_a}$ are decomposed in the body frame.

Since $\boldsymbol{F_a}$ is defined with respect to the velocity frame, $\boldsymbol{F_a}$ is rewritten with respect to the body frame and denoted by $\boldsymbol{F_{at}}$:

$$\boldsymbol{F_{at}} = \boldsymbol{R_2}\boldsymbol{F_a} \tag{3.5}$$

where $\boldsymbol{R_2}$ is the transfer matrix from the velocity frame to the body frame.

To keep the notations consistent, $\boldsymbol{M_a}$ is rewritten by $\boldsymbol{M_{at}}$ and

$$\boldsymbol{M_{at}} = \boldsymbol{M_a}. \tag{3.6}$$

For the explicit expressions the axis forces and moment, there exist two approaches to process: the exact one and the approximate one.

For an airship which is flying with speed V, angle of attack α, and sideslip angle β, the axis forces, X_a, Y_a, and Z_a, and moment L_a, M_a, and N_a are presented through an exact approach as (Munk, 1924):

$$\begin{cases} Drag: & X_a = \frac{1}{2}\rho_a \nabla^{2/3} V^2 \left(C_{x0} + C_x^{\alpha}\alpha^2\right) \\ Sideforce: & Y_a = \frac{1}{2}\rho_a \nabla^{2/3} V^2 \left(C_{y0} + C_y^{\beta}\beta + C_y^{\Omega_3}\Omega_3\right) \\ Lift: & Z_a = \frac{1}{2}\rho_a \nabla^{2/3} V^2 \left(C_{z0} + C_z^{\alpha}\alpha\right) \\ Roll\ moment: & L_a = \frac{1}{2}\rho_a \nabla V^2 \left(C_{l0} + C_l^{\beta}\beta + C_l^{\Omega_1}\Omega_1 + C_l^{\Omega_3}\Omega_3\right) \\ Pitch\ moment: & M_a = \frac{1}{2}\rho_a \nabla V^2 \left(C_{m0} + C_m^{\alpha}\alpha + C_m^{\Omega_2}\Omega_2\right) \\ Yaw\ moment: & N_a = \frac{1}{2}\rho_a \nabla V^2 \left(C_{m0} + C_m^{\beta}\beta + C_n^{\Omega_1}\Omega_1 + C_n^{\Omega_3}\Omega_3\right) \end{cases} \tag{3.7}$$

Here, ρ_a is the density of ambient air, ∇ is the volume of the airship. The C_i's are the aerodynamic coefficients which are computed from wind tunnel experiments.

Note that since the buoyancy-driven airship has no the conventional control surface, such as the elevator and the rudder, the expressions of the aerodynamic forces do not include the deflection of the control surface which is usually denoted by an angle δ.

Since the airship moves slowly and the aerodynamic forces are weak, to simplify the analysis of the dynamics, these terms can be approximated as:

$$\begin{pmatrix} \boldsymbol{F_{at}} \\ \boldsymbol{M_{at}} \end{pmatrix} = \begin{pmatrix} F_{a1} \\ F_{a2} \\ F_{a3} \\ \hline L_a \\ M_a \\ N_a \end{pmatrix} = \begin{pmatrix} K_D v_1 \\ K_{SF} v_2 \\ K_L v_3 \\ \hline K_{ML} \Omega_1 \\ K_M \Omega_2 \\ K_N \Omega_3 \end{pmatrix} \tag{3.8}$$

where K_i are aerodynamic coefficients (Repoulias and Papadopoulos, 2008).

3.3.4 Gravity and buoyancy of the airship's body

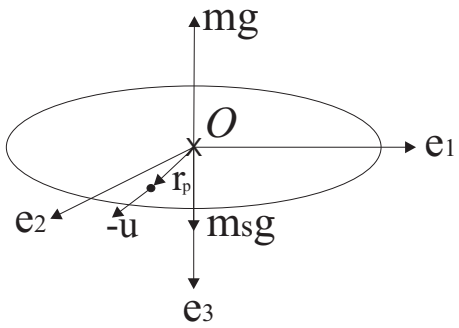

Figure 3.11: The rigid body and some forces.

For the airship's body, excepted the moveable mass, its mass is m_s, shown in Fig. 3.11. Besides the gravity, the buoyancy mg is applied on it. In the inertial frame, the composite effect of gravity and buoyancy is denoted by $\boldsymbol{F_{GB}}$ as follows,

$$\boldsymbol{F_{GB}} = (m_s - m)g\boldsymbol{k} = (m_0 - \bar{m})g\boldsymbol{k}$$

where $\boldsymbol{k}$ is a unit vector pointing in the direction of gravity. $\boldsymbol{F_{GB}}$ is transferred to the body frame as follows,

$$\boldsymbol{F_{GBt}} = (m_s - m)g\boldsymbol{R_1^T k} = (m_0 - \bar{m})g\boldsymbol{R_1^T k} \tag{3.9}$$

It is assumed that the center of gravity of the rigid body locates at point O. So there is no moment involved by m_s and the buoyancy of the airship. In the body frame, the latter moment is:

$$\boldsymbol{M}_{\boldsymbol{GBt}} = 0 \tag{3.10}$$

3.3.5 The internal forces and moments

There exists a reacting force $-\boldsymbol{u}$ on the rigid body (see Fig. 3.11), and this is a significant difference from the conventional airship and airplane. These interactions $\boldsymbol{F}_{\boldsymbol{int}}$ and $\boldsymbol{M}_{\boldsymbol{int}}$ are given by:

$$\begin{aligned} \boldsymbol{F}_{\boldsymbol{int}} &= -\boldsymbol{u} \\ \boldsymbol{M}_{\boldsymbol{int}} &= \boldsymbol{r}_{\boldsymbol{p}} \times (-\boldsymbol{u}) \end{aligned}$$

3.4 Two Modelling Approaches

Here, two modelling approaches for a buoyancy-driven airship with internal moveable masses are presented, which are different from the views of the system's structure. For the first modelling approach, the rigid body and internal moveable masses are viewed independently. The force of interaction between the rigid body and the moveable mass is treated as a control. The advantage of this approach is that the interconnection between the airship's body and the moveable mass is clearly presented, and the modelling of the airship's body can refer that of the conventional airship which is available in many reference. This is also the reason why the first approach is chosen to set up the model in this thesis. For the second approach, the rigid body and internal moveable masses are viewed globally. The above force is treated as an internal force. The system's dynamics are described in terms of the total system dynamics and the moveable mass dynamics. Since the control is an internal force, the total momentum is conserved for any variation of control. The advantage of this approach is that it is useful for studying stability of the system. Meanwhile, the disadvantage is that this approach is more complicate than the first one.

As depicted in Fig. 3.12, the airship's rigid body and the moveable mass are synthesized as two point masses. The two modelling approaches are presented as in the following.

3.4.1 The rigid body and the moveable mass are viewed independently

For the first approach, the two subsystems, the rigid body and the moveable mass, are viewed independently. Thus, the equations of motion involve the translational and angular motions of the rigid body and the moveable mass. For simplicity, the dynamics is represented by the momentum of the object.

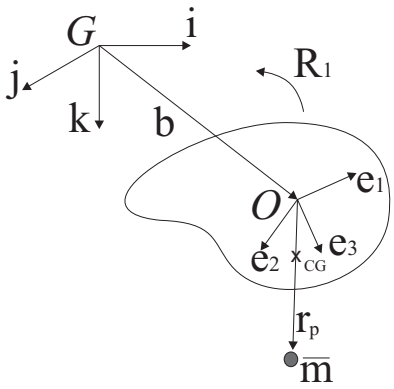

Figure 3.12: The rigid body and the moveable mass with respect to the inertial frame and the body frame.

Let $\boldsymbol{p}$, $\boldsymbol{\pi}$, and $\boldsymbol{p_p}$ denote the translational, angular momentum of the rigid body and the translational momentum of the moveable mass, respectively. Note that $\boldsymbol{p}$, $\boldsymbol{\pi}$, and $\boldsymbol{p_p}$ are all of these in the inertial frame. Accordingly, $\boldsymbol{P}$, $\boldsymbol{\Pi}$, and $\boldsymbol{P_p}$ denote these states in the body frame. According to the Newton's laws, the total external force and moment are denoted as:

$$\begin{cases} \dot{\boldsymbol{\pi}} = \sum \boldsymbol{\tau_{ext}} - \boldsymbol{r_p} \times \left(\boldsymbol{R_1^T u} \right) \\ \dot{\boldsymbol{p}} = \sum \boldsymbol{f_{ext}} - \bar{m} g \boldsymbol{k} - \boldsymbol{R_1^T u} \\ \dot{\boldsymbol{p}}_p = \bar{m} g \boldsymbol{k} + \boldsymbol{R_1^T u} \end{cases} \tag{3.11}$$

where $\sum \boldsymbol{f_{ext}}$ denotes the total external force, besides $\bar{m}g$ and $\boldsymbol{u}$, applied to the rigid body. $\sum \boldsymbol{\tau_{ext}}$ denotes the total external torque, besides the torque of $\bar{m}g$ and $\boldsymbol{u}$.

With the transformation between the inertial frame and the body frame, one gets:

$$\begin{cases} \boldsymbol{\pi} = \boldsymbol{R_1 \Pi} + \boldsymbol{b} \times \boldsymbol{p} \\ \boldsymbol{p} = \boldsymbol{R_1 P} \\ \boldsymbol{p_p} = \boldsymbol{R_1 P_p} \end{cases} \tag{3.12}$$

Differentiating (3.12) and substituting the kinematic equation (3.1) gives:

$$\begin{cases} \dot{\boldsymbol{\pi}} = \boldsymbol{R_1} \left(\dot{\boldsymbol{\Pi}} + \boldsymbol{\Omega} \times \boldsymbol{\Pi} \right) + \boldsymbol{Rv} \times \boldsymbol{p} + \boldsymbol{b} \times \dot{\boldsymbol{p}} \\ \dot{\boldsymbol{p}} = \boldsymbol{R_1} \left(\dot{\boldsymbol{P}} + \boldsymbol{\Omega} \times \boldsymbol{P} \right) \\ \dot{\boldsymbol{p}}_p = \boldsymbol{R_1} \left(\dot{\boldsymbol{P}}_p + \boldsymbol{\Omega} \times \boldsymbol{P}_p \right) \end{cases} \tag{3.13}$$

Substituting (3.11) into (3.13), yields the following equations of motion in the body frame:

$$\begin{cases} \dot{\boldsymbol{\Pi}} = \boldsymbol{\Pi} \times \boldsymbol{\Omega} + \boldsymbol{P} \times \boldsymbol{v} + \boldsymbol{R^T} \sum \boldsymbol{\tau_{ext}} - \boldsymbol{r_p} \times \boldsymbol{u} \\ \dot{\boldsymbol{P}} = \boldsymbol{P} \times \boldsymbol{\Omega} + \boldsymbol{R_1^T} \sum \boldsymbol{f_{ext}} - \bar{m} g \left(\boldsymbol{R^T k} \right) - \boldsymbol{u} \\ \dot{\boldsymbol{P}}_p = \boldsymbol{P}_p \times \boldsymbol{\Omega} + \bar{m} g \left(\boldsymbol{R^T k} \right) + \boldsymbol{u} \end{cases} \tag{3.14}$$

From the $\dot{\boldsymbol{P}}$ equation and $\dot{\boldsymbol{P}}_p$ equation in (3.14), the rigid body sustains a counterforce with the magnitude $\boldsymbol{u}$ from the moveable mass. This result is supported by the figure 3.11 and the above analysis. The control force $\boldsymbol{u}$ couples the body and moveable masses as a multi-body system.

3.4.2 The rigid body and the moveable mass are viewed globally

Rather than considering the momentum of the rigid body separately from that of the moveable mass, one may consider the total system momentum and angular momentum which are specified by a tilde, $'\ \tilde{}\ '$. But for the moveable mass, the expression of the momentum is constant. To keep the uniformity of the notation, it is rewritten as $\tilde{p}_p$.

For this case, the (3.11) transforms into:

$$\begin{cases} \dot{\tilde{\boldsymbol{\pi}}} = \sum \boldsymbol{\tau}_{ext} + \boldsymbol{r}_p \times (\bar{m}g\boldsymbol{k}) \\ \dot{\tilde{\boldsymbol{p}}} = \sum \boldsymbol{f}_{ext} \\ \dot{\tilde{\boldsymbol{p}}}_p = \bar{m}g\boldsymbol{k} + \boldsymbol{R}_1^T\boldsymbol{u} \end{cases} \tag{3.15}$$

where $\bar{m}g$ and $\boldsymbol{u}$ do not belong to external forces any more.

After the transformation, the variables with respect to the inertial frame in this case is given by:

$$\begin{cases} \dot{\tilde{\boldsymbol{\Pi}}} = \tilde{\boldsymbol{\Pi}} \times \boldsymbol{\Omega} + \tilde{\boldsymbol{P}} \times \boldsymbol{v} + \boldsymbol{R}^T \sum \boldsymbol{\tau}_{ext} + \boldsymbol{r}_p \times \left(\bar{m}g\boldsymbol{R}^T\boldsymbol{k}\right) \\ \dot{\tilde{\boldsymbol{P}}} = \tilde{\boldsymbol{P}} \times \boldsymbol{\Omega} \\ \dot{\tilde{\boldsymbol{P}}}_p = \tilde{\boldsymbol{P}}_p \times \boldsymbol{\Omega} + \bar{m}g\left(\boldsymbol{R}^T\boldsymbol{k}\right) + \boldsymbol{u} \end{cases} \tag{3.16}$$

Note that $\boldsymbol{u}$ does not appear in the equation of $\dot{\tilde{\boldsymbol{\Pi}}}$ and $\dot{\tilde{\boldsymbol{P}}}$, which reflects the fact that internal actuation can not alter the total system momentum.

By this analysis, the internal dynamic structure has been recognized and exploited. These two models are used for different purposes; they also aid the analysis and the control design for other types vehicles, as well, including spacecraft and atmospheric re-entry vehicles.

3.5 The Dynamics Equations of the System

Even though the translational and angular momenta, $\boldsymbol{\Pi}$, $\boldsymbol{P}$, $\boldsymbol{P}_p$, can be used as the states of the system, they do not directly and visually present the system's condition. The translational and angular velocity of the system, $\boldsymbol{\Omega}$, $\boldsymbol{v}$, $\dot{\boldsymbol{r}}_p$ are better to display the airship's motion. Thus, the translational and angular velocity are used as the states of the system in the following.

In this section the dynamics equations with new coordinates of the system are derived through the first approach in section 3.4: the airship's body and the moveable mass are viewed independently.

The dynamics of the moveable mass is firstly derived, and then, those of the airship's body is derived based on the force analysis in the previous section.

3.5.1 Dynamics of the moveable mass

If the airship is rotating with angular velocity $\boldsymbol{\Omega}$. According to the relation between the absolute velocity and the relative velocity, the absolute velocity $\boldsymbol{v_p}$ of the ballast in the body frame is as follows,

$$\boldsymbol{v_p} = \boldsymbol{v} + \dot{\boldsymbol{r}}_{\boldsymbol{p}} + \boldsymbol{\Omega} \times \boldsymbol{r_p}. \tag{3.17}$$

The total external force acting on the moveable mass is given by:

$$\boldsymbol{F_p} = (\bar{m}\boldsymbol{v_p}) \times \boldsymbol{\Omega} + \bar{m}g\boldsymbol{R}_1^T\boldsymbol{k} + \boldsymbol{u}. \tag{3.18}$$

According to Newton's Second Law $\boldsymbol{F_p} = \bar{m}\dot{\boldsymbol{v}}_{\boldsymbol{p}}$, with (3.17) and (3.18), the acceleration of the moveable mass is derived as:

$$\ddot{\boldsymbol{r}}_{\boldsymbol{p}} = -\dot{\boldsymbol{v}} - \dot{\boldsymbol{\Omega}} \times \boldsymbol{r_p} - \boldsymbol{\Omega} \times \dot{\boldsymbol{r}}_{\boldsymbol{p}} + g(\boldsymbol{R}_1^T\boldsymbol{k}) + \boldsymbol{v_p} \times \boldsymbol{\Omega} + \boldsymbol{u}/\bar{m}. \tag{3.19}$$

Since the moveable mass does not move in the e_3 direction, namely r_{p3} is a constant. Thus, $\dot{r}_{p3} = 0$ and $\ddot{r}_{p3} = 0$, from (3.19), one gets:

$$\begin{aligned} u_3 =& \bar{m}\big(\dot{v}_3 + \dot{\Omega}_1 r_{p2} - \dot{\Omega}_2 r_{p1} + \Omega_1(2\dot{r}_{p2} + v_2) - \Omega_2(2\dot{r}_{p1} + v_1) \\ & -g\cos\theta\cos\phi - \Omega_2^2 r_{p3} + \Omega_2\Omega_3(r_{p2} + r_{p1}) - \Omega_1^2 r_{p3}\big) \end{aligned} \tag{3.20}$$

3.5.2 Dynamics of the airship's body

Let $\boldsymbol{B_s}$ and $\boldsymbol{K_s}$ be the translational and angular momenta of the airship's body. They are expressed as,

$$\boldsymbol{B_s} = m_s\boldsymbol{v} \tag{3.21}$$

$$\boldsymbol{K_s} = \boldsymbol{J_s}\boldsymbol{\Omega} \tag{3.22}$$

where $\boldsymbol{J_s}$ is the matrix of the moment of inertia of m_s of the airship's body.

Thus, the total force , denoted by $\boldsymbol{F_s}$, and moment, denoted by $\boldsymbol{M_s}$, acting on the body are derived through the above translational and angular momenta as follows:

$$\begin{aligned} \boldsymbol{F_s} &= \frac{d\tilde{\boldsymbol{B}}_{\boldsymbol{s}}}{dt} = \frac{d\boldsymbol{B_s}}{dt} + \boldsymbol{\Omega} \times \boldsymbol{B_s} \\ &= m_s\dot{\boldsymbol{v}} + \boldsymbol{\Omega} \times (m_s\boldsymbol{v}) \end{aligned} \tag{3.23}$$

$$\begin{aligned} \boldsymbol{M_s} &= \frac{d\tilde{\boldsymbol{K}}_{\boldsymbol{s}}}{dt} = \frac{d\boldsymbol{K_s}}{dt} + \boldsymbol{\Omega} \times \boldsymbol{K_s} + \boldsymbol{v} \times \boldsymbol{B_s} \\ &= \boldsymbol{J_s}\dot{\boldsymbol{\Omega}} + \boldsymbol{\Omega} \times (\boldsymbol{J_s}\boldsymbol{\Omega}) + \boldsymbol{v} \times (m_s\boldsymbol{v}) \end{aligned} \tag{3.24}$$

From the analysis in section 3.3, $\boldsymbol{F_s}$ and $\boldsymbol{M_s}$ are derived as follows:

$$\begin{aligned}\boldsymbol{F_s} &= \boldsymbol{F_I} + \boldsymbol{F_{at}} + \boldsymbol{F_{GB}} + \boldsymbol{F_{int}} \\ &= -\boldsymbol{M_f}\dot{\boldsymbol{v}} + \left(\boldsymbol{M_f v}\right) \times \boldsymbol{\Omega} + \boldsymbol{F_{at}} + (m_0 - \bar{m})g\boldsymbol{R_1^T k} - \boldsymbol{u} \qquad (3.25)\\ \boldsymbol{M_s} &= \boldsymbol{M_I} + \boldsymbol{M_{at}} + \boldsymbol{M_{GB}} + \boldsymbol{M_{int}} \\ &= -\boldsymbol{J_f}\dot{\boldsymbol{\Omega}} + \left(\boldsymbol{J_f \Omega}\right) \times \boldsymbol{\Omega} + \left(\boldsymbol{M_f v}\right) \times \boldsymbol{v} + \boldsymbol{M_{at}} + \boldsymbol{r_p} \times (-\boldsymbol{u}) \qquad (3.26)\end{aligned}$$

Obviously, combining (3.23) and (3.25), (3.24) and (3.26), the dynamics equations of the airship's body are derived as follows:

$$\dot{\boldsymbol{v}} = \boldsymbol{M^{-1}}\left(\boldsymbol{Mv} \times \boldsymbol{\Omega} + \boldsymbol{F_{at}} + (m_0 - \bar{m})g\boldsymbol{R_1^T k} - \boldsymbol{u}\right) \qquad (3.27)$$

$$\dot{\boldsymbol{\Omega}} = \boldsymbol{J^{-1}}\left(\boldsymbol{J\Omega} \times \boldsymbol{\Omega} + \boldsymbol{Mv} \times \boldsymbol{v} + \boldsymbol{M_{at}} - \boldsymbol{r_p} \times \boldsymbol{u}\right) \qquad (3.28)$$

where the mass matrix $\boldsymbol{M}$ and the moment of inertia matrix $\boldsymbol{J}$ are given by:

$$\begin{aligned}\boldsymbol{M} &= \boldsymbol{m_s}\mathcal{I} + \boldsymbol{M_f} = \mathrm{diag}\{m_1 \;\; m_2 \;\; m_3\} = \mathrm{diag}\{m_s + m_{11} \;\; m_s + m_{22} \;\; m_s + m_{33}\} \\ \boldsymbol{J} &= \boldsymbol{J_s} + \boldsymbol{J_f} = \mathrm{diag}\{J_1 \;\; J_2 \;\; J_3\} = \mathrm{diag}\{I_x + m_{44} \;\; I_y + m_{55} \;\; I_z + m_{66}\}\end{aligned}$$

Actually, the dynamics equations of the airship's body can be simplified as the following form:

$$\begin{cases} \dot{\boldsymbol{v}} = \boldsymbol{M^{-1}}\left(\boldsymbol{F_d} + \boldsymbol{F_{at}} + \boldsymbol{F_{GB}} + \boldsymbol{F_{int}}\right) \\ \dot{\boldsymbol{\Omega}} = \boldsymbol{J^{-1}}\left(\boldsymbol{M_d} + \boldsymbol{M_{at}} + \boldsymbol{M_{GB}} + \boldsymbol{M_{int}}\right) \end{cases} \qquad (3.29)$$

Here, the force vector $\boldsymbol{F_d}$ contains the Coriolis force and the centrifugal force of the dynamic model, and $\boldsymbol{M_d}$ contains the moment of the Coriolis force and the centrifugal force. $\boldsymbol{F_d}$ and $\boldsymbol{M_d}$ are given by:

$$\begin{aligned}\boldsymbol{F_d} &= \boldsymbol{Mv} \times \boldsymbol{\Omega} \\ \boldsymbol{M_d} &= \boldsymbol{J\Omega} \times \boldsymbol{\Omega} + \boldsymbol{Mv} \times \boldsymbol{v}\end{aligned}$$

3.6 The 8-DOF Mathematical Model

As the airship is driven by change of the net lift, and it is necessary to control the mass of ballonets, through the input u_4, as $m_b = u_4$. Thus $m_0 = m_h + \bar{m} + u_4 - m$, which means that m_0 in the mathematical model includes a control input.

Combining equations (3.1), (3.2), (3.27), (3.28), and (3.19), the mathematical model of a 8 DOF

buoyancy-driven airship is obtained as

$$\begin{pmatrix} \dot{\boldsymbol{b}} \\ \dot{\boldsymbol{\eta}} \\ \dot{\boldsymbol{v}} \\ \dot{\boldsymbol{\Omega}} \\ \ddot{\boldsymbol{r}}_p \end{pmatrix} = \begin{pmatrix} \boldsymbol{R}_1 \boldsymbol{v} \\ \boldsymbol{R}_3 \boldsymbol{\Omega} \\ \boldsymbol{M}^{-1} \bar{\boldsymbol{F}} \\ \boldsymbol{J}^{-1} \bar{\boldsymbol{K}} \\ \bar{\boldsymbol{T}} \end{pmatrix} \tag{3.30}$$

where

$$\begin{aligned} \bar{\boldsymbol{K}} &= \boldsymbol{J}\boldsymbol{\Omega} \times \boldsymbol{\Omega} + \boldsymbol{M}\boldsymbol{v} \times \boldsymbol{v} + \boldsymbol{M}_{\boldsymbol{at}} - \mathrm{diag}\{1\ 1\ 0\} \cdot (\boldsymbol{r}_p \times \boldsymbol{u}) \\ \bar{\boldsymbol{F}} &= \boldsymbol{M}\boldsymbol{v} \times \boldsymbol{\Omega} + \boldsymbol{F}_{\boldsymbol{at}} + (m_0 - \bar{m}) g \boldsymbol{R}_1^T \boldsymbol{k} - \boldsymbol{u} \\ \bar{\boldsymbol{T}} &= -\dot{\boldsymbol{v}} - \dot{\boldsymbol{\Omega}} \times \boldsymbol{r}_p - \boldsymbol{\Omega} \times \dot{\boldsymbol{r}}_p + g(\boldsymbol{R}_1^T \boldsymbol{k}) + \boldsymbol{v}_p \times \boldsymbol{\Omega} + \boldsymbol{u}/\bar{m}. \end{aligned}$$

3.7 Conclusion

A full mathematical model in 3D which has 8-DOF for the buoyancy-driven airship is derived for the first time in this chapter based on the Newton-Euler approach. These 8-DOF consist of 6-DOF for the airship's rigid body and 2-DOF of the moveable mass. Through the independent or global views of the rigid body and the moveable mass, the modelling is significantly simplified. According to this difference, two approach to set up the model are presented. These two approaches have respective advantages. Total forces and moments acting on the airship are analyzed and computed. The model derived in the chapter is this basis of the analysis for the rest of the thesis.

Chapter 4

Analysis and Control of the Longitudinal Dynamics

Contents

The complete 8-DOF model was derived in the previous chapter. Various open-loop simulations are necessary to do with this mathematical model. The goal of these simulations is not only to verify the mathematical model, but also to further understand the dynamic properties of the airship. Through various simulations, the reactions of the airship to the actuators (internal air bladder, moveable mass) and its behaviors under instant disturbances are clearly and directly presented.

Note that the so-called *open-loop* simulation in this chapter is not a strict open-loop, since the real control of the airship is the force $\boldsymbol{u}$ and the mass of the internal air bladder u_4. Here, the force $\boldsymbol{u}$ acts through the airship's body to control the translation of the moveable mass. To clearly display the connection between the translation of the moveable mass and the behavior of the airship, in some simulations of this chapter, a feedback control is used on the internal force $\boldsymbol{u}$ to keep the moveable mass at certain constant places. With these simulations, how the position of the moveable mass impacts the airship is clearly presented.

The dynamics of the airship in the longitudinal plane is considered since this dynamics is the most fundamental and important for the airship. But it is not easy to analyze and control this dynamics due to its complex nonlinearity. The longitudinal dynamics consists of six states and two controls. A

common approach to control a nonlinear system consists in linearizing the system around an equilibrium, and then analyze and control this linear system taking the place of the original nonlinear system. An approach based on LQR is presented first in this chapter. The LQR is an important and classical theory of optimal control and used to solve the LQG problem which is one of the most fundamental problems in control theory. However, as everyone knows, a drawback of the linear control based on LQR theory is the limit of validity of the linear control for the original nonlinear system due to the linearizing approximation.

A nonlinear control for the system is necessary. In this prespective, a reasonable simplification is made. During the ascending and descending periods, the airship just adjusts the position of the moveable mass to cope with general disturbances. Therefore, the net lift, namely m_b, m_0, and u_4, is constant during these periods. When the airship transfers between the ascent and the descent, the mass of the internal air bladder m_b is subject to an open-loop bang-bang control. Thus, for the longitudinal dynamics, there is only one control, the internal force u_1, which is subject to a nonlinear control.

One major achievement of modern nonlinear control is feedback linearization (Isidori, 1989; Conte et al., 2007; Isidori and Moog, 1988). This theory has been widely applied for flight controls (Lane and Stengel, 1988; Sun and Clarke, 1994). Unfortunately the airship system is not fully linearizable, the main drawback is that a nonlinear internal dynamics will remain in the closed-loop system which may be unstable. The stability of the internal dynamics of the two nonlinear control scheme based on feedback linearization presented in chapter are proved, and surprisedly, analytical control solutions are shown to be computable. These nonlinear controls are parts of the mainly contribution of this research. Partial content of this chapter has been published in (Wu et al., 2009a,b, 2010, 2011a).

All control defined in this thesis are state feedbacks. The practical issue of measurement or of observer design is beyond the scope of the thesis. Obviously, a pragmatic application of the feedback controls will require additional work about available measurements and some state estimation.

This chapter is arranged as follows: section 4.1 explicitly presents two different control objectives which are adopted in this chapter. The longitudinal model is derived from the full model ant its equilibrium is computed in section 4.2. The reactions of the airship to the two control, the translation of the moveable mass and the mass of the internal air bladder, are simulation in section 4.3. It is demonstrated that the attitude of the airship is mainly controlled by the translation of the moveable mass and the ascent or descent is mainly controlled by the mass of the internal air bladder through simulations in this section. Section 4.4 presents two simple control scheme. One is based on LQR, and another is based on an input-output feedback linearization. Due to the drawback of these two controls, section 4.5 explicitly presents a control scheme based on maximal feedback linearization

with internal stability. In this progress, the dynamics in the longitudinal plane is deeply analyzed and many properties are displayed. Section 4.6 concludes this chapter.

4.1 Control Objective

For the autonomous flight control, generally, there exist two control objectives:

Goal 1: The aerial vehicle is controlled to follow a desired direction and speed. As shown in Fig. 4.1, a flight direction is defined by two angles: ξ and γ. Thus, for this objective, only the direction and speed need to be controlled.

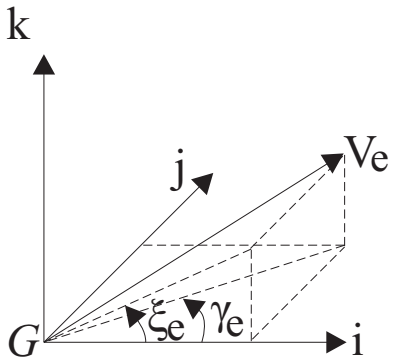

Figure 4.1: Reference flight angle and speed.

Goal 2: The aerial vehicle is controlled to track a desired path. As shown in Fig. 4.2, the objective is to decrease the error Δ between the actual flight path and the desired path.

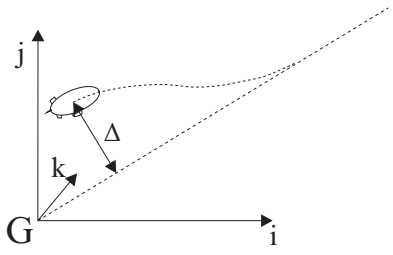

Figure 4.2: Vehicle controlled to track a path

In this chapter, the **Goal 1** is chosen as the control objective for the nonlinear control based on feedback linearization, and the desired direction is defined by ξ_e and γ_e; the desired speed is defined by V_e. The subscript e denotes the values of the states on the equilibrium. The analytical solutions for other variables on the equilibrium are solved in this chapter. The **Goal 2** is adopted for the linear control based on LQR in section 4.4. Thus, an additional variable $\triangle z$ is added.

4.2 The Longitudinal Dynamics and Equilibrium

The longitudinal dynamics is decoupled from the full model (3.30). The momentum of the moveable mass $\boldsymbol{P_p}$ can replace the state $\dot{\boldsymbol{r}}_{\boldsymbol{p}}$ in (3.30). Through that way, an alternative of the coordinate is offered. These two coordinates have respective advantages, and they are both used in the rest of this chapter.

4.2.1 The longitudinal dynamics

As a remark of the next chapter, the longitudinal motion can decouple from the lateral motion when the turn rate is small (the explanation locates section 5.1.2). Here, the turn rate is assumed to be zero, and the dynamics restricts in the longitudinal plane. The longitudinal dynamics is decoupled from the complete model (3.30). This is a general approach for aerial vehicles as done in (Beji et al., 2004; Hima, 2005; Kulczycki et al., 2008; Ouyang, 2003). As depicted in Fig. 2.9, the principal behavior of the airship is to fly in a sawtooth path. Thus, the longitudinal dynamics which restricts in the $i-k$ plane and e_1-e_3 plane is the most important and most fundamental dynamics of the airship. Here, the $i-k$ plane and e_1-e_3 plane overlap.

Since the airship only moves in the longitudinal plane, some variables are set to zero. Thus, attitude angles $\psi=\phi=0$, the translational velocity $v_2=0$, angular velocities $\Omega_1=\Omega_3=0$. Since the moveable mass only moves in the longitudinal plane, so $r_{p2}=0$, and $\dot{r}_{p2}=0$.

Substituting the above restricted conditions into the mathematical model (3.30), the motion equations in the longitudinal plane is derived. These equations are listed in (4.1):

$$\begin{cases} \dot{\theta} &= \Omega_2 \\ \dot{\Omega}_2 &= \frac{1}{J_2}\left(M_a - r_{p3}u_1 + r_{p1}u_3\right) \\ \dot{v}_1 &= \frac{1}{m_1}\left(F_{at1} + (\bar{m}-m_0)g\sin\theta - m_3 v_3\Omega_2 - u_1\right) \\ \dot{v}_3 &= \frac{1}{m_3}\left(F_{at3} + (m_0-\bar{m})g\cos\theta + m_1 v_1\Omega_2 - u_3\right) \\ \dot{r}_{p1} &= \dot{r}_{p1} \\ \ddot{r}_{p1} &= -\dot{v}_1 - \dot{\Omega}_2 r_{p3} - g\sin\theta - (v_3 - \Omega_2 r_{p1})\Omega_2 + u_1/\bar{m} \end{cases} \tag{4.1}$$

where $u_3 = \bar{m}\left(\dot{v}_3 + \dot{\Omega}_1 r_{p2} + \Omega_1(2\dot{r}_{p2}+v_2) - g\cos\theta - \Omega_1^2 r_{p3}\right)$, $F_{at1} = -\cos\alpha X_a + \sin\alpha Z_a$, and $F_{at3} = -\sin\alpha X_a - \cos\alpha Z_a$.

As an alternative of the model (3.30) and (4.1), the momentum of the moveable mass $\boldsymbol{P_p}$ is used to replace the $\dot{\boldsymbol{r}}_{\boldsymbol{p}}$ in (3.30). A new control input which represents the total force act on the moveable mass is defined as well, which is different from the model (3.30) and (4.1) where the control is only the force act by the rigid body. These two different coordinates are both used in the rest sections.

From (3.17), the momentum of the moveable mass is as:

$$\boldsymbol{P_p} = \bar{m}\boldsymbol{v_p} = \bar{m}\left(\boldsymbol{v} + \dot{\boldsymbol{r}}_{\boldsymbol{p}} + \boldsymbol{\Omega} \times \boldsymbol{r_p}\right). \tag{4.2}$$

Thus, the time-derivative of the above equation yields the relation between the $\dot{\boldsymbol{P}}_{\boldsymbol{p}}$ and $\ddot{\boldsymbol{r}}_{\boldsymbol{p}}$ as:

$$\dot{\boldsymbol{P}}_{\boldsymbol{p}} = \bar{m}\left(\dot{\boldsymbol{v}} + \ddot{\boldsymbol{r}}_{\boldsymbol{p}} + \dot{\boldsymbol{\Omega}} \times \boldsymbol{r_p} + \boldsymbol{\Omega} \times \dot{\boldsymbol{r}}_{\boldsymbol{p}}\right) \tag{4.3}$$

$$\tag{4.4}$$

From (4.2) and (4.3), the following state transformation is derived:

$$\dot{\boldsymbol{r}}_{\boldsymbol{p}} = \boldsymbol{P_p}/\bar{m} - \left(\boldsymbol{v} + \boldsymbol{\Omega} \times \boldsymbol{r_p}\right) \tag{4.5}$$

$$\ddot{\boldsymbol{r}}_{\boldsymbol{p}} = \dot{\boldsymbol{P}}_{\boldsymbol{p}}/\bar{m} - \left(\dot{\boldsymbol{v}} + \dot{\boldsymbol{\Omega}} \times \boldsymbol{r_p} + \boldsymbol{\Omega} \times \dot{\boldsymbol{r}}_{\boldsymbol{p}}\right) \tag{4.6}$$

Substituting (4.5) and (4.6) into the complete (3.30), the state $\dot{\boldsymbol{r}}_{\boldsymbol{p}}$ is replaced by a new state $\boldsymbol{P_p}$, and the differential equation of $\ddot{\boldsymbol{r}}_{\boldsymbol{p}}$ in (3.30) is replaced by:

$$\dot{\boldsymbol{P}}_{\boldsymbol{p}} = \boldsymbol{P_p} \times \boldsymbol{\Omega} + \bar{m}g(\boldsymbol{R}_1^T\boldsymbol{k}) + \boldsymbol{u}$$

Here, the total external force on the moveable mass is viewed as a new control $\tilde{\boldsymbol{u}}$ to replace the original control $\boldsymbol{u}$. Thus,

$$\dot{\boldsymbol{P}}_{\boldsymbol{p}} = \tilde{\boldsymbol{u}} = \boldsymbol{P_p} \times \boldsymbol{\Omega} + \bar{m}g(\boldsymbol{R}_1^T\boldsymbol{k}) + \boldsymbol{u} \tag{4.7}$$

From (4.7), the relation between the new control and the original control is defined as:

$$\boldsymbol{u} = \tilde{\boldsymbol{u}} - \boldsymbol{P_p} \times \boldsymbol{\Omega} - \bar{m}g(\boldsymbol{R}_1^T\boldsymbol{k}) \tag{4.8}$$

Substituting (4.5), (4.6), and (4.8) into the (3.30), the complete model with new coordinates is defined. Under this new coordinates, the longitudinal dynamics is given by:

$$\begin{aligned}
\dot{\theta} =& \Omega_2 \\
\dot{\Omega}_2 =& \frac{1}{J_2}\left((m_3 - m_1)\, v_1 v_3 - (r_{p1}P_{p1} + r_{p3}P_{p3})\Omega_2 + M_a - \bar{m}g(r_{p1}\cos\theta + r_{p3}\sin\theta) - r_{p3}\tilde{u}_1 + r_{p1}\tilde{u}_3\right) \\
\dot{v}_1 =& \frac{1}{m_1}\left(-m_3 v_3 \Omega_2 - P_{p3}\Omega_2 - m_0 g\sin\theta + X_a\cos\alpha - Z_a\sin\alpha - \tilde{u}_1\right) \\
\dot{v}_3 =& \frac{1}{m_3}\left(m_1 v_1 \Omega_2 + P_{p1}\Omega_2 + m_0 g\cos\theta + X_a\sin\alpha + Z_a\cos\alpha - \tilde{u}_3\right) \\
\dot{r}_{p1} =& \frac{1}{\bar{m}}P_{p1} - v_1 - r_{p3}\Omega_2 \\
\dot{P}_{p1} =& \tilde{u}_1
\end{aligned}$$

where $\tilde{u}_3 = \dot{P}_{p3} = \bar{m}(\dot{v}_3 - \dot{r}_{p1}\Omega_2 - r_{p1}\dot{\Omega}_2)$; the components of the moveable mass's momentum $P_{p1} = \bar{m}(\dot{r}_{p1} + v_1 + r_{p3}\Omega_2)$ and $P_{p3} = \bar{m}(v_3 - r_{p1}\Omega_2)$. If this model is totally expanded, it reads:

$$\begin{aligned}
\dot{\theta} &= \Omega_2 && (4.9)\\
\dot{\Omega}_2 &= T_1 H_1 + T_2 H_2 && (4.10)\\
\dot{v}_1 &= H_3/m_1 && (4.11)\\
\dot{v}_3 &= T_2 H_1 + T_3 H_2 && (4.12)\\
\dot{r}_{p1} &= P_{p1}/\bar{m} - v_1 - r_{p3}\Omega_2 && (4.13)\\
\dot{P}_{p1} &= \tilde{u}_1 && (4.14)
\end{aligned}$$

where

$$\begin{aligned}
T_1 &= \frac{m_3 + \bar{m}}{J_2\,(m_3 + \bar{m}) + \bar{m} m_3 r_{p1}^2}\\
T_2 &= \frac{\bar{m} r_{p1}}{J_2\,(m_3 + \bar{m}) + \bar{m} m_3 r_{p1}^2}\\
T_3 &= \frac{J_2 + \bar{m} r_{p1}^2}{J_2\,(m_3 + \bar{m}) + \bar{m} m_3 r_{p1}^2}
\end{aligned}$$

$$\begin{aligned}
H_1 &= (m_3 - m_1)\,v_1 v_3 - \bar{m} g \left(r_{p1}\cos\theta + r_{p3}\sin\theta\right)\\
&\quad - \left(r_{p1} P_{p1} + r_{p3}\bar{m}\left(v_3 - r_{p1}\Omega_2\right)\right)\Omega_2 + M_a\\
&\quad - r_{p3}\tilde{u}_1 + \bar{m} r_{p1}\Omega_2\left(v_1 + r_{p3}\Omega_2\right) - r_{p1}\Omega_2 P_{p1}\\
H_2 &= m_1 v_1 \Omega_2 + P_{p1}\Omega_2 + m_0 g\cos\theta - Z_a\cos\alpha\\
&\quad - X_a\sin\alpha - \bar{m}\Omega_2(v_1 - r_{p3}\Omega_2) + P_{p1}\Omega_2\\
H_3 &= -m_3 v_3 \Omega_2 - \bar{m}(v_3 - r_{p1}\Omega_2)\Omega_2 - m_0 g\sin\theta\\
&\quad + Z_a\sin\alpha - X_a\cos\alpha - \tilde{u}_1
\end{aligned}$$

With the model (4.9)-(4.14), the control $\tilde{u}_1$ is equal to zero at the equilibrium. However, these two models are the same in essence. From the above computation, it is clear that either model(4.1), or model (4.9)-(4.14), they are both complex.

4.2.2 Equilibrium of longitudinal dynamics

To compute the equilibrium of the states for a steady flight path in the longitudinal plane which is specified by a desired flight path angle ξ_e and a desired speed V_e, the left hand side of the equation

(4.1) is set to zero. The substitution $u_3 = -g\bar{m}\cos\theta$ yields:

$$0 = \Omega_{2e} \tag{4.15}$$

$$0 = \frac{1}{J_2}\left(K_m\alpha_e V_e^2 - \bar{m}g\cos\theta_e r_{p1e} - \bar{m}g\sin\theta_e r_{p3e}\right) \tag{4.16}$$

$$0 = \frac{1}{m_1}\left(-\cos\alpha_e(K_{d0} + K_d\alpha_e^2)V_e^2 + \sin\alpha_e K_l\alpha_e V_e^2 - m_{0e}g\sin\theta_e\right) \tag{4.17}$$

$$0 = \frac{1}{m_3}\left(-\sin\alpha_e(K_{d0} + K_d\alpha_e^2)V_e^2 - \cos\alpha_e K_l\alpha_e V_e^2 + m_{0e}g\cos\theta_e\right) \tag{4.18}$$

$$0 = -g\sin\theta_e + u_1/\bar{m} \tag{4.19}$$

where $K_{d0} = \frac{1}{2}\rho_a\nabla^{2/3}V^2C_{x0}$, $K_d = \frac{1}{2}\rho_a\nabla^{2/3}V^2C_x^\alpha$, $K_l = \frac{1}{2}\rho_a\nabla^{2/3}V^2C_z^\alpha$, $C_{z0} = 0$, and $K_m = \frac{1}{2}\rho_a\nabla V^2C_m^\alpha$.

From (4.17) and (4.18), the following equation is derived:

$$\frac{\sin\theta_e}{\cos\theta_e} = \frac{-\cos\alpha_e(K_{d0} + K_d\alpha_e^2) + \sin\alpha_e K_l\alpha}{\sin\alpha_e(K_{d0} + K_d\alpha_e^2) + \cos\alpha_e K_l\alpha_e} \rightarrow \tan\theta_e = \frac{\sin(\alpha_e - A)}{\cos(\alpha_e - A)} \rightarrow \tan\theta_e = \tan(\alpha_e - A)$$

where $\sin A = \frac{K_{d0}+K_d\alpha_e^2}{\sqrt{(K_{d0}+K_d\alpha_e^2)^2+(K_l\alpha_e)^2}}$, $\cos A = \frac{K_l\alpha_e}{\sqrt{(K_{d0}+K_d\alpha_e^2)^2+(K_l\alpha_e)^2}}$

Thus,

$$\theta_e = \alpha_e - A \rightarrow \tan A = -\tan(\theta_e - \alpha_e) = -\tan\xi_e$$

So,

$$\frac{K_{d0} + K_d\alpha_e^2}{K_l\alpha_e} = -\tan\xi_e \rightarrow K_d\alpha_e^2 + \tan\xi_e K_l\alpha_e + K_{d0} = 0$$

It is assumed that the above equation can be solved under the condition $(\tan\xi_e K_l)^2 - 4K_dK_{d0} \geq 0$ as:

$$\alpha_e = \frac{-\tan\xi_e K_l \pm \sqrt{(\tan\xi_e K_l)^2 - 4K_dK_{d0}}}{2K_d}$$

Since the flight path angle ξ is in the domain $(-\pi/2,\ \pi/2)$, and the approximate aerodynamic expression is valid only at small angles of attack, the solution of α is chosen as:

$$\alpha_e = -\frac{\tan\xi_e K_l}{2K_d} + \frac{1}{2K_d}\sqrt{(\tan\xi_e K_l)^2 - 4K_dK_{d0}} \tag{4.20}$$

Thus, the equilibrium of θ is as:

$$\theta_e = \xi_e + \alpha_e \tag{4.21}$$

Due to $\tan\alpha = \frac{v_3}{v_1}$,

$$v_{1e} = \cos\alpha V_e \tag{4.22}$$

$$v_{3e} = \sin\alpha V_e \tag{4.23}$$

From (4.16) and (4.17), the following equilibrium is derived:

$$r_{p1e} = \frac{K_m\alpha_e V_e^2}{\bar{m}g\cos\theta_e} - \tan\theta_e r_{p3} \tag{4.24}$$

$$m_{0e} = \frac{1}{g\sin\theta}\left(-\cos\alpha_e(K_{d0} + K_d\alpha_e^2)V_e^2 + \sin\alpha_e K_l\alpha_e V_e^2\right) \tag{4.25}$$

From the above computation, the equilibria of states are computed by (4.20) - (4.25)

4.3 Open-loop Simulation

To demonstrate the validity of the mathematical model in the previous chapter and to further understand the airship's behavior, the open-loop simulation is done based on the nonlinear model (3.30). The airship's equations are integrated into MATLAB/Simulink for rapid simulation. The simulink model is shown in Fig. 4.3.

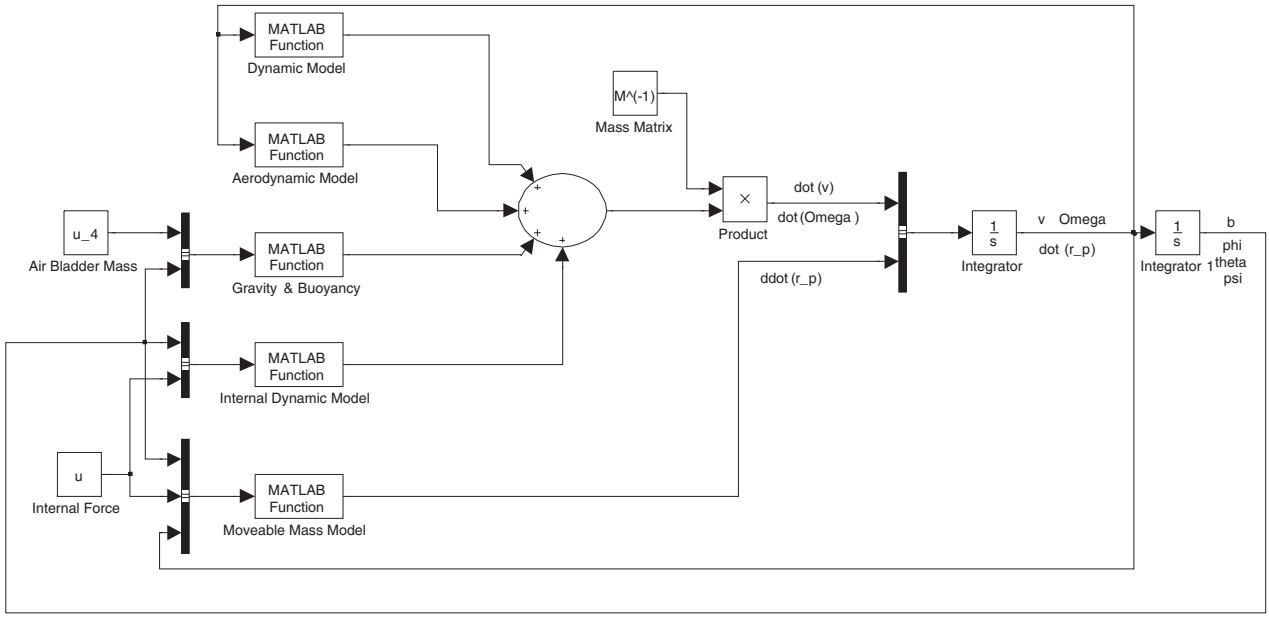

Figure 4.3: The airship's simulink model

4.3.1 The reaction to the variation of the mass of the internal air bladder

The function of the internal air bladder is to control the ascent and descent of the airship. Through the modification of the mass of the air bladder, the net buoyancy (lift) m_0 is changed. The airship keeps a stable status in the air if $m_0 = 0$, which has been simulated and are shown in Fig. 4.4. The airship ascends if $m_0 < 0$; the result of simulation is shown in Fig. 4.5 where $m_0 = -10\ kg$. On the contrary, the airship descends if $m_0 > 0$; the simulation is shown in Fig. 4.6. where $m_0 = 10\ kg$.

4.3.2 The reaction to the translation of the moveable mass

As depicted previously, the moveable mass is used to control the attitude of the airship. When the moveable mass moves in the longitudinal direction, the pitch angle of the airship is modified

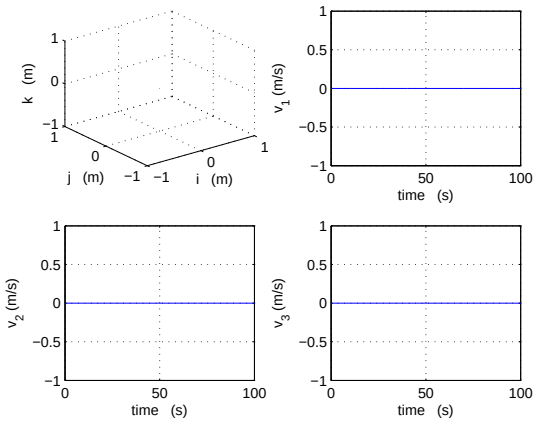

Figure 4.4: The airship stops in the air when the lift is equal to the weight

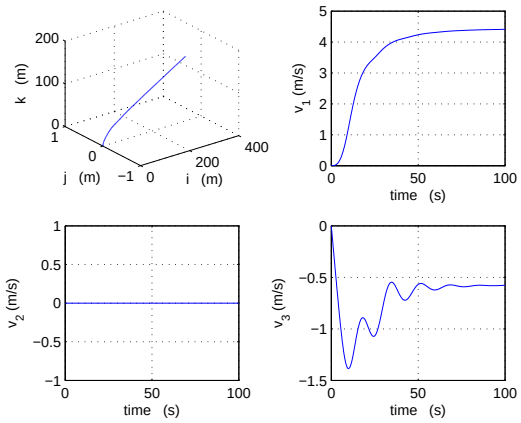

Figure 4.5: The airship ascends in the air when the lift is larger than the weight.

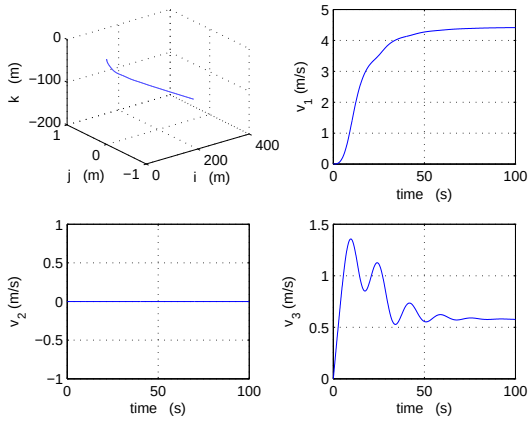

Figure 4.6: The airship descends in the air when the lift is smaller than the weight.

accordingly. Similarly, when the moveable mass moves in the lateral direction, the roll angle of the airship is modified accordingly. These behaviors are displayed through some open-loop simulations as following.

For the initial condition as $r_{p1} = -1.15\ m$ and all other variables are zero (similar to the case shown in Fig. 2.11 and 2.12), the airship has a pendulum motion in the longitudinal plane as shown in Fig. 4.7. In this case, the airship is similar to a pendulum to a certain extent. The fact that the pitch angle is mainly decided by the r_{p1} is explained in section 2.2. This is recalled and illustrated in Fig. 4.8. The equilibrium of r_{p1} is derived in (4.24). When the airship is static (no translational motion), the relation between the pitch angle θ and the longitudinal translation of the moveable mass r_{p1} is:

$$\tan\theta = \frac{r_{p1}}{r_{p3}}$$

On the equilibrium, the variation of the pitch angle according to the motion of the moveable mass is simulated and the result is shown in Fig. 4.9.

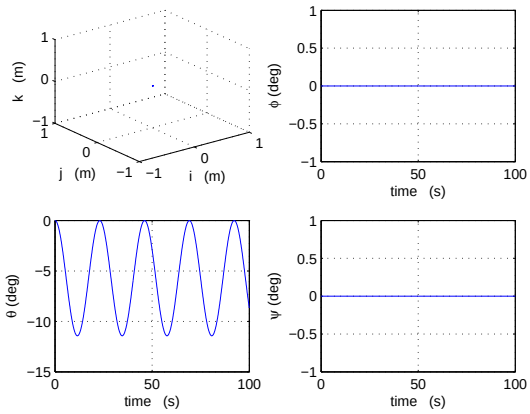

Figure 4.7: The pendulum motion of the airship according to the specified initial conditions

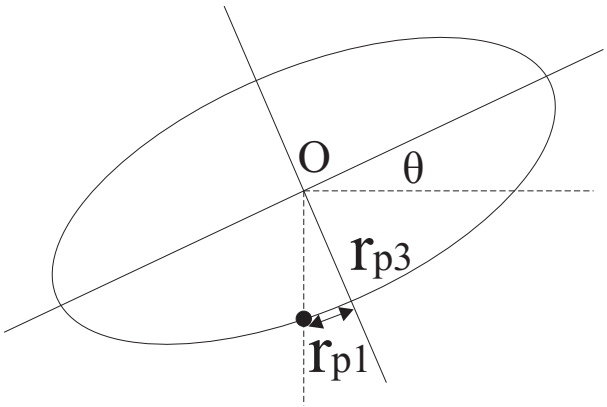

Figure 4.8: The stable situation of the pitch angle and the longitudinal translation of the moveable mass.

Similarly, for the lateral dynamics, the roll of the airship is controlled by the lateral translation of the moveable mass r_{p2}, which is shown by the simulation in Fig. 4.10. On the equilibrium, the relation between the roll angle and the lateral translation of the moveable mass is:

$$\tan\phi = \frac{r_{p2}}{r_{p3}}$$

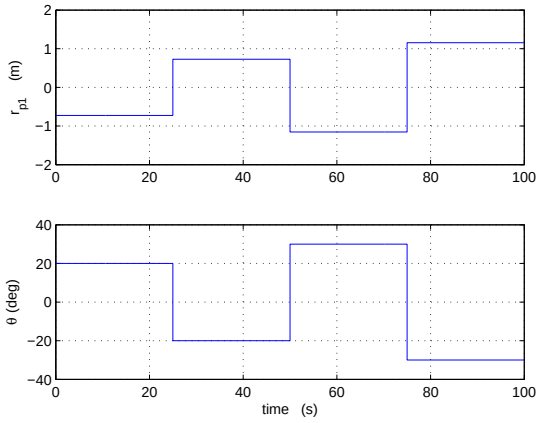

Figure 4.9: The pitch angle is mainly controlled by the longitudinal translation of the movable mass.

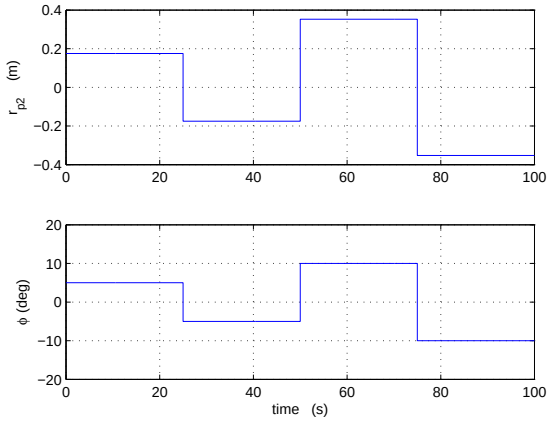

Figure 4.10: The roll angle is mainly controlled by the lateral translation of the movable mass.

4.3.3 Open-loop flight in the longitudinal plane

According to the equilibrium derived in the subsection 4.2.2, there is no doubt that the buoyancy-driven airship with the mathematical model (4.1) or (4.9)-(4.14) can fly follow the trajectories of ascending and descending as shown in Fig. 2.9, but it is interesting to check the airship's behavior

under the disturbance and if the airship can smoothly cover the transferring points as the A, B,and C in Fig. 2.9. Such open-loop simulations are done next.

From the result in the subsection 4.2.2, the nominal values of an ascending motion is calculated and listed in Tab. 4.1. Note that, according to the definition in section 2.1.3, the minus value of m_0 here means that the total weight of the airship is larger than the lift, and the net lift is minus.

Table 4.1: The nominal values of an ascending segment

Term	θ	r_{p1}	v_1	v_3	m_0
Ascent	25.4°	$-0.82\ m$	$3\ m/s$	$-0.24\ m/s$	$-3\ kg$

With this initial values, the airship steadily ascends in the longitudinal plane in a no-disturbance environment. However, Fig. 4.11 and 4.12 show the airship's behavior when it encounters disturbance on θ which is enlarged by 5.7° instantly.

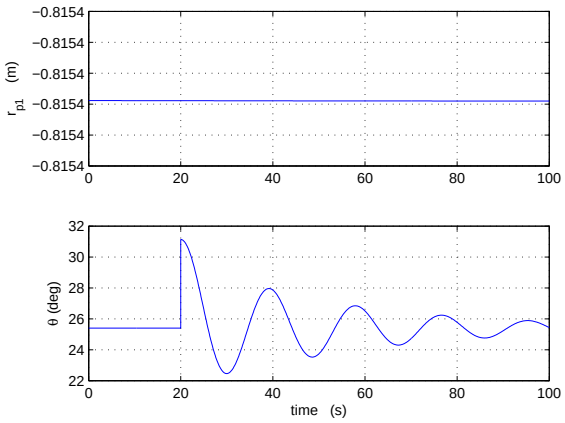

Figure 4.11: The pitch angle encounters an instant disturbance at the 20th second.

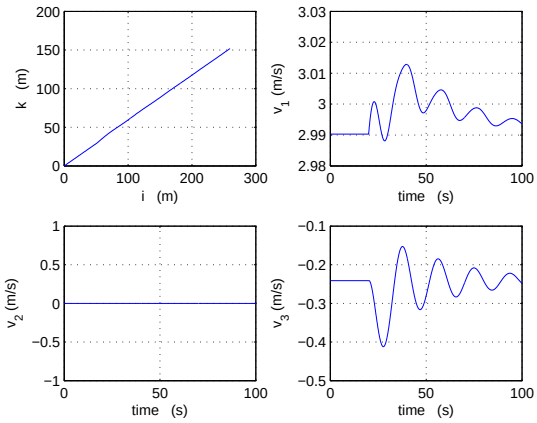

Figure 4.12: The dynamics of velocities and the trajectory under an instant disturbance.

Suffering this instantaneous disturbance, it seems that there is limited impact on the trajectory, but the other variables, such as the pitch angle θ, need a long time to recover the nominal regime.

The buoyancy-driven airship flies along a sawtooth trajectory as shown in Fig. 2.9. Whether the airship can smoothly cover the transferring points as A, B,and C in Fig. 2.9 with an open-loop bang-bang controlled moveable mass, deserves to be investigated (there is bang-bang control on the net lift too). The equilibria for the ascent and the descent are derived and listed in the Tab. 4.2.

According to the values in Tab. 4.2, an open-loop simulation is done to show a continuing fly of the airship whose ideal trajectory is shown in Fig. 2.9. These simulation results are shown in Fig. 4.13 and 4.14.

Table 4.2: The values on the nominal regime

Term	θ	r_{p1}	v_1	v_3	m_0
Ascent	$25.4°$	$-0.82\ m$	$3\ m/s$	$-0.24\ m/s$	$-3\ kg$
Descent	$-25.4°$	$0.82\ m$	$3\ m/s$	$0.24\ m/s$	$3\ kg$

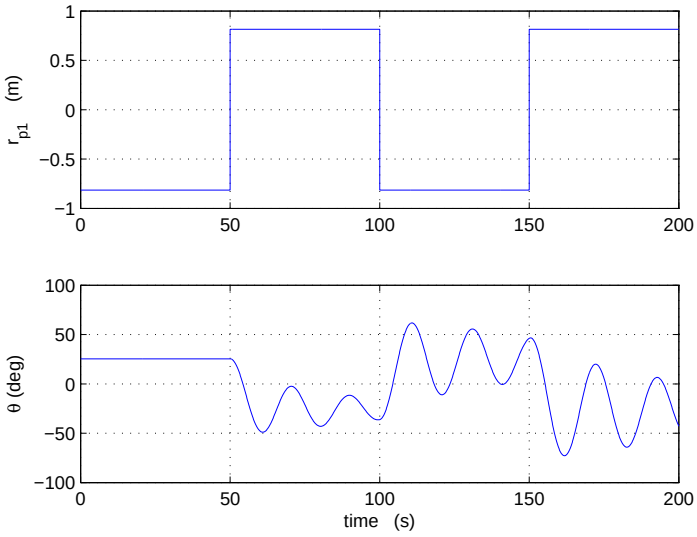

Figure 4.13: The dynamics of the pitch angle and of the open-loop controlled moveable mass

From the first ascending segment of this simulation, a stable ascent under a fixed moveable mass in a no-disturbance environment is smoothly done. But when it transfers to a descent, the airship swings. This swing is mainly caused by the instant translation of the moveable mass, which is similar to the swing of the airship in Fig. 4.7.

To minimize the swings of the variables in the open-loop, the change of motion of the moveable mass to a smooth motion is a feasible way. If the moveable mass spends 16 seconds to move between the $-0.82\ m$ and the $0.82\ m$ on the longitudinal direction, the swing of the airship is minimized as shown in the Fig. 4.15 and 4.16.

From the simulations in this section, disturbances will cause the swing of the system, and only bang-bang control is not good enough to eliminate this swing. In the rest of this chapter, controls, linear one or nonlinear one, are tried to achieve the goals and to stabilize the variables.

4.4 Two Basic Controls

From the above result, the longitudinal dynamics consists of six states and two controls (the net lift is subject to the bang-bang control sometimes). As some early results, two control schemes based

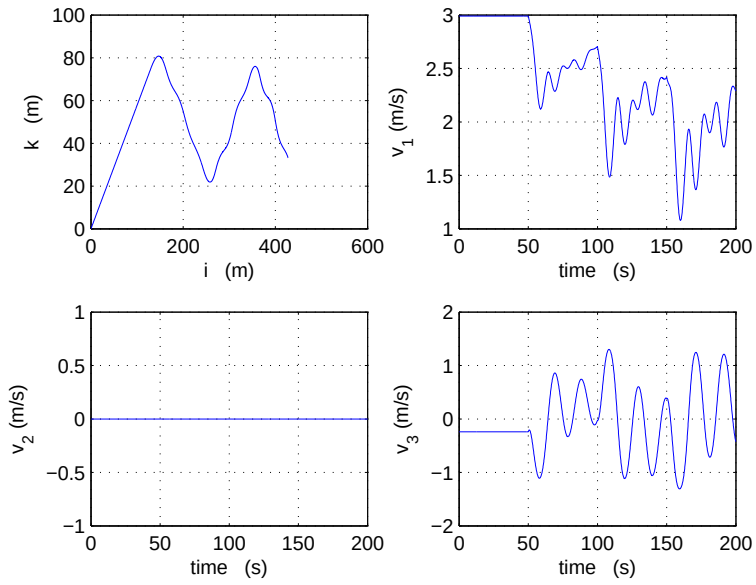

Figure 4.14: The moving trajectory of the airship and the velocities with respect to the body frame

on LQR and an input-output feedback linearization are considered respectively. These two theories, LQR and state feedback are basic and important theories for control problems. They are also easy to adopt. Thus, the results of this two approaches are presented first.

These two approaches adopt the model (4.9)-(4.14), and they both need the linearized model of this nonlinear one. Thus, its linearized model is derived first.

The motion of airship can be split into two motions, the reference motion $\boldsymbol{x_e}$ with $\tilde{u}_{1e} = 0$ and the disturbing motion $\Delta\boldsymbol{x}$ and $\Delta\tilde{u}_1$ which are the dynamics away from the equilibrium. Substituting $\boldsymbol{x} = \boldsymbol{x_e} + \Delta\boldsymbol{x}$ and $\boldsymbol{u}_1 = \Delta\tilde{u}_1$ into the nonlinear model (4.9)-(4.14), the result only keep the first-order of $\Delta\boldsymbol{x}$ and $\Delta\tilde{u}_1$, neglected high-order terms. Then, the linearized model by approximation, around the equilibrium point $\boldsymbol{x_e}$, is derived as:

$$\Delta\dot{\boldsymbol{x}} = A\Delta\boldsymbol{x} + B\Delta\tilde{u}_1 \tag{4.26}$$

where $\boldsymbol{x} = (\theta, \Omega_2, v_1, v_3, r_{p1}, P_{p1})^T$, A is a 6×6 constant system matrix, and B is a 6×1 input matrix. Note that (4.26) can not be confused with feedback linearization considered in section 4.4.2.

Given nominal values of states are $\boldsymbol{x_e} = (\theta_e, \Omega_{2_e}, v_{1_e}, v_{3_e}, r_{p1_e}, P_{p1_e})^T = (0.44, 0, 9.97, -0.8, -1, 299)^T$. These values are computed from (4.21)-(4.25). The linear approximation around this point is

$$\dot{\boldsymbol{x}} = A\boldsymbol{x} + B\tilde{u}_1 \tag{4.27}$$

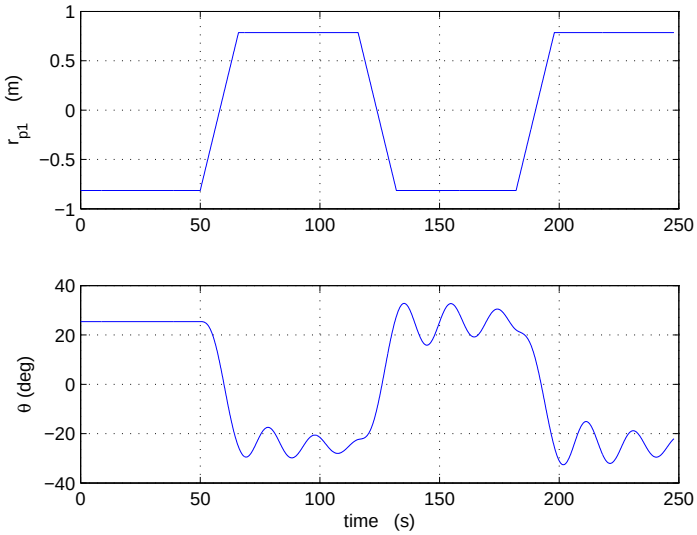

Figure 4.15: The dynamics of the pitch angle with respect to the smooth motion of the moveable mass

where,

$$A = \begin{pmatrix} 0 & 1 & 0 & 0 & 0 & 0 \\ -0.08 & 0.01 & -0.0004 & 0.004 & -0.03 & 0 \\ 0.57 & 0.93 & -0.063 & -0.17 & 0 & 0 \\ 0.24 & 9.13 & 0.05 & -0.62 & 0.002 & 0 \\ 0 & -2 & -1 & 0 & 0 & 0.03 \\ 0 & 0 & 0 & 0 & 0 & 0 \end{pmatrix}$$

$$B = \begin{pmatrix} 0 \\ -0.0002 \\ -0.002 \\ 0.00001 \\ 0 \\ 1 \end{pmatrix}$$

4.4.1 Linear control based on LQR

Since the **Goal 2** is adopted here, a new state which depicts the distance between the actual flight path and the commanded path is added.

As shown in Fig. 4.17, on the equilibrium, the commanded flight path (straight line) of the airship is defined and overlapped with the e_1 axis of the body frame. The inertial frame under this situation is defined as $i - G - k$ as shown in that figure. At time t, the actual position of the airship is (x, z) with respect to the inertial frame, and (x', z') with respect to the body frame. As known from the Fig. 4.17,

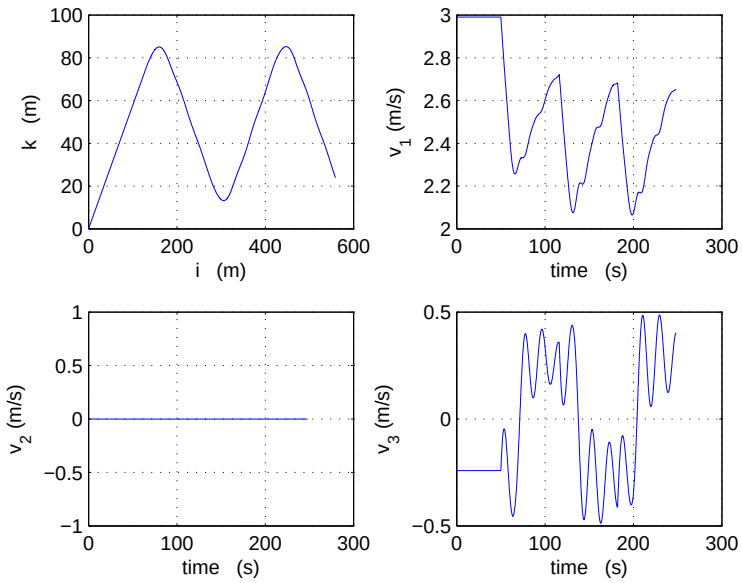

Figure 4.16: The moving trajectory of the airship and the velocities with respect to the smooth motion of the moveable mass

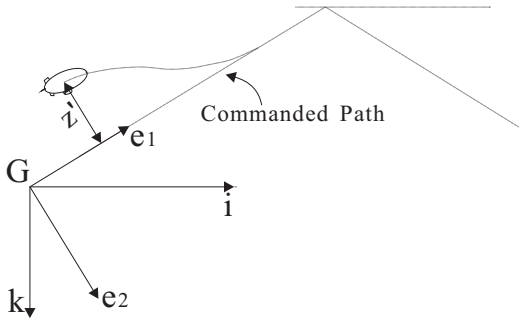

Figure 4.17: The airship tracks a desired flight path

$z^{'}$ is distance from the airship to the e_1 axis of the body frame. As depicted previously, $z^{'}$ is also the distant to the commanded path. By the rotation matrix, the distance from the airship to the desired path is

$$z^{'} = -\sin\xi_e x + \cos\xi_e z \tag{4.28}$$

Differentiating (4.28) and substituting v_1, v_3 and θ, the perpendicular velocity to desired path is

$$\dot{z}^{'} = -\sin\xi_e\left(v_1\cos\theta + v_3\sin\theta\right) + \cos\xi_e\left(-v_1\sin\theta + v_3\cos\theta\right) \tag{4.29}$$

Thus, for the **Goal 2**, a new state $z^{'}$ and 4.29 should be added to the model. Moreover, to follow a desired flight path, another control, the mass of the internal air bladder $m_b = u_4$ is needed. Thus, for a mission of **Goal 2**, 7 states $\left(\theta,\ \Omega_2,\ v_1,\ v_3,\ r_{p1},\ P_{p1},\ z^{'}\right)^T$ and 2 controls $(u_1,\ u_4)^T$ are involved.

The linear quadratic regulator is a well-known and efficient theory for control problems; it provides practical feedback gains. It is assumed that all states $\Delta \boldsymbol{x}$ are available for the control. The infinite horizon cost function is defined as:

$$J = \int_0^\infty \left(\boldsymbol{x}^T Q \boldsymbol{x} + \boldsymbol{u}^T R \boldsymbol{u} \right) dt$$

The weight matrices Q and R are tuning parameters. There is no general way to define the values of these parameters, and their values depend on their weight and the user's choices, which deeply impacts the performance of the closed loop system.

The feedback control law that minimizes the value of the cost is:

$$\boldsymbol{u} = -K(\boldsymbol{x} - \boldsymbol{x_e}) \tag{4.30}$$

where K is given by

$$K = R^{-1} B^T P$$

and P is found by solving the continuous time algebraic Riccati equation

$$A^T P + PA - PBR^{-1} B^T P + Q = 0$$

The above computation can be done in MATLAB® and the feedback gain K is derived by the command lqr$(A, B, Q, R, 0)$.

With the linear feedback (4.30), the airship tracks a desired flight path, which is simulated and shown in Fig. 4.18.

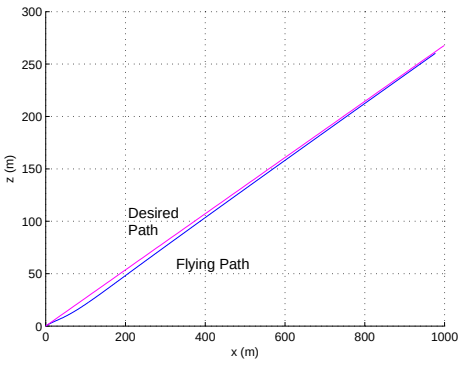

Figure 4.18: The airship with linear control tracks a commanded flight path.

Nevertheless, such a linear control for the original nonlinear system is only valid in a small neighborhood around the equilibrium. The linear control no more ensures stability and the airship crashes down when the disturbance is large, for instance when the disturbance on v_1 is larger than $+4.5\ m/s$.

4.4.2 Nonlinear control based on an I/O feedback linearization

Here, a nonlinear control based on input-output linearization is derived for the model (4.9)-(4.14) with internal stability is proved. The **Goal 1** is adopted here. The motion of the airship no more tracks a desired path, but tracks a desired flight angle ξ, shown in Fig. 4.19. Since $\xi = \theta - \alpha$, thus, the control objective is also to stabilize θ and α. As $\tan\alpha = v_3/v_1$, the stabilization of α can be achieved by stabilizing of v_1 and v_3. Thus, for the system (4.9)-(4.14) which involves six states and one control (the mass of the air bladder u_4 is subject to an open-loop bang-bang control), a state feedback is expected to stabilize all six states.

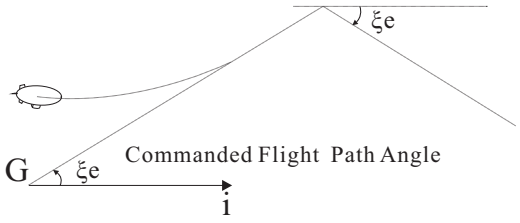

Figure 4.19: The airship tracks a commanded flight angle

Consider the output of the system $y = x$, in these six states, both θ and r_{p1} have relative degree 2. However, it is easy to check that the output $y = r_{p1}$ yields a non minimum phase systems and thus, the input-output linearization can not be applied; whereas the output function $y = \theta$ defines a minimum phase system. Let us check that $y = r_{p1}$ yields a non minimum phase system. This is done through the approximate linearization of the input-output system and through the computation of its zeros. Whenever, the linearized system has no zero on the imaginary axis, then, it is possible to conclude about the local minimum phase property of the nonlinear system. When the linearized system has a zero on the imaginary axis, and no zero in the right half complex plane, then, the nonlinear system may be either minimum phase or no minimum phase (Slotine and Li, 1991).

With the linearized form (4.27), the transfer function for the output $y = \theta$ is computed as:

$$TF_1 = \frac{-0.02s^4 - 0.02s^3 - 0.1s^2 - 0.08s - 0.005}{100s^6 + 67s^5 + 1.9s^4 - 2.3s^3 - 5s^2 - s}$$

and it for the output $y = r_{p1}$ is computed as:

$$TF_2 = \frac{3.6s^4 + 2.4s^3 + 0.3s^2 + 0.2s + 0.01}{100s^6 + 67s^5 + 1.9s^4 - 2.3s^3 - 5s^2 - s}$$

The four zeros of TF_1 have strictly negative real part, whereas some of TF_2 have positive real part and thus are unstable.

Since the linear approximation of the system (4.9)-(4.14) with the output $y = \theta$ has stable transmission zeros, the nonlinear system has locally stable zero dynamics and thus the system is minimum phase (Conte et al., 2007).

Note that the four zeros of TF_1 lie close to the imaginary axis, but in the left open half complex plane, thus, the system is weakly minimum phase. Feedback linearization of $y = \theta$ will yield some undesired oscillations.

I/O linearization of θ

Since the relative degree of the output $y = \theta$ is 2, it proposes the following desired error equation

$$\ddot{e} + \lambda_1 \dot{e} + \lambda_0 e = w_1$$

where $e = y - \theta_e$, θ_e is the desired value for θ, and w_1 denotes a new control. Equivalently,

$$\ddot{\theta} + \lambda_1 \dot{\theta} + \lambda_0(\theta - \theta_e) = w_1 \tag{4.31}$$

λ_1 and λ_0 assign the poles of the error dynamics. Substituting (4.9)-(4.14) into (4.31), the equation can be solved and the control $\tilde{u}_1$ is derived, as follows,

$$\tilde{u}_1 = T_4(H_4 - w_1 + \lambda_1 \Omega_2 + \lambda_0(\theta - \theta_e)) \tag{4.32}$$

where,

$$\begin{aligned} T_4 &= \frac{J_2 m_3 + J_2 \bar{m} + \bar{m} r_{p1}^2 m_3}{r_{p3}(m_3 + \bar{m})} \\ H_4 &= T_1(H_1 + r_{p3}\tilde{u}_1) + T_2 H_2 \end{aligned}$$

(4.32) is the nonlinear feedback control of the system. Let $w_1 = 0$, and substituting (4.32) into the system (4.9)-(4.14), the closed loop system will be derived.

The choice of the values of λ_1 and λ_0 not only has a direct impact on the motion of θ and Ω_2, but also a significant one on the states v_1, v_3, r_{p1} and P_{p1}. The impact on the θ and Ω_2 is easy to analyze, but the transient response of v_1, v_3, r_{p1} and P_{p1} remains unclear due to the nonlinear equations. By trying different values of λ_1 and λ_0, different performances of the controller are presented.

Simulation results

Only a ascending segment is considered here. The conditions in the descent are the same as the ascent with only reversed values of the commands and the net lift.

As to the values of λ_1 and λ_0, there is a tradeoff between the performance of θ and Ω_2 with respect to the one of states v_1, v_3, r_{p1} and P_{p1}, and thus they must be carefully chosen. Three different sets of λ_1 and λ_0 are chosen to compare. All of these simulations are under the same initial errors $\Delta\theta = +5^\circ$ and $\Delta v_1 = +2\ m/s$.

To compare the results of different parameters, the poles under different sets of parameters should have the same negative real part, so θ stabilizes in a similar period as shown in Fig. 4.20.

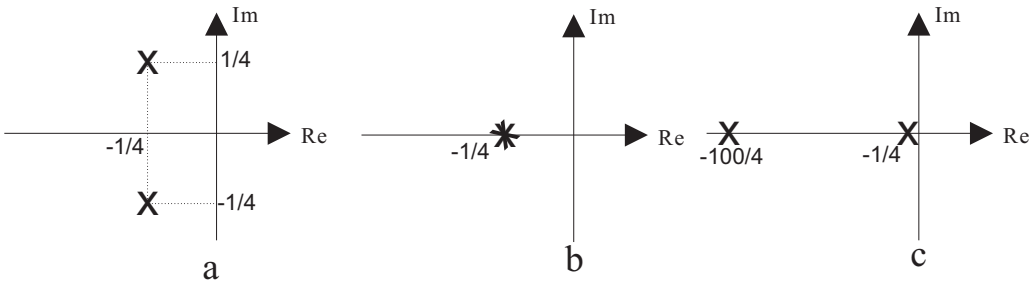

Figure 4.20: Three Different Assignments of Poles

1. First strategy: two complex poles

   The poles are chosen to be of the form $s = -a(1 \pm i)$. For the reported simulation, $a = 1/4$, so $\lambda_1 = 1/2$ and $\lambda_0 = 1/8$, see Fig. 4.20.a. This is called Controller No. 1.

2. Second strategy: a double real pole

   Both poles are placed at $-a$, with $a = -1/4$, see Fig. 4.20.b. So the controller No. 2 is with $\lambda_1 = 0.5$ and $\lambda_0 = 0.0625$.

3. Third strategy: a dominant real pole

   The last considered strategy is to obtain a first-order like response by placing a dominant pole. Controller No. 3 has two different negative real poles. One pole close to the imaginary axis, another is far away from the imaginary axis. Let $s_1 = -\frac{1}{4}$, $s_2 = -\frac{100}{4}$, see Fig. 4.20.c, so $\lambda_1 = 25.25$ and $\lambda_0 = 6.25$.

The dynamics of θ and Ω_2 under these controls are presented in Fig. 4.21 and 4.22. Fig. 4.23 and 4.24 are the dynamics of v_1 and v_3 with the controller No. 3. For different controllers, the difference on dynamics of v_1 and v_3 is the final amplitude. Fig. 4.25 - 4.27 are the dynamics of r_{p1} for different controls.

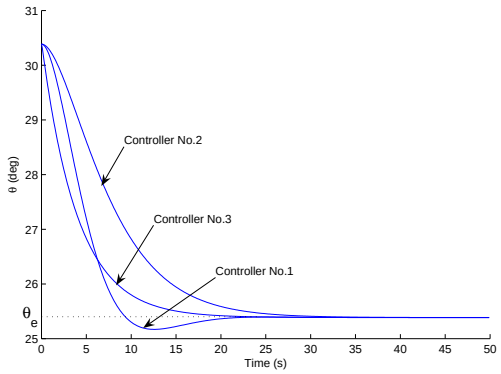

Figure 4.21: Comparison of Dynamics of θ

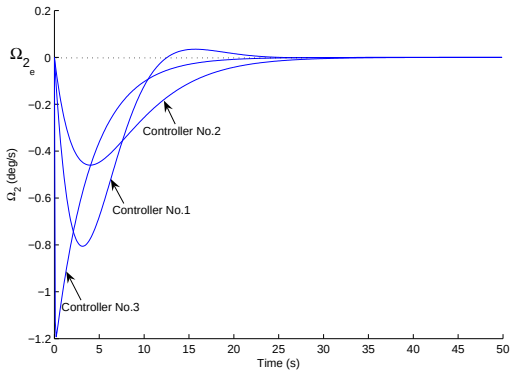

Figure 4.22: Comparison of dynamics of Ω_2

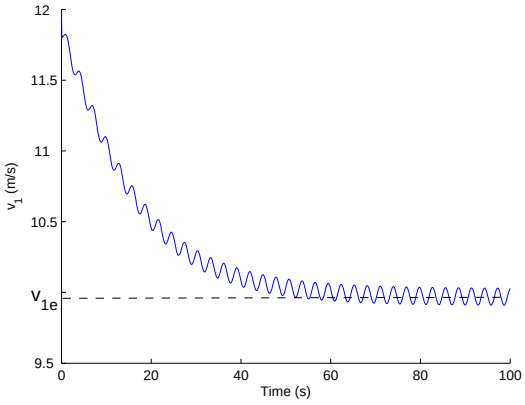

Figure 4.23: Dynamics of v_1

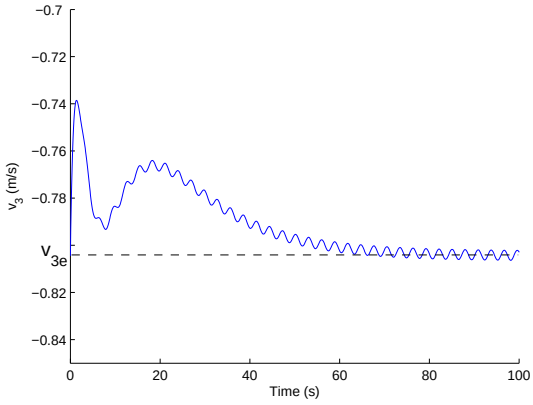

Figure 4.24: Dynamics of v_3

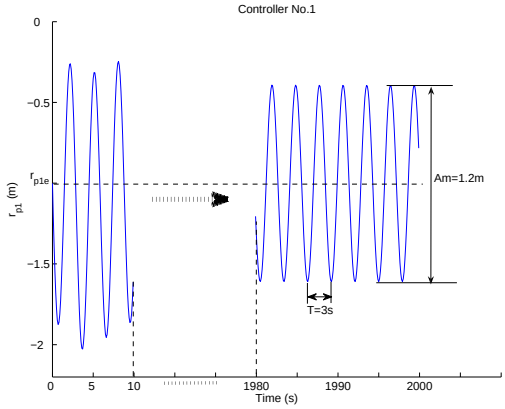

Figure 4.25: Dynamics of r_{p1} with Controller No.1

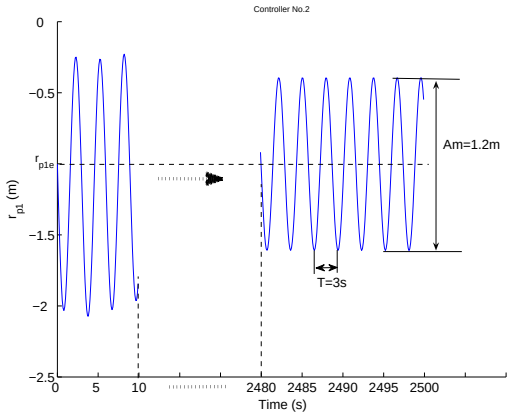

Figure 4.26: Dynamics of r_{p1} with Controller No.2

Analysis of the simulation result

Generally, from the simulation results, the system is stable under certain initial errors with these controllers, but the differences between three controllers are significant.

In detail, from Fig. 4.21, the three controllers have similar stationarity and rapidity, which is due to the same negative real parts, see Fig. 4.20. Both θ and Ω_2 stabilize at the equilibrium point quickly, which is the goal of these feedback controllers.

As v_1 and v_3, they have small periodic oscillations under three conditions, but the final amplitudes are different. With controller No. 1 and No.2, the final amplitudes are the same, 0.14 m/s, for v_1, and v_3, which is small enough to be ignored. The controller No. 3 has a slightly better performance. To v_1, the final amplitude is 0.01 m/s.

From Fig. 4.25 to 4.27, it is clear to find that the controller No. 3 is better than the two others. The amplitude of r_{p1} under controller No. 3 continually declines with the time, but it is constant under

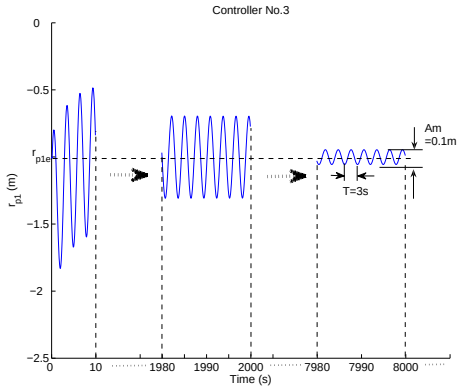

Figure 4.27: Dynamics of r_{p1} with Controller No.3

controllers No. 1 and No. 2.

With these controllers, v_1, v_3, r_{p3} and P_{p1} have periodic oscillations, with a period approximately of 3 s. These oscillations are caused by the zeros of the linear approximation which are close to the imaginary axis. Here, two of the zeros of TF_1 are $-2.85 \times 10^{-4} \pm 2.16i$.

Remark: The internal dynamics of the system with output $y = \theta$ is critical stable.

Thus, it is necessary to find an output with maximal relative degree to obtain the smallest and asymptotically stable internal dynamics.

4.5 Nonlinear Control Based on Maximal Feedback Linearization

This section contains the main result of this chapter. The model (4.1) and **Goal 1** are adopted here. In this section the dynamics is analyzed, and an advanced nonlinear control is derived.

To analyze the dynamics and to derive a nonlinear control for the system, a progressive approach from a simplified model to a complete one is adopted. The simplest airship model corresponds to the special case in which the airship freely rotates around its fixed center of volume. The model is identical to a prismatic-joint pendulum model. Basic properties are derived and a control law is explicitly computed which solves the maximal feedback linearization problem with internal stability. Based on this fundamental model, and by dropping some restrictions, two other less restrictive special cases are considered for the airship. Although models become more complex, it is shown that the results obtained for the most simple special case remain valid, including for the complete complex model.

For several different special cases in this section, dummy output functions are computed which define a minimum phase system and whose feedback linearization will achieve maximal linearization.

It is shown that the angular momentum of the airship plays a key role in these computations and

is instrumental for its full internal stabilization despite the intrinsic nonlinearity of the model.

This section is arranged as follows: section 4.5.1 introduces some basic knowledge on feedback linearization and zero dynamics. Section 4.5.2 is devoted to the modelling and control of the most restrictive special case of the airship whose center of volume is fixed and which is only subject to the motion of the moveable mass. The airship is liberated in Section 4.5.3 by dropping the assumption that the center of volume O is fixed, which means the airship can ascend and descend. In this case, the center of mass is subject to a ballistic motion and the controllable subsystem is shown to keep similar properties as the previous fundamental system. In Section 4.5.4, the airship model is completed with the inertial forces and Section 4.5.5 displays the full model in the longitudinal plane including the aerodynamic forces. Up to some approximation, the previous system structure is still valid and used to design a nonlinear control with similar performance. Section 4.5.6 presents simulation results of a continuing flight with the control in Section 4.5.5.

4.5.1 Preliminaries on maximal feedback linearization and zero dynamics

A standard way to control a nonlinear system consists in looking for a nonlinear state feedback that fully, or partially, cancels out all nonlinear terms in some suitable coordinates. This has been one major achievement in the early years of modern nonlinear control theory. For completeness some main results are recalled now that will be applied in the rest of this section.

Given a SISO nonlinear affine system,

$$\Sigma = \begin{cases} \dot{x} = f(x) + g(x)u \\ y = h(x) \end{cases} \tag{4.33}$$

where the state $x \in \mathbb{R}^n$, the input $u \in \mathbb{R}$, the dummy output $y \in \mathbb{R}$, and the entries of f, g are meromorphic functions. According to (Conte et al., 2007), if the relative degree of the output y is n, the system (4.33) can be fully and exactly linearized by feedback. Pick new coordinates $\boldsymbol{\xi} = (h,\ L_f h,\ \cdots,\ L_f^{n-1}h)^T$ and system (4.33) is transformed into

$$\begin{cases} \dot{\xi}_1 = \xi_2 \\ \dot{\xi}_2 = \xi_3 \\ \vdots \\ \dot{\xi}_n = \alpha(\boldsymbol{\xi}) + \beta(\boldsymbol{\xi})u \\ y = \xi_1 \end{cases}$$

for some suitable $\alpha(\boldsymbol{\xi})$ and $\beta(\boldsymbol{\xi})$.

Define the nonlinear state feedback as:

$$u = \frac{1}{\beta(\boldsymbol{\xi})}\left(-\alpha(\boldsymbol{\xi}) + v\right). \tag{4.34}$$

and the original nonlinear system is transformed into a linear system with transfer function $1/s^n$. By choosing $v = -\lambda_0\xi_1 - \lambda_1\xi_2 - \cdots - \lambda_{n-1}\xi_n$, the characteristic polynomial of this linearized system is

$$s^n + \lambda_{n-1}s^{n-1} + \cdots + \lambda_0 = 0.$$

which is easy to stabilize. The overall nonlinear feedback for the system (4.33) is as,

$$u = \frac{1}{\beta(\boldsymbol{\xi})}\left(-\alpha(\boldsymbol{\xi}) - \lambda_0\xi_1 - \lambda_1\xi_2 - \cdots - \lambda_{n-1}\xi_n\right).$$

Whenever the relative degree of the system (4.33) is γ and $\gamma < n$, partial feedback linearization is obtained as follows. Pick

$$\xi_1 = h(x), \quad \xi_2 = L_f h(x), \quad \cdots, \quad \xi_\gamma = L_f^{\gamma-1}h(x).$$

As system (4.33) is single input, the left kernel $g^\perp$ of $g(x)$ has dimension $n-1$ and it is fully integrable. Thus, $g^\perp$ can be written as

$$g^\perp = span\{d\xi_1, \cdots, d\xi_{\gamma-1}; d\zeta\}$$

where dim $\zeta = n - \gamma$. Consequently, in these new coordinates, system (4.33) reads

$$\begin{cases} \dot{\xi}_1 = \xi_2 \\ \vdots \\ \dot{\xi}_\gamma = \alpha(\boldsymbol{\xi}, \zeta) + \beta(\boldsymbol{\xi}, \zeta)u \\ \dot{\zeta} = \boldsymbol{q}(\boldsymbol{\xi}, \zeta) \\ y = \xi_1 \end{cases} \tag{4.35}$$

The dynamics $\dot{\zeta} = \boldsymbol{q}(\boldsymbol{\xi}, \zeta)$ are known as the internal dynamics and whenever y is constrained to zero, then it yields the so-called zero dynamics (Isidori and Moog, 1988)

$$\dot{\zeta} = \boldsymbol{q}(0, \zeta).$$

The nonlinear feedback

$$u = \frac{1}{\beta(\boldsymbol{\xi}, \zeta)}\left(-\alpha(\boldsymbol{\xi}, \zeta) + v\right) \tag{4.36}$$

yields a linear transfer function from the new input v to the output y as $\frac{1}{s^\gamma}$. The feedback also yields the unobservable dynamics $\dot{\zeta} = \boldsymbol{q}(\boldsymbol{\xi}, \zeta)$. The dummy output of system (4.33) is easily stabilized by pole placement as done in (4.36). However the internal stability is guaranteed if and only if the unobservable zero dynamics $\dot{\zeta}$ is stable. This is exactly what is called a minimum phase system and does depend on the choice of output only.

In the rest of this section, an output will be sought such that its relative degree is maximal, and such that it defines a minimum phase system.

4.5.2 The airship with fixed center of volume

The dynamics in the longitudinal plane is impacted by the following four parts:

1. the moveable mass which controls the pitch angle θ,
2. the mass of the internal air bladder which controls the flying altitude,
3. the inertial forces,
4. the aerodynamic forces.

Assuming that the airship is only subject to the motion of the moveable mass to control the pitch angle, and there is no other force affecting the airship. In this situation, the moveable mass actually impacts the angular momentum around the center point. The dynamics of the airship is not only restricted to the longitudinal plane, but it is also assumed that the center of volume O of the airship is fixed, which means that the airship can only rotate around O and the longitudinal and horizontal translation velocities v_3 and v_1 are zero, shown in Fig 4.28.

These assumptions are summarized as:

Assumptions:

A_1: No aerodynamic force.

A_2: No inertial force.

A_3: The center of volume O is fixed, and the airship has no translational velocities.

The mathematical model of this fundamental case is derived as follows.

Model of the airship with a fixed center of volume

In the situation described above, the airship rotates around O depending on the forward and backward motions of the moveable mass, as shown in Fig. 4.28, but O does not have any translation velocity.

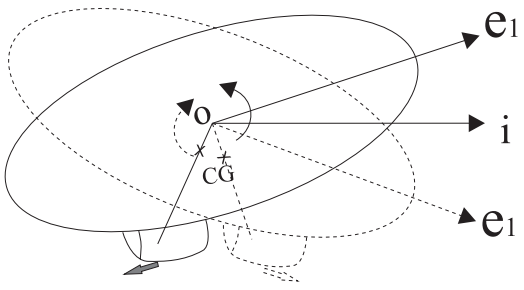

Figure 4.28: The rotation of the airship with the movement of the moveable mass.

In this case, the airship is identical to a prismatic-joint pendulum described in Fig. 4.29. The rotational joint at the point O is not actuated. The joint between the two links of the pendulum is prismatic and actuated. This pendulum, inverted or not, has been considered as a standard control example in many references (Wie, 1998).

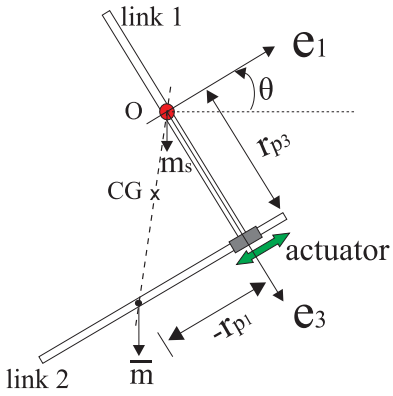

Figure 4.29: The airship system with a fixed point.

Here, the rigid body of the airship is represented by the link 1 which is fixed at the point O, and the moveable mass corresponds to the link 2 which can be moved by an actuator. The position of the center of mass of the moveable mass in the body frame in the longitudinal plane is $(r_{p1},\ r_{p3})$. The system can swing along with the actuator changing the position of $\bar{m}$, which is the same as the description in Section 2.1.2. Here, r_{p3} is constant, as shown in Fig. 4.29.

For this case, $\boldsymbol{F_s} = 0$. The moveable mass impacts the angular momentum, which is reflected by $\boldsymbol{M_s} = \boldsymbol{M_{GBt}}$ with the constrain that the velocity $\boldsymbol{v} = 0$. Combining equations (3.19), (3.23), and (3.24), the model is derived as,

$$\begin{cases} \ddot{\theta} \quad = \varrho_1 = -\frac{1}{J+\bar{m}r_{p1}^2}(\bar{m}r_{p3}r_{p1}\dot{\theta}^2 + 2\bar{m}r_{p1}\dot{r}_{p1}\dot{\theta} + \bar{m}gr_{p1}\cos\theta + r_{p3}u) \\ \ddot{r}_{p1} = \sigma_1 = \frac{1}{J+\bar{m}r_{p1}^2}\Big((Jr_{p1} + \bar{m}r_{p1}^3 + \bar{m}r_{p3}^2 r_{p1})\dot{\theta}^2 + 2\bar{m}r_{p3}r_{p1}\dot{r}_{p1}\dot{\theta} \\ \qquad\qquad -(J+\bar{m}r_{p1}^2)g\sin\theta + \bar{m}gr_{p3}r_{p1}\cos\theta + (\frac{J}{\bar{m}} + r_{p1}^2 + r_{p3}^2)u\Big) \end{cases} \tag{4.37}$$

where the input u_1 and J_y are rewritten as u and J, respectively. ζ_1 and σ_1 are suitable notations which will be used later on.

Maximal linearization of a minimum phase model

System (4.37) is a special case of $\dot{x} = f(x) + g(x)u$ where $x = (\theta,\ \dot{\theta},\ r_{p1},\ \dot{r}_{p1})$. It is fully accessible as it can be checked from standard computation (Isidori, 1989) that

$$\dim\ \overline{span\{g,\ ad_f g,\ ad_f^2 g\}} = 4.$$

The distribution spanned by $\{g,\ ad_f g,\ ad_f^2 g\}$ is not involutive, thus, system (4.37) is not fully linearizable by static state feedback. It is thus interesting to look for a maximal linearization as done in (Marino, 1986). Standard computation allow to check that the distribution spanned by $\{g,\ ad_f g\}$ is involutive. As done in (Marino, 1986), any state variable $h(x)$ such that $dh(x) \perp \{g,\ ad_f g\}$ will define a dummy output whose relative degree is 3 and whose feedback linearization yields a linear third order subsystem and first order zero dynamics.

According to the notations in (Conte et al., 2007) the following results are obtained from system (4.37):

$$\mathcal{H}_\infty = 0$$
$$\mathcal{H}_3 = span\{d\phi_1,\ \ d\phi_2\}$$

and $\mathcal{H}_4$ is not integrable. The condition $\mathcal{H}_\infty = 0$ means that the system is fully accessible. $\mathcal{H}_3$ represents the codistribution which consists of all differential forms whose relative degree is at least 3. Here, ϕ_1 and ϕ_2 are computed as,

$$\phi_1 = J\dot{\theta} + (r_{p1}^2\dot{\theta} + r_{p3}^2\dot{\theta} + r_{p3}\dot{r}_{p1})\bar{m}$$
$$\phi_2 = \theta + \frac{r_{p3}}{\sqrt{\frac{J}{\bar{m}} + r_{p3}^2}} \arctan \frac{r_{p1}}{\sqrt{\frac{J}{\bar{m}} + r_{p3}^2}}.$$

The mechanical interpretation of those functions is as follows. In ϕ_1, $J\dot{\theta}$ is the angular momentum of the static mass of the airship in the longitudinal plane, and $(r_{p1}^2\dot{\theta} + r_{p3}^2\dot{\theta} + r_{p3}\dot{r}_{p1})\bar{m}$ is a longitudinal plane component of the angular momentum of the moveable mass $\boldsymbol{r_p} \times \bar{m}\boldsymbol{v_p}$. So, ϕ_1 is the angular momentum of the whole airship computed at the point O. Note that ϕ_1 is different from $\boldsymbol{K}$ in Section 3.3.2 which is the angular momentum of the inertial forces. ϕ_1 and ϕ_2 also have the following relation:

$$\dot{\phi}_2 = \frac{1}{J + (r_{p1}^2 + r_{p3}^2)\bar{m}}\phi_1. \tag{4.38}$$

Up to some integrating factor, ϕ_2 represents an integral of the angular momentum ϕ_1.

At this stage, any combination of ϕ_1 and ϕ_2 has relative degree 3 and its feedback linearization will yield a linear controllable three-dimensional subsystem with a one-dimensional zero dynamics. The following result shows the possibility to ensure that the system is minimum phase which has a decisive impact on its internal stability and the feasibility of this control design.

***Theorem* 1**: The system (4.37) with the output $y = \phi_1 + k\phi_2$ has asymptotically stable zero dynamics for any $k > 0$.

Proof: As in Section 4.5.1, under this situation, a new coordinate is chosen as follows

$$\xi_1 = \phi_1 + k\phi_2 \tag{4.39}$$

$$\xi_2 = \dot{\phi}_1 + k\dot{\phi}_2 \tag{4.40}$$

$$\xi_3 = \ddot{\phi}_1 + k\ddot{\phi}_2 \tag{4.41}$$

$$\zeta = \phi_1. \tag{4.42}$$

From a practical point of view, the right hand side of equations (4.39)-(4.42) are computed using a computer algebra software, as the lengthy expression of those functions are trackable by computers. Their result is directly plugged in the simulation system for practical tests. For instance, equations (4.39) to (4.41) read:

$$\begin{cases} \xi_1 = \phi_1 + k\phi_2 = J\dot{\theta} + (r_{p1}^2\dot{\theta} + r_{p3}^2\dot{\theta} + r_{p3}\dot{r}_{p1})\bar{m} + k(\theta + \frac{r_{p3}}{\sqrt{\frac{J}{\bar{m}}+r_{p3}^2}}\arctan\frac{r_{p1}}{\sqrt{\frac{J}{\bar{m}}+r_{p3}^2}}) \\ \xi_2 = -mg(r_{p1}\cos\theta + r_{p3}\sin\theta) + \frac{k}{J+mr_{p1}^2+mr_{p3}^2}\left(J\dot{\theta} + mr_{p1}^2\dot{\theta} + mr_{p3}^2\dot{\theta} + mr_{p3}\dot{r}_{p1}\right) \\ \xi_3 = -mg\dot{r}_{p1}\cos\theta + mgr_{p1}\dot{\theta}\sin\theta - mgr_{p3}\dot{\theta}\cos\theta - k(mr_{p1}^3 g\cos\theta + 2mr_{p1}^3\dot{r}_{p1}\dot{\theta} \\ +mr_{p3}g\sin\theta r_{p1}^2 + mr_{p1}g\cos\theta r_{p3}^2 + 2mr_{p1}\dot{r}_{p1}^2 r_{p3} + 2mr_{p1}\dot{r}_{p1}\dot{\theta}r_{p3}^2 + mgr_{p3}^3\sin\theta \\ +r_{p1}gJ\cos\theta + 2r_{p1}\dot{r}_{p1}\dot{\theta}J + gr_{p3}\sin\theta J)m/(J^2 + 2Jmr_{p1}^2 + 2Jmr_{p3}^2 \\ +m^2r_{p1}^4 + 2m^2r_{p1}^2r_{p3}^2 + m^2r_{p1}^4) \end{cases} \tag{4.43}$$

The zero dynamics under this new coordinates is given by $\dot{\zeta}$ under the constraint $\phi_1 + k\phi_2 = 0$. Thus, $\dot{\phi}_1 = -k\dot{\phi}_2$. From (4.38) one gets

$$\dot{\zeta} = \dot{\phi}_1 = -k\dot{\phi}_2 = -k\frac{1}{J + (r_{p1}^2 + r_{p3}^2)\bar{m}}\phi_1.$$

Thus,

$$\dot{\zeta} = -k\frac{1}{J + (r_{p1}^2 + r_{p3}^2)\bar{m}}\zeta.$$

So, for any $k > 0$, the system is asymptotically stable as $J + (r_{p1}^2 + r_{p3}^2)\bar{m}$ is strictly positive and bounded.

Control design and simulation

The family of dummy outputs $y = \phi_1 + k\phi_2$ for a varying real number k is considered now. The special case (4.37) is stabilized through standard input-output linearization according to the above approvement. From ***Theorem* 1**, it is mandatory to pick $k > 0$ to ensure internal stability of the closed loop system. Its actual value is a tuning parameter which influences the velocity of the zero dynamics. According to the feedback design in Section 4.5.1, the following error equation is considered,

$$y^{(3)} + \lambda_2 y^{(2)} + \lambda_1 y^{(1)} + \lambda_0(y - y_e) = 0 \tag{4.44}$$

where y_e is the desired constant value for y; $y = \xi_1$; $y^{(1)} = \xi_2$; and $y^{(2)} = \xi_3$. Here, ξ_i are computed by equation (4.43). The term $y^{(3)}$ is an explicit function of the control u as $\dot{\xi}_\gamma$ in Section 4.5.1, which can be rewritten as $y^{(3)} = \alpha(\boldsymbol{\xi}, \boldsymbol{\zeta}) + \beta(\boldsymbol{\xi}, \boldsymbol{\zeta})u$. Substituted the model (4.37) into the first order time-derivative of $y^{(2)}$, these $\alpha(\boldsymbol{\xi}, \boldsymbol{\zeta})$ and $\beta(\boldsymbol{\xi}, \boldsymbol{\zeta})$ are derived by computer algebra software. Actually, they are with long expressions and useless for practitioners as the feedback is directly plugged in the control device. Thus, the control u is detailed in the Appendix of the thesis and reads as:

$$u = -\frac{1}{\beta(\boldsymbol{\xi}, \boldsymbol{\zeta})}\left(\lambda_2\xi_3^{(2)} + \lambda_1\xi_2^{(1)} + \lambda_0(\xi_1 - y_e) + \alpha(\boldsymbol{\xi}, \boldsymbol{\zeta})\right) \tag{4.45}$$

The control (4.45) requires the knowledge of all states available. Eventually its practical implementation will go through the design of a nonlinear observer which is out of the scope of this thesis.

For these simulations, parameters $k = 50$, $\lambda_2 = 2$, $\lambda_1 = 2$, $\lambda_0 = 1$. The initial values of θ, $\dot{\theta}$, r_{p1}, and $\dot{r}_{p1}$ are 41.5°, 0, -1.15 m, and 0, respectively, and their commanded values are 30°, 0, -1.15 m, and 0, respectively. All mechanical properties used in the simulations are listed in Table 4.3 where the aerodynamic coefficients are borrowed from (Ouyang, 2003).

Table 4.3: Physical properties of the airship

Terms	Values	Terms	Values	Terms	Values
$\bar{m}$	30 kg	J	8000 $kg \cdot m^2$	C_{x0}	0.059
m_s	269 kg	ρ_a	1.29 kg/m^3	C_x^α	0.016
m_1	400 kg	∇	296 m^3	C_{z0}	0
m_3	500 kg	C_m^α	0.255	C_z^α	1.269
r_{p3}	2 m	$C_m^{\Omega_2}$	0	C_{m0}	0

Fig. 4.30 and 4.31 are simulation results of the dynamics of θ, r_{p1} and the control input u. θ and r_{p1} are stabilized to the desired equilibrium 30° and -1.15 m after 30 s.

4.5.3 The airship with liberated center point

Aircrafts, as helicopters, rotate around the center of mass, not around the center of volume. In the first fundamental special case, the aircraft is assumed to rotate around the center of the volume O. So, by liberating the pivot O, the airship will rotate around the center of the gravity CG. The body frame is still attached to the point O.

In this case, assumption A_3 is dropped and the following assumptions do still hold.

Assumptions:

A_1: No aerodynamic force.

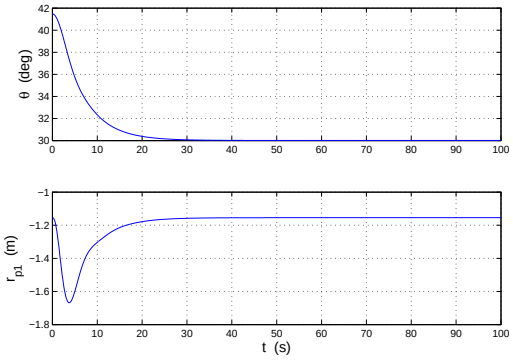

Figure 4.30: Dynamics of θ and r_{p1} with initial error.

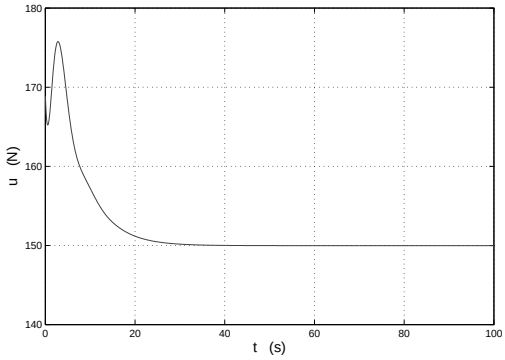

Figure 4.31: The behavior of input u.

$\mathbf{A_2}$: No fluid inertial force.

Model of the airship with liberated center point

In this case, only the gravity and the buoyancy are applied on the airship, which means that the right hand sides of equations (3.25) and (3.26) only include the gravity and the buoyancy terms. Equations (3.23) and (3.24) remain unchanged,

$$\boldsymbol{F_s} = \boldsymbol{F_{GBt}} \tag{4.46}$$

$$\boldsymbol{M_s} = \boldsymbol{M_{GBt}}. \tag{4.47}$$

Combining (3.19), (3.23), (3.24) (4.46), and (4.47), the mathematical model in the longitudinal plane is as follows,

$$\begin{cases} \ddot{\theta} &= \varrho_1 + \frac{1}{J+\bar{m}r_{p1}^2}(\dot{v}_3 - \dot{\theta}v_1)\bar{m}r_{p1} \\ \ddot{r}_{p1} &= \sigma_1 + \frac{1}{J+\bar{m}r_{p1}^2}\left(\bar{m}r_{p1}r_{p3}(\dot{\theta}v_1 - \dot{v}_3) - (J+\bar{m}r_{p1}^2)(\dot{\theta}v_3 + \dot{v}_1)\right) \\ \dot{v}_1 &= \frac{1}{m_s}(-m_s\dot{\theta}v_3 + (\bar{m}-m_0)g\sin\theta - u) \\ \dot{v}_3 &= \frac{1}{m_s+\bar{m}}\left((m_s+\bar{m})\dot{\theta}v_1 + m_0 g\cos\theta + \bar{m}r_{p3}\dot{\theta}^2 + 2\bar{m}\dot{\theta}\dot{r}_{p1} + \bar{m}r_{p1}\ddot{\theta}\right). \end{cases} \tag{4.48}$$

Comparing the special case (4.37) with model (4.48), it is easy to note that system (4.37) is a subsystem of the model (4.48). The additional parts in $\ddot{\theta}$ and $\ddot{r}_{p1}$ are due to the translation velocities of point O.

Maximal linearization of a minimum phase model

System (4.48) is now subject to a ballistic motion (the point CG). In other words, there exist some non-controllable states besides the controllable or accessible subsystem, which is explained in

the following. Again, following standard computation (Conte et al., 2007), one computes the non-controllable subsystem whose coordinates are denoted by ψ_1 and ψ_2:

$$\mathcal{H}_\infty = span\{d\psi_1, \quad d\psi_2\}$$

where

$$\psi_1 = (r_{p1}\dot{\theta} - \frac{m_s + \bar{m}}{\bar{m}}v_3)^2 + (\dot{r}_{p1} + r_{p3}\dot{\theta} + \frac{m_s + \bar{m}}{\bar{m}}v_1)^2$$
$$\psi_2 = (r_{p1}\dot{\theta} - \frac{m_s + \bar{m}}{\bar{m}}v_3)\cos\theta + (\dot{r}_{p1} + r_{p3}\dot{\theta} + \frac{m_s + \bar{m}}{\bar{m}}v_1)\sin\theta.$$

$(m_s+\bar{m})\psi_1$ is the kinetic energy of CG, and ψ_2 denotes the horizontal velocity of CG, which means that the CG of the airship is subject to a ballistic motion, shown in Fig. 4.35.

Thus the six-dimensional state system (4.48) can be decoupled into a two-dimensional non-controllable subsystem and a four-dimensional subsystem whose structural properties are similar to those of model (4.37). One gets

$$\mathcal{H}_3 = span\{d\tilde{\phi}_1, \quad d\tilde{\phi}_2\} \oplus \mathcal{H}_\infty$$

where

$$\tilde{\phi}_1 = J\dot{\theta} + (r_{p1}^2\dot{\theta} + r_{p3}^2\dot{\theta} + r_{p3}\dot{r}_{p1})\frac{\bar{m}m_s}{\bar{m} + m_s}$$
$$\tilde{\phi}_2 = \theta + \frac{r_{p3}}{\sqrt{\frac{\bar{m}+m_s}{\bar{m}m_s}J + r_{p3}^2}}\arctan\frac{r_{p1}}{\sqrt{\frac{\bar{m}+m_s}{\bar{m}m_s}J + r_{p3}^2}}.$$

Here, $\tilde{\phi}_1$ is exactly the angular momentum of the airship computed at the center of gravity CG. The relation of $\tilde{\phi}_1$ and $\tilde{\phi}_2$ is as follows,

$$\dot{\tilde{\phi}}_2 = \frac{1}{J + (r_{p1}^2 + r_{p3}^2)\frac{\bar{m}m_s}{\bar{m}+m_s}}\tilde{\phi}_1.$$

***Theorem* 2**: The system (4.48) with the output $\tilde{\phi}_1 + \tilde{k}\tilde{\phi}_2$ has asymptotically stable zero dynamics for any $\tilde{k} > 0$.

The proof is similar to that of ***Theorem* 1**.

Control design and simulation

The principle to derive the control is the same as in Section 4.5.2. Here, define the dummy output $y = \tilde{\phi}_1 + \tilde{k}\tilde{\phi}_2$ and substitute $y^{(1)} = \dot{\tilde{\phi}}_1 + \tilde{k}\dot{\tilde{\phi}}_2$, $y^{(2)} = \ddot{\tilde{\phi}}_1 + \tilde{k}\ddot{\tilde{\phi}}_2$, $y^{(3)} = \dddot{\tilde{\phi}}_1 + \tilde{k}\dddot{\tilde{\phi}}_2$ into equation (4.44). The latter is solved in u through computer algebra to get the state feedback linearization.

Since the model becomes more complicated, the explicit expression of the control u becomes longer and only trackable by computers. By the way, these results are directly plugged in the control device and useless for the practitioners. These explicit expressions are not displayed.

For the simulations, the initial values of v_1, $\dot{v}_1$, v_3, and $\dot{v}_3$ are 1.8 m/s, 0, 0, and 0. Let $m_0 = 1\ kg$. Other parameters remain the same values. As done in the previous simulation results, similar dynamic behaviors of θ, r_{p1} and control input u are obtained and are not reproduced here. The ballistic motion of CG is shown in Fig. 4.35.

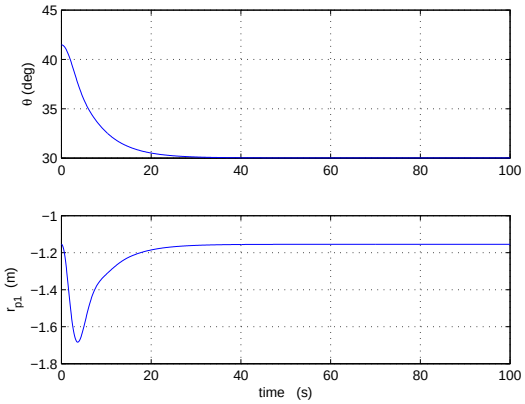

Figure 4.32: Dynamics of θ and r_{p1} with initial error in the second case.

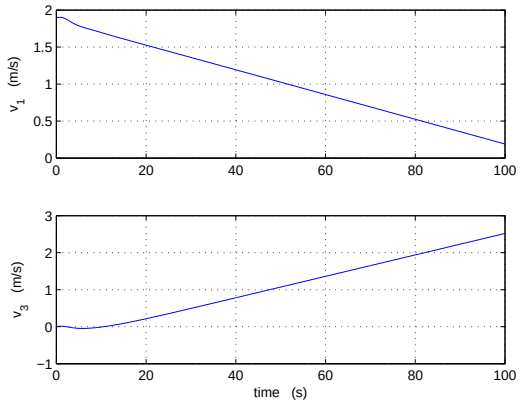

Figure 4.33: The behavior of input u.

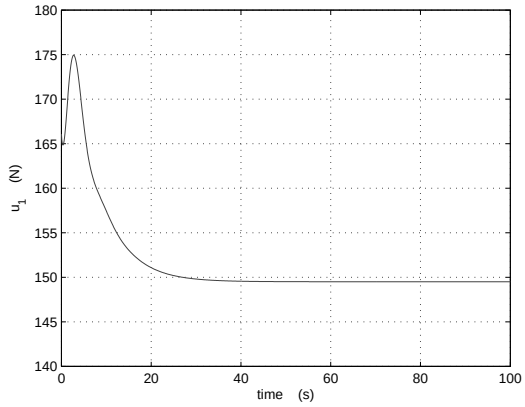

Figure 4.34: The behavior of input u in the second case.

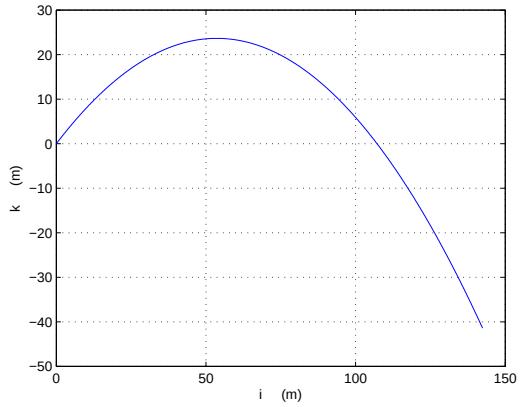

Figure 4.35: Ballistic motion of CG.

4.5.4 The airship with liberated center and added masses

The model in Section 4.5.3 is completed now by including the inertial forces. Assumption $\mathbf{A_2}$ is dropped and aerodynamic forces are still ignored.

Assumption:

A_1: No aerodynamic force.

In this case, the angular momentum will be affected by the inertial forces. The results from previous sections are extended and adapted to this more complete case.

Model of airship with liberated center and added masses

In this situation, $\boldsymbol{F_I}$ and $\boldsymbol{M_I}$ are included in $\boldsymbol{F_s}$ and $\boldsymbol{M_s}$, which means that equations (3.25) and (3.26) are modified as follows,

$$\boldsymbol{F_s} = \boldsymbol{F_I} + \boldsymbol{F_{GBt}} \tag{4.49}$$

$$\boldsymbol{M_s} = \boldsymbol{M_I} + \boldsymbol{M_{GBt}}. \tag{4.50}$$

Combining (3.19), (3.23), (3.24), (4.49), and (4.50), the model of the airship subject to the inertial forces is as follows,

$$\begin{cases} \ddot{\theta} & = \varrho_2 \\ \ddot{r}_{p1} & = \sigma_2 \\ \dot{v}_1 & = \varkappa_1 \\ \dot{v}_3 & = \varkappa_3 \end{cases} \tag{4.51}$$

where

$$\begin{aligned}
\varrho_2 =& -\frac{1}{J_2 + \bar{m} r_{p1}^2}\Big(\bar{m} r_{p3} r_{p1}\dot{\theta}^2 + 2\bar{m} r_{p1}\dot{r}_{p1}\dot{\theta} + \bar{m} g r_{p1}\cos\theta + r_{p3}u \\
& -(\dot{v}_3 - \dot{\theta} v_1)\bar{m} r_{p1}\Big) \\
\sigma_2 =& \frac{1}{J_2 + \bar{m} r_{p1}^2}\Big((J_2 r_{p1} + \bar{m} r_{p1}^3 + \bar{m} r_{p3}^2 r_{p1})\dot{\theta}^2 + 2\bar{m} r_{p3} r_{p1}\dot{r}_{p1}\dot{\theta} \\
& - (J_2 + \bar{m} r_{p1}^2) g\sin\theta + \bar{m} g r_{p3} r_{p1}\cos\theta + (\frac{J_2}{\bar{m}} + r_{p1}^2 + r_{p3}^2)u \\
& + \bar{m} r_{p1} r_{p3}(\dot{\theta} v_1 - \dot{v}_3) - (J_2 + \bar{m} r_{p1}^2)(\dot{\theta} v_3 + \dot{v}_1)\Big) \\
\varkappa_1 =& \frac{1}{m_1}\Big(-m_3 \dot{\theta} v_3 + (\bar{m} - m_0) g\sin\theta - u\Big) \\
\varkappa_3 =& \frac{1}{m_3 + \bar{m}}\Big((m_1 + \bar{m})\dot{\theta} v_1 + m_0 g\cos\theta + \bar{m} r_{p3}\dot{\theta}^2 + 2\bar{m}\dot{\theta}\dot{r}_{p1} + \bar{m} r_{p1}\ddot{\theta}\Big).
\end{aligned}$$

Note that (4.48) and (4.51) have the same form, with only J and m_s in (4.48) are modified to J_2, m_1 and m_3 in (4.51), and the other items remain the same. Therefore, model (4.51) reduces to the model (4.48) if $m_{11} = m_{33} = J_{22} = 0$ (no added mass).

Maximal linearization of a minimum phase model

The model (4.51) is decomposed into a non-controllable system and a controllable one as it was done for model (4.48). The dynamics of the center of gravity CG is not affected by the control input which means that CG has a similar ballistic motion as in Fig. 4.35. These non-controllable variables span the autonomous subspace $\mathcal{H}_\infty$ which reads as:

$$\mathcal{H}_\infty = span\{d\psi_1', \quad d\psi_2'\}$$

where

$$\begin{aligned}
\psi'_1 &= (r_{p1}\dot{\theta} - \frac{m_3+\bar{m}}{\bar{m}}v_3)^2 + (\dot{r}_{p1} + r_{p3}\dot{\theta} + \frac{m_1+\bar{m}}{\bar{m}}v_1)^2 \\
\psi'_2 &= (r_{p1}\dot{\theta} - \frac{m_3+\bar{m}}{\bar{m}}v_3)\cos\theta + (\dot{r}_{p1} + r_{p3}\dot{\theta} + \frac{m_1+\bar{m}}{\bar{m}}v_1)\sin\theta.
\end{aligned}$$

There is now only one single independent function $\tilde{\phi}_2'$ which has relative degree 3 for the model (4.51). More precisely, compute $\mathcal{H}_3$:

$$\mathcal{H}_3 = span\{d\tilde{\phi}_2', \quad \omega\} \oplus \mathcal{H}_\infty$$

where $\tilde{\phi}_2' = \theta + \frac{r_{p3}}{\sqrt{\frac{m_3(m_1+\bar{m})}{m_1(m_3+\bar{m})}}\sqrt{\frac{\bar{m}+m_1}{\bar{m}m_1}J+r_{p3}^2}} \arctan \frac{\sqrt{\frac{m_3(m_1+\bar{m})}{m_1(m_3+\bar{m})}}r_{p1}}{\sqrt{\frac{\bar{m}+m_1}{\bar{m}m_1}J+r_{p3}^2}}$ and $\mathcal{H}_3$ is no more fully integrable. ω denotes a suitable non integrable differential one-form.

Compute $\mathcal{H}_2$ as:

$$\mathcal{H}_2 = span\{dy_1', \quad dy_2', \quad d\tilde{\phi}_1'\} \oplus \mathcal{H}_\infty$$

where

$$\begin{aligned}
y_1' &= \frac{\bar{m}}{m_3+\bar{m}}r_{p1}\dot{\theta} - v_3 \\
y_2' &= \frac{\bar{m}}{m_1+\bar{m}}(\dot{r}_{p1} + r_{p3}\dot{\theta}) + v_1 \\
\tilde{\phi}_1' &= J_2\dot{\theta} + \frac{\bar{m}m_1}{\bar{m}+m_1}\left(\frac{m_3(m_1+\bar{m})}{m_1(m_3+\bar{m})}r_{p1}^2\dot{\theta} + r_{p3}^2\dot{\theta} + r_{p3}\dot{r}_{p1}\right).
\end{aligned}$$

As in the previous sections, $\tilde{\phi}_1'$ is an angular momentum, related to $\tilde{\phi}_2'$ by,

$$\dot{\tilde{\phi}}_2' = \frac{\frac{\bar{m}+m_1}{\bar{m}m_1}}{\frac{\bar{m}+m_1}{\bar{m}m_1}J_2 + \frac{m_3(m_1+\bar{m})}{m_1(m_3+\bar{m})}r_{p1}^2 + r_{p3}^2}\tilde{\phi}_1'.$$

Despite these dramatic changes in comparison to section 4.5.3, it is now argued that the control scheme which has been computed for the fundamental special case in the section 4.5.2 is still valid, up to some approximation. This is done next.

Control design and simulation

Since $\tilde{\phi}_1'$ does not have relative degree 3 as $\tilde{\phi}_2'$, the results in ***Theorem* 1 & 2** are not available anymore. However, the second-time derivative of $\tilde{\phi}_1'$ is argued to depend weakly on the control input u, so the coefficient of u is neglected.

More precisely, define again the output $y = \tilde{\phi}_1' + k\tilde{\phi}_2'$, for some $k > 0$.

Instead of the coordinate (4.39)-(4.42), define a new coordinate as:

$$\xi_1 = \tilde{\phi}_1' + k\tilde{\phi}_2' \tag{4.52}$$

$$\xi_2 = \dot{\tilde{\phi}}_1' + k\dot{\tilde{\phi}}_2' \tag{4.53}$$

$$\xi_3 = \ddot{\tilde{\phi}}_1' + k\ddot{\tilde{\phi}}_2' - \Delta u \tag{4.54}$$

$$\zeta = \tilde{\phi}_1' \tag{4.55}$$

where $\dddot{\tilde{\phi}}_1' = \Pi + \Delta u$ for some functions of the state variables Π and Δ.

Instead of solving equation (4.44), consider the following equation:

$$\dot{\xi}_3 + \lambda_2\xi_3 + \lambda_1 y^{(1)} + \lambda_0(y - y_e) = 0. \tag{4.56}$$

Note that equation (4.56) corresponds strictly to the equation (4.44) only if $\Delta = 0$. In the following when Δ is small, then (4.56) is an approximation of (4.44).

In (4.56), one has $\dot{\xi}_3 = \alpha'(\boldsymbol{\xi},\ \zeta) + \beta'(\boldsymbol{\xi},\ \zeta)u$. Solving (4.56) in u, yield

$$u = -\frac{1}{\beta'(\boldsymbol{\xi},\ \zeta)}\left(\lambda_2\xi_3 + \lambda_1\xi_2^{(1)} + \lambda_0(\xi_1 - y_e) + \alpha'(\boldsymbol{\xi},\ \zeta)\right)$$

and apply to the model (4.51). For the same reason, the explicit expression of u is not displayed here. $m_1 = 400\ kg$, $m_3 = 500\ kg$ and the other parameters have the same values as previously. Good control performances are obtained. The simulation results of the dynamics of θ, r_{p1} and the motion of CG are similar to the previous cases. The behavior of input u is displayed in Fig. 4.37.

4.5.5 The complete airship model in the longitudinal plane

In the last step, the aerodynamic forces are added to the system, which means that $\mathbf{A_1}$ is dropped. The addition of the aerodynamic forces causes a huge impact on the angular momentum, since a pitch moment is included by the aerodynamic forces.

Combining (3.19), (3.25), (3.26), (3.27), and (3.28) the complete model in the longitudinal plane is derived, which also can be obtained from the full model (3.30), as follows

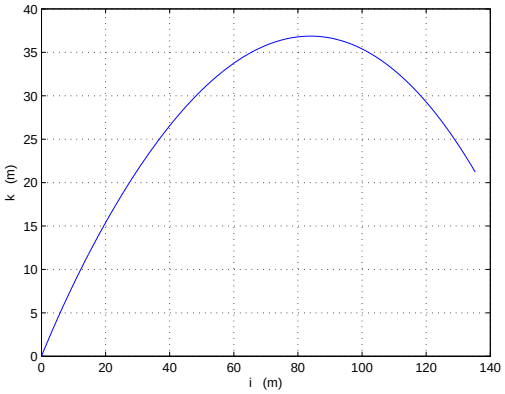

Figure 4.36: Ballistic motion of *CG* in the third case.

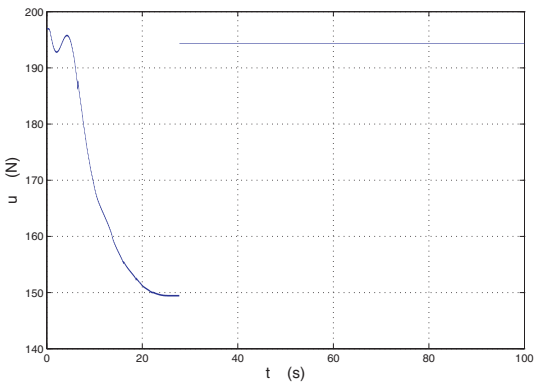

Figure 4.37: The behavior of input *u*.

$$\begin{cases} \ddot{\theta} & = \varrho_2 + \frac{M_a}{J+\bar{m}r_{p1}^2} \\ \ddot{r}_{p1} & = \sigma_2 + \frac{M_a r_{p3}}{J+\bar{m}r_{p1}^2} \\ \dot{\nu}_1 & = \varkappa_1 + \frac{F_{a1}}{m_1} \\ \dot{\nu}_3 & = \varkappa_3 + \frac{F_{a3}}{m_3+\bar{m}} \end{cases}$$

where

$$F_{a1} = -X_a \cos\alpha + Z_a \sin\alpha$$
$$F_{a3} = -X_a \sin\alpha - Z_a \cos\alpha$$

There is no ballistic motion anymore, and the system becomes fully accessible:

$$\mathcal{H}_\infty = 0.$$

The aerodynamic forces render all DOF controllable. For instance, the special cases in Section 4.5.3 and 4.5.4 are not fully controllable as no aerodynamic forces are considered, but the system in this section is fully accessible as all forces are considered. The airship's full model can be represented in Fig. 4.38.

The attitude of the airship is controlled by the position of the moveable mass ($\boldsymbol{r_p}$). Meanwhile, its position $\boldsymbol{r_p}$ is controlled by the internal forces $\boldsymbol{u}$. The guidance of the airship is impacted by the net lift (controlled by u_4), aerodynamic forces and torques, etc. The aerodynamic forces and torques introduce a new coupling which yields full accessibility, but they do not yield any new DOF. For the cases in Section 4.5.3 and 4.5.4, due to the absence of the aerodynamic force, the center of gravity *CG*

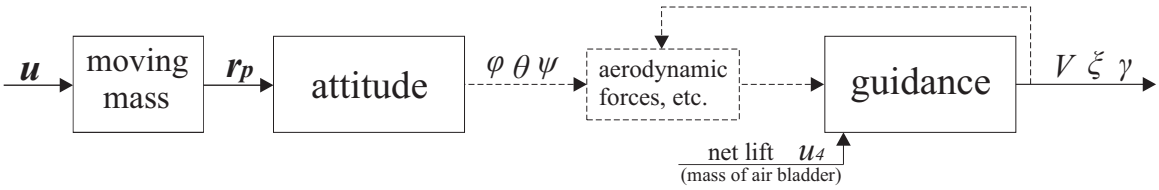

Figure 4.38: The aerodynamic forces render all DOF controllable.

of the airship is subject to an uncontrollable ballistic motion, but in this section where the aerodynamic force is considered, the motion of CG is controllable, shown in the next simulations.

Compute $\mathcal{H}_2$ and $\mathcal{H}_3$ as:

$$\mathcal{H}_2 = span\{dy_1', \ dy_2', \ d\tilde{\phi}_1', \ d\theta, \ dr_{p1}\}$$
$$\mathcal{H}_3 = span\{d\tilde{\phi}_2', \ \omega_1, \ \omega_2, \ \omega_3\}.$$

Here, $d\tilde{\phi}_1'$ and $d\tilde{\phi}_2'$ are the same as those in the section 4.5.4. ω_1, ω_2, and ω_3 are suitable possibly non integrable differential one-forms.

As in subsection 4.5.4, an advanced nonlinear control u is derived which achieves internal stabilization. But due to its long expression and useless for practitioners, the explicit expression of u is not displayed here.

The simulation results of this nonlinear control for the complete system are displayed in Fig. 4.39-4.40. The initial values for θ, $\dot{\theta}$, r_{p1}, $\dot{r}_{p1}$, v_1, and v_3 are 41.5°, 0, -2.5 m, 0, 10 m/s, and -0.69 m/s, respectively. The equilibrium values for these states are 30°, 0, -2.7 m, 0, 10.4 m/s, and -0.73 m/s, respectively. The angle of attack $\alpha = \theta - \xi = \arctan\frac{v_3}{v_1} = -4°$. In this situation, the airship no more displays any ballistic motion, but flies along the desired angle which is denoted by ξ, here, $\xi = 34°$ (see Fig. 4.42). Fig. 4.41 reflects the value of the control input u, which keeps in a reasonable domain.

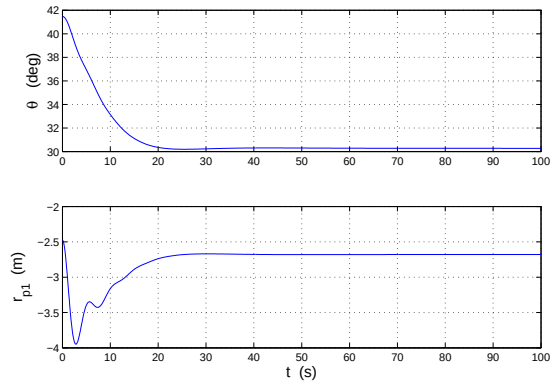

Figure 4.39: Dynamics of θ and r_{p1} with initial error of the complete model.

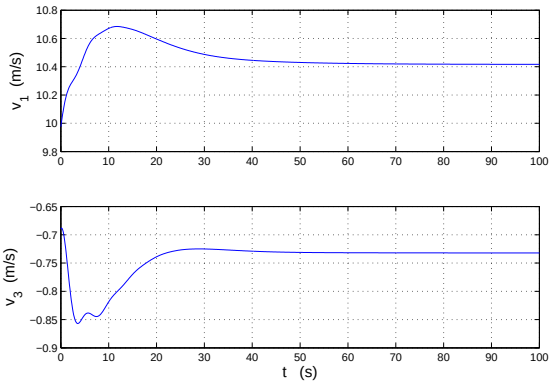

Figure 4.40: Dynamics of v_1 and v_3 with initial error of the complete model.

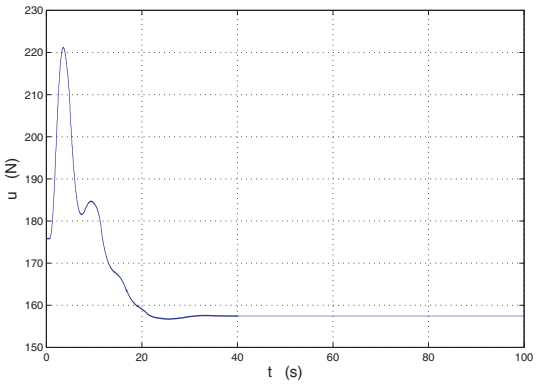

Figure 4.41: The behavior of input u.

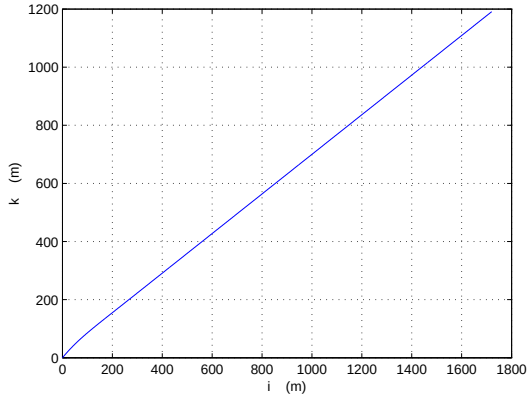

Figure 4.42: The movement of O.

4.5.6 Simulation of a typical trajectory tracking flight

In this section, a typical trajectory is considered, as depicted in Fig 2.9. It includes two cycles of ascending and descending segments. The goal is to show that the control laws developed in Section 4.5.5 are able to cope with a switching structure of the system. To implement a sawtooth flight as Fig 2.9, besides the input in Section 4.5.5 to control the movement of the moveable mass, the input u_4 is involved to control the ascent and the descent.

The flight path is shown in Fig 4.46, the variations of θ, r_{p1}, v_1, v_3 are shown in Fig 4.43 and 4.44. The input force is shown in Fig 4.45.

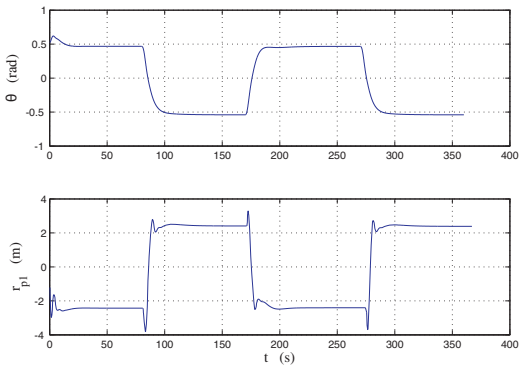

Figure 4.43: Dynamics of θ and r_{p1} of a continuing flight.

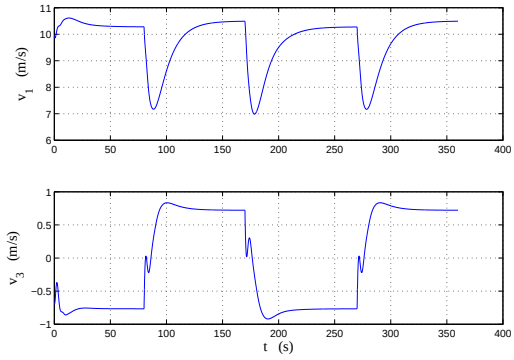

Figure 4.44: Dynamics of v_1 and v_3 of a continuing flight.

The control laws for ascending and descending segments are similar, up to the desired command y_e. On the transition points, besides the switches of the commands of the states, the net buoyancy of the airship is switching from 340 N to -340 N, which represent a bang-bang control for u_4. In this simulation, it is assumed that the release and the inflation of the air bladder are much faster than the motion of the airship, and this switch is considered to be instantaneous. It is shown by the simulation

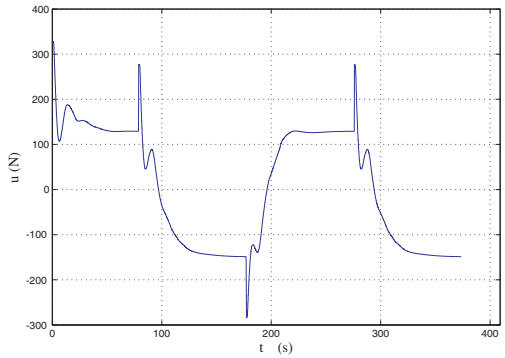

Figure 4.45: The behavior of input u.

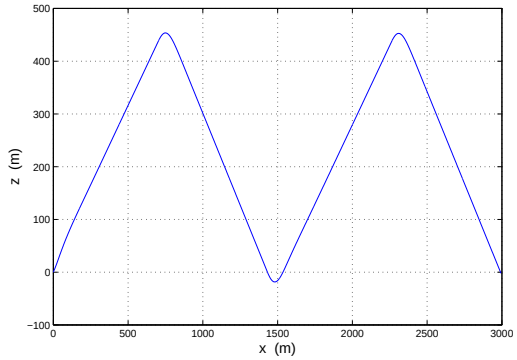

Figure 4.46: Flight path of two cycles.

that the behavior of the states and the control input is approximately symmetric. On the transition point, the variation of the input is acceptable as well.

4.6 Conclusion

As how to control the longitudinal dynamics of the airship, that is a challenge, due to the complex nonlinearity of the model. Two simple controls are derived firstly to verify the control performances. Due to the drawback of these two control, it is necessary to seek an advance nonlinear control. For certain mechanical systems with internal dynamics, references (Bloch et al., 1992; Woolsey and Leonard, 2002) investigated the use of the internal torques to stabilizer the system. To deal with this complex nonlinear mechanical system, this chapter offers a new approach which is to analyze the system with a maximal number of constraints, which are gradually relaxed. The maximally constrained model is assimilated to be the prismatic-joint pendulum shown in Section 4.5.2. Thanks to the angular momentum of the whole airship computed at the point O or CG which is denoted by ϕ_1, $\tilde{\phi}_1$ and $\tilde{\phi}'_1$ in this chapter, an explicit dummy output function is derived which defines a minimum phase system. Maximal feedback linearization with internal stability is performed, and good control performance is shown.

The dynamic analysis and control method displayed in this chapter makes sense for similar complex systems, and is also instrumental in dealing with other motions of this airship, for instance, the dynamics in the horizontal plane.

Chapter 5

Control Scheme for the Three Dimensional Case

Contents

The longitudinal dynamics of the vehicle has been analyzed in the chapter 4. Based on some special cases and the maximal feedback linearization with internal stability, an advanced nonlinear control has been derived for the attitude control and the guidance in longitudinal plane. For autonomous gliding vehicles, such as buoyancy-driven airships and underwater gliders, the lateral dynamics is similar to that of the longitudinal plane, only the parameters differ. By a similar approach as the one used in the longitudinal plane in the chapter 4, a nonlinear control has been derived for the attitude control and the guidance in the lateral plane in this chapter. Thus, for both longitudinal and lateral dynamics, nonlinear controllers are derived which solve the maximal linearization problem with internal stability.

To be able to superpose the longitudinal control and the lateral control, a singular perturbation approach is adopted as a tool to combine the two controllers designed for the longitudinal and lateral plane. In this case, the longitudinal dynamics is assumed to be slow and the lateral dynamics is assumed to be fast. The simulations show that this control scheme is acceptable for the control problem in three dimension. To the best of our knowledge, this is the first control solution for the 3D motion of the autonomous gliding vehicles, both aerial and underwater.

The singular perturbation approach developed here is different from the standard singular perturbation approach for the underwater or aerial vehicles, as depicted in (Naidu and Calise, 2001; Subudhi and Morris, 2003). Usually the problem is split into the attitude control problem and the guidance problem. Here, the singular perturbation method is used to superpose both control loops for

the longitudinal and lateral motions.

The contributions of the chapter consist of a derivation of the analytical solution of the equilibrium for three dimensional motion, and a control scheme for it based on the singular perturbation theory. The content of this chapter has been published in (Wu et al., 2011b).

The chapter is organized as follows: for the dynamics in 3D, due to the complexity of the model, the regular perturbation theory is involved to derived an approximate analytical solution of the equilibrium in section 5.1. The equilibrium is also derived in this section if the simplified aerodynamic model is adopted.

5.1 Open-loop Simulations and Equilibrium of the Dynamics in 3D

From 8-DOF model (3.30), the full model for the moveable mass controlled airship is as follows:

$$
\begin{cases}
\dot{\phi} &= \Omega_1 + \sin\phi\tan\theta\Omega_2 + \cos\phi\tan\theta\Omega_3 \\
\dot{\theta} &= \cos\phi\Omega_2 - \sin\phi\Omega_3 \\
\dot{\psi} &= \frac{\sin\phi}{\cos\theta}\Omega_2 + \frac{\cos\phi}{\cos\theta}\Omega_3 \\
\dot{\Omega}_1 &= \frac{1}{J_1}\left(L_a + (J_2 - J_3)\Omega_2\Omega_3 + r_{p3}u_2 - r_{p2}u_3\right) \\
\dot{\Omega}_2 &= \frac{1}{J_2}\left(M_a + (J_3 - J_1)\Omega_1\Omega_3 - r_{p3}u_1 + r_{p1}u_3\right) \\
\dot{\Omega}_3 &= \frac{1}{J_3}\left(N_a + (J_1 - J_2)\Omega_1\Omega_2\right) \\
\dot{v}_1 &= \frac{1}{m_1}\left(F_{at1} + (\bar{m} - m_0)g\sin\theta - m_3v_3\Omega_2 + m_2v_2\Omega_3 - u_1\right) \\
\dot{v}_2 &= \frac{1}{m_2}\left(F_{at2} + (m_0 - \bar{m})g\cos\theta\sin\phi + m_3v_3\Omega_1 - m_1v_1\Omega_3 - u_2\right) \\
\dot{v}_3 &= \frac{1}{m_3}\left(F_{at3} + (m_0 - \bar{m})g\cos\theta\cos\phi + m_1v_1\Omega_2 - m_2v_2\Omega_1 - u_3\right) \\
\ddot{r}_{p1} &= -\dot{v}_1 + \dot{\Omega}_3r_{p2} - \dot{\Omega}_2r_{p3} + \Omega_3\dot{r}_{p2} - g\sin\theta + (v_2 + \dot{r}_{p2} + \Omega_3r_{p1} - \Omega_1r_{p3})\Omega_3 \\
&\quad -(v_3 + \Omega_1r_{p2} - \Omega_2r_{p1})\Omega_2 + u_1/\bar{m} \\
\ddot{r}_{p2} &= -\dot{v}_2 - \dot{\Omega}_3r_{p1} - \Omega_3\dot{r}_{p1} + \dot{\Omega}_1r_{p3} + g\cos\theta\sin\phi + (v_3 + \Omega_1r_{p2} - \Omega_2r_{p1})\Omega_1 \\
&\quad -(v_1 + \dot{r}_{p1} + \Omega_2r_{p3} - \Omega_3r_{p2})\Omega_3 + u_2/\bar{m}
\end{cases}
\tag{5.1}
$$

where u_3 is deduced from (3.20) and $(\boldsymbol{mv}) \times \boldsymbol{v}$ in equation $\dot{\boldsymbol{\Omega}}$ of the model (3.30) is neglected since it is included in the aerodynamics (Ouyang, 2003).

5.1.1 Open-loop simulations

For the motion in 3D, there exists turning flights, more precisely, spiral motions as shown in 5.1. The spiral motion of a buoyancy-driven airship is considerably different from that of an aircraft. For an aircraft, this motion is commanded by the deflections of the rudder and the elevator. A spiral

motion for an buoyancy-driven airship is caused by the lateral translation of the moveable mass, namely the translation of the moveable mass along the e_2 direction, which is denoted by r_{p2}. The lateral translation of the moveable mass yields a roll of the airship, which generates a component of aerodynamic forces on the lateral plane. Thus, a spiral motion is produced.

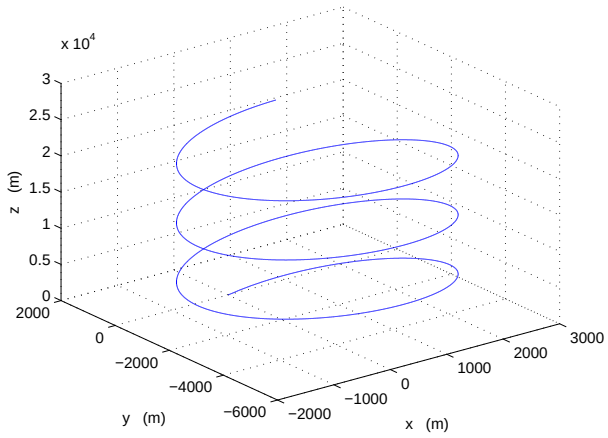

Figure 5.1: A spiral motion of the buoyancy-driven airship

With this spiral motion, the airship can enjoy a certain degree of freedom to turn the heading in space, which is demonstrated by an open-loop simulation as shown in Fig. 5.2, 5.3 and 5.4. From this simulation, it finds that the airship turns the direction in the horizontal plane while the motion in the longitudinal plane is only slightly impacted.

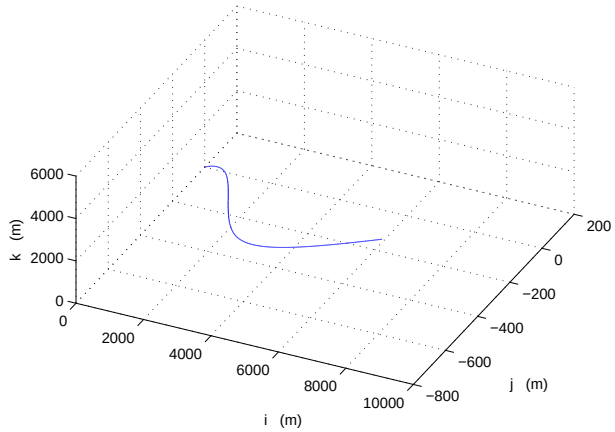

Figure 5.2: The airship change the heading in space

5.1.2 Equilibrium of the dynamics in 3D

For the analytical conditions of a stable spiral motion in 3D, two approximate computations are presented according to two different aerodynamic expressions.

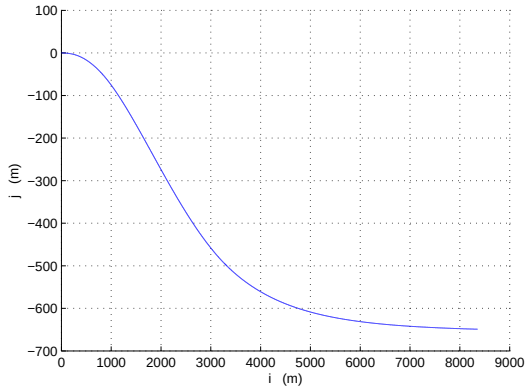

Figure 5.3: The motion of the airship in space maps in a horizontal plane

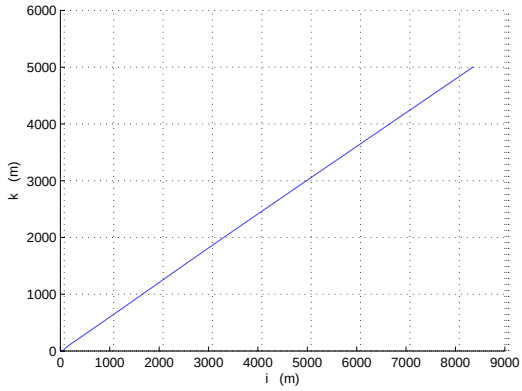

Figure 5.4: The motion of the airship in space maps in a longitudinal plane

For full aerodynamic model case

To derive the analytical condition of this spiral motion, the right-hand side of the 3D full model (5.1)are equal to zero and are solved in all variables. The challenge is that the 3D full model (5.1) is very difficult to solve directly due to its complexity. Thus, the regular perturbation is involved as a tool to find an approximate analytical solution for this spiral motion.

To apply the regular perturbation method, the turn rate of the spiral motion ω is arranged to be very small and let:

$$\omega = \epsilon \sqrt{\frac{g}{r_{p3}}} \tag{5.2}$$

Thus, the angular velocities with respect to the body frame are equal to:

$$\boldsymbol{\Omega} = \begin{pmatrix} \Omega_1 \\ \Omega_2 \\ \Omega_3 \end{pmatrix} = \begin{pmatrix} -\sin\theta \\ \cos\theta\sin\phi \\ \cos\theta\cos\phi \end{pmatrix} \omega \tag{5.3}$$

Let the translational velocity of the airship be V, then the translational velocities with respect to the body frame are written as:

$$\boldsymbol{v} = \begin{pmatrix} v_1 \\ v_2 \\ v_3 \end{pmatrix} = \begin{pmatrix} \cos\alpha\cos\beta \\ \sin\beta \\ \sin\alpha\cos\beta \end{pmatrix} V \tag{5.4}$$

To get the regular perturbation solution in ϵ, the steady longitudinal motion is viewed as a basic motion of the spiral motion in 3D. (5.2), (5.3), (5.4), and the following polynomial expansions are substituted to the $\dot{\Omega}_i$ and $\dot{v}_i$ equations of (5.1):

$$\begin{cases} V &= V_e + \epsilon V_1 \\ m_0 &= m_{0e} + \epsilon m_{01} \\ \alpha &= \alpha_e + \epsilon \alpha_1 \\ \phi &= 0 + \epsilon \phi_1 \\ \beta &= 0 + \epsilon \beta_1 \\ r_{p2} &= 0 + \epsilon r_{p21} \end{cases}$$

The coefficient equations of ϵ^0 are identical to the situation of the derivation of the equilibrium of the longitudinal motion in section 4.2.2. Solving the coefficient equations of ϵ^1 and ϵ^2 gives approximate solutions of the equilibrium of the spiral motion and which are presented in the following:

$$V_1 = 0 \tag{5.5}$$

$$\alpha_1 = 0 \tag{5.6}$$

$$m_{01} = 0 \tag{5.7}$$

$$\beta_1 = \pm\left(\frac{\sqrt{g/r_{p3}}\cos\theta\cos\alpha_e r_{p3}\bar{m}}{V_e\cos\alpha_e(m_3 - m_2)}\right)^{\frac{1}{2}} \tag{5.8}$$

$$\phi_1 = -\frac{V_e^2(K_{sf} + K_{d0} + K_d\alpha_e^2)}{\cos\theta m_{0e} g} \tag{5.9}$$

$$r_{p21} = -\frac{V_e^2 K_n\beta_1 - \cos\theta\tan\phi_1 r_{p3}\bar{m}g}{\bar{m}g\cos\theta} \tag{5.10}$$

where $K_n = \frac{1}{2}\rho_a \nabla V^2 C_l^\beta$, and $K_{sf} = \frac{1}{2}\rho_a \nabla^{2/3} V^2 C_y^\beta$.

From this approximate analytical solution of the equilibrium in 3D, it is implied that the longitudinal motion is decoupled from the lateral motion when the turn rate is small since V, α and m_0 remain constant to the small turn rate and are identical to the equilibrium of the longitudinal motion. Thus, a remark can be concluded as follows:

Remark: The longitudinal motion is decoupled from the lateral motion when the turn rate is small.

For simplified aerodynamic model case

If the aerodynamic force is given by a simple form as (3.8), the equilibrium of the state is derived as follows.

To compute the equilibrium for a specified flight path, the right hand side of (5.1) is set to zero.

From (3.1) and Fig. 4.1, the following equations are derived:

$$\tan\xi_e = \frac{-\sin\theta_e + \frac{-K_d\sin\phi_e}{K_{sf}\tan\theta_e}\cos\theta_e\sin\phi_e + \frac{-K_d\cos\phi_e}{K_l\tan\theta_e}\cos\theta_e\cos\phi_e}{\cos\psi_e\cos\theta_e+\frac{-K_d\sin\phi_e}{K_{sf}\tan\theta_e}(\cos\psi_e\sin\theta_e\sin\phi_e-\sin\psi_e\cos\phi_e)+\frac{-K_d\cos\phi_e}{K_l\tan\theta_e}(\cos\psi_e\sin\theta_e\cos\phi_e+\sin\psi_e\sin\phi_e)}$$

$$\tan\gamma_e = \frac{\sin\psi_e\cos\theta_e+\frac{-K_d\sin\phi_e}{K_{sf}\tan\theta_e}(\sin\psi_e\sin\theta_e\sin\phi_e+\cos\psi_e\cos\phi_e)+\frac{-K_d\cos\phi_e}{K_l\tan\theta_e}(\sin\psi_e\sin\theta_e\cos\phi_e-\cos\psi_e\sin\phi_e)}{\cos\psi_e\cos\theta_e+\frac{-K_d\sin\phi_e}{K_{sf}\tan\theta_e}(\cos\psi_e\sin\theta_e\sin\phi_e-\sin\psi_e\cos\phi_e)+\frac{-K_d\cos\phi_e}{K_l\tan\theta_e}(\cos\psi_e\sin\theta_e\cos\phi_e+\sin\psi_e\sin\phi_e)}$$

$$\tan\theta_e = \frac{-\sin\theta_e+\frac{-K_d\sin\phi_e}{K_{sf}\tan\theta_e}\cos\theta_e\sin\phi_e+\frac{-K_d\cos\phi_e}{K_l\tan\theta_e}\cos\theta_e\cos\phi_e}{\sqrt{\left(\cos\psi_e\cos\theta_e+\frac{-K_d\sin\phi_e}{K_{sf}\tan\theta_e}(\cos\psi_e\sin\theta_e\sin\phi_e-\sin\psi_e\cos\phi_e)+\frac{-K_d\cos\phi_e}{K_l\tan\theta_e}(\cos\psi_e\sin\theta_e\cos\phi_e+\sin\psi_e\sin\phi_e)\right)^2}}$$

$$+\left(\sin\psi_e\cos\theta_e+\frac{-K_d\sin\phi_e}{K_{sf}\tan\theta_e}(\sin\psi_e\sin\theta_e\sin\phi_e+\cos\psi_e\cos\phi_e)+\frac{-K_d\cos\phi_e}{K_l\tan\theta_e}(\sin\psi_e\sin\theta_e\cos\phi_e-\cos\psi_e\sin\phi_e)\right)^2$$

From those three equations, for given ξ_e and γ_e, the equilibria of ϕ_e, θ_e, and ψ_e can be computed.

From $\ddot{r}_{p1}$ and $\ddot{r}_{p2}$ equations in (5.1), the following u_1 and u_2 are computed as:

$$u_{1e} = \bar{m}g\sin\theta_e \tag{5.11}$$

$$u_{2e} = -\bar{m}g\cos\theta_e\sin\phi_e \tag{5.12}$$

and from (3.20), the equilibrium of u_3 is computed as:

$$u_{3e} = -\bar{m}g\cos\theta_e\cos\phi_e \tag{5.13}$$

Substituting (5.11)-(5.13) into equations $\dot{v}_1$, $\dot{v}_2$, and $\dot{v}_3$ of (5.1), and combining with the relation $v_{1e}^2+v_{2e}^2+v_{3e}^2 = V_e^2$, the equilibria of the speed and m_0 are computed as:

$$v_{1e} = \frac{K_lK_{sf}\tan\theta_e}{\sqrt{\tan^2\theta_eK_{sf}^2K_l^2+\sin^2\phi_eK_d^2K_l^2+K_d^2K_{sf}^2-K_d^2K_{sf}^2\sin^2\phi_e}}V_e$$

$$v_{2e} = \frac{\cos\theta_e\sin\theta_eK_dK_l}{\sqrt{K_{sf}^2K_l^2-K_{sf}^2K_l^2\cos^2\theta_e+K_d^2K_l^2\cos^2\theta_e-K_d^2K_l^2\cos^2\theta_e\cos^2\phi_e+K_d^2K_{sf}^2\cos^2\theta_e\cos^2\phi_e}}V_e$$

$$v_{3e} = \frac{\cos\theta_e\sin\theta_eK_dK_{sf}}{\sqrt{K_{sf}^2K_l^2-K_{sf}^2K_l^2\cos^2\theta_e+K_d^2K_l^2\cos^2\theta_e-K_d^2K_l^2\cos^2\theta_e\cos^2\phi_e+K_d^2K_{sf}^2\cos^2\theta_e\cos^2\phi_e}}V_e$$

$$\Omega_{1e} = \Omega_{2e} = 0$$

$$m_{0e} = \frac{K_d}{g\sin\theta_e}v_{1e}$$

where v_{1e}, v_{2e} and v_{3e} have the relations $v_{2e} = \frac{-K_d\sin\phi_e}{K_{sf}\tan\theta_e}v_{1e}$; $v_{3e} = \frac{-K_d\cos\phi_e}{K_l\tan\theta_e}v_{1e}$.

From the equations $\dot{\Omega}_1$, $\dot{\Omega}_2$, and $\dot{\Omega}_3$, the equilibriums of r_{p1} and r_{p2} are computed as:

$$
\begin{aligned}
r_{p1e} &= \frac{-r_{p3}\bar{m}g\sin\theta_e}{\bar{m}g\cos\theta_e\cos\phi_e} \\
r_{p2e} &= \frac{r_{p3}\bar{m}g\cos\theta_e\sin\phi_e}{\bar{m}g\cos\theta_e\cos\phi_e}
\end{aligned}
$$

5.2 Lateral Dynamics and Control

The lateral structure of the airship has been shown in Fig. 5.5. The lateral dynamics in the full model involve the roll DOF ϕ and Ω_1; velocities v_2 and v_3; and the moving mass dynamics r_{p2}. The lateral dynamic model is as follows:

$$
\begin{cases}
\dot{\phi} &= \Omega_1 \\
\dot{\Omega}_1 &= \frac{1}{J_1}\left(L_a - r_{p2}u_3 + r_{p3}u_2\right) \\
\dot{v}_2 &= \frac{1}{m_2}\left((m_0-\bar{m})\,g\sin\phi + m_3v_3\Omega_1 + F_{a2} - u_2\right) \\
\dot{v}_3 &= \frac{1}{m_3}\left((m_0-\bar{m})g\cos\phi - m_2v_2\Omega_1 + F_{a3} - u_3\right) \\
\ddot{r}_{p2} &= -\dot{v}_2 + \dot{\Omega}_1 r_{p3} + (v_3 + \Omega_1 r_{p2})\Omega_2 + g\sin\phi + u_2/\bar{m}
\end{cases}
\tag{5.14}
$$

where $F_{a2} = -\sin\beta X_a + \cos\beta Y_a$, $F_{a3} = Z_a$, and u_3 is also decided by (3.20).

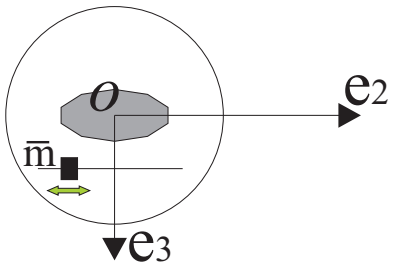

Figure 5.5: The lateral structure of the airship.

Note that the analysis of the longitudinal subsystem remains instrumental although parameters are different. Actually, the lateral control design has the same structure as that of the longitudinal dynamics. This remark is easy to understand when taking into account of the real physical system, see Fig. 4.28 and 5.5. The dynamics in the lateral plane has the same structure as the dynamics in the longitudinal plane; however the parameters are different.

As the result of the previous chapter, The angular momentum plays an important role in control. For the lateral dynamics, the angular momentum is:

$$
\Xi_1 = J_1\dot{\phi} + \frac{mm_3}{m+m_3}r_{p2}^2\dot{\phi} - \frac{mm_2}{m+m_2}(r_{p3}\dot{r}_{p2} - r_{p3}^2\dot{\phi})
$$

and there exist two functions Ξ_2 and ϱ', such that:

$$\dot{\Xi}_2 = \varrho' \Xi_1, \quad \varrho' > 0$$

$$\Xi_2 = \phi - \frac{r_{p3}}{\sqrt{\frac{J_1(m_2+\bar{m})}{m_2\bar{m}} + r_{p3}^2}\sqrt{\frac{m_3(m_2+\bar{m})}{m_2(m_3+\bar{m})}}} \arctan \frac{r_{p2}\sqrt{\frac{m_3(m_2+\bar{m})}{m_2(\bar{m}+m_3)}}}{\sqrt{\frac{J_1(m2+\bar{m})}{m_2\bar{m}} + r_{p3}^2}}$$

Ξ_1 and Ξ_2 have relative degree 3. Following a similar derivation, it is possible to prove that the lateral system with the output $y' = \Xi_1 + k\Xi_2$ has asymptotically stable zero dynamics for any $k > 0$. An error equation as Equation (4.44):

$$y'^{(3)} + \lambda_2' y'^{(2)} + \lambda_1' y'^{(1)} + \lambda_0'(y' - y_e') = 0 \tag{5.15}$$

is adopted to derive the nonlinear control u_2 to stabilize the flight path angle γ and speeds to commands in the lateral plane. The parameters of the control are represented by λ_2', λ_1', and λ_0'. The exact expression of u_2 is easily computable, although through tedious computations. Similar simulation results as that for the longitudinal dynamics are obtained for the dynamics in the lateral plane.

5.3 Control of the Dynamics in Three Dimension

Even though the dynamics of the airship can be decoupled into the longitudinal dynamics and the lateral dynamics, the direct superposition of the controls for the dynamics on these two planes will does not guarantee the stable of the system. The singular perturbation is needed to solve this problem.

The singular perturbation is used for the flight controls in many references (Wang and Stengel, 2005; Naidu and Calise, 2001; Subudhi and Morris, 2003; Calise, 1976; Bhatta, 2006; Bhatta and Leonard, 2008). A control scheme based on the singular perturbations for the longitudinal and the lateral dynamics in 3D is presented, see Fig. 5.6. Some simulations have been done to show the control performances for the attitude control and the guidance.

Through the simulation in 3D, it is found that if 6 poles of the error equations (4.44) and (5.15) are all arranged at the same places, namely $\lambda_i = \lambda_i'$, then the controls u_1 and u_2 are too large and exceed an acceptable domain. When the longitudinal dynamics is slow and the lateral dynamics is fast, the magnitude of u_1 and u_2 are acceptable. This also shows the necessity of a singular perturbation approach. This will be explicitly explained in the following.

5.3.1 Controller structure

The control u_1 is tuned through parameters λ_2, λ_1, and λ_0; u_2 is tuned through parameters λ_2', λ_1', and λ_0'. So that the dynamics in the longitudinal plane are slower than the dynamics in the lateral

plane by choosing $\lambda_2 = 3$, $\lambda_1 = 3$, $\lambda_0 = 1$, $\lambda_2' = 300$, $\lambda_1' = 300$, and $\lambda_0' = 1000$. The time response of the longitudinal motion in closed loop has been chosen to be 10 times longer than the time response of the lateral motion.

The control structure of the vehicle in 3D is shown in Fig. 5.6. Here, the longitudinal states consist of θ, Ω_2, v_1, v_3, r_{p1}, and $\dot{r}_{p1}$; the lateral states consist of ϕ, Ω_1, v_2, v_3, r_{p2}, and $\dot{r}_{p2}$. where u_1 is

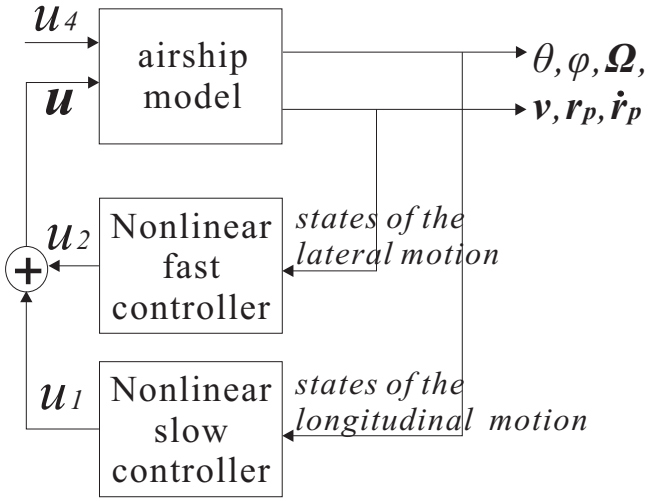

Figure 5.6: Structure of the singular perturbation controller

the control for the longitudinal dynamics (4.1) in Section 4.2.1; and u_2 is the controller for the lateral dynamics (5.14) in Section 5.2. The net lift $m_0 g$, namely u_4, is still subject to a open loop bang-bang control. For the autonomous gliding vehicle, the speed is mainly controlled by the net lift $m_0 g$, and the heading of the motion is controlled by the airship's attitude which is taken into account by u_1 and u_2, as shown in Fig. 4.38.

5.3.2 Simulations of nominal control responses

All mechanical properties used in the simulation are listed in Table 5.1 where the aerodynamic coefficients are borrowed from Ouyang (2003).

Control performances of the singular perturbation controllers are given in Fig 5.7 - 5.11.

Figure 5.7 shows the dynamics of the Euler angles when there exists initial errors. In this simulation, the commanded angle for θ is 26 degree, and the ϕ is expected to be zero. With initial errors, the three Euler angles are asymptotically stable. Fig. 5.8 represents the motion of the moveable masses in this process.

The simulation shown in Fig. 5.9 and 5.10 presents the turning case of the airship. Here, ϕ is stabilized at 10 degrees at first, and then it is commanded to zero. Shown in Fig. 5.10, the trajectory is turned to the $+e_2$ (namely $-y$) direction.

Table 5.1: Physical properties of the airship

Terms	Values	Terms	Values	Terms	Values
$\bar{m}$	30 kg	Volume	296 m^3	K_D	-2.16 Ns/m
m_s	269 kg	m_1	400 kg	K_{SF}	-7.21 Ns/m
m_2	400 kg	m_3	500 kg	K_L	-36.51 Ns/m
J_1	9000 $kg \cdot m^2$	J_2	8000 $kg \cdot m^2$	K_{ML}	-0.44 Ns/m
J_3	8000 $kg \cdot m^2$	r_{p3}	2 m	K_M	-49.97 Ns/m

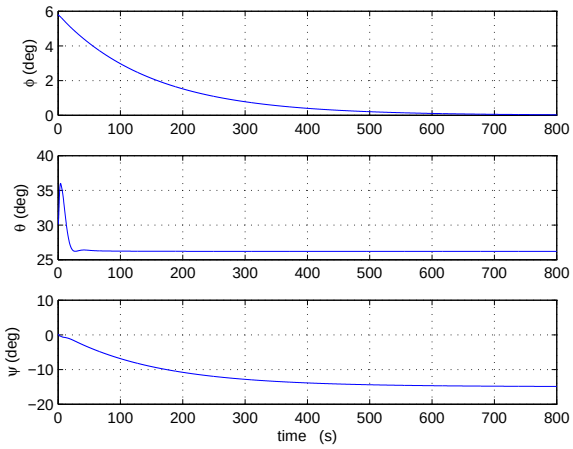

Figure 5.7: The dynamics of the Euler angles with initial errors.

Finally, a simulation on a continuing flight which consists of a rise segment and a fall segment (as shown in Fig 2.9) is presented by Fig 5.11, and this process goes with a the turn to $+e_2$ (namely $-y$) direction.

5.4 Conclusion

To present, the discussion on the control of the airship is mainly limited to one plane (i.e. the longitudinal plane). Through a singular perturbation scheme, a solution for three-dimensional attitude control has been derived for the first time. With the controller proposed here, not only the pitch angle (also the flight angle) can be stabilized, but also steady turning direction can be achieved by the feedback u_2. With this attitude controller scheme, a trajectory tracking controller can be derived based on it. The analysis of this paper offers a control scheme for similar mechanical systems.

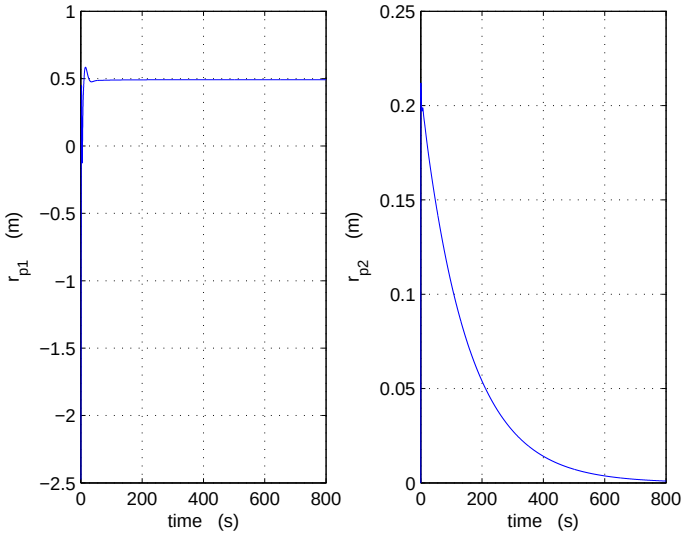

Figure 5.8: The motion of the moveable masses.

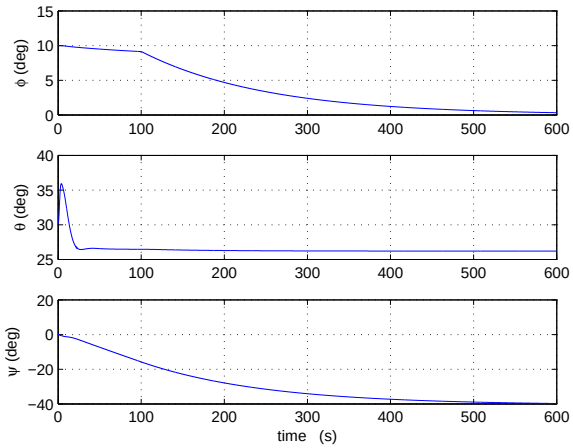

Figure 5.9: The dynamics of the Euler angles in turning case.

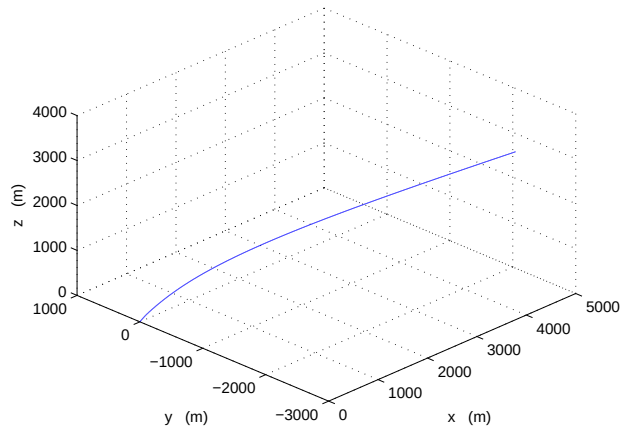

Figure 5.10: The trajectory in turning case.

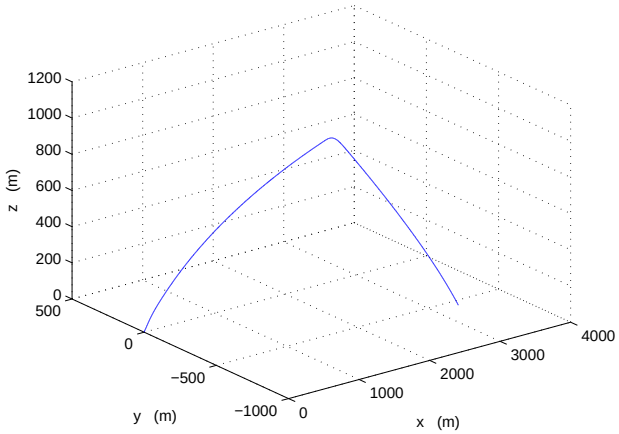

Figure 5.11: The trajectory for a continuing flight with changing direction.

Chapter 6

Conclusion

Even though the mechanical system of the buoyancy-driven airship is complicate, through the analysis of some constrained cases, such as presented in section 2.2, lots of fundamental properties are found. Through the analysis in the modelling, the relationship between the airship's body and the movable mass is clearly presented, and the modelling of such complicate system becomes easy to follow. For the control design in this thesis, actually, not only some control methods have been derived, but also the dynamic system has been deeply analyzed. In this process, the important roles of the angular momentum and the aerodynamic forces are found and demonstrated. The performance of the nonlinear control displayed in this thesis, both in 2D and 3D, are acceptable.

Airships are no longer used for passenger transportation, however, they are useful for other purposes, such as surveillance, communication relay, and heavy lift transportation, which has drawn a lot of attention in the recent years. This is the motivation of this research as well. But different from the conventional airship which is driven by propellers, rudders and elevators, a new-concept of buoyancy-driven airship is considered in this thesis. This new buoyancy-driven airship moves forward by moving an internal mass and by varying the total mass of the airship. The motivation of the research of this new airship is to design a new energy-saving aircraft which has longer airborne endurance. The buoyancy-driven airship has been introduced by R. Purandare in (Purandare (2007)), which is the first and the only monograph available on this domain. Thus, lack of references is also a challenge of this research. Nevertheless, the buoyancy-driven airship which employs an internal moving mass to control the attitude and an adjustable air bladder to control the altitude offers a novel mechanism for UAVs, and it is an exciting research topic, especially, since this mechanism is already successfully applied in some underwater gliders.

In this thesis, the main contributions consist of the following four aspects:

- A complete 8-DOF mathematical model for the buoyancy-driven airship in 3D is derived. In this progress, two approaches are offered. The rigid body and the moveable mass can be viewed

independently and globally. When the rigid body and the moveable mass are viewed independently, the coupling of these two subsystems only consists in a control force.

- The fundamental properties of the complex model are investigated by analysis, design and simulations. Through analysis and simulations, it is established that the attitude of the airship is mainly controlled by the translation of the moveable mass and the altitude is controlled by the variation of the net lift. Moreover, the aerodynamic forces offer couplings between the attitude control and the guidance control and render all DOF controllable. These are shown according to the following Fig 6.1.

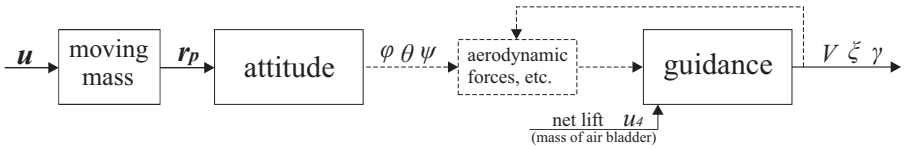

Figure 6.1: The structure of the buoyancy-driven arship (also the autonomous gliding vehicle).

The angular momentum of the airship plays an important role in the control the dynamics since it has the highest relative degree.

- Various controls of the planar dynamics are constructed. Besides a basic LQR approach and an input-output linearization, an advanced nonlinear control based on the maximal feedback linearization with internal stability is derived. This process is not easy to perform directly on the full model.

  It has been shown that the airship is not fully feedback linearizable. Maximal feedback has been solved. Although the latter techniques are usually not trackable for complex aeronautical models, it has been possible to derive analytic control solutions. A major challenge is internal stability and a suitable choice of linearizing coordinates could circumvent this issue and the internal stability has been proven.

- A control scheme based on singular perturbations for the motion in 3D is given for the first time. In this process, the analytical solution for a stable spiral motion is derived.

The buoyancy-driven airship is a novel object as it is not yet available on the market, and in this thesis only some preliminary theoretical issues are argued. There still exist a lot of open questions. The main points which are worth to be solved are listed in the following:

- In this thesis, lots of parameters are assumed to be constant, such as the moment of inertia and the aerodynamic coefficients. It is mandatory to investigate the robustness of the control under the variations of these parameters.

- Obviously, severe wind conditions are not considered here, and they may give the limits of the airship design and the minimal use of a standard propulsion may become mandatory. For further work, a hybrid airship which employs the buoyancy-driven and the standard propeller is worth to consider.

- The autonomous airship has finally to be considered in a framework of UAV. The complete control structure of autonomous UAVs is shown in Fig. 6.2. In this thesis, only the internal first and second loops are considered. Thus, the outer loops require additional research to complete the control structure.

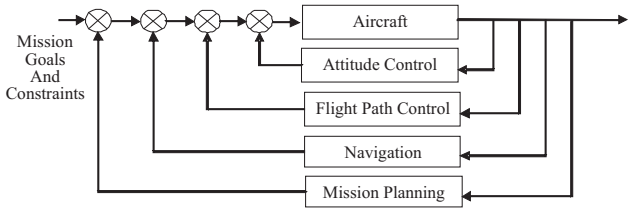

Figure 6.2: The control structure of autonomous UAVs.

Obviously, the most pragmatic aspects go through the construction of a demonstration airship to check the practical feasibility of this new UAV mechanism and the validity of the control in the thesis.

Chapter 7

Résumé en Français

Contents

Un nouveau concept de dirigeable sans propulseur, sans gouvernail de direction et sans gouvernail de profondeur est considéré dans cette thèse. Il est actionné par une masse amovible et une vessie d'air interne dont la masse est réglable. Ces deux actionneurs permettent de commander le mouvement du centre de gravité et la force de flottabilité nette (poussée d'archimède). Le développement de ce concept de dirigeable est motivé par les économies d'énergie. Un modèle complet a huit degrés de liberté de ce dirigeable est obtenu par la méthode de Newton-Euler. L'interconnexion entre le corps rigide du dirigeable et de la masse mobile est modélisée. La dynamique dans le plan longitudinal est analysée et contrôlé successivement par une commande LQR, un retour d'état assurant un plan placement de pôles, et la linéarisation maximale par bouclage. Grâce à la linéarisation maximale par bouclage, un commande non linéaire adéquate est obtenue. Dans ce processus, la modélisation, l'analyse et de contrôle sont résolus pour les cas particuliers du dirigeable de plus en plus complexes, afin de nous rapprocher du cas le plus général. Le cas le plus particulier se réduit à un système qui a deux degrés de liberté. Il est montré que les propriétés de base de certains systèmes mécaniques simples restent déterminantes pour l'analyse et la synthèse des dirigeables avancés. Ces propriétés sont loin d'être évidentes lorsque le modèle considéré est complexe. Nous montrons que l'étude du cas 3D est facilitée grâce à une approche de perturbations singulière. La superposition des deux actions de contrôle dans le plan longitudinal et dans le plan latéral est alors possible et permet de

parvenir au contrôle de la dynamique en trois dimensions.

7.1 Introduction

Bien que les dirigeables ne soient plus utilisés pour le transport de passagers, ils sont utiles à d'autres fins, telles que la publicité, les visites touristiques, la surveillance et la recherche (Elfes et al., 1998; Tozer and Grace, 2001; Bowes, W. C. and Engelland, J. and Fernandez, F. L. and Fratarangelo, P. and Kohn, Jr. E. and Lister, R. and Neal, W. A. and Polmar, N. and Rumpf, R. L, and Smith, T. B. and NRAC, 2006). Les principaux pays dans le monde ont mis en place indépendamment de nouveaux projets, par exemple, le programme de Northrop Grumman sur le dirigeable hybride(Northrop Grumman, 2010), le programme de Lockheed Martin(Defense Industry Daily, 2006; Lockheed Martin Corporation, 2008), le programme européen l'ESA-HALE, et quelques autres(Knaupp and Mundschau, 2004; Yokomaku, 2001).

La différence notable avec les anciens dirigeables est que la recherche moderne se concentre sur le dirigeable sans pilote humain à bord. Fondé sur la commande à distance, la commande par bouclage et la navigation autonome, un dirigeable moderne doit accomplir certaines tâches de manière automatique. De nombreux travaux ont été consacrés à la modélisation, le contrôle et de suivi de trajectoire des dirigeables(Gomes and Ramos Jr, 1998; Ouyang, 2003; Purandare, 2007).

La plupart de ces travaux ont contribué à des dirigeables qui sont entraînés par des propulseurs situés le long de la cellule, et dont l'attitude est contrôlée par des gouvernails ou d'une poussée vectorielle. Ces modèles mathématiques sont fondés sur le modèle Gomes(Gomes and Ramos Jr, 1998).

Dans cette thèse, un nouveau concept de dirigeable est considéré, mû par la force de flottabilité. Le déplacement d'un ballast interne et la variation de la masse totale du dirigeable permettent de déplacer l'engin.. La motivation de cette recherche est de développer un vol d'économie d'énergie qui a une longue endurance de suspension dans l'air.

A l'heure actuelle, la seule monographie sur le dirigeable à flottabilité motrice est la thèse(Purandare, 2007). C'est un défi de cette recherche. Une démonstration est mentionnée dans cette thèse, et qui montre la modification de la flottabilité nette de l'engin par un ventilateur, la modification de l'attitude, et la faisabilité d'un mouvement de petite amplitude vers l'avant. La faisabilité du projet a été prouvée cependant les technologies n'étaient pas mûres(Purandare, 2007). Ces travaux pionniers pionnier ont étudié la faisabilité, le modèle physique 2D de ce type de dirigeable, et la synthèse d'un contrôle PID pour le système. Les travaux ont été menés a été menée dans un environnement non perturbé. La conclusion fut que ce nouveau type de dirigeable pourrait voler de manière efficace

lorsque l'angle d'attaque est faible. Évidemment, les conditions de vents violents peuvent donner les limites de la conception aéronautique et l'utilisation minimale de propulseurs standard peut devenir obligatoire.

La présente thèse étudie les aspects théoriques seulement, et l'expérimentation réelle est au-delà de ses objectifs. Néanmoins, les principales contributions sont illustrés par un ensemble de résultats de simulation. Plus précisément, les contributions de cette thèse sont:

- Un modèle complet à 8 degrés de liberté d'un dirigeable à flottabilité motrice est obtenu en 3D. Deux approches sont proposées. La cellule rigide et la masse mobile sont modélisées soit en tant que deux sous-systèmes couplés, soit globalement.

- Les propriétés structurelles fondamentales du modèle complexe sont étudiées par l'analyse, la synthèse et les simulations. L'attitude du dirigeable est principalement contrôlée par la translation de la masse mobile, et l'altitude est contrôlée par la variation de la poussée nette. En aéronautique, les forces aérodynamiques induisent un couplage entre le contrôle d'attitude et de guidage. Par conséquent, les forces aérodynamiques rendent tous les degrés de liberté commandables. Elles sont indiquées par la figure 7.1.

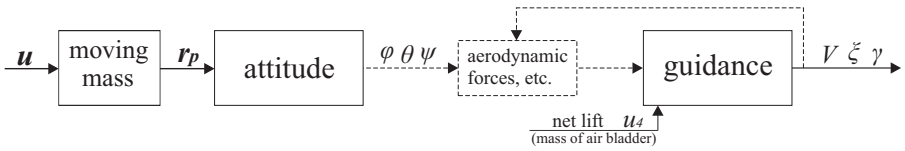

Figure 7.1: La structure du modèle du véhicule.

Un des fils rouges de nos travaux est la démonstration que le moment angulaire du dirigeable joue un rôle déterminant dans le contrôle de la dynamique, car il a un degré maximal.

- Divers mécanismes de commande de la dynamique plane, de l'approche LQR à une commande non linéaire fondée sur la linéarisation maximale par bouclage, sont construits. Il est montré que le dirigeable n'est pas complètement linearisable par bouclage. La linéarisation maximale est résolue. Bienque ces techniques soient en général difficiles à mettre en oeuvre sur des modèles complexes, des solutions analytiques sont calculées. Un défi majeur est la stabilité interne qui n'est malheureusement pas garantie. Le choix adéquat de coordonnées linéarisantes permet de résoudre ce problème et la stabilité interne du système en boucle fermée est démontrée.

- Une commande fondée sur les perturbations singulières pour le mouvement en 3D est donnée pour la première fois. Dans ce mémoire, la condition analytique pour un mouvement en spirale stable est déduit.

Les hypothèses importantes sont faites dans cette thèse. Dans ces premiers résultats, les questions théoriques sont débattues. Les perturbations, comme le vent, et la variation de la densité de l'air ou de la température, ne sont pas considérées.

Le chapitre est organisé comme suit: le dirigeable à flottabilité motrice est introduit brièvement dans la section 7.2. Le dirigeable est complètement modélisé dans la section7.3. La section 7.4 montre les commandes utilisées pour la dynamique longitudinale. La dynamique du véhicule est également analysée dans cette section. La section 7.5 propose une commande fondée sur la théorie des perturbations singulières pour le mouvement en 3D. La section 7.6 conclut ce chapitre.

7.2 Description Générale du Dirigeable Soumis à une Force de Flottabilité

La structure de base du dirigeable est montrée dans la figure 7.2. La coque du dirigeable est gonflée à l'hélium et l'air ambiant est contenu dans deux vessies isolées. Les vessies d'air interne sont symétriques et élastiques; leur masses peuvent être ajustées par un ventilateur et des vannes. Comme le volume du dirigeable est fixe, la force de flottabilité du dirigeable demeure constante. En ajustant la masse de la vessie d'air interne, le dirigeable monte ou descend.

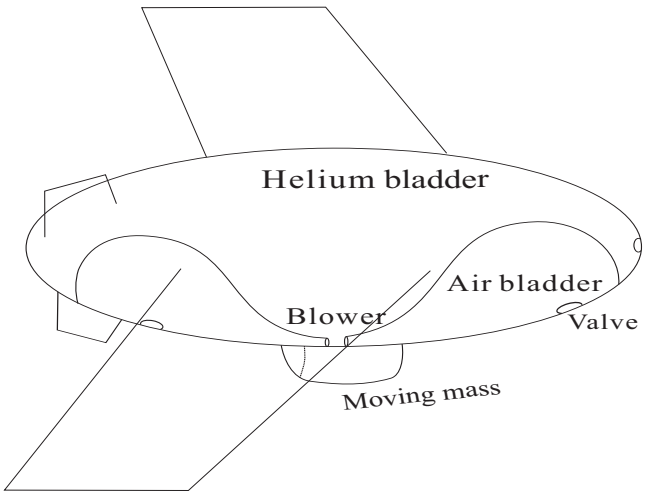

Figure 7.2: Structure du dirigeable de flottabilité à moteur.

Il y a une masse mobile située à la bas du dirigeable. Elle peut se déplacer le long des directions e_1 et e_2 du repère mobile. Avec le mouvement de masse mobile, le centre de gravité CG se déplace, ce qui conduit à la variation de l'attitude du dirigeable.

Le dirigeable est également équipé de quelques ailettes qui contribuent à augmenter les forces aérodynamiques, cependant il n'y a pas de gouvernail.

Le mécanisme actionnant ce type du dirigeable est décrit comme suit. Lorsque l'air est libéré de la vessie d'air interne, la masse du dirigeable se réduit, par conséquent, la poussée nette devient positif et le dirigeable monte. Lorsque simultanément, la masse mobile se déplace vers l'arrière du dirigeable, le dirigeable obtient un angle de montée positive, et cela induit une composante de force aérodynamique vers l'avant sur le dirigeable. Cette composante de force meut le dirigeable vers l'avant (voir la figure 7.3 et le segment BC de la figure 7.5). Inversement, quand l'air est pompé dans la vessie d'air interne, la masse du dirigeable augmente, donc par conséquent, la poussée nette devient négative et le dirigeable descend. Lorsque la masse mobile se déplace simultanément vers l'avant, l'angle de montée devient négatif. Cela induit également une composante de force aérodynamique vers l'avant. Par conséquent, le dirigeable se déplace vers le bas et vers l'avant (voir la figure 7.4 et le segment AB de la figure 7.5).

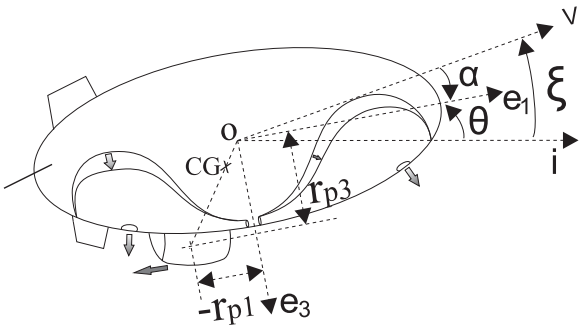

Figure 7.3: Le dirigeable se déplace vers le haut et vers l'avant.

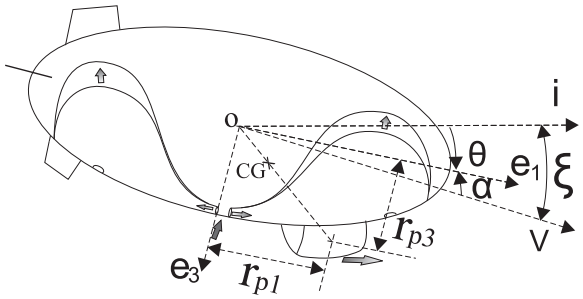

Figure 7.4: Le dirigeable se déplace vers le bas et vers l'avant.

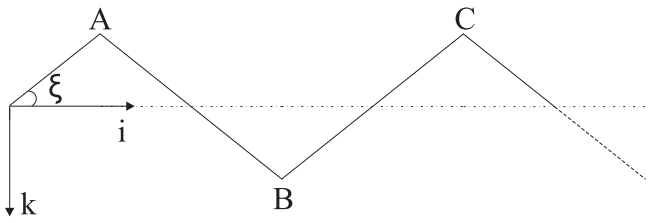

Figure 7.5: Trajectoire typique d'un dirigeable.

7.3 Deux Approches pour la Modélisation

Ici, deux approches de modélisation pour le dirigeable avec la masse mobile sont présentées. Ces deux approches appréhendent la dynamique du système de manière différente. Pour la première approche de modélisation, la dynamique des corps rigides et interne masse mobile sont considérés de manière indépendante. La force d'interaction entre le corps rigide et la masse mobile est considrée

comme une variable de commande intermédiaire. De ce point de vue, l'interconnexion entre ces deux sous-systèmes est claire. Pour la deuxième approche, la dynamique du système est décrite en termes de la dynamique totale du système rigide et la dynamique de la masse mobile. Comme la force de contrôle est une force interne, la quantité de mouvement totale est conservée pour tout choix de la commande.

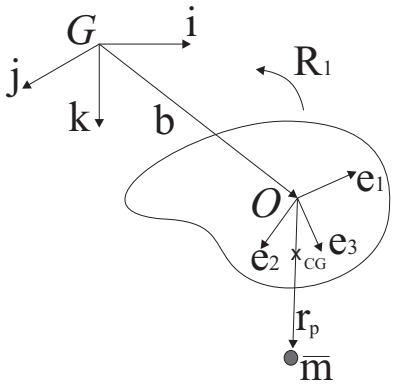

Figure 7.6: Le corps rigide et la masse mobile

Comme représenté sur les figures 7.6, le corps rigide du dirigeable et la masse mobile sont représentés comme deux points matériels. Les deux approches de modélisation sont présentées comme suit.

Certains résultats de cette section sont publiés dans (Wu et al., 2009a, 2010).

7.3.1 Le corps rigide et la masse mobile sont deux sous-systèmes indépendants

Comme noté ci-dessus, dans ce cas, le seule connexion entre le corps rigide et la masse mobile se compose d'une force qui est utilisée pour actionner la masse mobile par le corps. Les équations du mouvement du système comprennent les mouvements de translation et angulaires du corps rigide et de la masse mobile.

Soit $\boldsymbol{p}$ la quantité de mouvement, $\boldsymbol{\pi}$ la moment cinétique du corps rigide, et $\boldsymbol{p_p}$ la quantité de mouvement de la masse mobile, respectivement. Noter que $\boldsymbol{p}$, $\boldsymbol{\pi}$, et $\boldsymbol{p_p}$ sont calculés par rapport au repère inertiel. $\boldsymbol{P}$, $\boldsymbol{\Pi}$, et $\boldsymbol{P_p}$ sont calculés par rapport au repère mobile.

$$\begin{cases} \dot{\boldsymbol{\pi}} = \sum \boldsymbol{\tau_{ext}} - \boldsymbol{r_p} \times \left(\boldsymbol{R_1^T u} \right) \\ \dot{\boldsymbol{p}} = \sum \boldsymbol{f_{ext}} - \bar{m} g \boldsymbol{k} - \boldsymbol{R_1^T u} \\ \dot{\boldsymbol{p}}_{\boldsymbol{p}} = \bar{m} g \boldsymbol{k} + \boldsymbol{R_1^T u} \end{cases} \tag{7.1}$$

où $\sum \boldsymbol{f_{ext}}$ est la force extérieuer total et n'inclut pas les moments de $\bar{m}g$ et $\boldsymbol{u}$, agi sur le corps. $\sum \boldsymbol{\tau_{ext}}$ est le moment extérieure totale, excepté les moment de $\bar{m}g$ et $\boldsymbol{u}$.

Grâce à la transformation entre le repère inertiel et le repère mobile, les équations du mouvement par rapport au repère inertiel sont obtenues comme:

$$\begin{cases} \dot{\boldsymbol{\Pi}} = \boldsymbol{\Pi} \times \boldsymbol{\Omega} + \boldsymbol{P} \times \boldsymbol{v} + \boldsymbol{R}^T \sum \boldsymbol{\tau}_{ext} - \boldsymbol{r}_p \times \boldsymbol{u} \\ \dot{\boldsymbol{P}} = \boldsymbol{P} \times \boldsymbol{\Omega} + \boldsymbol{R}_1^T \sum \boldsymbol{f}_{ext} - \bar{m} g \left(\boldsymbol{R}^T \boldsymbol{k} \right) - \boldsymbol{u} \\ \dot{\boldsymbol{P}}_p = \boldsymbol{P}_p \times \boldsymbol{\Omega} + \bar{m} g \left(\boldsymbol{R}^T \boldsymbol{k} \right) + \boldsymbol{u} \end{cases} \tag{7.2}$$

Des équations $\dot{\boldsymbol{P}}$ et $\dot{\boldsymbol{P}}_p$ dans Eq. (7.2), on conclut que le corps rigide subit une force antagoniste à la grandeur $\boldsymbol{u}$ de la masse mobile. Ce résultat est confirmé par la figure 3.11 et l'analyse ci-dessus. La force de contrôle $\boldsymbol{u}$ associe le corps rigide et la masse mobile comme un système multi-corps.

7.3.2 Le corps rigide et la masse mobile sont considérés globalement

Plutôt que de considérer la dynamique du corps rigide séparément de celle de la masse mobile, on peut considérer la dynamique totale du système qui est notée par un tilde ′ ˜ ′. Dans ce cas, la quantité de mouvement est contstante. Pour maintenir l'uniformité de la notation, elle est reécrite comme $\tilde{p}_p$.

Dans ce cas, Eq. (7.1) se transforme en:

$$\begin{cases} \dot{\tilde{\boldsymbol{\pi}}} = \sum \boldsymbol{\tau}_{ext} + \boldsymbol{r}_p \times (\bar{m} g \boldsymbol{k}) \\ \dot{\tilde{\boldsymbol{p}}} = \sum \boldsymbol{f}_{ext} \\ \dot{\tilde{\boldsymbol{p}}}_p = \bar{m} g \boldsymbol{k} + \boldsymbol{R}_1^T \boldsymbol{u} \end{cases} \tag{7.3}$$

où $\bar{m}g$ et $\boldsymbol{u}$ n'apparaissent pas dans la force et le moment externes.

Après la transformation, les variables par rapport au repère inertiel dans ce cas sont donnés par:

$$\begin{cases} \dot{\tilde{\boldsymbol{\Pi}}} = \tilde{\boldsymbol{\Pi}} \times \boldsymbol{\Omega} + \tilde{\boldsymbol{P}} \times \boldsymbol{v} + \boldsymbol{R}^T \sum \boldsymbol{\tau}_{ext} + \boldsymbol{r}_p \times \left(\bar{m} g \boldsymbol{R}^T \boldsymbol{k} \right) \\ \dot{\tilde{\boldsymbol{P}}} = \tilde{\boldsymbol{P}} \times \boldsymbol{\Omega} \\ \dot{\tilde{\boldsymbol{P}}}_p = \tilde{\boldsymbol{P}}_p \times \boldsymbol{\Omega} + \bar{m} g \left(\boldsymbol{R}^T \boldsymbol{k} \right) + \boldsymbol{u} \end{cases} \tag{7.4}$$

Notez que $\boldsymbol{u}$ n'entre pas dans l'équation du $\dot{\tilde{\boldsymbol{\Pi}}}$ and $\dot{\tilde{\boldsymbol{P}}}$. Cela reflète le fait que l'actionnement interne ne peut pas modifier la dynamique globale du système.

Par cette analyse, la structure dynamique a été reconnue et exploitée. Ces deux modèles sont utilisés à des fins différentes. Ils sont également d'excellents candidats pour faciliter l'analyse et la conception des contrôles pour les autres véhicules qui comprennent les engins spatiaux et les véhicules de rentrée atmosphérique.

7.3.3 Le modèle mathématique complet

Puisque le dirigeable est entraîné par le changement de la poussée nette, il est nécessaire de contrôler la masse du ballonnets par la l'entrée de commande u_4, soit $m_b = u_4$. Donc $m_0 = m_h + \bar{m} + u_4 - m$, cela implique que m_0 dans le modèle mathématique comprend une entrée de commande.

Mais l'utilisation de la quantité de mouvement et du mouvement cinétique comme états du modèle ne convient pas, et il est préférable d'exprimer la quantité de mouvement en fonction de la vitesse.

En combinant les équations de la cinématique par rapport au repère inertiel, le modèle mathématique qui a huit degrés de liberté est obtenu comme suit:

$$\begin{pmatrix} \dot{\boldsymbol{b}} \\ \dot{\boldsymbol{\eta}} \\ \dot{\boldsymbol{v}} \\ \dot{\boldsymbol{\Omega}} \\ \dot{\boldsymbol{r}}_p \\ \ddot{\boldsymbol{r}}_p \end{pmatrix} = \begin{pmatrix} \boldsymbol{R}_1 \boldsymbol{v} \\ \boldsymbol{R}_3 \boldsymbol{\Omega} \\ \boldsymbol{M}^{-1} \bar{\boldsymbol{F}} \\ \boldsymbol{J}^{-1} \bar{\boldsymbol{K}} \\ \dot{\boldsymbol{r}}_p \\ \bar{\boldsymbol{T}} \end{pmatrix} \tag{7.5}$$

où

$$\begin{aligned} \bar{\boldsymbol{K}} &= \boldsymbol{J}\boldsymbol{\Omega} \times \boldsymbol{\Omega} + \boldsymbol{M}\boldsymbol{v} \times \boldsymbol{v} + \boldsymbol{M}_{at} - \boldsymbol{r}_p \times \boldsymbol{u} \\ \bar{\boldsymbol{F}} &= \boldsymbol{M}\boldsymbol{v} \times \boldsymbol{\Omega} + \boldsymbol{F}_{at} + (m_0 - \bar{m}) g \boldsymbol{R}_1^T \boldsymbol{k} - \boldsymbol{u} \\ \bar{\boldsymbol{T}} &= -\dot{\boldsymbol{v}} - \dot{\boldsymbol{\Omega}} \times \boldsymbol{r}_p - \boldsymbol{\Omega} \times \dot{\boldsymbol{r}}_p + g(\boldsymbol{R}_1^T \boldsymbol{k}) + \boldsymbol{v}_p \times \boldsymbol{\Omega} + \boldsymbol{u}/\bar{m}. \end{aligned}$$

7.4 Contrôle de la Dynamique Longitudinale

La dynamique du dirigeable dans le plan longitudinal est considéré puisque cette dynamique est la plus fondamentale et importante. Mais il n'est pas facile de l'analyser et de la commander en raison de sa non-linéarité. La dynamique longitudinale est formée de six états et de deux entrées de commande. Diverses simulations en boucle ouverte sont effectuées pour vérifier le modèle. Une approche commune pour contrôler un système non linéaire consiste à linéariser le système autour d'un point équilibre, et puis l'analyse et la commande de ce système linéairesont utilisées pour le système nonlinéaire d'origine. Une approche basée sur la commande LQR est d'abord présentée dans cette section. Toutefois, en raison de l'inconvénient de l'approche LQR, un contrôle non linéaire du système est nécessaire.

Une réussite majeure du contrôle non-linéaire moderne est linéarisation par bouclage (Isidori, 1989; Conte et al., 2007). Malheureusement, le système du dirigeable n'est pas entièrement linéarisable,

et le principal inconvénient est qu'une dynamique non-linéaire qui peut être instable restera dans le système en boucle-fermée. Deux commandes non-linéaires fondées sur linéarisation par bouclage sont présentées dans cette section et la stabilité de la dynamique interne est prouvée. Ces commandes non linéaires sont des sont certaines des contributions de ces travaux de recherche.

Certains résultats de cette section sont publiés dans (Wu et al., 2009a,b, 2010, 2011a).

7.4.1 Modèle de la dynamique longitudinale

Pour étudier la dynamique dans le plan longitudinal, le modèle complet a été limité au plan $e_1 - e_2$, c'est-a-dire que seulement les degrés de liberté dans le plan longitudinal dans le modèle complet sont conservés, comme θ, Ω_2, v_1, v_3, r_{p1}, et m_0. Le modèle longitudinal est alors donné comme suit:

$$\begin{cases} \dot{\theta} & = \Omega_2 \\ \dot{\Omega}_2 & = \frac{1}{J_2}(M_a + r_{p1}u_3 - r_{p3}u_1) \\ \dot{v}_1 & = \frac{1}{m_1}\left((\bar{m} - m_0)\, g \sin\theta - m_3 v_3 \Omega_2 + F_{a1} - u_1\right) \\ \dot{v}_3 & = \frac{1}{m_3}\left((m_0 - \bar{m}) g \cos\theta + m_1 v_1 \Omega_2 + F_{a3} - u_3\right) \\ \ddot{r}_{p1} & = -\dot{v}_1 - \dot{\Omega}_2 r_{p3} - (v_3 - \Omega_2 r_{p1})\Omega_2 - g\sin\theta + u_1/\bar{m} \\ \dot{m}_0 & = u_4 \end{cases} \tag{7.6}$$

où u_3 n'est pas une entrée de commande et est fixée par Eq. (3.20). L'équilibre de la dynamique longitudinale est calculé à partir de ce modèle.

7.4.2 Commande LQR

La commande LQR est une théorie importante et classique pour le contrôle optimal, et elle est utilisée pour résoudre le problème LQG qui est l'un des problèmes les plus fondamentaux de la théorie du contrôle. Cependant, comme chacun le sait, un inconvénient de toute commande linéaire est la limite du domaine de validité de la commande linéaire contrôle linéaire pour le système non linéaire d'origine, en raison de l'approximation de la linéarisation.

La théorie LQR pour des problèmes de contrôle fournit les gains de rétroaction pratiques. Il est supposé que tous les états $\boldsymbol{x}$ sont disponibles pour le contrôle. La fonction de coût est définie comme:

$$J = \int_0^\infty \left(\boldsymbol{x}^T Q \boldsymbol{x} + \boldsymbol{u}^T R \boldsymbol{u}\right) dt$$

Les matrices de pondération Q et R sont des paramètres de réglage. Il n'y a pas de manière générale pour définir les valeurs de ces paramètres et elles dépendent du choix de l'utilisateur. Elles ont des répercussions profondes sur la performance du système en boucle fermée.

La loi de commande de rétroaction qui minimise la valeur du coût est la suivante:

$$\boldsymbol{u} = -K(\boldsymbol{x} - \boldsymbol{x_e}) \tag{7.7}$$

où K est la solution de l'équation de Lyapunov et peut être calculée aisément par MATLAB®.

Avec le bouclage linéaire (7.7), le dirigeable suit une trajectoire déterminée, qui est simulé et montré dans la figure. 4.18.

Néanmoins, un tel contrôle linéaire pour le système non linéaire d'origine n'est valable que dans un petit domaine autour de l'équilibre. Le contrôleur linéaire seul assure la stabilité locale et le dirigeable s'écrase lorsqu'il est soumis à une perturbation significative, par exemple lorsque la perturbation sur v_1 est supérieure à $+4.5\ m/s$.

7.4.3 Linéarisation entrée-sortie

Ici, une simplification raisonnable est faite. Pendant la montée et la descente, le dirigeable ajuste simplement la position de la masse mobile de manière à résister aux perturbations générales. Par conséquent, m_b, m_0, et u_4 sont constants au cours de ces périodes. Lorsque le dirigeable commute entre la montée et la descente, la masse la vessie d'air interne m_b est soumise à une commande bang-bang en boucle ouverte . Ainsi, pour la dynamique longitudinale, il n'y a qu'une seule commande effective, la force interne.

En choisissant la sortie du système $y = x$, ou bien θ ou bien r_{p1} on vérifie que le système a un degré relatif égal à 2. Toutefois, il est facile de vérifier que la sortie $y = r_{p1}$ conduit à un système à non minimum de phase. Donc, la linéarisation entrée-sortie ne peut pas être appliquée. Par contre, la fonction de sortie $y = \theta$ définit un système à minimum de phase.

Puisque le degré relatif de la sortie $y = \theta$ est de 2, il suffit de considérer l'équation d'erreur suivante:

$$\ddot{e} + \lambda_1 \dot{e} + \lambda_0 e = w_1$$

où $e = y - \theta_e$, θ_e est la valeur désirée de θ, et w_1 représente une nouvelle entrée de commande du système en boucle fermée.

$$\ddot{\theta} + \lambda_1 \dot{\theta} + \lambda_0(\theta - \theta_e) = w_1 \tag{7.8}$$

λ_1 et λ_0 assignent les pôles de la dynamique d'erreur. En substituant (4.9) et (4.10) en (4.31), l'équation peut être résolue et la commande $\tilde{u}_1$ est calculée.

7.4.4 Linéarisation maximale par bouclage avec stabilité interne

Le modèle (7.6) est complexe et il est difficile de calculer une sortie ayant le degré relatif le plus élevé. Mais un modèle simplifié peut être d'une grande pertinence dans l'analyse de la stabilité et la conception du contrôle. Le modèle complexe du dirigeable est simplifié en un pendule prismatique qui est au coeur de sa dynamique.

Il est clair que la dynamique dans le plan longitudinal est affecté par les quatre parties suivantes:

- la masse mobile $p1$ qui contrôle l'angle de montée θ,
- la flottabilité nette $m_0 g$ qui contrôle la montée et la descente de dirigeable,
- les forces d'inertie qui sont désignées par des masses ajoutées m_{ii},
- les forces aérodynamiques $\boldsymbol{F_a}$ et $\boldsymbol{M_a}$.

Il est supposé que le dirigeable est fixé au point O et est seulement soumis au mouvement de la masse mobile pour contrôler l'angle de montée, et il n'y a aucune autre force qui affecte dirigeable. Dans cette situation, le système peut être simplifié au maximum, et le dirigeable tourne autour du centre du volume O, ce qui conduit le système à un pendule prismatique décrit dans la figure 7.7. La liaison de rotation au point O n'est pas actionné. L'articulation entre les deux corps du pendule est prismatique et actionnées. Ce pendule, inversé ou non, a été considéré comme un exemple de commande standard dans de nombreuses références (Wie, 1998).

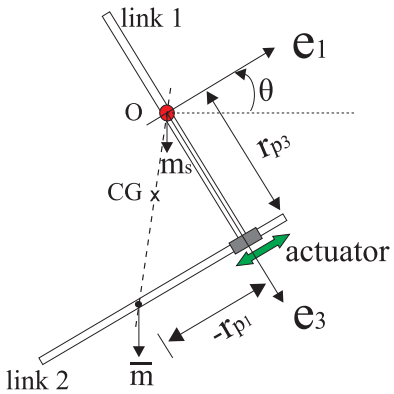

Figure 7.7: Le système du dirigeable simplifié est identique à un pendule à liaison prismatique.

Le systéme du dirigeable simplifiéest identique à un pendule à liaison prismatique.

Le modèle mathématique pour ce cas particulier est un sous-système de (7.6). Son modèle à quatre dimensions est intrinsèquement non linéaire dans le sens où elle n'est pas entièrement linéarisable par bouclage. Néanmoins, il peut être linéarisé partiellement. Malheureusement, le choix d'une sortie aléatoire de linéarisation ne donnera pas de stabilité interne. Il s'agit d'un phénomène bien connu

et est formalisé par la notion célèbre de dynamique de zéro (Isidori and Moog, 1988). Le résultat principal est le calcul explicite d'une sortie qui donne un sous-système linéaire d'ordre 3, avec une dynamique de zéro asymptotiquement stable.

Pour un point de vues non-réclamés , le moment cinétique Π_1 du système a un degré relatif égal à 3 et il reste inchangé lorsque les forces de supplémentaires, comme la flottabilité nette, la force d'inertie, et la force aérodynamique, etc, s'appliquent sur le dirigeable. Le moment cinétique Π_1 du modèle longitudinal complet (7.6) est :

$$\Pi_1 = J_2\dot{\theta} + \frac{\bar{m}m_1}{\bar{m}+m_1}\left(\frac{m_3(m_1+\bar{m})}{m_1(m_3+\bar{m})}r_{p1}^2\dot{\theta} + r_{p3}^2\dot{\theta} + r_{p3}\dot{r}_{p1}\right).$$

Grâce à un certain facteur intégrant ϱ, le moment angulaire Π_1 peut être intégré. Plus précisément, il existe Π_2 tel que:

$$\dot{\Pi}_2 = \varrho\Pi_1, \quad \varrho > 0$$

$$\Pi_2 = \theta + \frac{r_{p3}}{\sqrt{\frac{m_3(m_1+\bar{m})}{m_1(m_3+\bar{m})}}\sqrt{\frac{\bar{m}+m_1}{\bar{m}m_1}J + r_{p3}^2}}\arctan\frac{\sqrt{\frac{m_3(m_1+\bar{m})}{m_1(m_3+\bar{m})}}r_{p1}}{\sqrt{\frac{\bar{m}+m_1}{\bar{m}m_1}J + r_{p3}^2}}$$

Toute combinaison de Π_1 et Π_2 a un degré relatif égal à 3 et sa linéarisation par bouclage va transformer (7.6) dans un sous-système linéairelinéaire de dimension 3 commandable avec une dynamique de zéro dimension 3 (Marino, 1986). Le résultat suivant montre la possibilité d'assurer que le système soit à minimum de phase. Cela a un impact décisif sur sa stabilité interne et la faisabilité de ce commande.

Théorème: Le système avec la sortie $y = \Pi_1 + k\Pi_2$ a un une dynamique de zéro stable quand $k > 0$.

Donc, pour $k > 0$, le système est asymptotiquement stable puisque ϱ est strictement positif et borné fonction d'inertie.

De ce théorème, il est obligatoire de choisir $k > 0$ pour assurer la stabilité interne du système en boucle fermée. Sa valeur réelle est un paramètre de réglage qui influe sur la vitesse de la dynamique de zéro. L'équation d'erreur suivante est considérée,

$$y^{(3)} + \lambda_2 y^{(2)} + \lambda_1 y^{(1)} + \lambda_0(y - y_e) = 0 \tag{7.9}$$

Dans l'équation (7.9), le terme $y^{(3)}$ est un une fonction explicite de de l'entrée u_1. L'équation (7.9) est résolue en u_1 et conduit au retour d'état statique qui est calculé explicitement après quelques calculs certes lourds, mais directs.

Les résultats de simulation

Une trajectoire typique est considérée, comme le montre la figure 2.9. L'équilibre des états est également présenté dans le tableau. Le but de cette simulation est de montrer que les lois de commande non linéaires sont capables de commander les états et de faire face à une structure de commutation du entre la montée et la descente.

Pour mettre en oeuvre un vol en dents de scie comme en figure 2.9, en plus de l'entrée u_1 qui commande le mouvement de la masse mobile, l'entrée u_4 dans l'équation (7.6) est impliquée pour contrôler la montée et la descente.

La trajectoire de vol est indiquée sur la figure 7.11; les variations de θ, r_{p1}, v_1, et v_3 sont représentées sur les figures 7.8 et 7.9. La force d'entrée est représentée sur la figure 7.10.

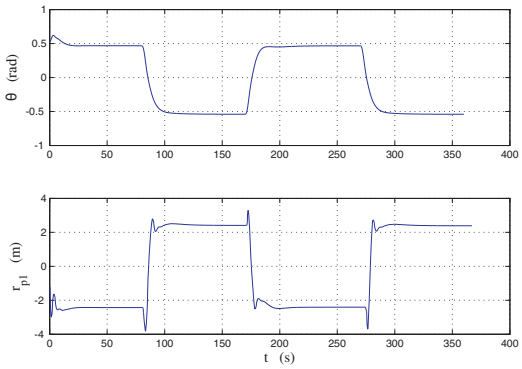

Figure 7.8: Dynamique de θ et r_{p1} d'un vol typique.

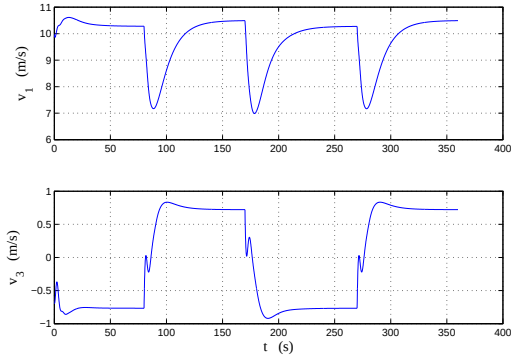

Figure 7.9: Dynamique de v_1 et v_3 d'un vol typique.

Sur les points de transition, en plus des transformations des commandes des états, la flottabilité nette du dirigeable est passée de 62 N à -62 N, ce qui représente un contrôle bang-bang pour u_4. Il est démontré par la simulation que le comportement des états et l'entrée de commande est à peu près symétrique. Sur les points de transition, la variation de l'entrée est aussi acceptable.

7.5 Contrôle en Trois Dimensions

La condition analytique du mouvement en spirale stable en 3D est résolu. A partir de ce résultat, on constate que la dynamique longitudinale peut être découplée de la dynamique latérale lorsque le

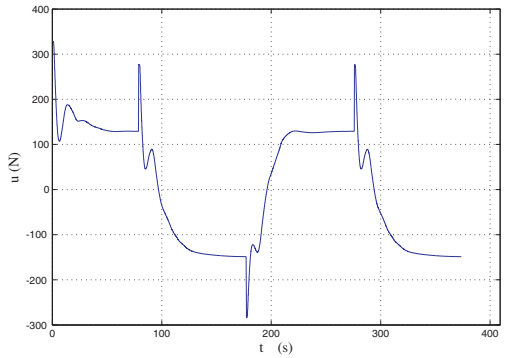

Figure 7.10: Le comportement de l'entrée u.

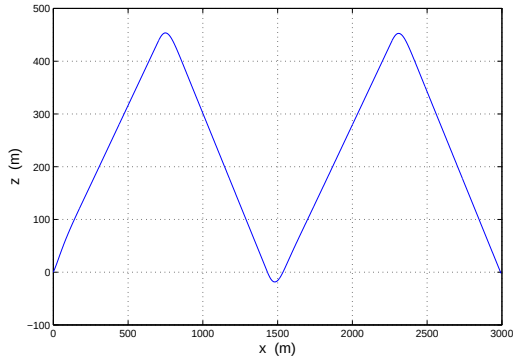

Figure 7.11: La trajectoire de vol de deux cycles.

taux de rotation est faible. Dans cette section, la dynamique latérale est d'abord présentée. Le principe de sa commande est semblable à la commande non linéaire de la dynamique longitudinale. Grâce à une approche de perturbations singulières, la superposition de ces deux actions de commande dans le plan longitudinal et dans le plan latéral est faite afin d'obtenir obtenir du contrôle de la dynamique en trois dimensions. Les simulations du véhicule pour un suivi d'un attitude de référence, la direction du déplacement et la vitesse en trois dimensions sont présentées.

Certains résultats de cette section sont publiés dans (Wu et al., 2011b).

7.5.1 Commande de la dynamique latérale

La structure latérale du dirigeable est représenté sur la figure 7.12. La dynamique latérale comprend l'angle de roulis ϕ, la vitesse angulaire ω_1, les vitesses v_2, v_3, la position de la masse mobile r_{p2}, et la vitesse de la masse mobile $\dot{r}_{p2}$. Le modèle dynamique transversal est le suivant:

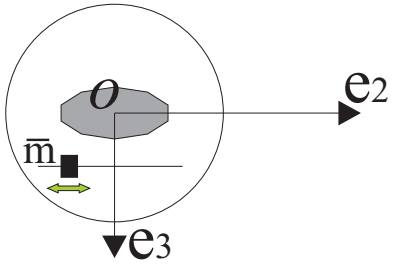

Figure 7.12: La structure latérale du dirigeable.

$$\begin{cases} \dot{\phi} & = \Omega_1 \\ \dot{\Omega}_1 & = \frac{1}{J_1}\left(L_a - r_{p2}u_3 + r_{p3}u_2\right) \\ \dot{v}_2 & = \frac{1}{m_2}\left((m_0 - \bar{m})\, g \sin\phi + m_3 v_3 \Omega_1 + F_{a2} - u_2\right) \\ \dot{v}_3 & = \frac{1}{m_3}\left((m_0 - \bar{m}) g \cos\phi - m_2 v_2 \Omega_1 + F_{a3} - u_3\right) \\ \ddot{r}_{p2} & = -\dot{v}_2 + \dot{\Omega}_1 r_{p3} + (v_3 + \Omega_1 r_{p2})\Omega_2 + g\sin\phi + u_2/\bar{m} \\ \dot{m}_0 & = u_4 \end{cases} \tag{7.10}$$

où u_3 provient également de (3.20).

L'analyse du sous-système longitudinal reste instrumentale bien que les paramètres soient différents. En fait, la conception du contrôle latéral est le même que celui de la dynamique longitudinale. Cette remarque est facile à comprendre si l'on tient compte de système physique réel, voir Fig. 4.28 et Fig. 7.12. La dynamique dans le plan latéral a la même structure que la dynamique dans le plan vertical, mais les paramètres sont différents.

Le moment cinétique de la dynamique latérale est:

$$\Xi_1 = J_1\dot{\phi} + \frac{mm_3}{m+m_3} r_{p2}^2 \dot{\phi} - \frac{mm_2}{m+m_2}(r_{p3}\dot{r}_{p2} - r_{p3}^2\dot{\phi})$$

et il existe deux fonctions Ξ_2 et ϱ', donc:

$$\dot{\Xi}_2 = \varrho'\Xi_1, \quad \varrho' > 0$$

$$\Xi_2 = \phi - \frac{r_{p3}}{\sqrt{\frac{J_1(m_2+\bar{m})}{m_2\bar{m}} + r_{p3}^2}\sqrt{\frac{m_3(m_2+\bar{m})}{m_2(m_3+\bar{m})}}} \arctan \frac{r_{p2}\sqrt{\frac{m_3(m_2+\bar{m})}{m_2(\bar{m}+m_3)}}}{\sqrt{\frac{J_1(m2+\bar{m})}{m_2\bar{m}} + r_{p3}^2}}$$

Ξ_1 et Ξ_2 ont degré relatif 3. De la même façon, il est facile de prouver que le système avec $y' = \Xi_1 + k\Xi_2$ a une dynamique de zéro stable pour tout $k > 0$. Considérons une équation d'erreur semblable à l'équation (7.9):

$$y'^{(3)} + \lambda_2' y'^{(2)} + \lambda_1' y'^{(1)} + \lambda_0'(y' - y_e') = 0 \tag{7.11}$$

La commande u_2 afin de stabiliser l'angle de la trajectoire de vol γ et la vitesse dans le plan latéral. Les paramètres de la commande sont représentés par λ_2', λ_1', et λ_0'. Le retour d'état u_2 est alors facilement obtenu. Les résultats de la simulation sont similaires à ceux de la dynamique longitudinale et sont obtenus pour la dynamique dans le plan latéral.

7.5.2 Structure de commande en 3D

La décomposition en deux échelles de temps du système complet est fondée sur l'hypothèse que la dynamique des états dans le plan longitudinal est plus lente que la dynamique des états dans le plan

latéral, voir figure 5.6. Les états dans le plan longitudinal se composent de θ, Ω_2, v_1, v_3, r_{p1},et $\dot{r}_{p1}$; les états dans le plan latéral se composent de ϕ, Ω_1, r_{p2}, v_2, v_3, et $\dot{r}_{p2}$. Il est démontré a posteriori que cette décomposition en deux échelles de temps est la clé pour le succès de la commande de l'attitude en 3D d'attitude en 3D.

La commande u_1 est ajustée par des paramètres λ_2, λ_1, et λ_0; u_2 est ajusté par des paramètres λ_2', λ_1', et λ_0'. Donc, la dynamique dans le plan longitudinal est plus lente que la dynamique dans le plan latéral par le choix $\lambda_2 = 3$, $\lambda_1 = 3$, $\lambda_0 = 1$, $\lambda_2' = 300$, $\lambda_1' = 300$, et $\lambda_0' = 1000$.

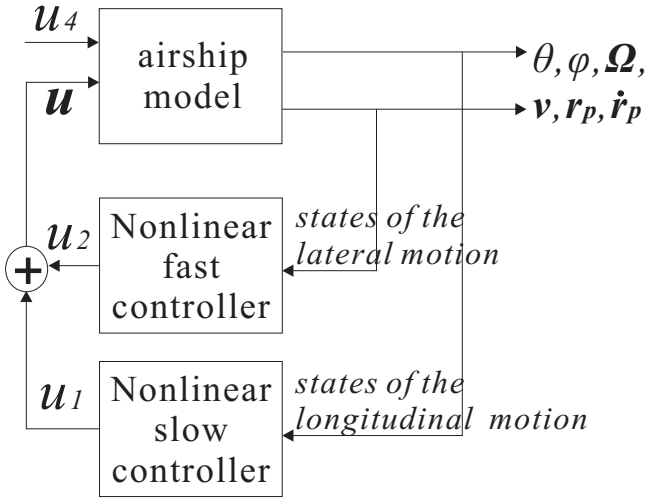

Figure 7.13: Structure de la commande fondée sur les perturbations singulières

où la flottabilité nette $m_0 g$, nommément u_4, est toujours soumise à une commande en boucle ouverte bang-bang.

7.5.3 Simulations des réponses à la commande nominale

Les performances de la commande proposée sur la base des perturbations singulières sont donnés dans la figure 7.14 - 7.17.

La figure 7.14 illustre la dynamique des angles d'Euler lorsqu'il existe des erreurs initiales. Dans cette simulation, l'angle de commande de θ est de 26 degrés, et l'angle ϕ désiré est zéro. Avec des erreurs initiales, les trois angles d'Euler sont asymptotiquement stables. La Figure 7.15 représente le mouvement de masse mobile dans ce processus.

Les simulations présentées dans la figure. 7.16 et 7.17 présentent le cas d'une rotation du dirigeable. Ici, ϕ est stabilisé à 10 degrés dans un premier temps, puis il est commandé à zéro. Dans la Fig. 7.17, la trajectoire est tournée vers la direction de $+e_2$.

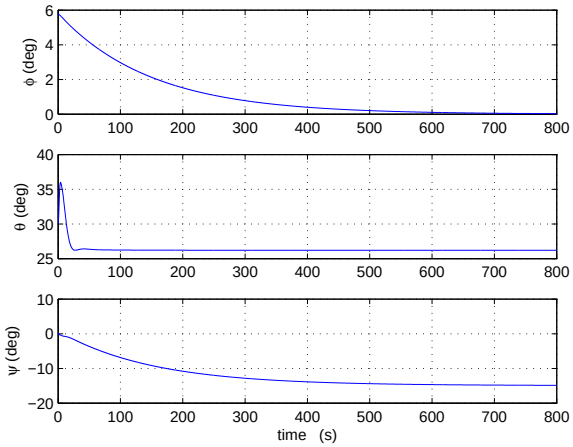

Figure 7.14: La dynamique des angles d'Euler avec des erreurs initiales.

7.6 Conclusion

Le nouveau concept de dirigeable autonome qui utilise de masse mobile interne pour contrôler l'attitude et une vessie d'air réglable pour contrôler l'altitude offre un nouveau mécanisme pour les drones. Grâce à l'approche Newton-Euler, un modèle 3D avec 8 degrés de liberté est obtenu, qui est plus complexe que le modèle des dirigeables classiques autonomes à cause de l'existence de la dynamique interne et de l'actionnement spécifique de la flottabilité. Cette thèse considère la masse mobile interne et le corps rigide du véhicule, comme deux sous-systèmes indépendants, ce qui rend la modélisation claire et facile. L'analyse montre également le rôle des forces aérodynamiques pour la dynamique de ce dirigeable, il introduit un couplage entre le contrôle d'attitude et du contrôle de guidage et rend de l'accessibilité complète des tous les degrés de liberté du système.

Pour un système non linéaire complexe, les approches de commande fondées sur la méthode LQR et la linéarisation entrée-sortie montrent des inconvénients qui conduisent à la nécessité de la synthèse d'une commande non linéaire avancée. Comme le modèle considéré n'est pas complètement linéarisable par bouclage, cette thèse propose une nouvelle approche qui consiste à analyser le système dans des cas particuliers de moins en moins contraints. Cette nouvelle méthodologie de commande est élaborée par la linéarisation maximale avec stabilité interne. La linéarisation maximale est résolue. Bienque ces techniques soient en général difficiles à mettre en oeuvre sur des modèles complexes, des solutions analytiques sont calculées. Un défi majeur est la stabilité interne qui n'est malheureusement pas garantie. Le choix adéquat de coordonnées linéarisantes permet de résoudre ce problème et la stabilité interne du système en boucle fermée est démontrée. Grâce au moment cinétique du dirigeable, une des fonctions de sortie est obtenue explicitement qui définit un système à minimum de phase.

Grâce à une approche fondée sur la technique des perturbations singulières, une solution pour la

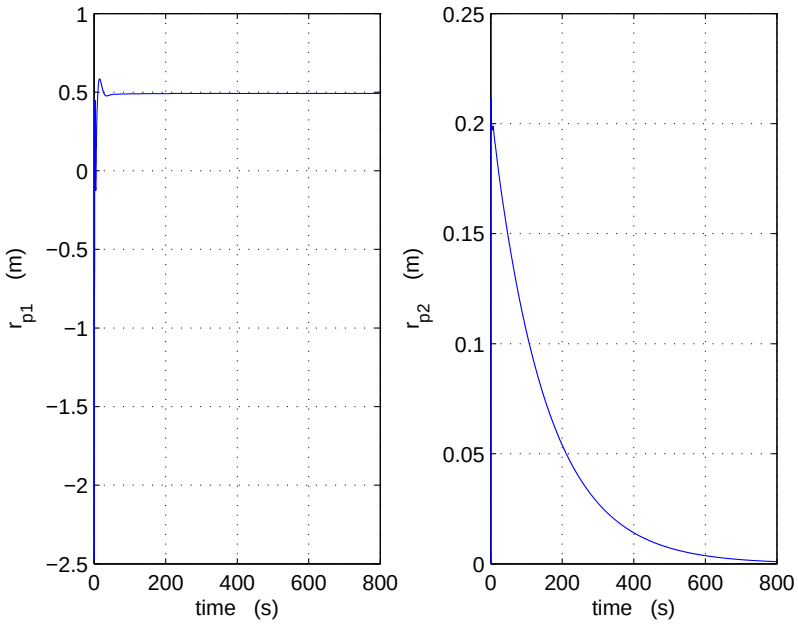

Figure 7.15: La translation de la masse mobile.

commande de l'attitude en trois dimensions a été calculée pour la première fois. Avec la commande proposée ici, non seulement l'angle de tangage (l'angle de la trajectoire de vol) peut être stabilisé, mais aussi la rotation stable peut être obtenue par la commande u_2. Avec ce système de contrôle d'attitude, un contrôle suivi de trajectoire peut être établi par la suite.

Le dirigeable propulsé par la force de flottabilité est un nouveau concept non-disponible sur le marché. Dans cette thèse, certaines questions préliminaires théoriques ont été considérées. Il existe encore de nombreuses questions ouvertes. Les principaux points qui méritent d'être résolus sont énumérés ci-après: (1) il est obligatoire d'examiner la robustesse de la commande sous les variations des paramètres etsous l'action des perturbations externes, (2) pour la faisabilité, un dirigeable hybride qui emploie la force de flottabilité et des propulseurs standard doit être considéré, (3) la navigation et la planification de la mission doivent être définies.

L'approche de modélisation, l'analyse dynamique et les solutions de commande données dans cette thèse sont pertinents pour des systèmes complexes similaires, tels que le planeur sous-marin et ou les véhicules de rentrée atmosphérique.

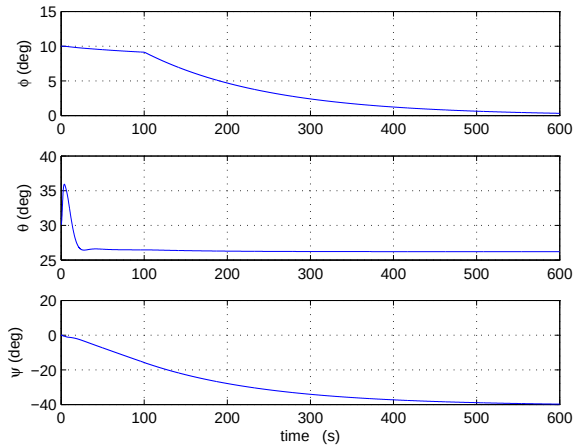

Figure 7.16: La dynamique des angles d'Euler en tournant cas.

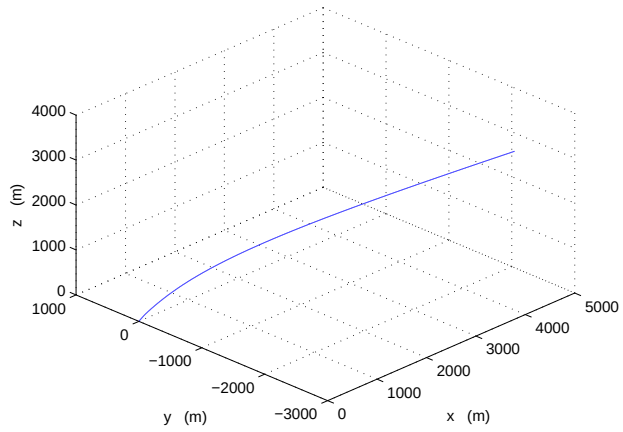

Figure 7.17: La trajectoire dans le cas d'une rotation.

Bibliography

Bowes, W. C. and Engelland, J. and Fernandez, F. L. and Fratarangelo, P. and Kohn, Jr. E. and Lister, R. and Neal, W. A. and Polmar, N. and Rumpf, R. L, and Smith, T. B. and NRAC, 2006. Lighter-than-air systems for future naval missions. Group study document, 110 pages.

Myasishchev Design Bureau, 2002. High-altitude m-55 geophysica aircraft. In: Investigators Handbook, Third edition. Myasishchev Design Bureau,Russia.

Abkowitz, M., 1975. Stability and motion control of ocean vehicles.

Aragón-Zavala, A., Cuevas-Ruíz, J. L., Delgado-Penin, J. A., 2008. High-Altitude Platformsfor Wireless Communications. John Wiley & Sons, West Sussex, UK.

Astolfi, A., Chhabra, D., Ortega, R., 2002. Asymptotic stabilization of some equilibria of an underactuated underwater vehicle. Systems & control letters 45 (3), 193–206.

Azouz, N., Bestaoui, Y., Lemaitre, O., November 2002. Dynamic analysis of airships with small deformations. In: The Proceedings of the Third International Workshop on Robot Motion and Control. Poznań, Polan, pp. 209–215.

Beji, L., Abichou, A., Bestaoui, Y., November 2002. Stabilization of a nonlinear underactuated autonomous airship-a combined averaging and backstepping approach. In: The Proceedings of the Third International Workshop on Robot Motion and Control. Poznań, Polan, pp. 223–229.

Beji, L., Abichou, A., Bestaoui, Y., 2004. Position and attitude control of an underactuated autonomous airship. International Journal of Differential Equations and Applications 8 (3), 231–255.

Bennaceur, S., 2009. Modélisation et commande d'engins volants flexibles. Ph.D. thesis, L'Université d'Evry Val d'Essonne, Evry, France.

Bhatta, P., 2006. Nonlinear stability and control of gliding vehicles. Ph.D. thesis, Princeton, US.

Bhatta, P., Leonard, N. E., 2008. Nonlinear gliding stability and control for vehicles with hydrodynamic forcing. Automatica 44 (5), 1240–1250.

Bhattacharyya, R., 1978. Dynamics of marine vehicles. Wiley.

Bloch, A. M., Krishnaprasad, P. S., Marsden, J. E., De Alvarez, G. S., 1992. Stabilization of rigid body dynamics by internal and external torques. Automatica 28 (4), 745–756.

Brennen, C., 1982. A review of added mass and fluid inertial forces. NASA STI/Recon Technical Report 82, 21535.

Cai, Z., Qu, W., Xi, Y., Wang, Y., 2007. Stabilization of an underactuated bottom-heavy airship via interconnection and damping assignment. International Journal of Robust and Nonlinear Control 17 (18), 1690–1715.

Calise, A., 1976. Singular perturbation methods for variational problems in aircraft flight. IEEE Transactions on Automatic Control 21 (3), 345–353.

Conte, G., Moog, C., Perdon, A., 2007. Algebraic methods for nonlinear control systems - theory and applications, 2nd Edition. Vol. 242 of Lecture Notes in Control and Information Sciences. Springer Verlag, New York, US.

Cook, M. V., 1990. The linearised small perturbation equations of motion for an airship. Working paper WP8 of Cranfield institute of technology.

Coron, J. M., 1999. On the stabilization of some nonlinear control systems: results, tools, and applications. Nonlinear Analysis, Differential Equations and Control, 307–367.

Davis, R., Eriksen, C., Jones, C., 2002. Autonomous buoyancy-driven underwater gliders. The Technology and Applications of Autonomous Underwater Vehicles, 37–58.

Defense Industry Daily, 2006. Lockheed wins $149.2m contract for high altitude airship (updated). http://www.defenseindustrydaily.com/lockheed-wins-1492m-\contract-for-hig

Diehl, W. S., 1922. Surface area coefficients for airship envelopes. Tech. rep., National Advisory Committee for Aeronautics.

Eichstedt, D., Morehead, J., Kalisz, J., 2001. Semi-buoyant vehicle with aerodynamic lift capability. US Patent 6,196,498.

Elfes, A., Bueno, S., Bergerman, M., Ramos, J., Gomes, S., 1998. Project aurora: development of an autonomous unmanned remote monitoring robotic airship. Journal of the Brazilian Computer Society 4, 70–78, sciELO Brasil.

Eriksen, C., Osse, T., Light, R., Wen, T., Lehman, T., Sabin, P., Ballard, J., Chiodi, A., 2001. Seaglider: A long-range autonomous underwater vehicle for oceanographic research. Oceanic Engineering, IEEE Journal of 26 (4), 424–436.

Fossen, T. I., 1994. Guidance and control of ocean vehicles. John Wiley & Sons Ltd., New York, US.

Friedrich, S., 1923. Rigid airships. Tech. rep., National Advisory Committee for Aeronautics.

Furlong, M. E., McPhail, S. D., Stevenson, P., 2007. A concept design for an ultra-long-range survey class auv. OCEANS Europe.

Gomes, S., Ramos Jr, J., May 1998. Airship dynamic modeling for autonomous operation. In: IEEE International Conference on Robotics and Automation. Leuven, Belgium, pp. 3462–3467.

Gomes, S. B. V., 1990. An investigation into the flight dynamics of airships with application to the yez-2a. Ph.D. thesis, Cranfield University, Bedfordshire, UK.

Goodyear Aerospace Corp., 1975. Contract NAS2-8643.

Grace, D., Mohorcic, M., Horwath, J., Capstick, M. H., Pallavicini, M. B., Fitch, M., November 2004. Communications from aerial platform networks delivering broadband for all - an overview of the capanina project. In: The proceeding of The International HAPS Workshop. Seoul, Korea.

Grace, D., Oodo, M., Mitchell, P., 2005. An Overview of the CAPANINA Project and its Proposed Radio Regulatory Strategy for Aerial Platforms. Communications 12 (5).

Haas, R., Dietzius, A., 1918. The stretching of the fabric and the deformation of the envelope in nonrigid balloons. Tech. rep., National Advisory Committee for Aeronautics.

Haifeng, W., Bifeng, S., Bin, L., Weigang, A., 2007. Exploring configuration design of high altitude airship. Journal northwestern polytechnical univerisity 25 (1), 56.

Healey, A., Lienard, D., 1993. Multivariable sliding mode control for autonomous diving and steering of unmanned underwater vehicles. Oceanic Engineering, IEEE Journal of 18 (3), 327–339.

Hima, S., 2005. Planification des trajectoires d'un dirigeable autonome. Ph.D. thesis, L'Université d'Evry Val d'Essonne, Evry, France.

Hopkins, J., 2010. Craft is lighter than air - and don't pollute it. http://www.nytimes.com/2010/07/20/business/global\/20iht-ravblimp.html.

Isidori, A., 1989. Nonlinear control systems: an introduction, 2nd Edition. Springer, New York, US.

Isidori, A., Moog, H. C., 1988. On the nonlinear equivalent of the notion of transmission zeros. Modelling and Adaptive Control, 146–158.

Jenkins, S., Humphreys, D., Sherman, J., Osse, J., Jones, C., Leonard, N., Graver, J., Bachmayer, R., Clem, T., Carroll, P., et al., 2003. Underwater glider system study. Tech. rep., Office of Naval Research, US.

Kanikdale, T., 2004. Optimization of airship envelope shape using computational fluid dynamics, . Master's thesis, Indian Institute of Technology, Department of Aerospace Engineering.

Khoury, G., Gillett, J., 1999. Airship technology. Cambridge university press.

Kim, J., Keller, J., Kumar, V., 2003. Design and verification of controllers for airships. In: The proceedings of the IEEE Intelligent Robots and Systems. Vol. 1. Las Vegas, US, pp. 54–60.

Knaupp, W., Mundschau, E., 2004. Solar electric energy supply at high altitude. Aerospace Science and Technology 8, 245–254.

Kulczycki, E. A., Johnson, J. R., Bayard, D. S., Elfes, A., Quadrelli, M. B., August 2008. On the development of parameterized linear analytical longitudinal airship models. In: AIAA Guidance, Navigation and Control Conference and Exhibit. Honolulu, US.

Lane, S., Stengel, R., 1988. Flight control design using non-linear inverse dynamics. Automatica 24 (4), 471–483.

Lavan, C., 2007. Inflatable endurance unmanned aerial vehicle. US Patent 7,306,187.

Leonard, N., 1997a. Stability of a bottom-heavy underwater vehicle. Automatica 33 (3), 331–346.

Leonard, N., 1997b. Stabilization of underwater vehicle dynamics with symmetry-breaking potentials. Systems & control letters 32 (1), 35–42.

Lewitt, E. H., 1922. The rigid airship. Sir Isaac Pitman and Sons Ltd.

Liao, L., Pasternak, I., 2009. A review of airship structural research and development. Progress in Aerospace Sciences 45 (4-5), 83–96.

Lindstrand, P., September 2000. Esa-hale airship research and development program. In: The proceeding of the 2nd Stratospheric Platform Systems Workshop. Tokyo, Japan, pp. 15–21.

Liu, y., 2009. Stratospheric autonomous airship: model, dynamics and control (in chinese). Ph.D. thesis, South China University of Technology, Guangzhou, China.

Lockheed Martin Corporation, 2008. High altitude airship information. available at http://www.lockheedmartin.com/products/HighAltitudeAirship/.

Lutz, T., Wagner, S., 1998. Drag reduction and shape optimization of airship bodies. Journal of Aircraft 35 (3), 345–351.

Marcy, W. L., 1978. Rigid airship concept for future naval operations. Journal of Aircraft 15 (5), 298–303.

Marino, R., 1986. On the largest feedback linearizable subsystem. Systems & Control Letters 6 (5), 345–351.

Morin, P., Samson, C., December 1995. Time-varying exponential stabilization of the attitude of a rigid spacecraft with two controls. In: Proceedings of the 34th IEEE Conference on Decision and Control. Vol. 4. New Orleans, US, pp. 3988–3993.

Mueller, J., Paluszek, M., Zhao, Y., September 2004. Development of an aerodynamic model and control law design for a high altitude airship. In: The proceeding of the AIAA Unmanned Unlimited Conference. No. AIAA-6479. Chicago, US.

Munk, M., 1923. The drag of zeppelin airships. Tech. rep., National Advisory Committee for Aeronautics.

Munk, M., July 1924. The aerodynamic forces on airship hulls. Tech. Rep. 106, National Advisory Committee for Aeronautics.

Munk, M. M., 1922. Notes on aerodynamic forces iii : the aerodynamic forces on airships. Tech. rep., National Advisory Committee for Aeronautics.

Naidu, D., Calise, A., 2001. Singular perturbations and time scales in guidance and control of aerospace systems: A survey. Journal of Guidance Control and Dynamics 24 (6), 1057–1078.

Northrop Grumman, 2010. Photo release – northrop grumman awarded $517 million agreement for u.s. army airship with unblinking eye. http://www.irconnect.com/noc/press/pages/news_releases.html?d=194252.

Ortega, R., Spong, M., Gómez-Estern, F., Blankenstein, G., 2002. Stabilization of a class of underactuated mechanical systems via interconnection and damping assignment. IEEE Transactions on Automatic Control 47 (8), 1218–1233.

Ouyang, J., 2003. Research on modeling and control of an unmanned airship (in chinese). Ph.D. thesis, Shanghai Jiaotong University, Shanghai, China.

Pettersen, K., Egeland, O., 1999. Time-varying exponential stabilization of the position and attitude of an underactuated autonomous underwater vehicle. IEEE Transactions on Automatic Control 44 (1), 112–115.

Pourzanjani, M. M. A., Roberts, G. N., 1991. Modelling and control of Marine craft. Elsevier, New York, US.

ProjetSol'R, 2010. http://www.projetsolr.com.

Purandare, R. Y., 2007. A buoyancy-propelled airship. Ph.D. thesis, New Mexico State University, Las Cruces, New Mexico, US.

Repoulias, F., Papadopoulos, E., 2008. Robotic airship trajectory tracking control using a backstepping methodology. In: The proceeding of the IEEE International Conference on Robotics and Automation. Pasadena, US, pp. 188–193.

Rizzo, F., 1924. A study of static stability of airships. Tech. rep., National Advisory Committee for Aeronautics.

Shapiro, A. D., 2010. Yellow submarine. IEEE Spectrum 47 (3), 36–41.

Shi, D., 1995. Operation of the Submarine (in chinese). National Defense Press, Beijing, China.

Slotine, J., Li, W., 1991. Applied nonlinear control. Prentice hall Englewood Cliffs, New Jersey.

Stommel, H., 1989. The slocum mission. Oceanography 2 (1), 22–25.

Subudhi, B., Morris, A. S., 2003. Singular perturbation approach to trajectory tracking of flexible robot with joint elasticity. International Journal of Systems Science 34 (3), 20.

Sun, X. D., Clarke, T., November 1994. Advanced aircraft flight control using nonlinear inverse dynamics. In: IEE Proceedings Control Theory and Applications. Vol. 141. pp. 418–426.

Thomasson, P., 2000. Equations of motion of a vehicle in a moving fluid. Journal of Aircraft 37 (4), 630–639.

Toglia, C., Vendittelli, M., 2010. Modeling and motion analysis of autonomous paragliders. Technical Reports of Department of Computer and System Sciences 2 (5).

Tozer, T., Grace, D., 2001. High-altitude platforms for wireless communications. IEE Electronics and communication engineering journal 13 (3), 127–137, iEEE.

US Navy, 2008. US Navy revives airship interest after 50-year gap. Flight international.

Vittek, J. F., 1975. In: Proceedings of the interagency workshop on lighter-than-air vehicles. MIT, Flight Transportation Laboratory.

Wang, Q., Stengel, R. F., 2005. Robust nonlinear flight control of a high-performance aircraft. IEEE Transactions on Control Systems Technology 13 (1), 15–26.

Widiawan, A. K., Tafazolli, R., 2006. High altitude platform station (HAPS): a review of new infrastructure development for future wireless communications. Wireless Personal Communications 42 (3), 387–404, issue entitled ”Advances in Wireless Communications: Enabling Technologies for 4G”.

Wie, B., 1998. Space vehicle dynamics and control. AIAA Education.

Wikipedia, 2010. Airship. available at http://en.wikipedia.org/wiki/Airship.

Wikipedia, 2011. Drag. available at http://en.wikipedia.org/wiki/Drag.

Woolsey, C. A., Leonard, N. E., 2002. Stabilizing underwater vehicle motion using internal rotors. Automatica 38 (12), 2053–2062.

Wu, X., Moog, C. H., Hu, Y., August 2009a. Modelling and linear control of a buoyancy-driven airship. In: Proceedings of the 7th Asian Control Conference. Hong Kong, China, pp. 75–80.

Wu, X., Moog, C. H., Marquez-Martinez, L., Hu, Y., December 2009b. Nonlinear control of a buoyancy-driven airship. In: Proceedings of the 48th IEEE Conference on Decision and Control. Shanghai, China, pp. 2849–2854.

Wu, X., Moog, C. H., Marquez-Martinez, L., Hu, Y., September 2010. Modeling and Control of a Complex Buoyancy-Driven Airship. In: Proceedings of the 8th IFAC Symposium on Nonlinear Control Systems. Bologna, Italy, pp. 1134–1139.

Wu, X., Moog, H. C., Hu, Y., 2011b. A Singular Perturbation Approach to Moving Mass Control of a Buoyancy-Driven Airship in Three Dimension, (submitted). Transactions of Nanjing University of Aeronautics and Astronautics.

Wu, X., Moog, H. C., Marquez-Martinez, L., Hu, Y., 2011a. Full Model of a Buoyancy-Driven Airship and Its Control in the Vertical Plane. Control Engineering Practice, (submitted).

Yokomaku, Y., September 2001. Current progress in the spf airship r&d program of japan. The proceeding of the 3rd Stratospheric Platform Systems Workshop, 15–19.

Zahm, A. F., 1926. Stability equations for airship hulls. Tech. rep., National Advisory Committee for Aeronautics.

Zaitsev, P., Formalskii, A., 2008. Autonomous longitudinal motion of a paraglider. Mathematical simulation, synthesis of control. Journal of Computer and Systems Sciences International 47 (5), 786–794.

APPENDICES

Appendix A

Appendix

The explicit expression of u in Eq. (4.45) is as follows:

$$u = -\frac{1}{\beta}\left(\lambda_2\xi_3^{(2)} + \lambda_1\xi_2^{(1)} + \lambda_0(\xi_1 - y_e) + \alpha\right)$$

where $\alpha = \alpha_1 + \alpha_2$ and $\beta = \beta_1 + \beta_2$, and they are computed as follows:

$$\phi_1^{(3)} = \alpha_1 + \beta_1 u$$

$$\alpha_1 = -g(-\cos\theta g \sin\theta m J - 2m\dot{r}_{p1}\sin\theta\dot{\theta}J - mr_{p3}\sin\theta\dot{\theta}^2 J)/(J + mr_{p1}^2)$$

$$\beta_1 = (\cos\theta J + \cos\theta m r_{p1}^2 + mr_{p1}\sin\theta r_{p3})/(J + mr_{p1}^2)$$

$$\phi_2^{(3)} = \alpha_2 + \beta_2 u$$

$$\alpha_2 = -(2\dot{\theta}^3\bar{m}^4 r_{p1}^8 + 2\bar{m}^3\dot{r}_{p1}^2 r_{p3}^4\dot{\theta}J + 4\bar{m}^2\dot{r}_{p1}^2 r_{p3}^2\dot{\theta}J^2 + \bar{m}g r_{p3}cos(\theta)\dot{\theta}J^3$$
$$+\bar{m}^3\dot{r}_{p1}gcos(\theta)r_{p3}^4 J + \bar{m}^3 g r_{p3}^5 cos(\theta)\dot{\theta}J + 2\bar{m}^2 g r_{p3}^3 cos(\theta)\dot{\theta}J^2$$
$$+\bar{m}\dot{r}_{p1}gJ^3 cos(\theta) - 3r_{p1}^7 gsin(\theta)\dot{\theta}\bar{m}^4 + 3r_{p1}^6\bar{m}^4\dot{\theta}g r_{p3}cos(\theta) - 3r_{p1}^6\bar{m}^4 gcos(\theta)\dot{r}_{p1}$$
$$+6r_{p1}^6\bar{m}^4\dot{\theta}^2 r_{p3}\dot{r}_{p1} - 6r_{p1}^5\bar{m}^4 gsin(\theta)\dot{\theta}r_{p3}^2 - 6r_{p1}^5\bar{m}^4 r_{p3}gsin(\theta)\dot{r}_{p1}$$
$$-9r_{p1}^5\bar{m}^3 gsin(\theta)\dot{\theta}J + 12r_{p1}^4\bar{m}^4\dot{r}_{p1}r_{p3}^3\dot{\theta}^2 + 2\bar{m}^2\dot{r}_{p1}gJ^2 cos(\theta)r_{p3}^2$$
$$+6r_{p1}^4\bar{m}^4\dot{\theta}r_{p3}^3 gcos(\theta) + 7r_{p1}^4\bar{m}^3 g r_{p3}cos(\theta)\dot{\theta}J - 10r_{p1}^4\bar{m}^3\dot{\theta}^2\dot{\theta}J + 12r_{p1}^4\bar{m}^3\dot{\theta}^3 r_{p3}^2 J$$
$$-5r_{p1}^4\bar{m}^3\dot{r}_{p1}gJcos(\theta) + 12r_{p1}^4\bar{m}^3\dot{\theta}r_{p3}\dot{\theta}^2 J - 3r_{p1}^3\bar{m}^4 gsin(\theta)\dot{\theta}r_{p3}^4 - 6r_{p1}^3\bar{m}^4 r_{p3}^3 gsin(\theta)\dot{\theta}$$
$$-12r_{p1}^3\bar{m}^3 gsin(\theta)\dot{\theta}r_{p3}^2 J - 12r_{p1}^3\bar{m}^3 r_{p3}gsin(\theta)\dot{\theta}J - 9r_{p1}^3\bar{m}^2 gJ^2 sin(\theta)\dot{\theta}$$
$$+3r_{p1}^2\bar{m}^4\dot{\theta}r_{p3}^5 gcos(\theta) + 6r_{p1}^2\bar{m}^4\dot{r}_{p1}r_{p3}^5\dot{\theta}^2 + 3r_{p1}^2\bar{m}^4\dot{r}_{p1}gcos(\theta)r_{p3}^4 - 4r_{p1}^2\bar{m}^3\dot{r}_{p1}^3 r_{p3}J$$
$$+12r_{p1}^2\bar{m}^3\dot{r}_{p1}r_{p3}^3\dot{\theta}^2 J + 4r_{p1}^2\bar{m}^3\dot{r}_{p1}^2 r_{p3}^2\dot{\theta}J + 2r_{p1}^2\bar{m}^3\dot{r}_{p1}gcos(\theta)r_{p3}^2 J + 6r_{p1}^2\bar{m}^3\dot{\theta}^3 r_{p3}^4 J$$
$$+8r_{p1}^2\bar{m}^3 g r_{p3}^3 cos(\theta)\dot{\theta}J - 2r_{p1}^2\bar{m}^2\dot{r}_{p1}^2\dot{\theta}J^2 + 6r_{p1}^2\bar{m}^2\dot{\theta}^3 r_{p3}^2 J^2 - r_{p1}^2\bar{m}^2\dot{r}_{p1}gJ^2 cos(\theta)$$
$$+5r_{p1}^2\bar{m}^2 g r_{p3}cos(\theta)\dot{\theta}J^2 + 6r_{p1}^2\bar{m}^2\dot{r}_{p1}r_{p3}\dot{\theta}^2 J^2 - 3r_{p1}\bar{m}^3 gsin(\theta)\dot{\theta}r_{p3}^4 J$$

$$
\begin{aligned}
&-6r_{p1}\bar{m}^2 r_{p3} g sin(\theta)\dot{r}_{p1}J^2 - 3r_{p1}\bar{m}gJ^3 sin(\theta)\dot{\theta} - 6r_{p1}\bar{m}^3 r_{p3}^3 g sin(\theta)\dot{r}_{p1}J \\
&+2\bar{m}^3 J\dot{r}_{p1}^3 r_{p3}^3 + 2\bar{m}^2\dot{r}_{p1}^3 r_{p3}J^2 + 2\bar{m}\dot{r}_{p1}^2\dot{\theta}J^3 + 6r_{p1}^2\bar{m}^4\dot{r}_{p1}^2 r_{p3}^4\dot{\theta} \\
&+6r_{p1}^6\bar{m}^4\dot{\theta}^3 r_{p3}^2 - 6r_{p1}^6\bar{m}^4\dot{r}_{p1}^2\dot{\theta} + 6r_{p1}^6\dot{\theta}^3 J\bar{m}^3 + 6r_{p1}^4\bar{m}^4\dot{\theta}^3 r_{p3}^4 \\
&-6r_{p1}^4\bar{m}^4\dot{r}_{p1}^3 r_{p3} + 6r_{p1}^4\dot{\theta}^3 J^2\bar{m}^2 + 2r_{p1}^2\bar{m}^4\dot{r}_{p1}^3 r_{p3}^3 + 2r_{p1}^2\bar{m}^4\dot{\theta}^3 r_{p3}^6 + 2r_{p1}^2\dot{\theta}^3 J^3\bar{m} \\
&-6r_{p1}\bar{m}^2 gJ^2 sin(\theta)\dot{\theta}r_{p3}^2)/(J^4 + 4J^3\bar{m}r_{p1}^2 + 6J^2\bar{m}^2 r_{p1}^4 \\
&+9J\bar{m}^3 r_{p1}^4 r_{p3}^2 + 3J^2\bar{m}^2 r_{p3}^4 + 6J\bar{m}^3 r_{p3}^4 r_{p1}^2 + \bar{m}^4 r_{p1}^8 + 3\bar{m}^4 r_{p1}^6 r_{p3}^2 + 3\bar{m}^4 r_{p1}^4 r_{p3}^4 \\
&+\bar{m}^3 r_{p3}^6 J + \bar{m}^4 r_{p3}^6 r_{p1}^2 + 9J^2\bar{m}^2 r_{p3}^2 r_{p1}^2 + 4J\bar{m}^3 r_{p1}^6 + 3J^3\bar{m}r_{p3}^2)
\end{aligned}
$$

$$
\begin{aligned}
\beta_2 = &(2r_{p1}\dot{\theta}J^3 + 6r_{p1}\bar{m}\dot{\theta}r_{p3}^2 J^2 + 2r_{p1}^7\dot{\theta}\bar{m}^3 + 2r_{p1}\bar{m}\dot{r}_{p1}r_{p3}J^2 + 6r_{p1}\bar{m}^2\dot{\theta}r_{p3}^4 J \\
&+4r_{p1}\bar{m}^2\dot{r}_{p1}r_{p3}^3 J + 2r_{p1}\bar{m}^3\dot{\theta}r_{p3}^6 + 2r_{p1}\bar{m}^3\dot{r}_{p1}r_{p1}^5 + 6r_{p1}^3\dot{\theta}J^2\bar{m} \\
&+6r_{p1}^5\bar{m}^3\dot{\theta}r_{p3}^2 + 2r_{p1}^5\bar{m}^3\dot{r}_{p1}r_{p3} + 6r_{p1}^5\dot{\theta}J\bar{m}^2 + 6r_{p1}^3\bar{m}^3\dot{\theta}r_{p3}^4 \\
&+4r_{p1}^3\bar{m}^3\dot{r}_{p1}r_{p3}^3 + 4r_{p1}^3\bar{m}^2\dot{r}_{p1}r_{p3}J + 12r_{p1}^3\bar{m}^2\dot{\theta}r_{p3}^2 J)/(J^4 + 4J^3\bar{m}r_{p1}^2 + 6J^2\bar{m}^2 r_{p1}^4 \\
&+9J\bar{m}^3 r_{p1}^4 r_{p3}^2 + 3J^2\bar{m}^2 r_{p3}^4 + 6J\bar{m}^3 r_{p3}^4 r_{p1}^2 + \bar{m}^4 r_{p1}^8 + 3\bar{m}^4 r_{p1}^6 r_{p3}^2 + 3\bar{m}^4 r_{p1}^4 r_{p3}^4 \\
&+\bar{m}^3 r_{p3}^6 J + \bar{m}^4 r_{p3}^6 r_{p1}^2 + 9J^2\bar{m}^2 r_{p3}^2 r_{p1}^2 + 4J\bar{m}^3 r_{p1}^6 + 3J^3\bar{m}r_{p3}^2)
\end{aligned}
$$

Appendix B

Publications

Journal Papers

X. WU, C. H. Moog, L.A. Marquez-Martinez and Y. Hu. Full Model of a Buoyancy-Driven Airship and Its Control in the Vertical Plane. *Control Engineering Practice. (under the third review)*

X. WU, C. H. Moog, and Y. Hu, A Singular Perturbation Approach to Moving Mass Control of a Buoyancy-Driven Airship in Three Dimension. *Transactions of Nanjing University of Aeronautics and Astronautics. (under review)*

Conference Papers

X. WU, C. H. Moog, Y. Hu. Modelling and linear control of a buoyancy-driven airship. *The Proceeding of 7th Asian Control Conf.*, Hong Kong, August 2009.

X. WU, C. H. Moog, L.A. Marquez-Martinez and Y. Hu. Nonlinear Control of a Buoyancy-Driven Airship. *The Proceeding of 48th IEEE Conf. on Decision and Control, Shanghai, December 2009.*

X. WU, C. H. Moog, L.A. Marquez-Martinez and Y. Hu. Modeling and Control of a Complex Buoyancy-Driven Airship, *The Proceeding of 8th IFAC Symposium on NonlinearControl Systems, Bologna, Italy, September 2010.*

附录 A　中文综述

本课题研究了一种新型的浮力驱动的飞艇，该飞艇利用可移动的质量块和变化的净浮力来驱动，从而取代了常规的利用螺旋桨和舵机的驱动方式。这种新型飞艇的可移动质量块用于改变这个系统的重心，从而改变飞艇的姿态；通过净浮力的改变，使得飞艇能够自如的上升和下降。两种控制的相互配合，来驱动飞艇做指定的运动。开发这种新型飞艇的动机就是为了获得一种更加节能的飞行机制，从而使得飞行器具有更长的滞空时间或更远的巡航距离。本论文首先通过牛顿-欧拉方法，推导出这种新型飞艇的八自由度数学模型。由于对飞艇机体和其可移动质量块之间相互关系的不同视角，本文介绍了两种不同的建模方法。对这种飞艇在纵向平面的运动，本文设计了几种不同的控制方法，分别有基于线性二次型调节器（LQR）的线性控制器、基于输入输出线性化的非线性控制器、以及基于最大精确反馈线性化的非线性控制器。前两种控制器都不同程度的存在一些缺陷，通过本文提出的基于最大精确反馈线性化得到的非线性控制器能够很好的达到控制目的。在推导这个非线性的控制器的过程中，分析、建模、和控制了多个逐步变复杂的飞艇子模型，直到最后把在部分简化了的模型上得到的结论推导并应用在飞艇完整的模型上。在这个过程当中，最简化的飞艇模型是一个具有二自由度的倒立摆系统。通过在简化了的系统上推导出的结论，最后都证明了通过适当的修正，这些结论可以适用于进一步变复杂、完整的模型。由于模型的复杂性，对于一完整的模型，这些特性或者结论往往很难被直接发现。文章的最后通过奇摄动理论提出了一种三维空间的运动控制方法。通过叠加在纵向面的运动控制和在侧向的运动控制，可以获得一个用于三维空间的控制结构，并且通过仿真显示控制效果是可以接受的。

A.1　绪论

尽管飞艇早已经不再作为交通工具运输旅客，但是它在一些新的领域却发挥着重要的作用，例如广告展示、观光旅游、高空平台、以及作为三维运动控制平台(Elfes et al., 1998; Tozer and Grace, 2001; Bowes et al., 2006)。世界上一些主要的大国都开展了这方面的研究，例如美国两大军

工巨头Northrop Grumman 和Lockheed Martin 各自独立的高空飞艇研究项目(Northrop Grumman, 2010；Defense Industry Daily, 2006; Lockheed Martin Corporation, 2008)、欧洲的ESA-HALE 高层平台项目、以及在中国的航天五院与上海交通大学联合的平流层飞艇项目。另外在巴西、日本、以及以色列都有类似的项目(Knaupp and Mundschau, 2004; Yokomaku, 2001)。

飞艇的上一个研究高峰期是在上世纪20到30年代。现代飞艇研究和以前的研究最为显著的一个区别就是现代飞艇研究多聚集在飞艇的无人自主控制方面。飞艇基于完全自主或者部分的远程遥控、反馈控制、以及自主的路标导航等技术，现代无人飞艇被期望能够自主的完成各种各样的任务。目前有很多研究就集中在如何解决这个过程中遇到的关于建模、控制、导航等方面的问题(Gomes and Ramos Jr, 1998; Ouyang, 2003; Purandare, 2007)。在这些研究中，大部分的研究对象都是常规飞艇，也就是利用螺旋桨和舵机驱动的飞艇。这种常规的无人飞艇最早是由Gomes提出并给出了这种飞艇的一般建模方法(Gomes and Ramos Jr, 1998)。现在的绝大多数无人飞艇的模型都是来源于此。

本论文考虑了一种新型的浮力驱动的飞艇，它是由一个内部可移动的质量块和可调节的净浮力驱动。研究这种新型飞艇的目的在于探索一种更为节能的飞行方式，从而使航行器具有更高的滞空时间或者更远的航行距离。到目前为止，对这种新型飞艇的研究文献仅有一篇博士论文(Purandare, 2007)。这也是本课题研究的挑战之一。在该论文中给出的新型飞艇概念图如图A.1所示。一些验证性的实验已经证明了这种新机制的飞艇，在利用阀门和充气机改变净浮力、飞艇的上升或下沉、前向的运动等方面都是可行的，但是这些技术还不成熟，需要进一步的探索(Purandare, 2007，12页)。在这篇先驱性的文献研究了这种新型飞艇的可行性、在二维纵向平面的模型以及PID控制。根据这篇文献的结论，与常规飞艇相比，这种新型飞艇在飞行攻角比较小的时候可以获得最大的效率。显而易见的是这种新型飞艇抗风扰动的能力不是很强，因此将常规的螺旋桨与这种新型的滑动机制相结合是一个十分有潜力的方向。

这篇论文主要研究了这种新型飞艇的一些理论性问题，实际的实验不在这篇论文的范围以内。这篇论文所做的一些创新通过很多的仿真来表现。总的来说，本论文主要做出了如下四个方面的贡献。这四个方面分别是：

- 本文推导了这种新型滑翔式飞艇的三维空间完整八自由度数学模型。在

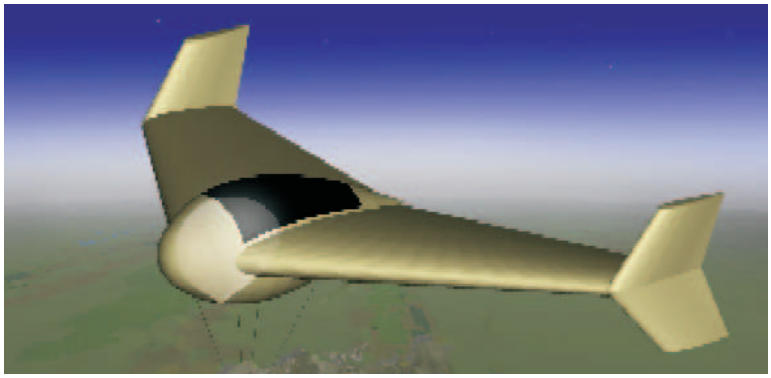

图 A.1: 浮力驱动的飞艇概念图来源 (Purandare, 2007)。

这个模型当中，飞艇的可移动质量块、可变化的净浮力都被考虑。为了简化建模，本文把这种飞艇看作由飞艇机体和可移动质量块组成的两个质点系统。依据看待这两个质点的不同视角，本文提供了两种建模思路。

- 飞艇完整的八自由度模型是十分复杂的，本文研究、分析、控制和仿真了这个复杂模型的一些基本结构，得到了很多对于了解这种新型飞艇结构、对设计完整模型控制器十分有意义的重要结论。经本文研究，该飞艇的基本结构如图A.2 所示：飞艇的姿态主要由可移动质量块的位置决定，而其位置是由系统的输入-机体对质量块的作用力-控制的。系统的航迹主要有飞艇的空气动力决定。并且空气动力在此起到　合姿态控制和航迹控制的重要作用。

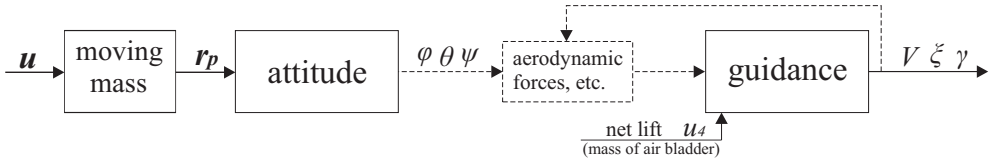

图 A.2: 飞艇模型的基本结构.

- 对于飞艇纵向平面的运动，本文设计了多种不同的控制器。推导和比较了分别基于LQR、输入输出反馈线性化、和最大精确反馈线性化的控制器。经过推导发现飞艇的模型并不能够进行完全的反馈线性化，本文推导了该模型的最大反馈线性化，并且计算了非线性控制器的解析解。这

些结论通常对于复杂的航行器模型来说是很难直接得到的。对于用部分反馈线性化设计非线性控制器，最大的挑战在于如何确保系统的内部动态的稳定性，也就是零动态的稳定性。这些问题在本文也得到了解决。

- 提出了一种基于奇摄动理论的三维空间运动控制框架。在这里，也利用正则摄动理论推导了飞艇在三维空间稳定螺旋上升或下降运动的近似解析稳态解。

需要注意的是，本文主要在无扰动环境下讨论该型飞艇的相关问题，一些环境的扰动，例如风、变化的空气密度和温度等等都将在后续的研究中继续解决。

本章的安排如下：A.2节具体介绍这种靠浮力驱动、以滑翔方式运动的新型飞艇的结构和运行机制。A.3节介绍通过把飞艇机体和可移动质量块看成两个质点的两种建模思路。A.4节介绍了针对纵向平面运动的几种控制方法，其中详细介绍了基于最大精确反馈线性化的控制器设计方法。A.5节提出了基于奇摄动理论的一种三维运动控制方法。最后A.6节总结了本章。

A.2 浮力驱动的飞艇的总体介绍

正如在前一节中所介绍的，浮力驱动的飞艇和常规飞艇的主要不同在于其用可移动的质量块和变化的净浮力驱动，取代常规的利用螺旋桨和舵机驱动的方式。这种新的驱动方式已经在水下滑翔器上得到验证，并且证明了其巨大的节能潜力。这一节详细介绍这种新型飞艇的结构、运动机制、以及它的效率问题。关于这一节的详细内容可以参考论文的第2章。

A.2.1 浮力驱动的飞艇的基本结构

浮力驱动的飞艇的基本结构见图A.3，该飞艇弃用了常规飞艇的推进器以及各种舵机。该飞艇主要由机体、翼、可移动的质量块、以及可以伸缩的内部空气囊组成。

飞艇增加的翼是为了增大滑翔运动过程中的空气动力。飞艇的机体是刚性的，也就是说其体积是不变的，从而飞艇的浮力是不变的。关于飞艇外形的选择，最重要的考虑是如果降低整个系统的阻力。对于飞艇的外形来说，阻力主要来自两个方面：一个是外形导致的阻力，另外一个是表面的摩擦阻力。为了

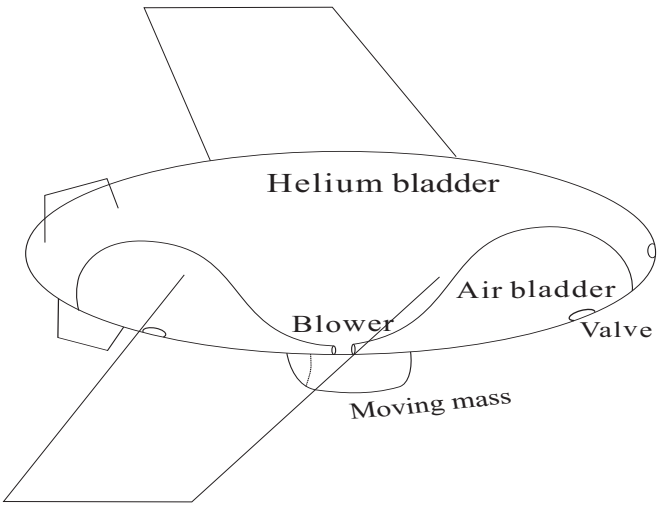

图 A.3: 浮力驱动的飞艇的结构。

降低这两个方面的阻力的总和，该飞艇的机体外形符合NACA0050型机翼轮廓线旋转而成的水滴型椭球体，如图A.4所示。

为了简化分析，以及空气动力等等并不是本文的研究的重点，在之后的内容中将用一个标准的椭球体来代替图A.4所示的不规则椭球体。

图A.5示意了该飞艇系统的充气/放气系统。通过对内部空气囊充入空气，就可以使得飞艇的质量增大，从而使得真个飞艇的净浮力减少。如果将空气囊里面的空气排出，真个系统的质量就减少，从而使得净浮力得到增加。该飞艇利用这种机制控制飞艇的净浮力，从而使得飞艇可以被控制上升或者下沉。

该飞艇在底部装配了一个可以在二维平面运动的质量块，见图A.6，该质量块可以用机载电源块或者是其他设备来充当。其运动是由机体上的电机来驱动的，这也是整个系统的控制之一。其运动的平面位于飞艇水平对称平面的下方，这是为了确保这个系统的重心位于飞艇的下部，从而确保航行器基本的稳定性。同时假设质量块运动是平行于机体系的$O-e_1$和$O-e_2$ 轴的。便随着质量块的运动，整个系统的重心也随之发生移动，这从而改变飞艇的姿态。用移动的质量块改变系统的姿态是一种很重要的机制，它也被用于一些返回式卫星或者弹道导弹的姿态控制，现在受到越来越多的关注。

A.2.2　飞艇的运行机制

总的来说，该新型飞艇主要作一种锯齿状循环滑行运动，如图A.7所示。

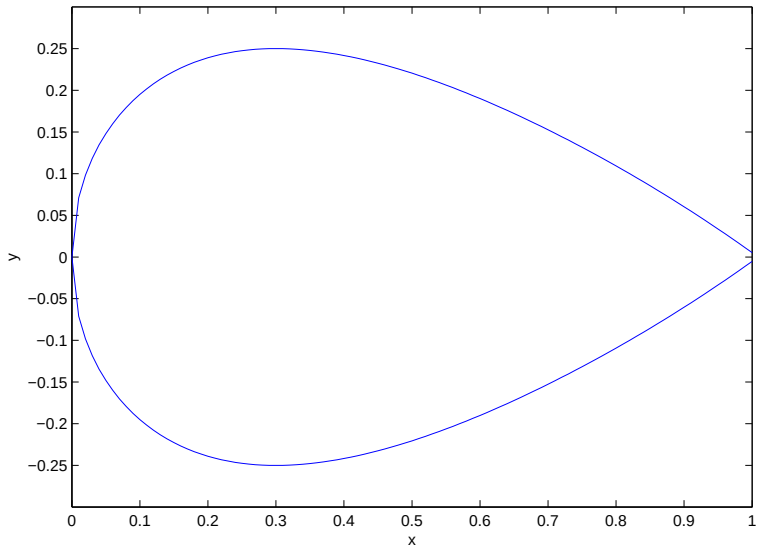

图 A.4: 由NACA0050机翼轮廓线旋转而成的机体外形。

其上升滑行是由如下操作来控制的：飞艇首先将空气从内部的气囊排出，这导致飞艇质量变小，净浮力变为正，从而使得飞艇上浮。同时伴随质量块向飞艇的尾部移动，改变其姿态，使得其具有正的俯仰角θ，这就导致飞艇的空气动力有一个前向的分力来驱动飞艇向前运动。上述两种控制相结合，如图A.8所示，就使得飞艇斜向前方滑行，例如图A.7的BC段。与之相应，如果飞艇向内部空气囊充气，使得净浮力变为负，飞艇下降。同时伴随质量块向头部运动，系统获得负的俯仰角，这时同样可以产生一个前向的空气动力分力来驱动飞艇向前运动，如图A.9所示。这段运动轨迹就如图A.7的AB段所示。

如果质量块沿横向运动，将导致飞艇滚转，由此可以产生一个使得飞艇转向的力矩，从而实现飞艇的转向。

A.2.3 系统的基本分析

通过一些基本的分析，可以得到关于该飞艇的一些重要的结论。首先分析可移动质量块与飞艇机体之间的关系。设想飞艇净浮力为零，其悬停在空中。此时只有质量块移动，这必将导致飞艇相应的顺时针或逆时针转动，如图A.10和A.11所示。最终飞艇稳定的状态必定是体积中心O、重心CG、以及当做质点的质量块三点位于铅垂线上。

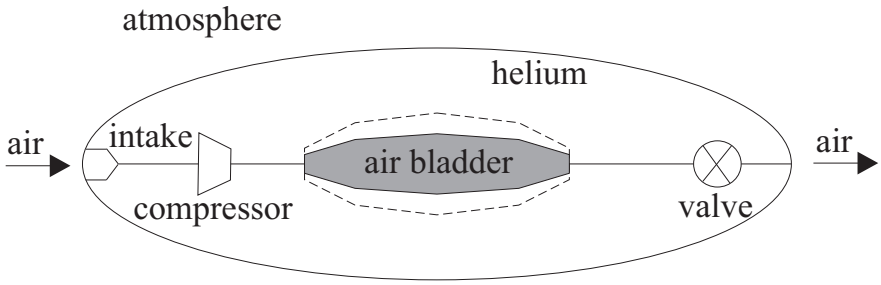

图 A.5: 飞艇的内部空气囊，以及充气/放气系统。

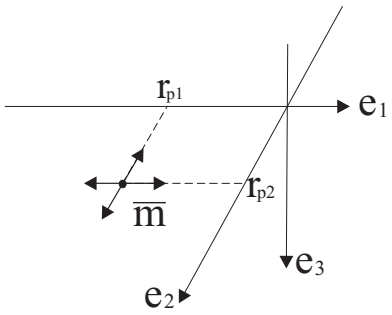

图 A.6: 质量块沿着平行于$O-e_1$和$O-e_2$ 轴的方向运动。

机体对质量块的驱动力用$\boldsymbol{u}$表示，质量块的位置用$\boldsymbol{r_p}$表示，系统的姿态用欧拉角ϕ、θ、及ψ表示。因此这上述的质量块与机体的之间的关系可以用图A.12表示。

上面的分析把飞艇看做由机体和可移动质量块组成的两个部分，在这里把飞艇看做一个整体，分析飞艇稳定上升和稳定下降阶段的受力情况，其结果如图A.13 和A.14所示。通过力的分解，以及稳态下合外力为零，可以推导出如果飞艇上升阶段和下降阶段的飞行轨迹角ξ是大小相等的话，那么这两个阶段净浮力也是大小相等，方向相反的，如式(A.1)所示。

$$W - B = \pm\sqrt{D^2 + L^2} \tag{A.1}$$

这里W表示系统的重力，B表示浮力，D 和L 是升力和阻力。

在平衡稳定的状态下，结合空气动力与速度的关系，结合(A.1)，可以推导出如下速度和净浮力之间的关系：

$$V^2 = \frac{B - W}{\frac{1}{2}\rho_a \nabla^{2/3}\sqrt{C_D^2 + C_L^2}} \tag{A.2}$$

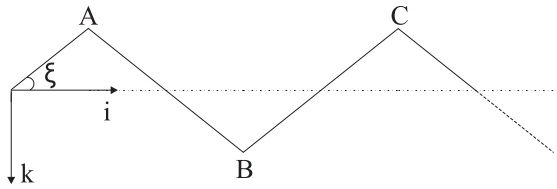

图 A.7: 浮力驱动的飞艇的典型运动轨迹。

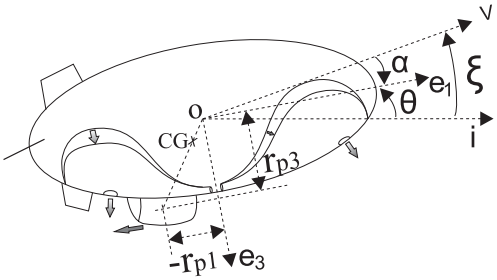

图 A.8: 飞艇斜向上滑行分析。

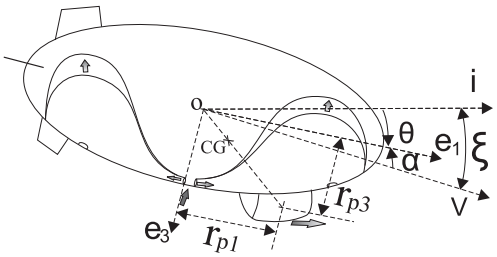

图 A.9: 艇斜向下滑行分析。

由此可以得出结论：该飞艇的飞行速度的大小是由净浮力决定的。对于给定的飞艇，更具体的来说，速度是由飞艇的内部空气囊的质量决定的，这也就是该系统的另外一个控制u_4。另外在稳态时，也可以推出飞行轨迹角ξ与空气动力的关系是：$\tan\xi = D/L$。由此飞艇的运动方向主要有空气动力决定。这些关系可以通过图A.15 来表示。这里把有关飞艇的速度，运动方向等问题称作导航(guidance)问题。

另外很显然空气动力一般由航行器的运动速度V，以及攻角α、侧滑角β决定。就角α来说，有关系$\alpha = \theta - \xi$。因此可以说空气动力是由飞行速度、欧拉角、以及飞行轨迹角等决定的，如图A.16所示。

综合上面的图A.12、A.15、以及A.16，飞艇的这个结构可以用图A.17来表示。图A.16也揭示了空气动力在整个系统中的重要作用，他起到　合姿态控制和导航控制的作用。从图上可以直接观察得到，如果系统没有空气动力，将导致系统的飞行速度和方向不可控。这一点将在后续的章节中被验证。

A.2.4　效率比较

这一小节将浮力驱动的飞艇与常规飞艇的驱动效率问题做一个对比，最后给出了一些比较有趣的结论。

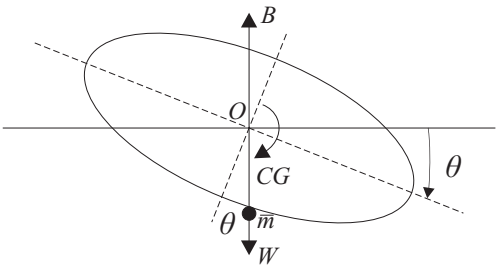

图 A.10: 机体的顺时针转动。

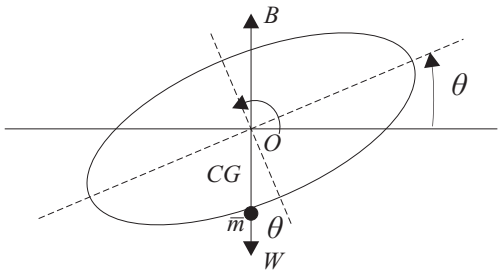

图 A.11: 机体的逆时针转动。

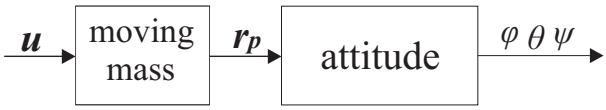

图 A.12: 飞艇姿态控制架构。

首先通过分析可以推出对于常规飞艇对单位质量所需的驱动功率为：

$$P_{CS} = \frac{P_C}{W} = \frac{\frac{1}{2}\rho_a C_{D0} \nabla^{2/3} u^3}{W} \tag{A.3}$$

注意这里的u表示飞艇的速度。从式A.3可以得知飞艇单位质量所需的驱动功率是和飞艇运动速度的立方成正比的。这也暗示飞艇只适合与低俗运动的应用。对于固定翼飞机来说，位质量所需的驱动功率是和飞机的运动速度成线性关系的。

对于浮力驱动的飞艇来说，它存在上升和下降两种模态。分别求出这两种模态下的所必须的驱动功率，然后做平均，得出浮力驱动的飞艇的单位质量所需的功率为：

$$P_{BS} = \frac{P_B}{W} = \frac{1}{2W}\rho_a \nabla^{2/3} u^3 \frac{C_D}{C_L}(1 + \frac{C_D^2}{C_L^2})\sqrt{C_D^2 + C_L^2} \tag{A.4}$$

下面比较浮力驱动的飞艇与常规飞艇的单位质量所需的功率，这个比值用r_{sp}来表示。结合式A.3和A.4, 这个比值为：

$$\begin{aligned} r_{sp} &= \frac{P_{BS}}{P_{CS}} = \frac{\frac{1}{2W}\rho_a \nabla^{2/3} u^3 \frac{C_D}{C_L}(1 + \frac{C_D^2}{C_L^2})\sqrt{C_D^2 + C_L^2}}{\frac{1}{2W}\rho_a C_{D0} \nabla^{2/3} u^3} \\ &= \frac{C_D}{C_{D0} C_L}(1 + \frac{C_D^2}{C_L^2})\sqrt{C_D^2 + C_L^2} \end{aligned} \tag{A.5}$$

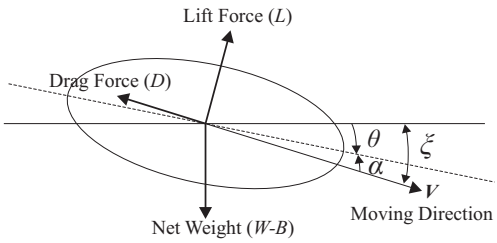

图 A.13: 下降阶段受力分析。

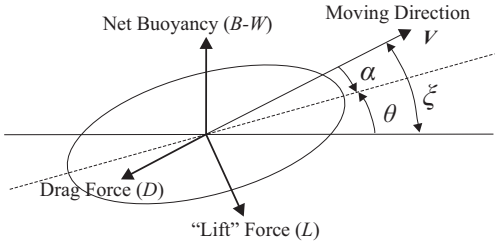

图 A.14: 上升阶段分析。

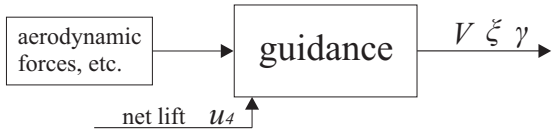

图 A.15: 飞艇的运动速度及方向控制架构。

这里

$$\begin{aligned} C_{D0} &= 0.0589 \\ C_D &= 0.0589 + 0.016\alpha^2 \\ C_L &= 1.269\alpha \end{aligned}$$

这里的空气动力系数来源于(Ouyang, 2003)。由此可见r_{sp}是攻角α的一个函数。图A.18给出了r_{sp}的值随α变化的情况。

由图A.18可见，r_{sp}的值没有小于1的情况，也就说对于单位质量所需的功率，常规飞艇要比浮力驱动的飞艇小。这便和浮力驱动机制所追求的节能相违背。而且实际上这样浮力驱动机制已经被试验证实具有更高的效率，例如在最近的一次水下滑翔机器人的实验中，其通过携带的电能完成了跨越大西洋的航行。实际上，如果考虑到两种驱动机制的有用功率，就可以发下浮力驱动的飞艇是可以比常规飞艇具备更高的节能型的。常规飞艇一般采用柴油机驱动螺旋桨的方式来推荐，柴油机的有用功率一般在30%左右。而靠浮力驱动的飞艇，其能量转化为有用功的效率相比可以高很多。因此，在新型飞艇处于合适的攻角飞行的时候，整个系统的能源有用功率要比常规飞艇的高很多，从而实现了更加节能的航行。

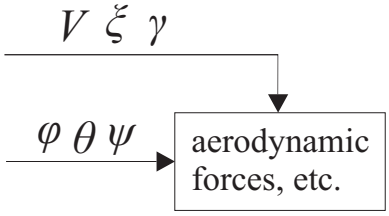

图 A.16: 空气动力由飞行速度、欧拉角、以及飞行轨迹角来决定。

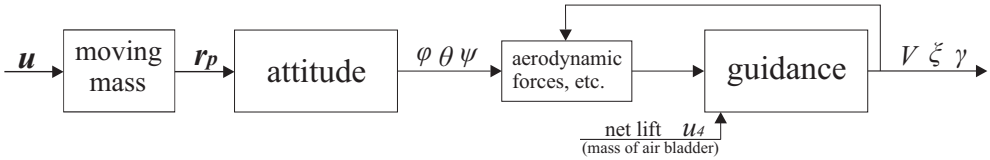

图 A.17: 飞艇的模型结构。

A.3　两种建模途径

相对于常规飞艇来说，浮力驱动的飞艇更加的复杂。如果选择不恰当的建模方法，将会导致建模过程十分的复杂，并且也很难利用得到的模型分析系统的特性。在这一节，创新性的将飞艇的刚性机体和可移动质量块看做为两个质点，整个飞艇系统就是由这两个质点组成的系统，由此建模得到了大大的简化。通过各种物理定理以及牛顿-欧拉方法推导了浮力驱动的飞艇的八自由度模型。这是第一次提出这种飞艇的完整模型，也是本研究的贡献之一。这个模型也是下文分析和控制设计的对象。关于这一节的详细内容可以参见论文的第3章，或者部分已发表的论文(Wu et al., 2009a, 2010)。

如上所述，如果将飞艇视作由机体质点和可移动质量块质点组成的系统，如图A.19所示。通过将这两个质点视作相互独立的个体，或者视为一个整体将得到两种不同的建模途径和两种不同的模型。这两种模型都有各自的长处以及不足。通常的建模方法就是把这两个系统看做一个整体来处理，这种方法的的长处就是产生的模型对于分析系统的稳定比较方便，不足之处就是建模过程复杂。如果把两个子系统独立看待，这将大大简化系统的建模，因为对机体的建模可以参考传统飞艇。其不足之处就是不便于对系统整体的分析。本文主要采用将两个子系统独立看待的建模方法。

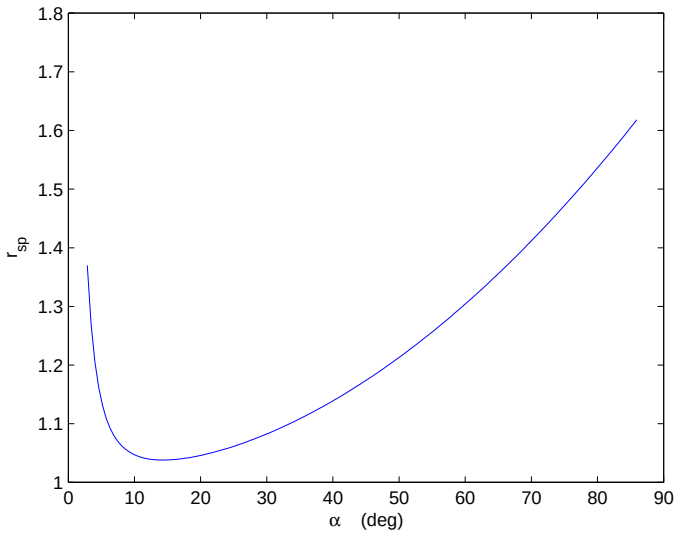

图 A.18: r_{sp}值随α变化的情况。

A.3.1 独立分析飞艇的刚性机体和可移动的质量块

如果独立的分析飞艇的刚性机体和可移动的质量块，那么飞艇的模型就由飞艇机体的动量、转动量、以及质量块的动量来定义。这三个量对应于惯性系和机体系分别用小写$\boldsymbol{p}$、$\boldsymbol{\pi}$、$\boldsymbol{p_p}$的和大写的$\boldsymbol{P}$、$\boldsymbol{\Pi}$、$\boldsymbol{P_p}$来表示。依据牛顿定律，在惯性系中刚性机体以及移动质量块所受的合外力为：

$$\begin{cases} \dot{\boldsymbol{\pi}} = \sum \boldsymbol{\tau_{ext}} - \boldsymbol{r_p} \times \left(\boldsymbol{R_1^T u}\right) \\ \dot{\boldsymbol{p}} = \sum \boldsymbol{f_{ext}} - \bar{m} g \boldsymbol{k} - \boldsymbol{R_1^T u} \\ \dot{\boldsymbol{p}}_{\boldsymbol{p}} = \bar{m} g \boldsymbol{k} + \boldsymbol{R_1^T u} \end{cases} \tag{A.6}$$

这里的$\boldsymbol{u}$ 代表机体对可移动质量块的作用力。

由惯性系和机体系之间的相互转换关系可以得到：

$$\begin{cases} \boldsymbol{\pi} = \boldsymbol{R_1 \Pi} + \boldsymbol{b} \times \boldsymbol{p} \\ \boldsymbol{p} = \boldsymbol{R_1 P} \\ \boldsymbol{p_p} = \boldsymbol{R_1 P_p} \end{cases} \tag{A.7}$$

求导(A.7)，可以得到:

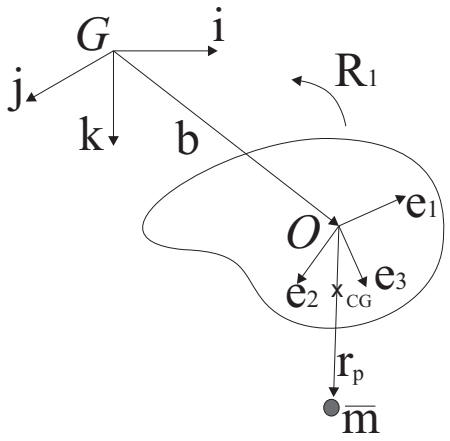

图 A.19: 把飞艇视作由体质点和可移动质量块质点组成的系统

$$\begin{cases} \dot{\boldsymbol{\pi}} = \boldsymbol{R_1}\left(\dot{\boldsymbol{\Pi}} + \boldsymbol{\Omega} \times \boldsymbol{\Pi}\right) + \boldsymbol{Rv} \times \boldsymbol{p} + \boldsymbol{b} \times \dot{\boldsymbol{p}} \\ \dot{\boldsymbol{p}} = \boldsymbol{R_1}\left(\dot{\boldsymbol{P}} + \boldsymbol{\Omega} \times \boldsymbol{P}\right) \\ \dot{\boldsymbol{p}}_{\boldsymbol{p}} = \boldsymbol{R_1}\left(\dot{\boldsymbol{P}}_{\boldsymbol{p}} + \boldsymbol{\Omega} \times \boldsymbol{P}_{\boldsymbol{p}}\right) \end{cases} \tag{A.8}$$

代入(A.6) 到(A.8)中, 就推导出飞艇在机体系中的运动方程:

$$\begin{cases} \dot{\boldsymbol{\Pi}} = \boldsymbol{\Pi} \times \boldsymbol{\Omega} + \boldsymbol{P} \times \boldsymbol{v} + \boldsymbol{R}^{\boldsymbol{T}} \sum \boldsymbol{\tau}_{\boldsymbol{ext}} - \boldsymbol{r}_{\boldsymbol{p}} \times \boldsymbol{u} \\ \dot{\boldsymbol{P}} = \boldsymbol{P} \times \boldsymbol{\Omega} + \boldsymbol{R}_{\boldsymbol{1}}^{\boldsymbol{T}} \sum \boldsymbol{f}_{\boldsymbol{ext}} - \bar{m} g \left(\boldsymbol{R}^{\boldsymbol{T}} \boldsymbol{k}\right) - \boldsymbol{u} \\ \dot{\boldsymbol{P}}_{\boldsymbol{p}} = \boldsymbol{P}_{\boldsymbol{p}} \times \boldsymbol{\Omega} + \bar{m} g \left(\boldsymbol{R}^{\boldsymbol{T}} \boldsymbol{k}\right) + \boldsymbol{u} \end{cases} \tag{A.9}$$

通过观察(A.9)中的$\dot{\boldsymbol{P}}$式和$\dot{\boldsymbol{P}}_{\boldsymbol{p}}$式，可以发现机体与质量块之间有大小相等，方向相反的作用力和反作用力$\bar{m} g \left(\boldsymbol{R}^{\boldsymbol{T}} \boldsymbol{k}\right) + \boldsymbol{u}$. 系统的控制-机体对质量块的作用力-对系统各部分的影响就很明显的呈现了出来，它取到联系机体和可移动质量块的作用。这也就是这种建模方法的优点，它很清晰的体现了系统不同部分之间的相互联系。

A.3.2　整体分析飞艇的刚性机体和可移动的质量块

如果把刚性机体和可移动质量块当做一个整体，那么机体对质量块的作用力就只是一个内力的。此时飞艇的运动方程由整个飞艇的动量、转动量、以及质量块的动量表示，这些量统一用一个上飘带来标注。只不过不同的是，这

里$\tilde{\boldsymbol{\pi}}$、$\tilde{\boldsymbol{\Pi}}$、$\tilde{\boldsymbol{p}}$、以及$\tilde{\boldsymbol{P}}$表示整个飞艇系统的相关量，包括机体和移动质量块。这里可移动质量块的动量是不变的。

在这种情况下，式(A.6)应修改为：

$$\begin{cases} \dot{\tilde{\boldsymbol{\pi}}} = \sum \boldsymbol{\tau_{ext}} + \boldsymbol{r_p} \times (\bar{m} g \boldsymbol{k}) \\ \dot{\tilde{\boldsymbol{p}}} = \sum \boldsymbol{f_{ext}} \\ \dot{\tilde{\boldsymbol{p}}}_{\boldsymbol{p}} = \bar{m} g \boldsymbol{k} + \boldsymbol{R}_1^{\boldsymbol{T}} \boldsymbol{u} \end{cases} \tag{A.10}$$

这里$\bar{m}g$ 和$\boldsymbol{u}$ 不再属于外力，因此没有出现在上式中。

结果类似的惯性系到机体系的转换，可得到运动方程为：

$$\begin{cases} \dot{\tilde{\boldsymbol{\Pi}}} = \tilde{\boldsymbol{\Pi}} \times \boldsymbol{\Omega} + \tilde{\boldsymbol{P}} \times \boldsymbol{v} + \boldsymbol{R}^{\boldsymbol{T}} \sum \boldsymbol{\tau_{ext}} + \boldsymbol{r_p} \times \left(\bar{m} g \boldsymbol{R}^{\boldsymbol{T}} \boldsymbol{k} \right) \\ \dot{\tilde{\boldsymbol{P}}} = \tilde{\boldsymbol{P}} \times \boldsymbol{\Omega} \\ \dot{\tilde{\boldsymbol{P}}}_{\boldsymbol{p}} = \tilde{\boldsymbol{P}}_{\boldsymbol{p}} \times \boldsymbol{\Omega} + \bar{m} g \left(\boldsymbol{R}^{\boldsymbol{T}} \boldsymbol{k} \right) + \boldsymbol{u} \end{cases} \tag{A.11}$$

注意到这里$\boldsymbol{u}$不再出现在$\dot{\tilde{\boldsymbol{\Pi}}}$ 和$\dot{\tilde{\boldsymbol{P}}}$中, 这反映出此时$\boldsymbol{u}$作为内力，它的变化不影响整体的动量或者转动量。

通过上面的分析，加深了对飞艇系统的了解，也使得建模问题变得明了和简单，例如在第一种建模方法中，对机体的建模就可以参考常规飞艇的建模。

A.3.3 系统的八自由度完整模型

飞艇的升降式是由内部空气馕的质量变化决定的。因此系统的另外一个控制u_4定位于控制飞艇的空气囊的质量。令$m_b = u_4$。$m_0 = m_h + \bar{m} + u_4 - m$,。因此在此之后，凡是包含$m_0$t地方都暗示包含一个输入。另外利用动量和转动量表示的系统方程不是很方便，最好将其转化为速度和转速度表示的系统模型。最后经过转化之后的八自由度完整模型为式(A.12)：

$$\begin{pmatrix} \dot{\boldsymbol{b}} \\ \dot{\boldsymbol{\eta}} \\ \dot{\boldsymbol{v}} \\ \dot{\boldsymbol{\Omega}} \\ \ddot{\boldsymbol{r}}_{\boldsymbol{p}} \end{pmatrix} = \begin{pmatrix} \boldsymbol{R_1 v} \\ \boldsymbol{R_3 \Omega} \\ \boldsymbol{M^{-1} \bar{F}} \\ \boldsymbol{J^{-1} \bar{K}} \\ \bar{\boldsymbol{T}} \end{pmatrix} \tag{A.12}$$

这里

$$\begin{aligned}\bar{\boldsymbol{K}} &= \boldsymbol{J\Omega}\times\boldsymbol{\Omega}+\boldsymbol{Mv}\times\boldsymbol{v}+\boldsymbol{M_{at}}-\boldsymbol{r_p}\times\boldsymbol{u}\\ \bar{\boldsymbol{F}} &= \boldsymbol{Mv}\times\boldsymbol{\Omega}+\boldsymbol{F_{at}}+(m_0-\bar{m})g\boldsymbol{R_1^T k}-\boldsymbol{u}\\ \bar{\boldsymbol{T}} &= -\dot{\boldsymbol{v}}-\dot{\boldsymbol{\Omega}}\times\boldsymbol{r_p}-\boldsymbol{\Omega}\times\dot{\boldsymbol{r}}_{\boldsymbol{p}}+g(\boldsymbol{R_1^T k})+\boldsymbol{v_p}\times\boldsymbol{\Omega}+\boldsymbol{u}/\bar{m}.\end{aligned}$$

A.4　纵向平面的运动控制

对于大多数航行器的分析来说，一般都采取把模型分解到几个平面上单独分析。纵向平面的运动对大多数航行器来说，都是最为基础也最为重要的运动。但是对于浮力驱动的飞艇来说，即使是把模型限制在一个平面，它的模型还是很复杂。本论文对纵向平面的模型做了多种开环仿真，来验证模型的有效性。这些开环分析的详细情况见本论文的第4章。对于航行器非线性模型的控制问题，常见的方法就是采取把模型在一个平衡态附件线性化，然后对线性系统设计一个线性控制器，最后把这个得到的线性控制器用于原非线性系统。这也就是本节第一种基于LQR的控制器的设计方法。但是这种控制器显而易见的缺陷就是它的有效范围受到很大的制约。因此寻求一个非线性控制器是很有必要的。之后本节探索了一种基于输入输出反馈线性化的非线性控制器，

现代非线性控制理论一个主要的成就就是反馈线性化理论的建立(Isidori, 1989; Conte et al., 2007)，但是这种方法的困难在于，当系统不能完全精确反馈线性化的时候，有时很难确保系统的零动态的稳定性(Isidori and Moog, 1988)。非常不幸的是本文研究的飞艇就是这样的一个系统，它不能被完全反馈线性化。本节推导的第二种基于简单的输入输出反馈线性化得到的非线性控制器，就因为其零动态是临界稳定，导致控制后的系统存在稳定的振动。因此实现最大的精确反馈线性化，并且证明系统的零动态是渐进稳定是寻找合适的非线性控制的主要挑战。这个难题在本论文中通过分析一些简化的系统，得到了很好的解决。这也是本文的主要贡献之一。本节的相关内容发布在(Wu et al., 2009a,b, 2010, 2011a)上。

A.4.1　纵向平面的模型

为了研究纵向平面的动态性能，就要把完整模型(A.12) 限制在e_1-e_2 平面，也就是说只保留完整模型中在纵向平面上的自由度，例如：θ, Ω_2, v_1, v_3, 和r_{p1}。因此纵向平面的模型为:

$$\begin{cases} \dot{\theta} & = \Omega_2 \\ \dot{\Omega}_2 & = \frac{1}{J_2}(M_a + r_{p1}u_3 - r_{p3}u_1) \\ \dot{v}_1 & = \frac{1}{m_1}\left((\bar{m} - m_0)\, g \sin\theta - m_3 v_3 \Omega_2 + F_{a1} - u_1\right) \\ \dot{v}_3 & = \frac{1}{m_3}\left((m_0 - \bar{m}) g \cos\theta + m_1 v_1 \Omega_2 + F_{a3} - u_3\right) \\ \ddot{r}_{p1} & = -\dot{v}_1 - \dot{\Omega}_2 r_{p3} - (v_3 - \Omega_2 r_{p1})\Omega_2 - g\sin\theta + u_1/\bar{m} \end{cases} \tag{A.13}$$

注意这里的u_3不是一个控制，而是一个确定的关系式。纵向平面的平衡态的解析解在第4章有详细介绍。

A.4.2 基于LQR的控制

LQR是优化控制里面一个非常重要和经典的理论。LQR理论为控制问题提供非常实用的反馈增益。它假设所有的状态$\boldsymbol{x}$ 都是可直接获得的。假设成本方程设为：

$$J = \int_0^\infty \left(\boldsymbol{x}^{\boldsymbol{T}} Q \boldsymbol{x} + \boldsymbol{u}^{\boldsymbol{T}} R \boldsymbol{u}\right) dt$$

这里权重矩阵Q 和R 都是调节参数，没有统一的方法来确定它们的值。它们的值由每个状态的权重以及用户的选择来决定。令上述成本方程具有最小值的反馈控制为：

$$\boldsymbol{u} = -K(\boldsymbol{x} - \boldsymbol{x_e}) \tag{A.14}$$

这里的K 是一个黎卡迪方程的解，其可以借助MATLAB®求解。

图A.20显示了利用线性控制器(A.14)来跟踪一条指定轨迹的仿真过程。

但是基于众所周知的原因，由于线性化的近似处理，使得LQR线性控制器的有效范围很有限，一般来说它只在平衡态附近一个有限的局域里面有效。例如对于上述的反馈，当在速度v_1 上的扰动大于+4.5 m/s的时候，控制器就失效，飞艇有坠毁的可能性。

A.4.3 基于输入输出反馈线性化并确保内部动态稳定的非线性控制

反馈线性化理论的建立(Isidori, 1989; Conte et al., 2007)是现代非线性控制理论一个主要的成就，但是当一个系统不能完全精确反馈线性化的时候，有时就很难确保系统的零动态的稳定性(Isidori and Moog, 1988)，这是应用这种方法设计非线性控制器的一个主要困难所在。本文研究的飞艇就是这样的一个系

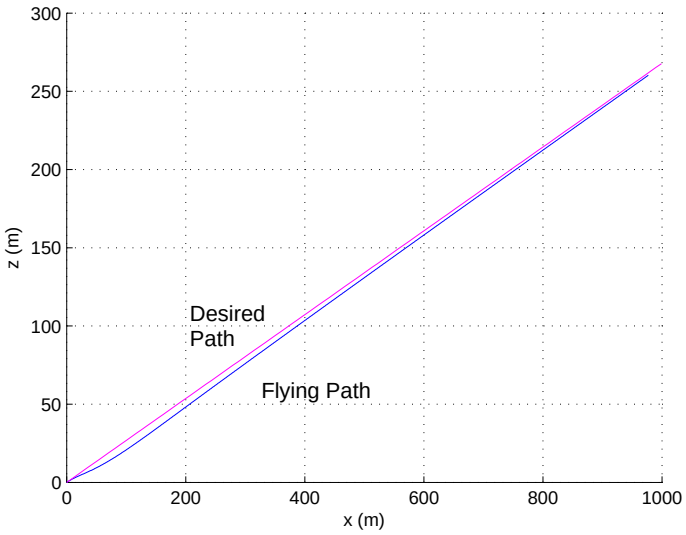

图 A.20: The airship with linear control tracks a commanded flight path.

统，它不能被完全反馈线性化。本文所做的一个重要贡献就是在此种情况下，通过合理的选择新的状态，证明了这个系统不能线性化的内部动态的渐进稳定。详细的过程可以参考论文的相关章节。

这里首先做一个合适的假设，那就是飞艇上升和下降滑翔过程中，飞艇仅改变质量块的位置，来应付此过程中的扰动，飞艇的净浮力保持不变。因此在此过程中m_b, m_0, 和u_4都是恒定的。当飞艇在上升和下降之间跳变的时候，内部空气囊的质量，也就是净浮力服从一个开环的bang-bang 控制。由此这里只考虑作用于可移动质量块的作用力u_1一个控制。

如果考虑系统的输出$y = x$，则当状态x为θ 或r_{p1}时，输出y具有2阶的相对阶。但是非常容易的发现当输出$y = r_{p1}$ 时，系统不是最小相位的，只有当$y = \theta$时，系统才是最小相位的。因此选择输出$y = \theta$做输入输出反馈线性化。由于$y = \theta$的相对阶是2，因此定义如下的误差方程：

$$\ddot{e} + \lambda_1 \dot{e} + \lambda_0 e = w_1$$

这里$e = y - \theta_e$，θ_e 是状态θ 的期望值，并且w_1 表示一个新的控制。相应的可以得到：

$$\ddot{\theta} + \lambda_1 \dot{\theta} + \lambda_0(\theta - \theta_e) = w_1 \tag{A.15}$$

参数λ_1 和λ_0 的值可以使误差方程不同的极点分布。代入(A.13) 到(A.15)中，可以求出控制u_1 的解。

从第4章给出的仿真结果来看，利用这种控制器的系统存在稳定的振动。究其原因，就是因为系统具有输出$y = \theta$时，系统具有临界稳定的内部动态性能。具体分析可以见第4章。

A.4.4 基于最大反馈线性化的非线性控制

由于模型(A.13)相对比较复杂，因此比较困难找到具有较高相对阶的输出。但是通过对一些简化的模型的分析，可以获得对飞艇模型更深入的了解，以及对控制器设计很重要的线索。首先分析飞艇在纵向平面的动态主要受到如下4种影响：

- 可移动质量块控制俯仰角θ，
- 净浮力$m_0 g$ 控制飞艇的上升或者下沉，
- 用m_{ii}表示的惯性力，
- 空气动力$\boldsymbol{F_a}$ 及力矩$\boldsymbol{M_a}$.

这里分析问题的思路是：首先通过假设上述的4种影响中的三种暂时不存在，只保留可移动的质量块来控制系统的俯仰角θ。这样就得到了纵向平面上复杂模型最为简化的一种情况。在这种情况下飞艇类似于一个变形的倒立摆，如图A.21所示。这种倒立摆是控制理论教学里面的经典模型(Wie, 1998)。这个简单的二自由度结构就是飞艇模型最为核心和基础的结构。通过对这个二自由度简化模型的建模和分析，可以发现系统相对于重心CG的转动惯量具有最高为3的相对阶。这个简化的系统是4维的，另外一个未被线性化的状态也被证明是渐进稳定的。

分析的第二步是减弱第一步的假设，也就是设想飞艇的净浮力不为零，同时飞艇可以在平面自由运动。但是仍然假设系统没有惯性力，也没有空气动

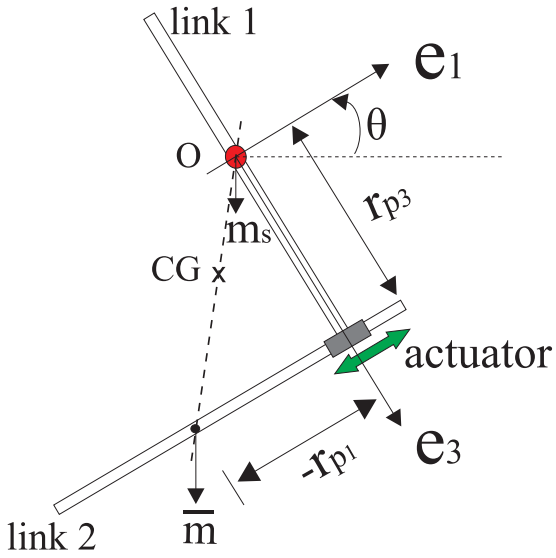

图 A.21: 飞艇简化的模型如同一个倒立摆。

力。这种情况下飞艇的模型比第一步变复杂了，也接近了完整模型。在这种情况下，经验证发现系统相对于重心CG的转动惯量仍具有最高为3的相对阶。但此时的系统具有6维。但是由于不存在空气动力，飞艇重心的运动不可控。对系统来说，也就是存在二维不可控状态。另外还存在一维的内部动态，通过类似第一步中的方法，该一维的内部动态被证明是稳定的。

第三步是进一步放宽假设，令系统具有惯性力，但仍不具有空气动力。这种情况下的模型也就越接近完全模型。建立这种情况下的飞艇模型，计算相对于重心CG的转动惯量，并验证其相对阶。这种情况绕重心CG的转动惯量不严格具有3的相对阶，但是通过分析发现，通过适当的近似处理，该转动惯量仍具有3的相对及。这种情况下的其他特性和前一种情况基本一样。

最后一步就是放弃所有的假设，飞艇受到空气动力的影响。这时就是飞艇在纵向面的完整模型。在第三种情况下推导的所有结论都可以直接应用现在的完整模型。同时由于具有了空气动力的影响，系统所有的自由度都受控，不再具有不可控的状态。通过仿真，显示出利用最大反馈线性化得到的非线性控制器具有很好的控制效果。

由上面的分析可以看出，在这个控制器的设计过程中，绕重心CG的转动惯量具有相当重要的作用。对于纵向面的完整模型来说，其绕心CG的转动惯量Π_1可计算为：

$$\Pi_1 = J_2\dot{\theta} + \frac{\bar{m}m_1}{\bar{m}+m_1}\left(\frac{m_3(m_1+\bar{m})}{m_1(m_3+\bar{m})}r_{p1}^2\dot{\theta} + r_{p3}^2\dot{\theta} + r_{p3}\dot{r}_{p1}\right).$$

同时存在一个Π_1的积分形式Π_2也具有3的相对阶。存在一个适当的函数ϱ，使得下面两个式子成立：

$$\dot{\Pi}_2 = \varrho\Pi_1, \quad \varrho > 0$$

$$\Pi_2 = \theta + \frac{r_{p3}}{\sqrt{\frac{m_3(m_1+\bar{m})}{m_1(m_3+\bar{m})}}\sqrt{\frac{\bar{m}+m_1}{\bar{m}m_1}J + r_{p3}^2}}\arctan\frac{\sqrt{\frac{m_3(m_1+\bar{m})}{m_1(m_3+\bar{m})}}r_{p1}}{\sqrt{\frac{\bar{m}+m_1}{\bar{m}m_1}J + r_{p3}^2}}$$

所有Π_1 和Π_2 的组合都具有3的相对阶。通过这些组合，可以把原模型(A.13)转换为一个具有3维零动态的线性的3维可控系统(Marino, 1986)。本文通过一个证明了的定理确保了具有输出$y = \Pi_1 + k\Pi_2$的系统是最小相位的，也就说其零动态是渐进稳定的。这个定理是：

定理(Wu et al., 2010): 有输出为$y = \Pi_1 + k\Pi_2$ 的系统，在满足$k > 0$时，具有渐进稳定的零动态。

这里对于任何一种简化的情况，用于推导反馈控制的误差方程都类似于：

$$y^{(3)} + \lambda_2 y^{(2)} + \lambda_1 y^{(1)} + \lambda_0(y - y_e) = 0 \tag{A.16}$$

解出A.16中$y^{(3)}$所包含的控制u_1,就得到了所需的非线性反馈，一般来说这个求解过程比较简单，但是计算数据量比较大，通常需要计算机代数软件辅助计算。这里的参数λ_2、λ_1、和λ_0的值的选择将影响系统零动态的速度。

A.4.5 仿真结果

利用上面推导的基于最大反馈线性化得到的非线性控制器来控制飞艇实现一个典型的连续飞行，如图A.7。其仿真结果由图A.22到A.25 给出。这个仿真的目的在显示这种非线性控制可以平稳的渡过轨迹的转折点。更多的仿真和更详细的分析见第4章。

图A.25显示了飞艇的飞行轨迹, θ、r_{p1}、v_1、and v_3 的动态变化由图A.22和A.23展示。图A.24反应了输出作用力的变化情况。

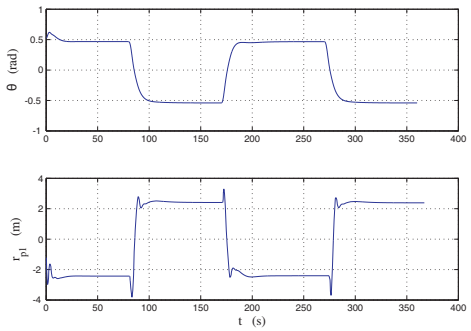

图 A.22: θ 和r_{p1} 的动态.

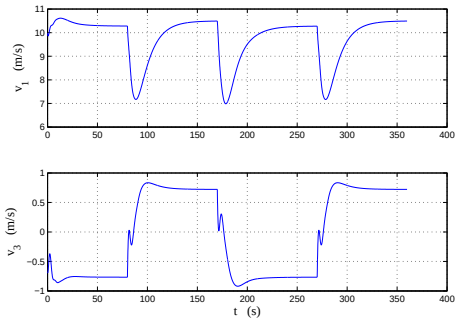

图 A.23: v_1 和v_3 的动态.

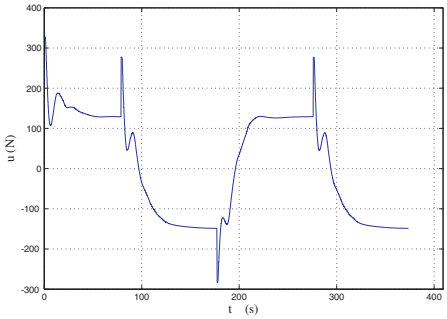

图 A.24: 输入u的动态.

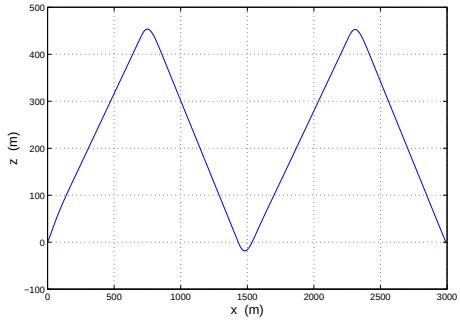

图 A.25: 两个循环的飞行轨迹.

A.5　三维空间的运动控制

在三维空间，飞艇存在一种稳定的螺旋上升或者下降运动，在论文的第5章详细的介绍了利用正则摄动法近似求解这种稳态运动的解析解。这个近似求解结果表面，如果当飞艇转动的角度比较小的时候，飞艇在纵向面的运动和在侧向的运动相互互不干扰，可以相互解　。这部分内容参考论文的第5章。在这一节中，首先推导飞艇在侧向的运动方程。由于飞艇在侧向具有和纵向类似的控制结构，因此可以参考纵向面控制器的设计方法对侧向平面的动态设计非线性控制器。借助奇摄动的方法，把飞艇在纵向和侧向的控制相叠加，从而获得一个三维空间运动的控制架构。最后给出了利用这种控制架构来控制飞艇

跟踪指定的姿态、运动方向、和速度的仿真结果。这一节的螺旋运动分析、以及基于奇摄动理论的三维运动控制架构是本文的创新之一，其部分结果发表在(Wu et al., 2011a)。

A.5.1 侧向运动控制

飞艇在侧向的结构可以如图A.26所示。侧向的自由度包括：滚转角ϕ、角速度Ω_1、速度v_2和v_3、以及质量块的在侧向的位置r_{p2}和速度$\dot{r}_{p2}$。飞艇在侧向面的运动模型如下：

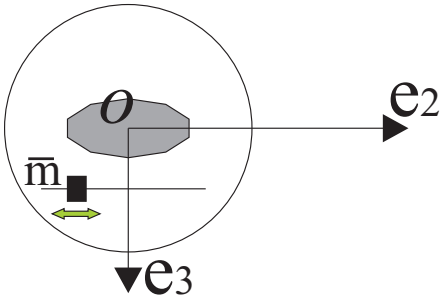

图 A.26: 飞艇的侧向结构。

$$\begin{cases} \dot{\phi} & = \Omega_1 \\ \dot{\Omega}_1 & = \frac{1}{J_1}\left(L_a - r_{p2}u_3 + r_{p3}u_2\right) \\ \dot{v}_2 & = \frac{1}{m_2}\left((m_0-\bar{m})\,g\sin\phi + m_3 v_3\Omega_1 + F_{a2} - u_2\right) \\ \dot{v}_3 & = \frac{1}{m_3}\left((m_0-\bar{m})g\cos\phi - m_2 v_2\Omega_1 + F_{a3} - u_3\right) \\ \ddot{r}_{p2} & = -\dot{v}_2 + \dot{\Omega}_1 r_{p3} + (v_3 + \Omega_1 r_{p2})\Omega_2 + g\sin\phi + u_2/\bar{m} \\ \dot{m}_0 & = u_4 \end{cases} \tag{A.17}$$

注意这里u_3 不是控制，而是一个确定的量。

由于飞艇的结构在纵向和在侧向具有类似性，它们之间仅是参数有所不同，所以前一节关于纵向运动的分析方法都适用于侧向运动模型。所以类似的直接求取侧向平面的关于重心的转动惯量为：

$$\Xi_1 = J_1\dot{\phi} + \frac{mm_3}{m+m_3}r_{p2}^2\dot{\phi} - \frac{mm_2}{m+m_2}(r_{p3}\dot{r}_{p2} - r_{p3}^2\dot{\phi})$$

同样这里也存在一个Ξ_1的积分形式Ξ_2 和一个适当的$\varrho^{'}$，有如下关系：

$$\dot{\Xi}_2 = \varrho^{'}\Xi_1, \quad \varrho^{'} > 0$$

$$\Xi_2 = \phi - \frac{r_{p3}}{\sqrt{\frac{J_1(m_2+\bar{m})}{m_2\bar{m}} + r_{p3}^2}\sqrt{\frac{m_3(m_2+\bar{m})}{m_2(m_3+\bar{m})}}} \arctan \frac{r_{p2}\sqrt{\frac{m_3(m_2+\bar{m})}{m_2(\bar{m}+m_3)}}}{\sqrt{\frac{J_1(m2+\bar{m})}{m_2\bar{m}} + r_{p3}^2}}$$

Ξ_1 和Ξ_2都具有3的相对阶。通过相同的方法可以证明对于具有输出为$y^{'} = \Xi_1 + k\Xi_2$ 的系统，当$k > 0$时，其有渐进稳定的零动态。依照式(A.16)，定义对于侧向运动的误差方程为：

$$y^{'(3)} + \lambda_2^{'}y^{'(2)} + \lambda_1^{'}y^{'(1)} + \lambda_0^{'}(y^{'} - y_e^{'}) = 0 \tag{A.18}$$

由方程A.18得到的控制器u_2可以稳定飞艇的航迹角γ 以及在侧向的速度。$\lambda_2^{'}$、$\lambda_1^{'}$、和$\lambda_0^{'}$是控制器的参数。

A.5.2　三维运动的控制架构

需要注意的是这里适用的奇摄动方法不同于用于其对一般航空器的标准方法，通常航空器控制问题被分割为姿态控制和导航控制两个方面(Naidu and Calise, 2001; Subudhi and Morris, 2003)。这里利用奇摄动方法作为一个工具来叠加纵向和侧向的两个控制环路。并且假定纵向的动态慢于侧向的动态。这是利用设定控制器的参数来实现的。

纵向控制器u_1 是由λ_2, λ_1, 和λ_0 等参数调节的; 侧向控制器u_2 是由参数$\lambda_2^{'}$, $\lambda_1^{'}$, 和$\lambda_0^{'}$来调节的。因此通过设定$\lambda_2 = 3$, $\lambda_1 = 3$, $\lambda_0 = 1$, $\lambda_2^{'} = 300$, $\lambda_1^{'} = 300$, 和$\lambda_0^{'} = 1000$来确保侧向的动态快于纵向的动态。利用奇摄动叠加这两个控制环的三维空间运动控制框架如图A.27所示。

A.5.3　三维运动控制仿真

图A.28 - A.31给出了基于奇摄动的三维控制器的控制效果。

图A.28 显示了当欧拉角有初始误差时的稳定过程。在这个仿真中，俯仰角θ 的指令时26度，并且滚转角ϕ是期望为零的。在有初始误差的情况下，三个欧拉角都渐进稳定。图A.29 显示了在这个过程中质量块的运动情况。

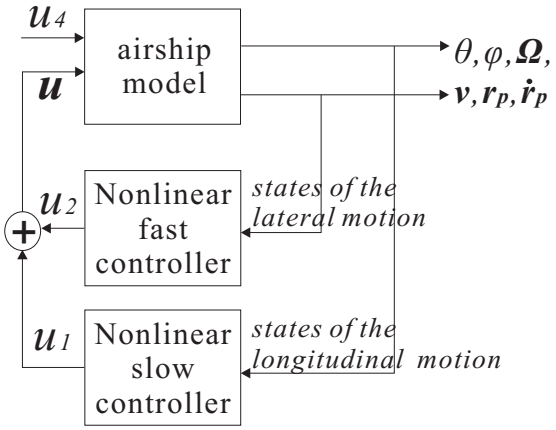

图 A.27: 基于奇摄动理论的三维运动控制框架

图A.30 和A.31 的仿真显示了飞艇在三维空间的转向情况。在这个仿真里，ϕ 在开始的100秒里被稳定在10 度，之后其被控制稳定到零度。图A.31显示飞艇朝$+e_2$ (也就是$-y$) 方向转向。

A.6 总结

本文所研究的一种利用可移动质量块控制姿态，用质量可调节的内部气囊控制升降的新型飞艇为无人自主航行器提供了一种新的驱动机制。通过牛顿-欧拉方法，本文第一次提出了这种飞艇在三维控制的八自由度完整模型。由于存在内部动态以及自身质量的变化，这种新型飞艇模型比常规飞艇的要复杂很多。这篇论文通过将飞艇的机体和可移动质量块看做两个独立的质点来建模，从而使得建模得到了简化。通过分析，以及大量的仿真，飞艇的基本性能得到了全面的展示。

对于复杂的非线性模型，本论文首先基于LQR和输入输出线性化推导了两种控制，但是结果显示这两个控制效果并不理想，因此寻求一个合适非线性控制器显得十分的必要，但这也是一个挑战。由于考虑的飞艇模型不能够被完全精确反馈线性化，本论文提出了一种新的分析思路，那就是从一些简化的模型入手，通过分析简化的模型得到的一些有用的结论。然后将这些结论推广到更为复杂，以至最后完整的模型。这种思路被证明是有效的。最后对于复杂模型获得了最大的反馈线性化，内部动态的稳定性得到了保证，并且得到了解析解。这些成果都是不可能直接从复杂模型上得到的。对各种简化特例中的飞艇

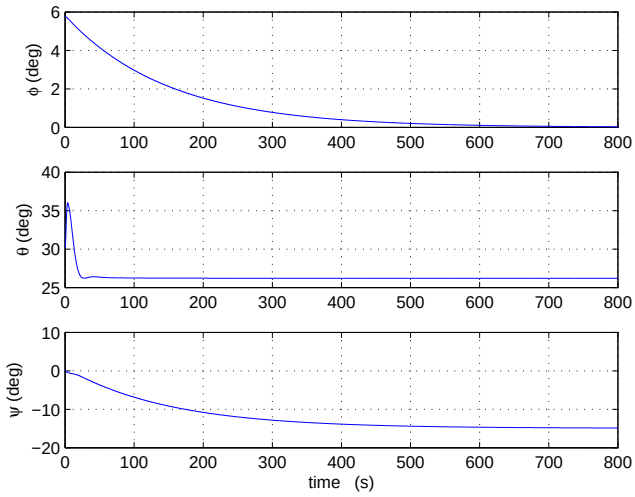

图 A.28: 在有初始误差的情况下，欧拉角的动态变化情况。

模型，绕重心的转动动量在设计非线性反馈控制器上起到了关键的作用。

本文通过奇摄动方法第一次建立这种机制的航行器在三维空间的姿态控制框架。通过本文提出的控制框架，飞艇在俯仰通道和滚转通道的姿态角、航迹角都能得到控制。在姿态角得到控制的基础上，轨迹的控制可以得到实现。

浮力驱动的飞艇是一种新型的概念，目前还处在研究的阶段。本论文研究了它的一些基本理论性问题，目前还存在大量尚未解决的问题，其中最主要的几个问题是：(1)需要验证这些控制器在系统参数发生变化时的鲁棒性，一般来说如果有内部可移动的质量块，这必将导致很多系统参数随着质量块的运动而变化。(2)这种依靠浮力驱动的飞艇虽然节能，可以取得更长的滞空时间和更远的航程。但是其在抗扰动的能力上肯定不足，因此这种浮力驱动的机制结合常规的动力推进就显得很有必要。(3)这种飞艇的导航以及任务的规划需要得到研究。

本文提出的建模方法、动态分析方法、以及控制器的设计对于类似机制的系统都是非常有意义的，例如对于水下滑翔机器人以及返回时卫星等等。

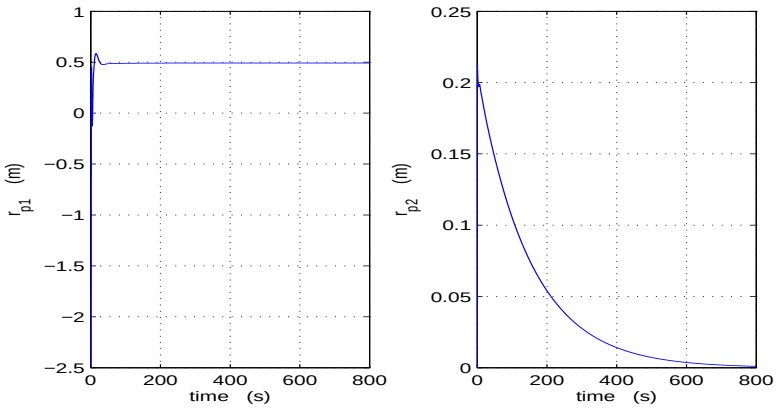

图 A.29: 质量块的运动情况。

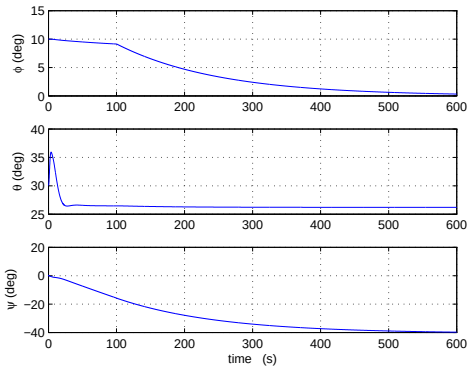

图 A.30: 在转向情况下欧拉角的动态

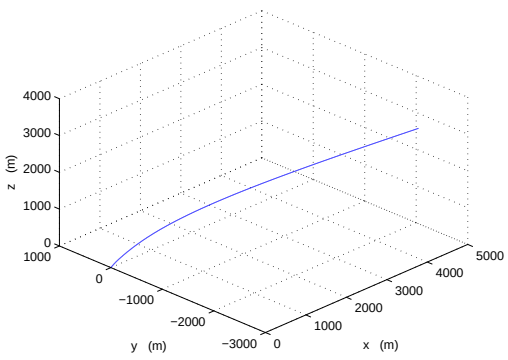

图 A.31: 转向情况下的轨迹